

BLDSC no:- DX227429



Pilkington Library

Author/Filing Title HILEY, M. J.

Accession/Copy No.

Vol. No.	Class Mark
---------------	------------------

*date due
for return :-
9 FEB 1999
No renewal*

~~Johns copy~~
REFERENCE ONLY

0401919749



BADMINTON PRES
UNIT 1 BROOK S
YSTON
LEICESTER, LE7 1
ENGLAND

MECHANICS OF THE GIANT CIRCLE ON HIGH BAR

by

MICHAEL JOHN HILEY


A Doctoral thesis

**Submitted in partial fulfilment of the requirements for the award of
Doctor of Philosophy of Loughborough University**

April 1998

**Supervisors : Dr M.R. Yeadon
Dr D.G. Kerwin**

© Michael John Hiley, 1998

 UNIVERSITY OF MICHIGAN Library
Date <i>Dec 98</i>
Class
Acc No. <i>040191974</i>

K0633923

ABSTRACT**Mechanics of the giant circle on high bar
M.J. Hiley, Loughborough University, 1998**

In Men's Artistic Gymnastics the accelerated backward giant circle on high bar is used to generate the rotation required for the subsequent skill. When used prior to a dismount at the end of a high bar routine the gymnast performs a number of backward giant circles in order to generate sufficient rotation to perform the dismount. The most common dismounts from high bar require the gymnast to perform two backward somersaults in the layout position. Of all the dismounts performed by elite male gymnasts it is the double layout somersault dismount which requires the most rotation. Observations of elite gymnasts have shown that two different techniques may be adopted in the accelerated giant circle performed before release. Since gymnasts are able to perform the dismount from both types the question arises: "What is the best technique for increasing rotation using accelerated backward giant circles?"

A four segment simulation model was developed comprising arms, torso, thigh and lower leg. The high bar and the gymnast's shoulder structure were modelled as damped linear springs. The inertia data for the model were obtained from anthropometric measurements of an elite gymnast using the inertia model of Yeadon (1990a). Joint angles in the form of piecewise quintic functions of time were used as input to the model. Joint torques predicted by the simulation model were limited using subject specific muscle data collected using an isokinetic dynamometer (King, 1998).

The simulation model was evaluated using kinetic and kinematic data recorded from the elite gymnast performing accelerated giant circles. Two video cameras were used to record the subject performing accelerated giant circles on a high bar instrumented with strain gauges. The simulation model was evaluated by driving the simulation model using splined joint angle time histories from the video analysis and comparing the whole body angles of rotation and reaction forces with the measured values.

The simulation model was implemented with an optimisation algorithm which was used to maximise the angular momentum about the model's mass centre after performing $1\frac{3}{4}$ giant circles. The optimisation algorithm manipulated the parameters which defined the joint angle time histories in order to obtain the optimum technique.

During the optimisation procedure two optima were found. The first had a slightly higher value for the angular momentum about the model's mass centre, and was called the "global" optimum. The two optima closely resembled the two different techniques used by gymnasts. However, these optima were so close that for different muscle strength the local optimum would become the global optimum. This explains why there are two distinct techniques used by gymnast.

PUBLICATIONS

Conference presentations

Hiley, M.J., Yeadon, M.R. & Kerwin, D.G. (1994). Simulation of a double layout dismount from high bar. *In Proceedings of the Biomechanics Section of the British Association of Sports and Exercise Science* **19**, 37-40. Glasgow: BASES.

Hiley, M.J., Yeadon, M.R. & Kerwin, D.G. (1995). A single segment simulation model of a gymnast on an elastic high bar. *In Proceedings of the Biomechanics Section of the British Association of Sports and Exercise Science* **20**, 45-48. Glasgow: BASES.

Hiley, M.J., Yeadon, M.R. & Kerwin, D.G. (1996). Optimisation of the accelerated backward giant circle on the high bar. *In Proceedings of the Biomechanics Section of the British Association of Sports and Exercise Science* **21**, 47-40. Glasgow: BASES.

ACKNOWLEDGEMENTS

I wish to express my thanks to:

My supervisors Dr M.R. Yeadon and Dr D.G. Kerwin for their advice and continued encouragement,

The Biomechanics research group for their assistance, friendship and support (Lesley, Jo, Sharon, Matt, Mark, Mark, John and Takeru),

James Boyes for his assistance with the data collection sessions,

Continental Sports Ltd for the use of the high bar,

David Britton and the Mechanical Engineering Department at Loughborough University for their help with the instrumentation of the high bar,

The High Performance Laboratory at Lilleshall for their help and the use of their Kin-Com isokinetic dynamometer,

DeMontfort University for the use of their Penny and Giles goniometers,

and

The Sports Council of Great Britain and Northern Ireland and the United Kingdom Sports Council for their financial support.

DEDICATION

Mum and Dad

TABLE OF CONTENTS

	Page
Abstract	i
Statement of responsibility	ii
Publications and Presentations	iii
Acknowledgements	iv
Dedication	v
Table of Contents	vi
List of Figures	xiv
List of Tables	xxiv
CHAPTER 1 : INTRODUCTION	1
1.1 The area of study	1
1.2 Previous research	2
1.3 Statement of purpose	3
1.4 Questions	4
1.5 Chapter organisation	6
CHAPTER 2 : REVIEW OF LITERATURE	8
2.1 Introduction	8
2.2 Development of the high bar and review of coaching literature	8
2.3 Research on the backward giant circle	17
2.3.1 Definitions of experimental and theoretical research	17
2.3.2 Observational/Experimental research	19
Summary	22
2.3.3 Theoretical research	23
2.3.4 Summary and views on theoretical optimisations	27
2.4 Techniques of investigation	29
2.4.1 Force measurement	29
Strain gauges	30
Summary	35
Isokinetic dynamometry and the determination of muscle parameters	35

Summary	40
2.4.2 Segmental inertia parameters	41
2.4.3 Three-dimensional analysis	45
Synchronisation of force and video data	47
Three-dimensional reconstruction	48
Accuracy of reconstruction	49
Curve fitting	50
Summary	52
2.4.4 Simulation	53
2.4.5 Optimisation	54
2.5 Summary	56
CHAPTER 3 : DEVELOPMENT OF A FOUR SEGMENT SIMULATION MODEL	57
3.1 Introduction	57
3.2 Development of a single segment simulation model of a gymnast swinging on an elastic high bar	57
3.2.1 Introduction	57
3.2.2 Methods	57
Equations of motion	59
Solution of equations	61
Input/Output	62
3.3 Development of a four segment elastic gymnast swinging on an elastic high bar	62
3.3.1 Introduction	62
3.3.2 Methods	63
Equations of motion	67
Solution of equations	73
Variable step length integration procedure	76
Output	76
Calculation of mass centre location and angle of rotation	77
Calculation of angular momentum	77
Calculation of the energy in the system	79
Input	80
Inertia parameters	80
Spring parameters	81
Joint angle time histories	81

Joint torque limit	85
3.4 Summary	86
CHAPTER 4 : MUSCLE PARAMETERS	87
4.1 Introduction	87
4.2 Methods	87
4.2.1 Data collection	87
Written consent	88
Calibration of the dynamometer	88
Calibration of the goniometer	88
Attaching the goniometer	90
Positioning the subject	90
Exercise protocol	90
4.2.2 Data analysis	91
Editing data files from the goniometer and dynamometer	91
Synchronisation of the goniometer and dynamometer data files	93
Optimisation procedure	94
Obtaining joint angle and joint angular velocity time histories	94
Corrections to synchronised muscle data	95
Conversion of crank force to crank torque	95
Segment weight correction	95
Conversion of crank torque to joint torque	95
Extrapolation of torque - angle relationship	96
4.2.3 Muscle model	97
Method - Six parameter double hyperbolic relationship	97
Extension of the torque - angular velocity relationship to include angle dependence	99
Optimisation procedure	100
Range of data for the surface fit	100
4.3 Summary	101
CHAPTER 5 : KINETIC ANALYSIS OF THE GIANT CIRCLE	102
5.1 Introduction	102
5.2 Inertia parameters	102

5.2.1	Introduction	102
5.2.2	Methods	102
5.3	Video analysis	103
5.3.1	Introduction	103
5.3.2	Data collection protocol	103
5.3.3	Analysis of video data	106
	Digitisation	106
5.4	Force measurement	108
5.4.1	Introduction	108
5.4.2	Calibration of the force measurement system	108
	Arrangement of the strain gauges	108
	Methods	109
	Analysis of the calibration data	112
5.4.3	Collection of force data	112
	Data collection	112
5.4.4	Analysis of force data	113
5.5	Synchronisation of force and video	113
5.5.1	Introduction	113
5.5.2	Collection of force and synchronisation data	113
5.6	Obtaining spring parameters	114
5.6.1	Introduction	114
5.6.2	Stiffness and damping coefficients of the bar	115
	Determination via static loading	115
	Data collection	115
	Data analysis	116
	Determination from kinetic and kinematic analysis	117
5.6.3	Stiffness and damping coefficients of the shoulder spring	118
	Initial estimate of shoulder spring stiffness coefficient	118
5.6.4	Optimisation of the spring parameters	118
	Methods	118
5.7	Summary	120
CHAPTER 6 :	RESULTS	121
6.1	Introduction	121
6.2	Muscle parameters	121
6.2.1	Introduction	121

6.2.2 Calibration of the Kin-Com machine and goniometer	121
Estimate of accuracy	121
6.2.3 Raw joint torque data	122
6.2.4 Smoothed 3-D joint torque surfaces	124
Estimate of accuracy	124
6.3 Kinematic analysis of the giant circle	126
6.3.1 Introduction	126
6.3.2 Inertia parameters	126
6.3.3 Estimation of accuracy and precision	127
6.3.4 Obtaining model parameters	128
Regular giant circles	128
Path and velocity of the mass centre	128
Bar displacements	130
Joint angle time histories	132
Accelerated giant circles	135
Path and velocity of the mass centre	135
Bar displacements	137
Joint angle time histories	140
Splined joint angle time histories	143
Segment lengths calculated from the reconstructed co-ordinates	145
6.3.5 Summary	149
6.4 Kinetic analysis of the giant circle	151
6.4.1 Introduction	151
6.4.2 Calibration of the force measurement system	151
The load cell	151
Cross talk	151
Regression/Calibration equations	152
6.4.3 Converting strain data into force	156
Estimate of accuracy	156
Comparison of the force produced during different trials/ circles	158
Regular giant circles	158
Accelerated giant circles	160
6.4.4 Summary	162
6.5 Synchronisation of force and video	163
6.5.1 Introduction	163
6.5.2 Synchronised data	163
Estimate of accuracy	163

Regular giant circles	164
Accelerated giant circles	165
6.6 Spring parameters	167
6.6.1 Introduction	167
6.6.2 Stiffness and damping coefficients of the bar	167
Determination via static loading	167
Determination from force analysis of the giant circle	168
6.6.3 Stiffness coefficient of the shoulders	175
Estimate obtained from displacement time history of the shoulders	175
6.6.4 Damping coefficient of the bar and shoulder springs	176
Initial estimates	176
6.7 Summary	180
CHAPTER 7 : EVALUATION OF THE SIMULATION MODELS	182
7.1 Introduction	182
7.2 One segment model vs. kinetic and kinematic analysis	183
7.2.1 Introduction	183
7.2.2 Methods	183
7.2.3 Results and Discussion	184
7.2.4 Conclusions	187
7.3 One segment model vs. four segment model	187
7.3.1 Introduction	187
7.3.2 Methods	188
7.3.3 Results and Discussion	189
7.3.4 Conclusions	190
7.4 Three segment model	191
7.4.1 Introduction	191
7.4.2 Methods	192
7.4.3 Results and Discussion	193
7.4.4 Conclusions	199
7.5 Four segment vs. kinetic and kinematic analysis	199
7.5.1 Introduction	199
7.5.2 Methods	199
7.5.3 Results and Discussion	200
7.5.4 Conclusions	206
7.6 Summary	207

CHAPTER 8 : OPTIMISATION OF THE ACCELERATED BACKWARD GIANT CIRCLE	209
8.1 Introduction	209
8.2 Three segment simulation model	209
8.2.1 Introduction	209
8.2.2 Methods	209
8.2.3 Results and Discussion	212
Without torque limit	212
With torque limit	216
Sensitivity analysis	218
Varying the function used to define the joint angle time histories	218
Varying the inertia data	220
8.2.4 Conclusions	221
8.3 Four segment simulation model	224
8.3.1 Introduction	224
8.3.2 Method	225
Sensitivity analysis	228
Varying the strength of the muscle models	228
Varying the inertia parameters	229
Varying the release angle	229
Varying the stiffness coefficients of the bar	229
Varying the initial angular velocity	230
8.3.3 Results and Discussion	231
Sensitivity analysis	238
Varying the strength of the muscle models	238
Varying the inertia parameters	250
Varying the release angle	252
Varying the stiffness coefficients of the bar	254
Varying the initial angular velocity	256
8.3.4 Conclusions	257
 CHAPTER 9 : SUMMARY AND DISCUSSION	 259
9.1 Introduction	259
9.2 Answers to the research questions	259
9.3 Future directions	264

9.3.1 Introduction	264
9.3.2 Data collection	264
9.3.3 Simulation	264
The bar	264
Knee flexion	265
Double layout backward somersault dismount	265
Strength of the muscle models	265
Airborne skills	266
Other skills	266
Asymmetric bars	266
REFERENCES	268
APPENDICES	280

LIST OF FIGURES

	Page
CHAPTER 1	
Figure 1.1. Two types of accelerated giant circle.	1
Figure 1.2. Components of the four segment simulation model.	4
CHAPTER 2	
Figure 2.1. F.I.G. high bar specifications.	10
Figure 2.2. Bar construction (Continental).	10
Figure 2.3. The Tkatchov.	11
Figure 2.4. The double layout backward somersault dismount.	11
Figure 2.5. The Kovacs.	11
Figure 2.6. The backward giant circle.	12
Figure 2.7. A handguard (adapted from Readhead, 1987).	12
Figure 2.8. The elementary swing.	14
Figure 2.9. Torque created by the gymnast during swinging.	15
Figure 2.10. Friction forces between the hands and the bar (adapted from Hay, 1990).	15
Figure 2.11. The beatswing action.	16
Figure 2.12. The two general techniques used by gymnasts winding up for a dismount.	17
Figure 2.13. Forward and inverse dynamics (adapted from Yeadon and Challis, 1994).	18
Figure 2.14. Experimental and theoretical model of scientific method (adapted from Yeadon and Challis, 1994).	18
Figure 2.15. The four quadrants of the backward giant circle.	20
Figure 2.16. Angular velocity during two accelerated and one dismount giant circle (adapted from Cheetham, 1985).	21
Figure 2.17. Mass centre trajectory for a backward giant circle (adapted from Bauer, 1983).	24
Figure 2.18. A foil alloy strain gauge.	31
Figure 2.19. Wheatstone bridge (adapted from Scott and Owens, 1992).	31
Figure 2.20. Quarter bridge circuit (adapted from Scott and Owens, 1992).	32
Figure 2.21. Half bridge circuit (adapted from Scott and Owens, 1992).	33
Figure 2.22. Strain gauge arrangement for measuring force on the high bar (adapted from Ishii and Komatsu, 1987).	34
Figure 2.23. Force - velocity relationship found by Hill (1970).	37
Figure 2.24. Force - velocity relationship found by Edman (1988).	38

Figure 2.25.	Inertia model of Yeadon (1990b) (adapted from Yeadon, 1990b).	45
Figure 2.26.	Collinearity condition.	49
 CHAPTER 3		
Figure 3.1.	Free body diagram of the single segment model.	58
Figure 3.2.	The angles defining the configuration of the four segment simulation model.	66
Figure 3.3.	Free body diagram of the four segment model.	66
Figure 3.4.	Free body diagram of the arm segment.	67
Figure 3.5.	Amended free body diagram of the arm segment.	67
Figure 3.6.	Free body diagram of the torso segment.	70
Figure 3.7.	Free body diagram of the thigh segment.	71
Figure 3.8.	Free body diagram of the shank segment.	71
Figure 3.9.	Definition of the rotation angle.	77
Figure 3.10.	The quintic function $q(x)$ used for changing joint angles.	83
Figure 3.11.	The first derivative of the quintic function $q(x)$ which defines the angular velocity of the angle change.	83
Figure 3.12.	The second derivative of the quintic function $q(x)$ which defines the angular acceleration of the angle change.	83
Figure 3.13.	The curve used for changing the joint angles using a square wave acceleration curve.	84
Figure 3.14.	The first derivative of the change in angle curve, using the squarewave acceleration curve, which defines the angular velocity of the angle change.	84
Figure 3.15.	The square wave acceleration curve which defines the acceleration of the angle change.	85
 CHAPTER 4		
Figure 4.1.	Mean ADC counts from calibration of the goniometer (filled circles used in the second linear regression).	89
Figure 4.2.	All files were edited to obtain the central eccentric - concentric portion of each trial.	91
Figure 4.3.	The start and finish of the eccentric and concentric portions of the trial were identified and labelled p1 to p4.	92
Figure 4.4.	Example of a goniometer file which has been edited to obtain the central eccentric - concentric portion.	93
Figure 4.5.	Force - velocity relationship found by Hill (1970).	97
Figure 4.6.	Force - velocity relationship found by Edman (1988).	97

Figure 4.7.	General shape of the four parameter exponential function.	98
Figure 4.8.	General shape of the two parameter exponential function.	98
Figure 4.9.	General shape of the six parameter exponential function.	99
 CHAPTER 5.		
Figure 5.1.	Arrangement of the video cameras and data capture system.	104
Figure 5.2.	Arrangement of the calibration poles and markers.	105
Figure 5.3.	Heights of the calibration markers used in the calibration volume.	105
Figure 5.4.	The photocell arrangement attached to the uprights of the high bar.	106
Figure 5.5.	Arrangement of strain gauges bonded to each end of the high bar.	109
Figure 5.6.	The data capture system used to collect the strain data.	109
Figure 5.7.	The load cell and loading system used for vertical calibration.	110
Figure 5.8.	The calibrated load cell used on the calibration of the force measurement system.	111
Figure 5.9.	The load cell and the loading system for horizontal calibration.	111
Figure 5.10.	Arrangement of loops and chains for loading the bar at two points.	112
Figure 5.11.	Location of the camera relative to the high bar during static loading.	115
Figure 5.12.	The calibration poles and markers in the field of view in order to determine the scale factor.	116
Figure 5.13.	Method used to load the high bar.	116
 CHAPTER 6		
Figure 6.1.	Raw data obtained using the average angle range for hip flexion.	123
Figure 6.2.	Raw data obtained using the average angle range for hip extension.	123
Figure 6.3.	Raw data obtained using the average angle range for shoulder flexion.	123
Figure 6.4.	Raw data obtained using the average angle range for shoulder extension.	124
Figure 6.5.	Surface fit using the average angle range for hip flexion.	125
Figure 6.6.	Surface fit using the average angle range for hip extension.	125
Figure 6.7.	Surface fit using the average angle range for shoulder flexion.	125
Figure 6.8.	Surface fit using the average angle range for shoulder extension.	126

Figure 6.9.	Path of the mass centre during one regular giant circle from trial 10.	128
Figure 6.10.	History of the angular velocity of the rotation angle during one regular giant circle from trial 10.	129
Figure 6.11.	Time history of the vertical displacement of the centre of the bar for the first regular giant circle of trial 10.	130
Figure 6.12.	Time history of the horizontal and lateral displacement (dashed line) of the centre of the bar for the first regular giant circle of trial 10.	131
Figure 6.13.	History of the horizontal and vertical displacement of the centre of the bar plotted against rotation angle for the second regular giant circle from trail 10.	132
Figure 6.14.	History of the hip angle against rotation angle for the third regular giant circle of trial 10	133
Figure 6.15.	History of the shoulder angle against rotation angle for the third regular giant circle of trial 10.	134
Figure 6.16.	Path of the mass centre during an accelerated giant circle with release (trial 4).	136
Figure 6.17.	Time history of the angular velocity of the rotation angle (trial 4).	136
Figure 6.18.	Time history of the vertical displacement of the centre of the bar during trial 4.	138
Figure 6.19.	Time history of the horizontal displacement of the centre of the bar during trial 4.	138
Figure 6.20.	Histories of the horizontal and vertical displacements of the bar (trial 4).	140
Figure 6.21.	Histories of the horizontal and vertical velocities of the bar (trial 4).	140
Figure 6.22.	History of the hip angle against rotation angle from trial 4.	141
Figure 6.23.	History of the shoulder angle against rotation angle from trial 4.	142
Figure 6.24.	History of the knee angle against rotation angle from trial 4.	142
Figure 6.25.	<i>Splined and raw hip and shoulder angles from trial 4.</i>	143
Figure 6.26.	Angular velocities obtained from the splined joint angle time histories of the hips and shoulders from trial 4.	144
Figure 6.27.	Angular accelerations obtained from the splined joint angle time histories of the hips and shoulders from trial 4.	145
Figure 6.28.	Arm length during trial 10.	147
Figure 6.29.	Torso length during trial 10.	147
Figure 6.30.	Sum of the arm, torso and leg segment lengths during trial 10.	148

Figure 6.31.	Sum of the arm and torso segment lengths during trial 10 (dashed line is the sum of the arm, torso and leg lengths overlaid).	149
Figure 6.32.	Data points obtained during the calibration of the load cell.	152
Figure 6.33.	Strain recorded in the vertical direction (filled circles) plot against vertical load with strain recorded simultaneously in the horizontal direction (filled squares).	153
Figure 6.34.	Strain recorded in the vertical direction plot against vertical load with strain recorded simultaneously in the horizontal direction after correcting for the offset.	153
Figure 6.35.	Linear regression between the load applied to the bar and the strain recorded in the vertical direction.	154
Figure 6.36.	Linear regression between the load applied to the bar and the strain recorded in the vertical direction when loading at two points.	155
Figure 6.37.	Linear regression between the load applied to the bar and the strain recorded in the horizontal direction.	155
Figure 6.38.	Vertical force trace with error estimates (the dashed lines) for a regular giant circle.	157
Figure 6.39.	Horizontal force trace for a regular giant circle.	157
Figure 6.40.	Vertical force trace for two regular giant circles.	159
Figure 6.41.	Horizontal force trace for two regular giant circles.	159
Figure 6.42.	Vertical force trace for two accelerated giant circles.	161
Figure 6.43.	Horizontal force trace for two accelerated giant circles.	162
Figure 6.44.	The vertical and horizontal force recorded in trail 10 plot against rotation angle.	165
Figure 6.45.	The resultant force recorded in trail 10 plot against rotation angle.	165
Figure 6.46.	Horizontal and vertical reaction forces plot against rotation angle (trail four).	166
Figure 6.47.	Regression line and single points for load against vertical bar displacement.	167
Figure 6.48.	Vertical and horizontal bar displacements for the first regular giant circle of trial 10.	168
Figure 6.49.	Estimated force and recorded force against vertical bar displacement.	172
Figure 6.50.	Recorded force (a) and estimated force (b) against vertical bar displacement.	175
Figure 6.51.	History of the cost function value.	178

Figure 6.52.	History of the stiffness coefficients.	179
Figure 6.53.	History of the shoulder spring damping coefficient.	179
Figure 6.54.	History of the bar spring damping coefficient.	180
CHAPTER 7		
Figure 7.1.	Total energy in the system and its components when the bar is modelled as a linear spring with no damping.	185
Figure 7.2.	Contributions of the kinetic energies (linear and rotational) and strain energy to the total energy when the bar is modelled as a damped linear spring.	186
Figure 7.3.	Vertical bar displacement when the bar is modelled as a linear spring with no damping.	186
Figure 7.4.	Total energy in the four segment system and its components when the bar is modelled as a linear spring with no damping.	189
Figure 7.5.	Joint angle time history of the shoulder joint from simulation one.	193
Figure 7.6.	Time history of the rotation angle from simulation one.	194
Figure 7.7.	Time history of the vertical reaction force during simulation one.	194
Figure 7.8.	Time history of the shoulder joint angular velocity (solid line) and acceleration (dashed line, in $.s^{-1}$) from simulation one.	195
Figure 7.9.	Time history of the shoulder torque during simulation one.	195
Figure 7.10.	Time history of the energy during simulation one.	196
Figure 7.11.	Angle at the hip during simulation two.	196
Figure 7.12.	Time history of the shoulder joint angular velocity (solid line) and acceleration (dashed line, in $.s^{-1}$) from simulation two.	197
Figure 7.13.	Torque at the hip during simulation two (solid line) along with the torque at the hip had the angle change not occurred.	198
Figure 7.14.	Energy during simulation two.	198
Figure 7.15.	The simulated (solid line) and recorded (dashed line) time history of the rotation angle from trail four.	201
Figure 7.16.	The simulated (solid line) and recorded (dashed line) time history of the horizontal bar displacements from trail 11.	202
Figure 7.17.	The simulated (solid line) and recorded (dashed line) time history of the vertical bar displacements from trail 11.	203
Figure 7.18.	The simulated (solid line) and recorded (dashed line) time history of the horizontal force at the bar from trail 11.	203
Figure 7.19.	The simulated (solid line) and recorded (dashed line) time history of the vertical force at the bar from trail 11.	204

Figure 7.20.	Joint torques at the shoulders obtained from the simulation model (solid line) and the maximum joint torques estimated by the 3D muscle surfaces (dashed line) during trial 11.	205
Figure 7.21.	Joint torques at the hips obtained from the simulation model (solid line) and the maximum joint torques estimated by the 3D muscle surfaces (dashed line) during trial 11.	205
Figure 7.22.	Joint torques at the hips obtained from the simulation model (solid line) and the angular velocity of the hip joint (dashed line) during trial 11.	206

CHAPTER 8

Figure 8.1	Angles at the hips and shoulders.	211
Figure 8.2.	Optimal solution with no joint torque limit.	212
Figure 8.3.	Angular velocity at a rotation angle of 270° against rotation angle at mid-flexion.	213
Figure 8.4.	The four quadrants of the giant circle.	213
Figure 8.5.	Torques required to maintain a straight body during a backward giant circle.	214
Figure 8.6.	Two flexion actions performed either side of the lowest point.	215
Figure 8.7.	Two extension actions performed either side of the highest point.	215
Figure 8.8.	Optimal solution with 250 Nm torque limit at the shoulders.	216
Figure 8.9.	The effect of joint torque limit on the optimal solution using the three segment simulation model.	217
Figure 8.10.	Peak shoulder joint torque against rotation angle at mid-flexion.	217
Figure 8.11.	Optimal solutions obtained using the function with the square acceleration curve to define the joint angle time histories.	219
Figure 8.12.	Optimal solutions obtained using the quintic function and the function with the square acceleration curve to define the joint angle time histories when no joint torque limit was used.	219
Figure 8.13.	Histories of the joint angle from the optimum solutions where the joint angles were defined using the function with the square acceleration curve (solid line) and the quintic function (dashed line).	220
Figure 8.14.	The effect of using different inertia data on the optimal solution obtained using no joint torque limit.	221

Figure 8.15.	The effect of using different inertia data on the optimal solution obtained using a 250 Nm joint torque limit at the shoulders.	222
Figure 8.16.	Histories of the joint angle from the optimum solutions using the quintic function and the inertia data of tv01 (solid line) and jb01 (dashed line) and the joint torque limit.	223
Figure 8.17.	The joint angle time history comprised four non-overlapping quintic functions.	226
Figure 8.18.	Simulation of an actual double layout somersault dismount performance from the Seoul Olympics (adapted from Yeadon et al., 1990).	232
Figure 8.19.	Sequence of figures representing the optimum technique.	232
Figure 8.20.	Joint angle time histories of the hip and shoulder joints from the optimal solution.	233
Figure 8.21.	Histories of the hip and shoulder joints from the optimal solution plot against rotation angle.	233
Figure 8.22.	History of the maximum shoulder torques given by the muscle models and the torques produced by the simulation model.	234
Figure 8.23.	History of the maximum hip torques given by the muscle models and the torques produced by the simulation model.	235
Figure 8.24.	Histories of the horizontal and vertical displacements of the bar during the optimal solution.	236
Figure 8.25.	Displacements (a) and velocities (b) of the bar prior to release in the optimum solution.	237
Figure 8.26.	Histories of the horizontal and vertical reaction forces at the bar produced by the optimal solution.	238
Figure 8.27.	Histories of the hip and shoulder joint angles from the optimisation where the strength of the muscle models was increased by 10% (original optimisation overlaid in dashed lines).	239
Figure 8.28.	History of the maximum shoulder torques given by the muscle models and the torques produced by the simulation model where the strength of the muscle models was increased by 10%.	240
Figure 8.29.	History of the maximum hip torques given by the muscle models and the torques produced by the simulation model where the strength of the muscle models was increased by 10%.	240

Figure 8.30.	History of the horizontal and vertical displacements of the bar during the the optimum simulation where the joint torque limits were increased.	241
Figure 8.31.	Histories of the hip and shoulder joint angles from the optimisation where the strength of the muscle models was decreased by 10%.	242
Figure 8.32.	History of the maximum shoulder torques given by the muscle models and the torques produced by the simulation model where the strength of the muscle models was decreased by 10%.	242
Figure 8.33.	History of the maximum hip torques given by the muscle models and the torques produced by the simulation model where the strength of the muscle models was decreased by 10%.	243
Figure 8.34.	History of the horizontal and vertical displacements of the bar during the the optimum simulation where the joint torque limits were decreased.	244
Figure 8.35.	Histories from the first three optimisations of the horizontal and vertical bar displacements overlaid.	244
Figure 8.36.	Histories of the hip and shoulder joint angles from the optimisation where the strength of the muscle model was decreased by 25%.	246
Figure 8.37.	History of the maximum shoulder torques given by the muscle models and the torques produced by the simulation model when the strength of the muscle models was decreased by 25%.	246
Figure 8.38.	History of the maximum hip torques given by the muscle models and the torques produced by the simulation model when the strength of the muscle models was decreased by 25%.	247
Figure 8.39.	History of the horizontal and vertical displacements of the bar during the optimum simulation where the joint torque limits were decreased by 25%.	247
Figure 8.40.	Sequence of figures representing the local optimum technique.	248
Figure 8.41.	Histories of the hip and shoulder joint angles from the optimisation used to find the local optimum.	249
Figure 8.42.	History of the horizontal and vertical displacements of the bar during the local optimum simulation.	250

Figure 8.43.	History of the shoulder joint torques and the maximum joint torques given by the muscle models when the optimum joint angle time histories were used with the inertia data of subject tv01.	251
Figure 8.44.	History of the hip joint torques and the maximum joint torques given by muscle model when the optimum joint angle time histories were used with the inertia data of subject tv01.	251
Figure 8.45.	Histories of the hip and shoulder joint in the optimisation where the inertia data of subject tv01 was used.	252
Figure 8.46.	History of the hip joint torques and the maximum joint torques given by the muscle models during the optimum solution when the inertia data of subject tv01 was used with the torque limits of jb01.	253
Figure 8.47.	History of the shoulder joint torques and the maximum joint torques given by the muscle models during the optimum solution when the inertia data of subject tv01 was used with the torque limits of jb01.	253
Figure 8.48.	Histories of the hip and shoulder joint angles from the optimisation where each simulation finished at 607°.	254
Figure 8.49.	Histories of the horizontal and vertical bar displacements from the optimisation where each simulation finished at 607°.	254
Figure 8.50.	Time history of the hip and shoulder joint torques produced by the simulation model expressed as a percentage of the peak torques given by the muscle models when the stiffness of the bar was increased.	255
Figure 8.51.	Time history of the hip and shoulder joint torques produced by the simulation model expressed as a percentage of the peak torques given by the muscle models when the stiffness of the bar was decreased.	256
Figure 8.52.	Time histories of the hip and shoulder joint angles from the optimisation where the initial angular velocity of the model was reduced by half.	257

LIST OF TABLES

	Page
CHAPTER 6	
Table 6.1. Ranges of motion during hip flexion	122
Table 6.2. Rms differences between the raw data and the surface fits	124
Table 6.3. The four, three and single segment inertia data for subject jb01	127
Table 6.4. The four, three and single segment inertia data for subject tv01	127
Table 6.5. Peak angular velocities for regular giant circles (trial 10)	130
Table 6.6. The range of vertical and horizontal bar displacement during regular giant circles	131
Table 6.7. Rms values for the difference on bar displacement (m) between regular giant circles from trial 10	132
Table 6.8. Rms values for the difference in hip and shoulder angle time histories (°) between regular giant circles from trial 10	135
Table 6.9. Peak angular velocities for accelerated giant circles	137
Table 6.10. The range in vertical and horizontal displacements during the accelerated giant circles	137
Table 6.11. Rms values for the difference in bar displacement between the accelerated giant circle trials	139
Table 6.12. Rms values for the difference in hip and shoulder joint angle time histories (°) between accelerated giant circles from trials 4 and 11	143
Table 6.13. Segment lengths calculated from trial 10 (regular giant circles)	146
Table 6.14. New inertia parameters for subject jb01	147
Table 6.15. Results of linear regressions forced through the origin	153
Table 6.16. Peak forces expressed in Newtons and bodyweights for trial 10	158
Table 6.17. Rms values for the difference in force between regular giant circles from trial 10 (also expressed as a percentage of the range of force)	159
Table 6.18. Peak forces expressed in Newtons and bodyweights for trials 4 and 11	160
Table 6.19. Peak forces for the giant circle performed before the three-quarter circle containing the release for trials 4 and 11	160
Table 6.20. Rms values for the difference in force between two accelerated giant circle trials (also expressed as a percentage of the range of force)	161
Table 6.21. Rotation angle at peak horizontal and vertical reaction forces (trial 4)	164

Table 6.22.	Rotation angle at peak horizontal and vertical bar displacements (trial 4)	166
Table 6.23.	Peak bar displacements in the horizontal and vertical directions for trial 10	169
Table 6.24.	Peak bar displacements in the horizontal and vertical directions for trial 4 and 11	169
Table 6.25.	Results of linear regressions between vertical bar displacement and force	170
Table 6.26.	Results of linear regressions between horizontal bar displacement and force	171
Table 6.27.	Rms difference between estimated and recorded vertical force	172
Table 6.28.	Rms difference between estimated and recorded horizontal force	172
Table 6.29.	Results of linear regressions between vertical bar displacement and velocity and vertical force	174
Table 6.30.	Results of linear regressions between horizontal bar displacement and velocity and force	174
Table 6.31.	Rms difference between estimated and recorded vertical force	175
Table 6.32.	Rms difference between estimated and recorded horizontal force	175
Table 6.33.	Results of the regressions performed on the wrist to hip length and the resultant reaction force at the bar	176
Table 6.34.	Initial spring parameters used in the optimisation procedure	177
Table 6.35.	Final spring parameters obtained from the optimisation procedure	177
Table 6.36.	Spring parameters obtained from the initial plateau in cost function	180

CHAPTER 7

Table 7.1.	Inertia data used in the single segment simulation model (jb01)	183
Table 7.2.	Stiffness and damping coefficients used in the single segment model	184
Table 7.3.	Initial bar displacements and velocities obtained from the video analysis of the accelerated giant circle	184
Table 7.4.	Results obtained from the simulations using the single segment model and those obtained from the video analysis	185
Table 7.5.	Inertia data used in the four segment simulation model (jb01)	188

Table 7.6.	Results obtained from the simulations using the single and four segment model and those obtained from the video analysis	190
Table 7.7.	Vertical bar displacements obtained from the simulations using the single and four segment model and those obtained from the video analysis	190
Table 7.8.	Inertia data used in the three segment simulation model (jb01)	192
Table 7.9.	Maximum and rms differences between simulated and recorded rotation angles	201
Table 7.10.	Maximum and rms differences between simulated and recorded bar displacements	202
Table 7.11.	Maximum and rms differences between simulated and recorded forces	204
 CHAPTER 8		
Table 8.1.	Inertia data used in the three segment optimisation of the backward giant circle	210
Table 8.2.	The optimum accelerated giant circle (without joint torque limit)	212
Table 8.3.	The optimum accelerated giant circle with torque limit	216
Table 8.4.	The optimum accelerated giant circle using the function with a square acceleration curve	219
Table 8.5.	The optimum accelerated giant circle with and without torque limit using the inertia data tv01	220
Table 8.6.	Inertia parameters for subject jb01	225
Table 8.7.	Spring parameters used in the optimisation	225
Table 8.8.	Initial bar displacements and velocities obtained from the video analysis of the accelerated giant circles	226
Table 8.9.	Inertia parameters for subject tv01	229
Table 8.10.	Spring parameters used in the sensitivity analysis	230
Table 8.11.	Initial bar displacements and velocities obtained from the video analysis of the regular giant circles	231
Table 8.12.	Displacement and velocity of the mass centre at release	231
Table 8.13.	Maximum and minimum reaction forces during the optimum simulation	238

CHAPTER 1

INTRODUCTION

1.1 The area of study

In Artistic Gymnastics the men compete on six pieces of apparatus: the floor, pommel horse, rings, vault, parallel bars and high bar. Of the six pieces only routines performed on the parallel bars, rings and high bar include swings in the vertical plane. On the rings and the parallel bars held strength positions are performed which form pauses between the swings. It is only on the high bar that a routine is comprised from only circling skills. A high bar performance in Men's Artistic Gymnastics is made up from a number of swinging skills which must include a release and regrasp skill and a dismount. Many of the swinging skills are linked by regular giant circles, whereas the release and dismount skills are preceded by accelerated giant circles. The backward giant circle is therefore a fundamental skill upon which the majority of the routine is based.

For a regular giant circle the aim is merely to swing from handstand to handstand, whereas the purpose of the accelerated giant circle is to increase the gymnast's rotation about the bar. The basic technique of the backward giant circle comprises flexion of the body in the lower part of the circle and extension in the upper part. From observation of film and video all gymnasts flex at the hips and shoulders as they pass through the lower part of the giant circle, as shown in Figure 1.1. However, the timing of the extension in the upper part of the circle varies considerably. The two most common techniques are either to extend at or very close to the highest point of the circle (Figure 1.1a) or to maintain the piked body shape through the highest point and extend at or near to the horizontal (Figure 1.1b). The mechanics underlying these techniques is not yet clear.

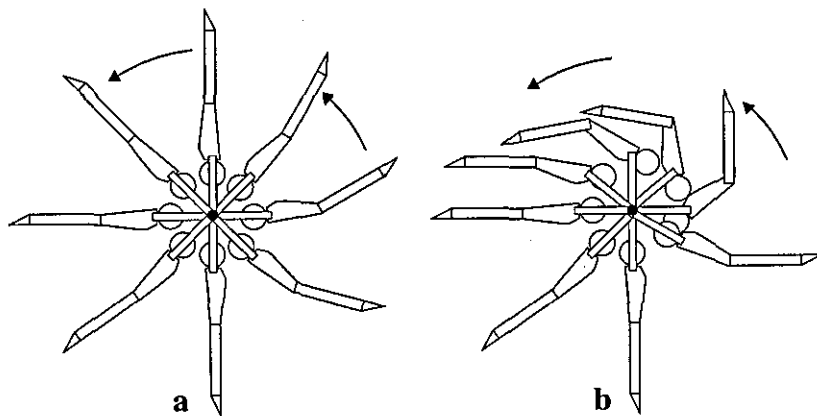


Figure 1.1. Two types of accelerated giant circle.

1.2 Previous research

Previous research on the backward giant circle has been both experimental (based on the collection of data) and theoretical. The experimental research has provided valuable information about the kinetics and kinematics of the backward giant circle. Cheetham (1984) distinguished between three different types of giant circles: the regular giant circle, where the aim is only to swing from handstand to handstand; the accelerated giant circle, where the aim is to increase the angular velocity; and the giant circle immediately prior to a dismount, where the aim depends on the particular dismount used. This study showed that there exist differences in technique between the regular and accelerated backward giant circles. Brüggemann, Cheetham, Alp and Arampatzis (1994) established profiles for the different dismount and regrasp skills to identify similarities and differences between the skills under study. Part of this study looked at the giant circle prior to release. It was found that the major changes of mechanical energy were determined by shoulder and hip flexion and extension movements. It was also found that the knee joint action contributed to energy changes. Another valuable experimental study was carried out by Kopp and Reid (1980) who presented maximum values for the torque and reaction force at the bar during forward and backward giant circles. This information will be useful for comparison with the results of simulations and experimental studies presented in this thesis.

Theoretical studies have modelled the gymnast as a rigid link system swinging in a two-dimensional plane. Dainis (1968) presented a three segment link system. The input to the model took the form of joint torque time histories. Morlock and Yeadon (1988) used a two segment model and applied it to three separate cases of swinging. Again input to the model was in the form of joint torques. Both of these papers have shown that a gymnast circling the high bar may be modelled using rigid links. They have demonstrated that a sufficiently developed model could be a useful tool in explaining gymnastic technique. However, they have also highlighted difficulties in controlling joint angles using joint torques due to difficulties in obtaining joint torques that would produce given joint angle changes. More recently Arampatzis and Brüggemann (1995) presented a 15 segment gymnast with a 12 segment high bar as a method of optimising the giant circle prior to release. The definition of the optimal solution was based on the energy possessed by the gymnast after the giant circle and so the timing of joint actions were linked with storing and retrieving energy from the bar.

Both the experimental and the theoretical studies that have been carried out have limitations. The majority of the experimental studies have investigated regular giant circles giving only a descriptive analysis of the skill. No analysis has been performed on the different body shapes that may be observed as the gymnast passes through the highest point in the accelerated giant circle.

To answer questions about various skills using simulation, the model must be capable of attaining the body configurations used by gymnasts. This requires more detailed modelling of the body than the two segments used by Morlock and Yeadon (1988) and the three segments used by Dainis (1968). However, the model should still be simple enough to facilitate the understanding of the underlying mechanics.

In previous research the elastic properties of the gymnast have been neglected. Although Arampatzis and Brüggemann (1995) modelled the bar as an elastic structure the elastic properties of the shoulder joint were ignored. Neglecting these elastic qualities may lead to an over-estimation of the angular velocity predicted by a simulation model. Any lengthening of the gymnast caused by the extension in the shoulders will lead to an increase in the gymnast's moment of inertia about the bar. At the same time if the shoulder structure behaves like a spring, energy may be stored within this spring and may be returned later to the gymnast/model. These assumptions may lead to limitations in the accuracy of any simulations performed.

The studies of Dainis (1968) and Yeadon and Morlock (1988) used joint torques to alter the joint angles of their models. This approach has the drawback that the resulting joint angles are unknown until the simulation has run. A better method of describing a technique may be in terms of the body shapes the gymnast must achieve. This suggests a more appropriate input for such a simulation model might be time histories of the joint angles rather than joint torques. However, care must be taken using this method as simulations could be performed which exceed the strength characteristics of the gymnast.

1.3 Statement of purpose

In section 1.1 it was highlighted that the backward giant circle is a fundamental skill which forms the basis of the more advanced movements (Kopp and Reid, 1980). Since two gymnasts may use different techniques in the *giant circle* prior to the same release skill, it is the intention of this research project to explain why this occurs. To facilitate this a computer simulation model of a gymnast swinging on the high bar will be developed. The simulation model will be used to provide explanations of the mechanics underlying the techniques of the backward giant circle and to suggest possible improvements. The following research question will be used as a focus for the research project.

What is the optimum technique for the accelerated backward giant circle on high bar ?

As the purpose of the accelerated giant circle is to increase the gymnast's rate of rotation about the bar, the best technique may be defined as that which increases the gymnast's rate of rotation the most. The criterion for the optimised accelerated backward giant circle will therefore be to maximise the angular momentum possessed by the gymnast. Since the more advanced skills preceded by the accelerated backward giant circle require the gymnast to leave go of the bar, the angular momentum about the gymnast's mass centre will be maximised. That is, after the model has performed a flexion action through the lowest point and an extension through the highest point the model should possess greatest angular momentum about its mass centre.

The model will comprise four rigid segments and two damped linear springs to represent the elastic properties of the bar and gymnast (Figure 1.2). The model will use personalised inertia data and use joint angle time histories as input.

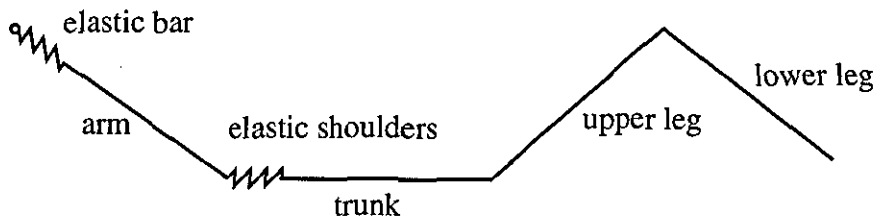


Figure 1.2. Components of the four segment simulation model.

1.4 Questions

In addressing the statement of purpose the following research questions should and will be answered.

Question 1

How does the gymnast's technique differ between regular and accelerated giant circles ?

By definition the gymnast should finish an accelerated giant circle with a higher angular velocity than when he started. But how do the actions performed at the hips, shoulders and knees differ between regular and accelerated giant circles ?

Question 2

What are the reaction forces exerted by the bar on the gymnast as he performs both regular and accelerated giant circles ?

Kopp and Reid (1988) presented the reaction forces experienced by gymnasts performing regular forward and backward giant circles. Gervais (1993) recorded the force on a gymnast performing giant circles prior to a dismount. However, a comparative study of a gymnast performing both regular and accelerated giant circles has not been conducted.

Question 3

Does the high bar behave like a damped linear spring? If it does can the kinetic and kinematic analysis of regular and accelerated giant circles be used to obtain stiffness and damping coefficients for such a spring?

The FIG measures, dimensions, and forms manual (FIG, 1979) require the bar to deform by $0.10 \text{ m} \pm 0.01 \text{ m}$ in the vertical direction when loaded statically with 2200 N at its centre. On removing this load the bar must return to its natural resting position. If the bar behaves as a linear spring then the displacements of the bar will be proportional to the reaction force at the bar. If the force at the bar and the displacements were known the stiffness coefficient of the bar may be determined using Hooke's law. Similarly if the bar behaves as a damped linear spring the damping coefficients of the bar may be determined from the force recorded at the bar, and the bar displacements and velocities during a giant circle.

Question 4

Is there any evidence that the joints of the gymnast behave as elastic structures as he circles the high bar? If so which joints behave in this way?

Engin, Peindl, Berme and Kaleps (1984, a,b) and Engin and Peindl (1987) and Peindl and Engin (1987) have shown that the shoulders are a highly complex structure with a large range of motion. When force was applied to the shoulder it was found to become displaced and to offer resistance. During the application of the force the subject was requested to remain passive. However, during giant circles the muscles surrounding the shoulder joint would be active and may prevent any displacement in the shoulder. If a displacement did occur in the shoulder structure would displacements also occur in the spine and other joints?

Question 5

What are the mechanics behind the flexion and extension actions performed by gymnasts during regular and accelerated giant circles?

Bauer (1983) used a theoretical model to explain why a gymnast should flex instantaneously at the lowest point of the giant circle and extend instantaneously at the highest point of the giant circle. Gymnasts appear unable to perform this theoretical technique. Is this due to the gymnast's strength limitations or was the model used by Bauer (1983) too simple to model a gymnast ?

Question 6

How does the strength of the gymnast effect optimum technique ?

King (1998) presented a method of estimating subject specific peak joint torques based on data collected using an isokinetic dynamometer. These peak joint torques could be used to limit the strength of the simulation model during an optimisation. What would happen to the optimum technique if the peak joint torques were increased or decreased ? Varying the strength limits could be used to study the effect of strength on technique or to study the amount of effort required to perform the accelerated backward giant circle.

Question 7

Does optimum technique of the backward giant circle differ between gymnasts or is there a common technique that could be adopted by all gymnasts ?

Optimum technique may depend on the strength characteristics of the individual. Similarly the optimal solution may be sensitive to differences in the inertia parameters of the gymnast. Such considerations must be evaluated before generalisations may be made regarding optimum technique.

1.5 Chapter organisation

Chapter 2 reviews the literature relating to studies on the analysis of the backward giant circle and also reviews the literature relating to the techniques of investigation within the field of performance related biomechanics relevant to the present research.

Chapter 3 outlines the development of the four segment simulation model. The development includes a single segment model with a damped linear spring and the four segment, two spring simulation model. For both models the equations of motion and their solution are presented.

Chapter 4 describes the methods used to determine the muscle parameters for use in the four segment simulation model. It includes the protocol for collecting joint torque and

goniometer data from an elite gymnast and the subsequent determination of the torque function used in the four segment simulation model.

Chapter 5 outlines the methods for the kinematic and kinetic analysis of backward giant circles. The chapter contains the protocols for collecting force and video data and the analysis performed to determine model parameters.

Chapter 6 contains the results from the methods presented in Chapters 4 and 5.

In Chapter 7 the data obtained from Chapters 4 and 5 are used to evaluate the accuracy of the simulation models presented in Chapter 3.

In Chapter 8 the accelerated backward giant circle is optimised using a three segment model and a four segment simulation model. The sensitivity of the optimum technique to the model parameters is also determined.

Chapter 9 includes a summary of the results obtained and the answers to the questions raised in section 1.4. In addition there is a discussion which highlights the limitations of the present research and suggests possible areas for future research.

CHAPTER 2

REVIEW OF LITERATURE

2.1 Introduction

The review of literature is broken down into three sections. The first section reviews the literature relating to the development of the high bar as a piece of gymnastics equipment and those papers of a coaching nature. The second section reviews the literature on research into the backward giant circle. The final section reviews the techniques of investigation which relate to the present study.

2.2 Development of the high bar and a review of coaching literature

The beginnings of gymnastics are somewhat obscure, yet historians believe that they possibly began in China and Egypt over four and a half thousand years ago. However, it was not until the time of the Greek and Roman civilisations that the word gymnastics came into use. Between the ages of eighteen and twenty years young Greek males were required to undergo physical and military training (Munrow, 1963). This training included gymnastic type exercises such as tumbling, dancing, leaping and balancing. To perform these physical activities in their daily clothing would have been both difficult and dangerous, so they removed their clothes and performed naked. The Greek word for naked is "gumnos" and so these naked athletes were called gymnasts and the activities which they performed were called gymnastics (Prestidge, 1988). The Romans copied the physical training program of the Greeks to train their armies and cavalry. It is possible that this training may have included such activities as vaulting, for mounting horses, and pommel horse type work on the horse's saddle. These gymnastic activities can be found on the pottery and works of art that have survived to this day. It must also be noted that in all the specimens of art that have been found there has not been a single piece which depicts anything resembling modern day apparatus (Prestidge, 1988).

The beginnings of modern day 'Artistic' Gymnastics were cultivated from the work of the prominent physical educationist J. C. F. GutsMuths (1759-1839). This was done by the Swede P. H. Ling (1776-1839) and the German J. F. C. L. Jahn (1778-1852). Although these two men had similar backgrounds and reasons for developing their individual forms of gymnastics, it was the system of Jahn, often called German gymnastics, which has developed into modern day Artistic Gymnastics. As a school

teacher Jahn would organise excursions to a clearing in a nearby woods where the boys would exercise on apparatus developed from the works of GutsMuths. These apparatus were rather crude and barely resembled those which are used in modern gymnasiums. However, several of the apparatus invented by Jahn have evolved into pieces which are still used today. These include the high bar, (sometimes called the horizontal bar), parallel bars, side horse and vaulting buck (Loken and Willoughby, 1959). The exercises that the boys performed were dictated by the apparatus and were developed along a trial and error basis (Munrow, 1963). Once developed the exercises were displayed for the others to try; even in these early beginnings the exercises were performed competitively. Soon boys from other schools joined in these excursions and so began the movement which gave rise to German gymnastics. This type of gymnastics started with school boys but rapidly grew through both clubs and universities into a competitive sport at national and international levels.

Today Men's Artistic Gymnastics is made up of six pieces of apparatus, namely the floor, pommel horse, rings, vault parallel bars and high bar. This thesis is concerned with swinging on the high bar. During a competitive routine the gymnast is required to perform a number of complex circling skills culminating in a spectacular dismount where the gymnast may reach heights of up to four metres from the floor. The routine is performed on a 28 mm thick steel bar fixed some two and a half metres from the floor. The creation of this piece of apparatus can be credited to Friedrich Jahn who introduced the high bar into his famous playground in around 1812 (Loken and Willoughby, 1959). Knowing how children liked to play in the branches of trees he visualised the high bar as being a strong level branch which the children could swing and perform on. This high bar would probably have been made of wood with no fixed diameter or height above the ground.

Around the turn of the century the high bar had developed into a fixed bar approximately seven feet from the floor. The construction of the bar itself varied greatly, from a bar with a steel core covered with a thin casing of ash or leather, which was approximately 1¼ inches in diameter, to a polished steel bar without any covering at all (Wooten, 1934). The exercises performed consisted of simple circling skills, pull ups, various balancing skills and dismounts. Even with this crude apparatus the gymnasts were performing giant circles. It was not until the late fifties/early sixties that a common bar was used in competition.

Today the regulations as set down by the International Federation of Gymnastics (F.I.G.) require the bar to be made from stainless steel 2.4 m long and 0.028 m in diameter (Figures 2.1 and 2.2). The bar should be fixed 2.55 m above a mat which is 0.20 m deep (Figure 2.1). The bar is also required to produce a vertical deflection of 0.10 m when loaded with a weight of 2200 Newtons at its centre. When the weight is removed the bar must resume a straight line with no deviations from its original shape

(F.I.G., 1979). This indicates that the high bar behaves like a spring in that when it is loaded there is a deflection and when the load is removed it returns to its natural resting position. By defining how far the bar should deflect under a known load it is possible to determine the stiffness. The above requirement therefore defines the elastic properties of the high bar so that no matter which manufacturer has constructed the bar it should perform consistently within the regulations set down by the F.I.G.

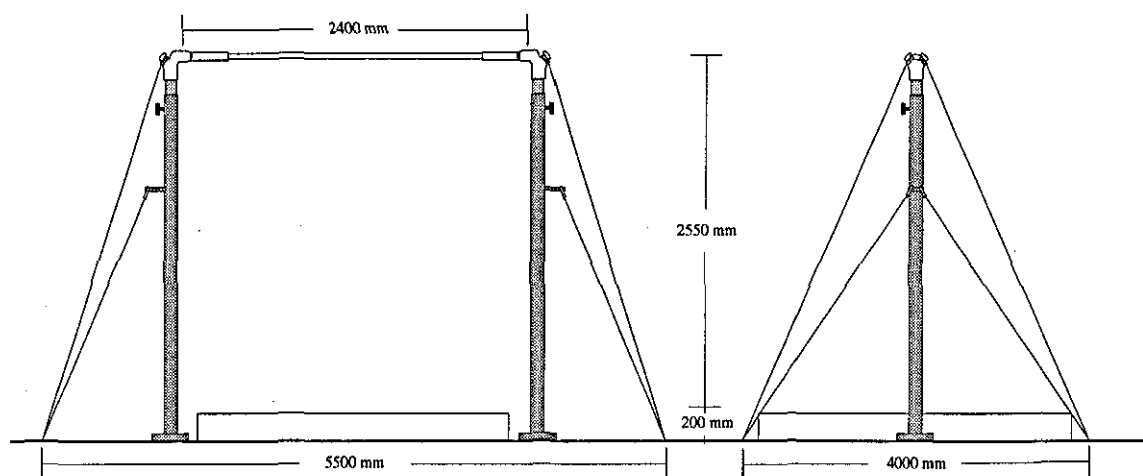


Figure 2.1. F.I.G. high bar specifications.

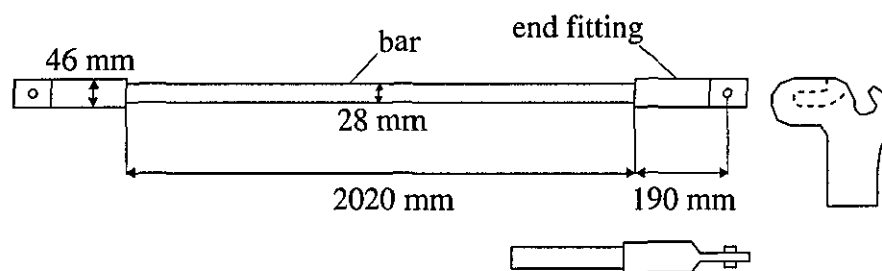


Figure 2.2. Bar construction (Continental).

As the bar has developed so has the complexity of the skills performed on it. Although skills had been developing through the years it was during the period between the early seventies to the early eighties that the greatest advances were made. In 1971 Mark Davis of America performed the first triple somersault dismount in competition. In 1974 Bernd Jaeger performed the first straddled forward somersault from a forward giant circle, then in 1975 the Russian gymnast Tkatchev performed the first backward straddle over the bar to regrasp (Figure 2.3). In 1977 Andrianov performed the first double layout somersault dismount in competition (Figure 2.4) and in the same year the first Gienger was performed. In 1979 Kovacs performed the first ever tucked somersault over the bar to regrasp from a backward giant circle (Figure 2.5). Then in 1981 Mitch Gaylord

performed a tucked somersault over the bar with a regrasp in reverse grip (Gajdos and Gohler, 1988). These skills are now common place in the exercises of today's elite performers who perform many of these skills in succession and in various combinations.

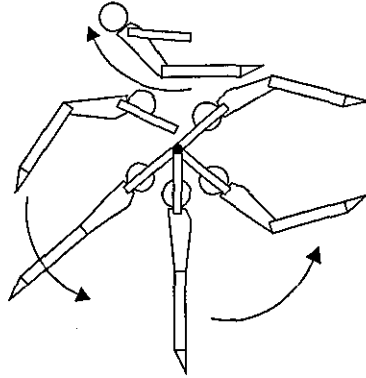


Figure 2.3. The Tkatchov.

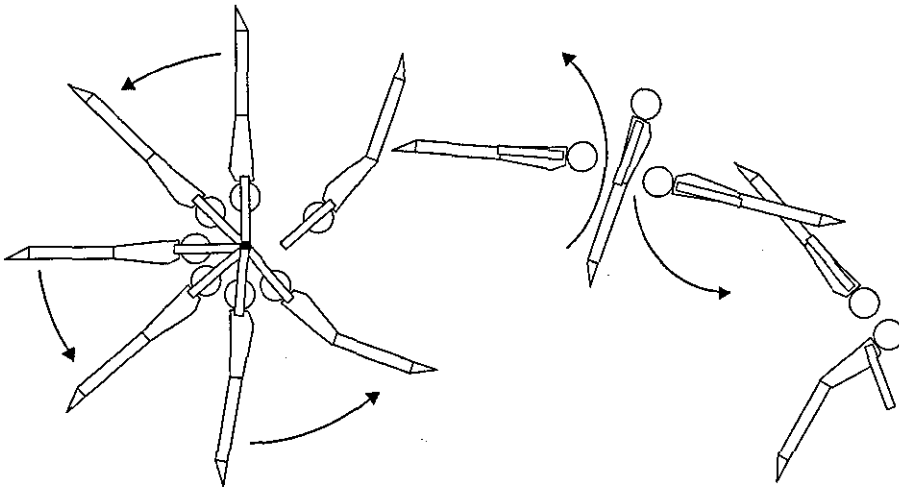


Figure 2.4. The double layout backward somersault dismount.

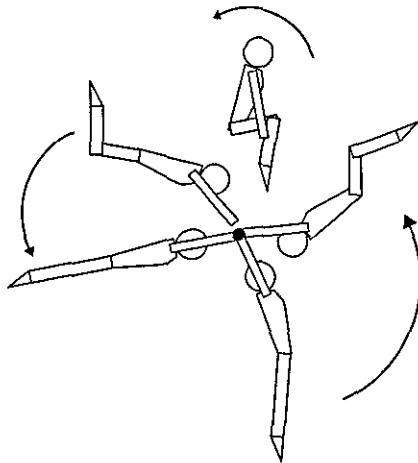


Figure 2.5. The Kovacs.

The double layout somersault dismount, the Tkatchov, Kovacs and Gienger all have one thing in common. This is that they are all performed from a backward giant circle (Figure 2.6). The backwards giant circle is a core skill which forms the basis of more advanced work on the high bar. Due to the development of the gymnast's handguards - handguards are worn by the gymnast to separate the hand from the bar to reduce the abrasion to the hands. They are made with a small dowel (Figure 2.7) whose function is to ensure a more positive grip and transfer a greater load from the hand to the handguard (Readhead, 1987) - gymnasts are able to perform accelerated giant circles which result in high angular velocities since they are more able to cope with the associated reaction forces at the bar. Gymnasts are able to perform one armed giant circles where the gymnast will experience a force at the supporting hand of up to four times his bodyweight (Enchun, 1989).

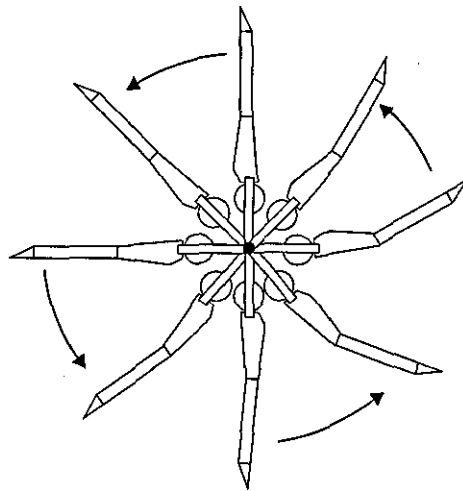


Figure 2.6. The backward giant circle.

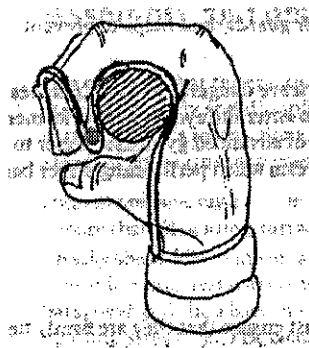


Figure 2.7. A handguard (adapted from Readhead, 1987).

The basic technique for a backward giant circle was described as follows by Lloyd Readhead (taken from "Men's Gymnastics Coaching Manual", Readhead 1987);

"In the handstand position the gymnast extends the body fully to gain maximum potential. A slight dish is introduced into the body to initiate the swing and this tensioned, extended body shape is held throughout the downswing. Before the gymnast reaches the lowest point of the swing the hips are relaxed to permit the hips to lead the swing under the bar. This hollow shape is introduced to produce an action, the reaction of which is to assist the rapid acceleration of the legs into the upswing. Once the gymnast has passed beneath the bar an angle is introduced into the shoulders and hips to help maintain the momentum of the upswing. The dished shape and shoulder angle are maintained until the force due to the bend in the bar is returned to the body. This occurs just before the handstand position and at this point the shoulder angle is rapidly removed and a wrist change introduced to give a regrasp of the hands. The dished body shape is still maintained so that the feet lead the swing to the handstand position where the body is again fully extended to commence the next downswing".

At the time of publication Lloyd Readhead was the Great Britain men's national coach. His description of the technique hints at a range of biomechanical terms and principles, such as angular momentum and the conservation of energy. The author explains that the gymnast should extend from the dished position once the bar has returned to its natural position. This comment raises such questions as "when does the bar return to its natural position?". Readhead (1987) states that this event occurs before the gymnast reaches the handstand position, but is this always the case and what is the benefit of re-grasping at this point? In addition, is there anything to be gained by extending either earlier or later?

The backward giant circle is an extension of the elementary swing (Figure 2.8), where the mass centre of the gymnast never passes the horizontal at the apexes of the swing. The mechanics of the elementary swing and the backwards giant circle may be considered from two biomechanical stand-points. During swinging the gymnast's weight and location of the mass centre are very important. Bauer (1983) suggests that swinging may be described as pendulum with variable length. In the downwards phase of the swing the gymnast aims to be as extended as possible so as to create a large torque about the bar. Torque is the angular equivalent of force and is calculated by multiplying force by the shortest distance from the line of action of the force to the axis of rotation (moment arm). In this case the force is that of the gymnast's weight and the axis of rotation is the bar. If the gymnast's weight is the only force acting during the giant circle then the torque about the bar is the gymnast's weight multiplied by the moment arm (Figure 2.9). Newton's Second Law for angular motion states:

The rate of change of angular momentum is directly proportional to the applied torque and occurs in the same direction as the torque.

That is, the greater the torque applied to a body the greater the change in angular momentum about the axis of rotation (angular momentum is the measure of the amount of rotational motion a body possesses and is found by multiplying angular velocity by moment of inertia). If the moment of inertia of the body is held constant, e.g. the gymnast maintains a fully extended body shape on the downswing of the giant circle then the angular acceleration experienced by the gymnast is proportional to the torque. Therefore by maintaining a fully extended body shape the gymnast creates a large torque about the bar which produces a large angular acceleration which leads to a large angular momentum as the gymnast passes through the lowest point. As the gymnast passes through the lowest point the moment arm become zero. Therefore the torque and the angular acceleration that the gymnast experiences becomes zero. Once the gymnast has passed through the lowest point the torque created by the gymnast's weight tends to accelerate the gymnast in the opposite direction to that of the swing. That is, the gymnast experiences a negative angular acceleration. To reduce the effect of the torque the gymnast adopts a dished body shape. This reduces the torque created by the gymnast's weight by reducing the moment arm. If the gymnast could "kick" to the dished shape instantaneously with no external torques acting, then the conservation of angular momentum could be applied. By dishing, the gymnast reduces his moment of inertia about the bar; therefore by the conservation of angular momentum the gymnast's angular velocity will increase. As the gymnast reaches the highest point of the giant circle the body is extended in preparation for the next downswing. Again by extending the gymnast's moment of inertia about the bar is increased, and the angular velocity possessed by the gymnast as he passes through the highest point is therefore reduced.

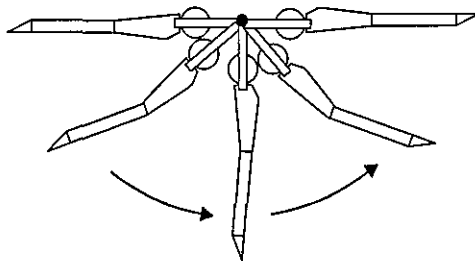


Figure 2.8. The elementary swing.

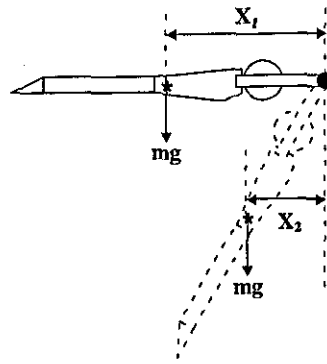


Figure 2.9. Torque created by the gymnast during swinging.

To say that the only force acting during a giant circle is that created by the acceleration due to gravity and the gymnast's mass would be untrue. In fact the force created by the friction between the gymnast's hands and the bar during swinging defines how the gymnast grasps the bar. When the gymnast swings, the hands tend to rotate with the rest of the body. This is opposed by frictional forces (Hay, 1994). During the downswing the torque created by friction acts in the opposite direction to the torque created by the gymnast's weight, thus reducing the gymnast's angular acceleration. On the upswing the torque created by friction acts in the same direction as the torque created by the gymnast's weight, tending to slow the gymnast down. Figure 2.10 shows the frictional forces as a gymnast swings forwards (Figure 2.10 a) and backwards (Figure 2.10 b) whilst gripping the bar in overgrasp (the grasp used during backward giant circles). Whilst swinging forwards the frictional forces have the effect of wrapping the gymnast's fingers around the bar. Thus strengthening the gymnast's grip. However, when swinging backwards the frictional forces tend to weaken the gymnast's grip. This explains why a gymnast will re-grasp the bar at the top of the backswing when performing elementary swings.

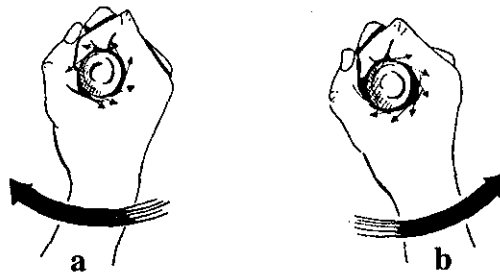


Figure 2.10. Friction forces between the hands and the bar (adapted from Hay, 1994).

The second approach to a mechanical description of swinging is to look at the energy transfers involved. In the vertical handstand position the gymnast has potential energy due his position relative to the ground. On the downswing the gymnast remains extended to maximise the effect of the gravitational moment (Smith, 1982). As the

gymnast passes through the lowest point the rotational energy he possesses is equivalent to the change in potential energy between the handstand and the hanging position minus any losses in energy due air resistance and friction between the gymnast's hands and the bar. The 'beatswing' action (Figure 2.11) which is seen as the gymnast passes through the lowest part of the swing is created using muscular energy and serves to replace the energy 'lost' due to friction, thus enabling the gymnast to return to the handstand position or in the case of the elementary swing to reach the horizontal. However, if the gymnast inputs more energy into the system during the beatswing than has been lost, then on completion of the giant circle the gymnast will have more energy than at the start of the circle. This extra energy appears in the form of rotational energy. On returning to the handstand position the gymnast will be rotating faster than at the start of the circle. This type of giant circle is often called an 'accelerated' giant circle and it is used to increase the gymnast's rotation about the bar in the 'wind up' to the dismounts and release and regrasp skills.

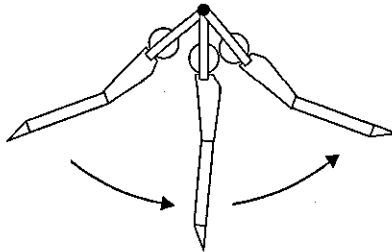


Figure 2.11. The beatswing action.

However, there appear to be two general techniques adopted by gymnasts in the giant circle prior to release for a dismount. In the first technique the gymnast performs the beatswing passing through the lowest point of the giant circle. The gymnast then extends at or very close to the vertical (Figure 2.12 a). In the second technique the gymnast performs the beatswing later than in the first technique (Figure 2.12 b). The gymnast then maintains this dish-shaped body shape until reaching the horizontal (Figure 2.12 b). Further to these existing techniques there are cases where a single gymnast may use both techniques when performing skills with similar release characteristics. Brüggemann et al. (1994) presented biomechanical profiles of release and regrasp skills on the high bar. It was found that a gymnast would require similar amounts of rotation at release to perform both the Kovacs and triple tucked backward somersault dismount. However, it is not uncommon for two gymnasts to use different techniques in order to achieve the rotation necessary for the double layout dismount or for a single gymnast to use the first technique prior to a Kovacs and the second technique prior to a triple tucked backward somersault dismount. Questions as to which is the more beneficial and what are the advantages of each technique may be raised.

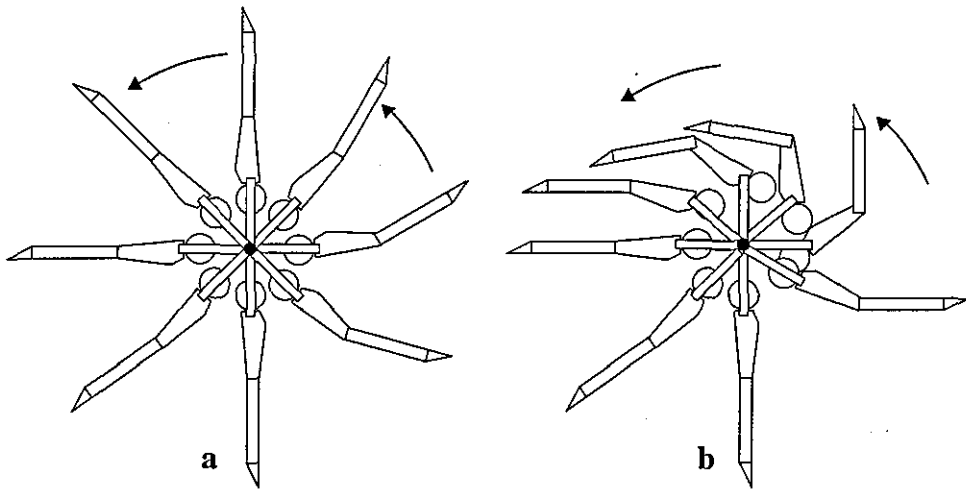


Figure 2.12. The two general techniques used by gymnasts winding up for a dismount.

2.3 Research on the backward giant circle

2.3.1 Definitions of experimental and theoretical research

In the area of performance related sports biomechanics the researcher is attempting to answer questions of the nature what, how and why (Yeadon and Challis, 1994). For example what is the best angle of release for a double layout dismount from the high bar? How does a gymnast reverse his direction of rotation during a Tkatchov release? Why do elite gymnasts adopt different body shapes whilst passing through the upper part of the accelerated backward giant circle? The traditional scientific method for answering these questions is for the researcher to perform an experiment where some data is collected and analysed. Another method is to use a theoretical approach. Theoretical approaches take the form of idealising the activity of interest (Yeadon and Challis, 1994). Often the idealisation takes the form of a model. In sports biomechanics movements of both the athlete and the equipment obey Newton's laws of motion. This makes the theoretical models mathematical formulations of Newtonian systems (Yeadon and Challis, 1994). These models may be used to give either forwards or inverse dynamic analyses (Figure 2.13). Forwards dynamics is often called simulation. Input to the model comprises the forces acting on the system, with the output being the subsequent motion caused by the input forces. Variations on this idea use joint angle time histories as input to a simulation model when it is decided that for the activity in question the forces created by the muscles are not of great importance (Yeadon, 1993a).

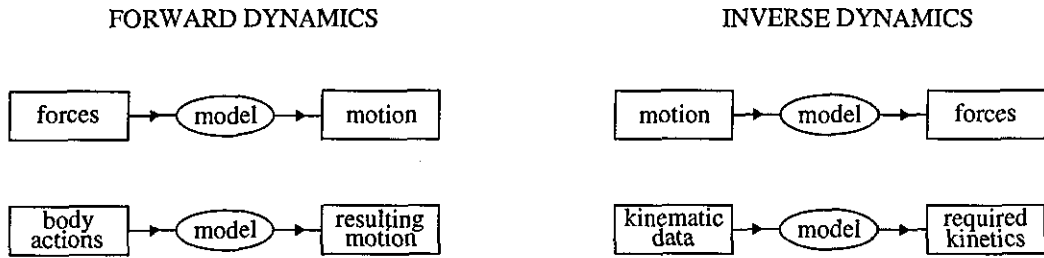


Figure 2.13. Forward and inverse dynamics (adapted from Yeadon and Challis, 1994).

However, theoretical research is not independent of experimental research. Yeadon and Challis (1994) presented a model for scientific method outlined in Figure 2.14. The method may be explained with the following example. The researcher often starts with a descriptive study. It may be decided to use a theoretical approach to address the research question. This may take the form of developing a simulation model. The next step is to obtain a theoretical prediction from the simulation model. At this point the accuracy of the theoretical prediction is unknown. The model therefore needs to be evaluated. This may be done by obtaining some experimental data to compare with the output of the model. After a comparison of the two sets of data it may be found that the model is not accurate enough and that the theory needs to be improved, i.e. the researcher enters the feedback loop (Figure 2.14). Alternatively the model/theory may prove to be sufficiently accurate and so the comparison can provide an indication of the accuracy of the model and hence the accuracy of any predictions made using it.

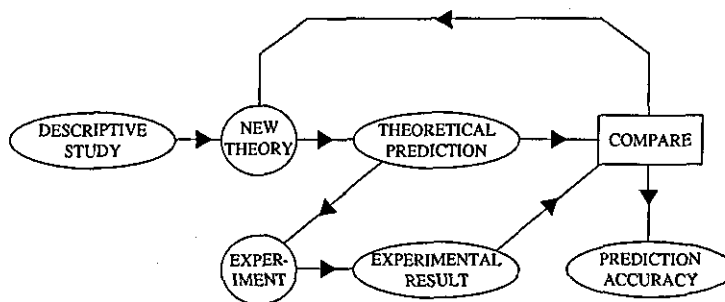


Figure 2.14. Experimental and theoretical model of scientific method (adapted from Yeadon and Challis, 1994).

Research tends to be termed either experimental or theoretical depending on how much they rely on experiment and theory (Yeadon and Challis, 1994). In a true experimental design the independent and dependent variables must be identified. The experiment should be designed whereby the independent variable may be manipulated in order to observe the effect on the dependent variable. In the perfect experiment there is absolute control, there are no systematic errors and internal and external validity are

maximised. Internal validity refers to how the effect on the dependent variable is due to the manipulation of the independent variable. External validity refers to the general applicability of the results obtained. That is, how the results apply to the real world. In an experimental situation the researcher may attempt to impose some control in order to manipulate the independent variable. This may take the form of asking a gymnast to perform a certain aspect of the skill in question at a slightly different time (e.g. in the case of the accelerated giant circle the gymnast might be asked to perform the flexion action later than he normally would). By trying to alter one aspect of technique the gymnast may alter other parts of his technique. It would then not be clear whether the effect seen on the dependent variable was due to the manipulation of the independent variable. The majority of the experimental research on the backward giant circle has been without intervention and as such is observational in nature. These include studies where the joint angle time histories of the hip and shoulders joints, time histories of the angular velocity of the gymnast's mass centre, reaction force at the gymnast's hands, joint forces and work done during a giant circle have been described.

2.3.2 Observational/experimental research

A number of papers in the literature have performed observational data collection (Borms et al., 1975; Boone, 1977; Cheetham, 1985; Okamoto, Sakurai, Ikegami and Yabe, 1987). From these papers the backward giant circle may be broken down into four quadrants (Figure 2.15). In quadrant one the gymnast is usually fully extended. In quadrant two the gymnast hyper-extends the hips. From the simple energy and torque analysis of the backward giant circle given in section 2.1 how can the hyper-extension of the hips be explained. Is this action performed to increase the angle through which the flexion is performed or are there other reasons? In the third quadrant the gymnast flexes and in the fourth quadrant the gymnast extends and reaches the handstand position.

Boone (1977) showed that the faster a gymnast rotated about the bar the greater the centripetal force. Therefore the faster a gymnast swings the greater effort required to maintain contact with the bar. He found that actions at the hips and shoulders were required to complete a giant circle. Closing the hip and shoulder angles after passing the lowest point appeared to increase the gymnast's angular velocity. Gymnasts could perform backward giant circles by using either the hips or the shoulders, but greater increases in angular velocity were observed when both hips and shoulders were used. Could this mean that the larger the flexion action through the lowest point the greater the increase in energy?

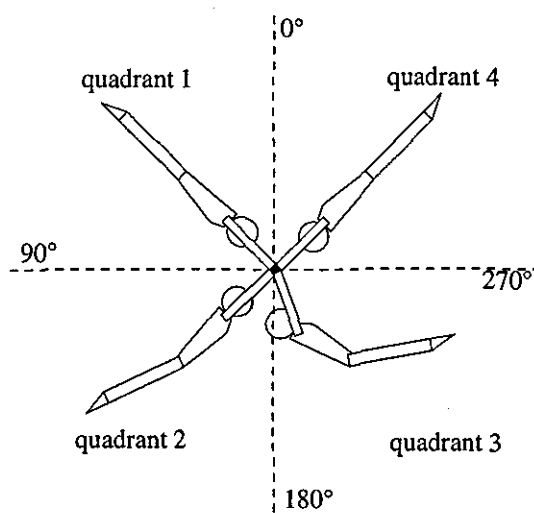


Figure 2.15. The four quadrants of the backward giant circle.

Okamoto et al. (1987) filmed five male gymnasts performing backward giant circles. An eight segment mathematical model was used for analysis. The model comprised segments for the head, trunk, upper arms, forearms, hand, thighs, shank and feet. Moments of force at each joint were obtained by solving the equations of motion and then the muscle power was calculated by multiplying this value by the angular velocity of each joint. By integrating the muscle power at each joint the mechanical work done by each joint was obtained.

The giant circle was broken down into four equal quadrants (Figure 2.15). During the first quadrant the gymnasts were extended. To maintain these angles flexor torques were required. The main feature of the second quadrant was the hyper-extension of the hip joint. In the third quadrant both the hip and shoulder angles began to flex. This was achieved using flexor torques. However, towards the end of the third quadrant as the hip and shoulder angle began to extend the torque at these joints was still a flexor torque. Therefore the muscles were being contracted eccentrically.

It was calculated that the hip and shoulder joints contributed 48% and 46% respectively to the total mechanical work done during the giant circle. The majority of this work was done in the first half of the upswing (quadrant three). How was the remaining energy made up? Did the gymnast perform any other action other than at the hips and shoulders?

Cheetham (1984) distinguished between three different types of giant circles: the regular giant circle, where the aim is only to swing from handstand to handstand; the accelerated giant circle, where the aim is to increase the angular velocity; and the giant circle immediately prior to a dismount, where the aims depend on the particular dismount used. The paths of the mass centre were compared with each other for the three types of giant circle. For the regular giant circle the mass centre followed a circular path during the downswing. During the upswing the mass centre was found to move closer to the bar

which made the path that the mass centre followed flatter. This was caused by the flexion action performed by the gymnasts which brought their mass centres closer to the bar. For the wind-up and accelerated giant circles the path of the mass centre was tilted over and ovular in shape. What caused the tilted over ovular shape? Although the author did not state the reason it is possible that the gymnasts used in the study were extending once they had passed through the highest point and had commenced the downswing.

Cheetham calculated the mass centre angular velocity for each of the gymnasts. He found that during all giant circles there were two peaks in angular velocity. The first peak coincided with the bottom of the downswing. However, in all three types of giant circle studied the first peak in angular velocity occurred just before the bottom of the downswing. Brüggemann et al. (1994) also found that during the backward giant prior to release for a tucked double somersault dismount the kinetic energy peaked just before the lowest point. It might be expected that the peak should occur at the very bottom of the downswing, so why does it occur before? Could this phenomenon be due to the gymnast's technique or to the energy being stored by the bar? The second peak in mass centre angular velocity was attributed to the flexion action performed by the gymnast. In the case of the accelerated giant circles this second peak was always larger than the first. In fact, during two accelerated giants prior to a double layout dismount it was shown that the peaks from successive giant circles increased until release (Figure 2.16).

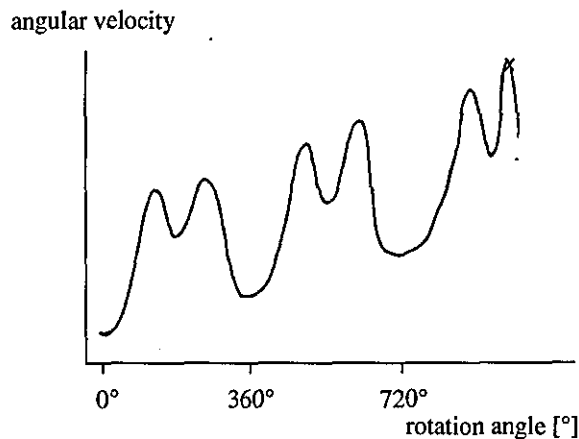


Figure 2.16. Angular velocity during two accelerated and one dismount giant circle (adapted from Cheetham, 1985).

Brüggemann et al. (1994) stated that in any dismount or flight with regasp the gymnast's objectives are threefold: firstly to generate sufficient angular momentum to execute the number of somersaults and twists required by the particular skill; secondly to obtain adequate height and thus have enough time in the air to complete the designated rotation; and thirdly to travel safely away from the bar while performing a dismount or to achieve a flight curve that guarantees the safe regasp of the bar and the continuation of

the bar routine after performing a release-regrasp skill. The successful achievement of all three objectives is dependent on the last swing prior to release. Brüggemann et al. (1994) filmed and analysed 70 release skills from the Barcelona Olympics. It was found that the major changes of mechanical energy were determined by shoulder and hip flexion and extension movements. The knee joint action was also found to contribute to energy changes. At the point of maximum knee flexion velocity the mass centre accelerated sharply. It appears as though the knee flexion and extension play an important role in the preparatory giant circle. It was found for a double backward tucked somersault dismount that the total kinetic energy peaked before the bottom of the giant circle (similar to the findings of Cheetham, 1984). This coincided with peak hip and shoulder hyper-extension and mass centre velocity. However, whole body angular momentum about the gymnast's mass centre was found to be only 60% of its eventual maximum at this point. The maximum angular momentum occurred at maximum hip flexion velocity. Additional high speed recordings of the bar indicated maximum bending of approximately ± 10 cm.

Kopp and Reid (1980) mounted strain gauges to a high bar in order to obtain data on reaction forces and torques at the gymnast's hands during forward and backward giant circles. The circles were regular giants under the classification of Cheetham (1984). The maximum reaction force recorded during the backward giant circles was between 3.45 and 3.70 times the gymnast's body weight with a mean value of 3.57 (approximately 2208 N for the gymnasts used in the study). This maximum reaction force occurred after the gymnasts had passed through the lowest point, at a mean angle of 210° (the vertical handstand being defined as 0°). The mean of the peak torques recorded was 23.3 Nm and occurred within 0.2 s of the maximum reaction force.

The use of strain gauges is a common method for obtaining the reaction force at the gymnast's hands. Using this method Ishii and Komatsu obtained values of 3.5 to 4.9 bodyweights for the peak vertical reaction force. Similarly Enchun (1989) obtained reaction forces between 3.5 and 3.9 bodyweights for single arm backward giant circles. However, none of these were accelerated giant circles. Gervais (1993) presented a method of calculating reaction forces at the hands from positional data. The calculated values were compared with those obtained from strain gauges. In one trial the subject performed two giant circles leading into a double somersault dismount. During the last giant circle the peak reaction force rose to approximately 3200 N (approximately 5.3 bodyweights).

Summary

The experimental/observational research has outlined the body actions which make up the backward giant circle. For the regular giant circle the major actions occur at the

hips and shoulders. As the gymnast passes through the lowest point the angle at the hips and shoulders are closed (i.e. flexion of the hip joint). It has been shown that this leads to an increase in angular velocity and energy. For the accelerated giant circles there is a possibility that there is an additional action created at the knees which may contribute to the gymnast's rotation. However, the mechanics of why the flexion action is performed after the lowest point has not been established, nor have any recommendations as to where the subsequent extension should be.

2.3.3 Theoretical research

Bauer (1983) simplified a number of swinging activities by modelling them as a pendulum of varying length. The mass of the pendulum was used to represent the mass centre of the gymnast with the length of the pendulum representing the distance of the mass from its point of rotation. The skills investigated were described in terms of the mass centre trajectories. Changes in pendulum length were assumed to occur instantaneously. This method was used to describe the technique of the backward giant circle. The maximum length of the pendulum was maintained during the downswing to make full use of the torque created by the weight of the pendulum. Once the mass reached the lowest point of the circle the length of the pendulum was instantaneously shortened. This new pendulum length was then maintained until the highest point of the circle was reached, at which point the pendulum length was instantaneously increased back to maximum length. This explanation implies that a real gymnast should flex as quickly as possible at the lowest point and then extend as quickly as possible at the highest point of the circle (Figure 2.17).

The author acknowledged that these instantaneous changes could not be performed by a real gymnast, but stated that these instantaneous changes in pendulum length coincide with the gymnast's "points of decision". This statement was made from observation and experience, and does not explain the underlying mechanics. A simple pendulum is not sufficient to model the gymnast's structure. Each of the gymnast's limbs has moments of inertia which complicate the mechanics beyond the scope of the simple pendulum. Also, if the decision point for the extension was at the highest point of the giant circle, by the time the gymnast had made the decision all of the extension would be performed after the highest point. This idea contradicts with most of the practical studies where the gymnast has been shown to initiate the extension before the highest point. Is this due to the regular "nature" of the giant circles studied to date or is there some other explanation?

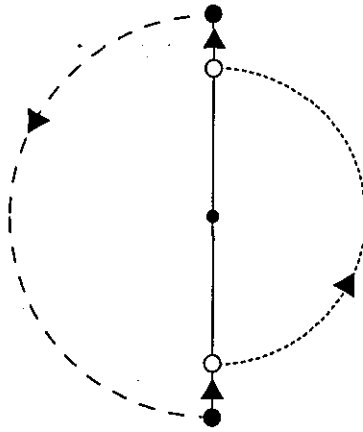


Figure 2.17. Mass centre trajectory for a backward giant circle (adapted from Bauer, 1983).

Bauer (1981) used a double pendulum as a two link model of the gymnast. The optimal hip joint movement was computed so that the gymnast exerted a minimum amount of energy. The model was used to simulate a giant circle. It was found that the optimal solution was consistent with data and theoretical formulations in biomechanics. This implies that the results agreed with the pendulum model. But does this explain the mechanics of the giant circle or rather the technique used by a gymnast? The result implies that gymnasts perform the flexion after the lowest point only because it requires less energy to perform. Would an alternative solution been found if the criterion for optimisation was to maximise the increase in energy?

Morlock and Yeadon (1988) presented a two segment model of a gymnast swinging on the high bar. One segment represented the legs and the other segment represented the rest of the body. The two rigid segments were linked by a frictionless pin joint which was used to represent the hip joint. The model was constrained to movements in the sagittal plane and assumed a rigid frictionless bar. The equations of motion were derived using a Newtonian approach. The model was applied to three separate cases of swinging. In the first case the model was allowed to swing with the torque at the pin joint set to zero. As the authors stated this was a purely theoretical situation. For the second case the torque at the hip joint was determined so that the angle at the hip was maintained at zero degrees (fully extended). In the third case the torque at the hips, obtained from case two, was modified in order to represent the flexion action observed in gymnasts performing backward giant circles.

In case one it was found that during the downswing (swinging from handstand to hang) that setting the joint torque at the hip to zero caused the angle to open. For a gymnast this would result in hyper-extension of the hips. This action is similar to that of a toppling chimney. When the base is blown and the chimney starts to topple it breaks into sections. The more distal sections tend to lag behind the proximal sections. On the

upswing it was shown that setting the joint torque to zero resulted in hip flexion. Case two backed up this result by showing that in order to swing from handstand to handstand with an extended body shape a flexor torque must be exerted during the downswing and an extensor torque must be exerted at the hips during the upswing. The third case showed that by performing a flexion action at the hips through the lowest point of a giant circle followed by an extension during the upper part of the circle energy could be input to the system. Could these same actions be used to reduce the energy in the system? This question really asks how is energy input to the system and what are the techniques to do this. The authors highlighted that a more sophisticated model which would include a shoulder joint and three segments could be used to optimise the gain in energy after one cycle. The model was relatively simple yet was able to demonstrate the mechanics of swinging. However, no account was given to the effect of modelling the elastic properties of the bar.

The two papers reviewed so far have used only two segments to represent the gymnast. The experimental research would suggest that any model should contain at least four segments so that the actions at the hips, shoulders and knees may be studied. Dainis (1968) presented a method for obtaining two-dimensional models which comprised n rigid links, fixed at one extremity and joined by $n - 1$ pin joints. Lagrange's equations of motion were used. A three segment model was implemented using this technique for the purpose of representing a gymnast swinging on the high bar. Friction at the bar hand interface was assumed to be zero, the author stated that this would be "a good approximation" - Komor and Ubukata (1977) stated from their analysis that the frictional forces at the hands were approximately zero. Two computer programs were developed. The first was a forward dynamics model which was called the synthesis program. The input to the model was the joint torque time histories for the hip and shoulder joints. The output from the model was the joint angles, angular velocities and angular accelerations of each segment. The second program was an inverse dynamics model. The input comprised the body configurations (segment angle time histories) with the output being the joint torques necessary to bring the model to successive configurations from the preceding one.

It was found that using joint torques was a difficult method for reproducing specific skills. The outcome of simulations could not be predicted due to the interdependence of the joint torques. The analysis program proved more successful. Joint torques for the hip and shoulder joints were calculated for two different giant circles, one performed with "excellent" technique, the other with "poor" technique. The giant circle performed with excellent technique had a peak shoulder torque (the torque represented that of the combined torques at each shoulder) of approximately 320 Nm and a peak hip torque of approximately 272 Nm. For the gymnast with poor technique these values were 500 Nm and 400 Nm respectively.

Duck (1980) developed a three segment simulation model with a frictional torque at the hands. The model was driven using joint angle time histories based on Fourier analysis of film data. Using this model Duck was able to simulate closely the path of the mass centre for a number of swinging skills. The frictional torque was determined from the normal reaction force at the hands multiplied by a constant of proportionality. From an experimental study this constant was found to be 0.07 for forward and backward giant circles. When the frictional torque is calculated for a backward giant circle using the force data from Kopp and Reid (1980) a peak torque of 155 Nm is obtained (based on peak force of 2208 N). This value is nearly seven times greater than the peak torque obtained by Kopp and Reid. Since Duck modelled the bar as a rigid structure it is likely that the coefficient of proportionality was used to account for the energy stored in the loaded bar and the increase in the gymnast's moment of inertia about the neutral resting bar position had it been modelled as an elastic structure.

More recently Arampatzis and Brüggemann (1995) presented a 15 segment gymnast with a 12 segment high bar as a method of optimising the giant swing prior to release. The definition of the optimal solution was based on the energy possessed by the gymnast after the giant circle. The timing of joint actions was linked with storing and retrieving energy from the bar.

Gatto and Neal (1992) presented a single segment model of a gymnast swinging on the high bar. The bar was modelled as two linear springs (one for the vertical displacement and one for the horizontal displacement) with constant stiffness coefficients. The friction at the gymnast's hands was modelled using a constant coefficient of proportionality in a similar manner to Duck (1980). Results were compared between conditions where the bar was modelled as a spring and where it was modelled as a rigid structure. The model was allowed to swing from a stationary position 1° from the vertical. When the bar was modelled as a rigid rod the peak reaction force was 4.56 bodyweights. When the bar was modelled as an elastic structure the peak reaction force dropped to 4.33 BW. This represented only a small reduction in peak reaction force (approximately 5%). Since the model comprises only one segment the reaction force at the bar could be approximated using the force due to the model's weight and its centripetal force. For the peak reaction force to be less, when modelling the bar as an elastic structure, the model's centripetal force must also be less. The reduction in centripetal force will be in part due to the increase in radius of the mass centre trajectory and to a decrease in angular velocity of the mass centre about the origin of the system (the neutral resting position of the bar). It is therefore argued that modelling the bar as a rigid structure leads to an over-estimation in the angular velocity of any simulation. The stiffness value used was approximately twice that predicted using Hooke's law and the apparatus norms set out by the FIG (1979). However, it was demonstrated that both doubling and halving this value made only small changes to the peak reaction force.

In addition to the displacement of the bar it has been suggested that the gymnast increases in length during the backward giant circle. The majority of this is believed to occur in the structures of the shoulders and spine. An increase in wrist to hip distance of between 0.10 m and 0.20 m was confirmed by Professor Nicoli Suchilin (personal correspondence). An extension in the gymnast would have the same implications on the reaction force that the elasticity of the high bar has. Incorporation of the gymnast's elasticity may lead to improvements in estimating both reaction forces and angular velocities.

2.3.4 Summary and views on theoretical optimisations

Both the experimental and theoretical studies that have been carried out have limitations. The majority of the experimental studies have investigated regular giant circles giving only a descriptive analysis of the skill. No analysis has been performed on the different body shapes that may be observed as the gymnast passes through the highest point in the accelerated giant circle and no attempt has been made to attribute any mechanical benefits to them.

In general when attempting to answer such questions using a theoretical approach, the model should be sufficiently complex to simulate all the important actions and mechanisms which define the system under study. For the simulation of swinging skills this requires more segments than the two and three used by Morlock and Yeadon (1988), Dainis (1968) and Duck (1979). However, the model should still be simple enough to facilitate the understanding of the underlying mechanics.

In previous research the elastic properties of the gymnast have been neglected. Although Arampatzis and Brüggemann (1995) modelled the bar they did not model the elastic properties of the shoulder joint structure. Neglecting these elastic qualities may lead to an over-estimation of the angular velocity predicted by a simulation model in the same way as modelling a rigid bar would. These assumptions may lead to limitations in the accuracy of any simulations performed.

The studies of Dainis (1968) and Yeadon and Morlock (1988) used joint torques to alter the joint angles of their models. This approach has the drawback that the effect on joint angles is unknown until the simulation is run. A better method of describing a technique may be in terms of the body shapes the gymnast must achieve. This suggests a more appropriate input for such a simulation model might be time histories of the joint angles rather than the joint torques. However, care must be taken using this method as simulations could be performed which exceed the strength characteristics of the gymnast.

In section 2.2 of the literature review the backward giant circle was introduced as a movement which is used to link skills and provide the necessary rotation for the more

complex skills. The aim of the theoretical studies outlined above have been to understand the mechanics of swinging. Morlock and Yeadon (1988) suggested that their model and hence other similar models may be used to optimise the technique of the backward giant circle. However, choosing an optimisation criterion for the backward giant circle is not as obvious as one might first think.

Consider the following experimental studies on release skills performed on the high bar. Kerwin, Yeadon and Lee (1990) obtained the release characteristics for gymnasts performing two dismounts from the high bar in the 1988 Seoul Olympics. Half the dismounts studied were triple tucked backward somersaults whilst the remainder were double layout backward somersaults. It was found that rotation and time of flight were the two characteristics which were required for the successful completion of both dismounts. Each of the dismounts require different amounts of these two characteristics; the problem was therefore one of relative importance. From the analysis of the competitors it was clear that rotation was a premium for the double layout somersaults, whereas for the triple tucked somersaults the time of flight was paramount. The optimum backward giant circle would therefore be different for each of the dismounts. To perform a double layout somersault dismount the gymnast would require a preceding backward giant circle which produced the greatest angular momentum, whilst to perform the triple somersault dismount the preceding giant circle should be geared to producing a greater time of flight.

Similarly Brüggemann et al. (1994) was able to distinguish between three movement classes identified in terms of their propulsion mechanism when investigating release skills on the high bar. These groups were called backward rotation category I (BRCI), backward rotation category II (BRCII) and forward rotation category I (FRCI). BRCI contained the tucked double, layout double and triple tucked backward somersaults, Kovacs and Giengers. BRCII contained the Tkatchovs, straight Tkatchovs and Mariniches, while FRCI contained Fliffes, the Gaylords and Jaegers. It was found that certain skills had similar release characteristics such as the double and triple tucked somersaults. However the double layout differed from these two skills by requiring greater angular momentum. This agrees with the study of Kerwin et al. (1990). The BRCII differed from the BRCI group in that during release the direction of rotation was reversed resulting in negative angular momentum in flight for the Tkatchov and Marinich skills. All skills preceded by a backward giant circle that maintained a uniform direction of rotation (BRCI) demonstrated almost identical strategies. The BRCII group displayed a similar strategy to the BRCI group but with phase shift of both timing and position. It was speculated that the general propulsion strategy, which includes the possibility of storing energy in the bar and using this energy on the upswing, contributed in all variations.

These studies (Kerwin et al., 1990; Brüggemann et al., 1994) indicate the different

requirements of the backward giant circle when it is used to provide the necessary rotation for a release skill. If the backward giant circle were to be optimised it could be argued that the optimisation criterion could be to maximise the angular momentum about the gymnast's mass centre. This would then be a suitable optimisation for a backward giant circle prior to the double layout backward somersault dismount. Similarly for the triple somersault dismount, optimising the angular momentum prior to the characteristic puck shape at release may be feasible. Conversely, for a Tkatchov or Marinich type skills, the gymnast desires rotation in the opposite direction after release, "negative" angular momentum, and the optimum technique for the backward somersaults may not be appropriate for these skills. Section 2.3.4 merely highlights the point that the optimised backward giant circle for one skill may not be the optimal solution for another. It must therefore be made clear, when performing an optimisation of technique, what is being optimised and for what purpose.

2.4 Techniques of investigation

The following sections review the techniques used in the field of performance related biomechanics. Techniques covered include the collection of force data, three-dimensional analysis, simulation and optimisation.

2.4.1 Force measurement

The measurement of force relies on one of two principles, either deformation or balancing. The balancing method requires the system to be in balance in order to determine the force, usually weight. The second method relies on the deformation of an elastic structure and the principle of Hooke's law to determine the force which has created the deformation. The structure which is being deformed may be a simple spring, as in a spring balance or a force transducer. A force transducer is a device which produces an electrical signal in response to an applied force. The spring balance may be used to measure a constant force; however, in the field of sports biomechanics the forces we wish to observe are often changing rapidly. This section will describe force transducers and their applications relative to this study.

Strain gauges

In 1856 Lord Kelvin discovered that the resistance of an electrical conductor changed when it was stretched. However, it was not until the 1930s that Edward Simmons and Arthur Ruge at independent institutes of technology in the United States suggested that this principle could be used in the measurement of strain.

Electrically conductive materials possess a stress/strain relationship defined as the ratio of relative electrical resistance change of the conductor to the relative change in its length. This strain sensitivity is a function of the dimensional changes which take place when the conductor is deformed, plus any change in the basic resistivity of the material with strain. The electrical resistance of a conductor is given by:

$$R = \rho l/A \quad (2.1)$$

where

- R resistance
- l length
- A cross sectional area
- ρ resistivity

Strain sensitivity (which is also called gauge factor) is a dimensionless relationship expressed mathematically as

$$F = \left(\frac{\Delta R}{R}\right) / \left(\frac{\Delta l}{l}\right) \quad (2.2)$$

From the above two equations the strain sensitivity due to the dimensional changes can be established, assuming the resistivity remains constant (Chalmers, 1992).

There are two main types of strain gauges which are easily distinguishable from each other. The first is a wire strain gauge which consists of a length of wire wrapped around the test component. Deformations in the test component cause a deformation in the wire (length or/and cross-sectional area). This in turn leads to a proportional change in the resistance of the wire which can be measured. The second and more commonly used type of strain gauge is the foil strain gauge. The gauge is usually bonded to the test component with a strong adhesive. Any deformation in the test component will result in deformation of the foil gauge. The foil strain gauge consists of a grid of zig-zag lines of alloy (Figure 2.18). The majority of foil strain gauges are produced by printed circuit techniques using the appropriate alloy precision rolled to exact thicknesses (Chalmers, 1992). Many different alloys may be used in the production of foil strain gauges; however, a copper-nickel alloy is most commonly used.

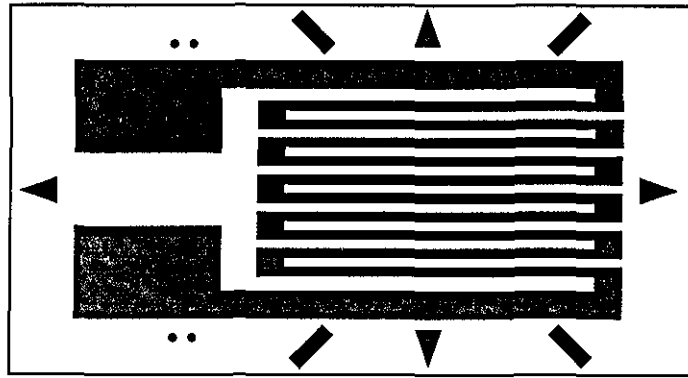


Figure 2.18. A foil alloy strain gauge.

The strain gauge may be considered as a passive resistor (Scott and Owens, 1992). In order to measure the strain in a stressed object the gauge requires a source of power and a method of measuring the change in resistance that occurs. Further, if the gauge is to be used to measure force, some manipulation of the output from the gauge is required to convert the measurement of strain into force. In the field these changes in resistance are measured using a 'bridge' circuit. This circuit is based on the Wheatstone bridge and comprises an arrangement of resistors (Figure 2.19) with a balanced voltage across them. When the resistance in one or more of the resistor arms changes an out-of-balance voltage is created. The small output will often need to be amplified and displayed or stored. The strain gauge, bridge circuit, amplifier and data logger are all components of the strain/force measurement system.

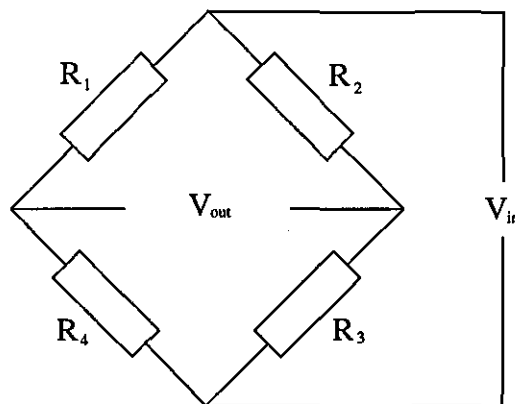


Figure 2.19. Wheatstone bridge (adapted from Scott and Owens, 1992).

The following is an example of how the Wheatstone bridge circuit works, and is taken from Scott and Owens (1992). Consider Figure 2.19 in which R_1 , R_2 , R_3 , R_4 are resistors. Assuming that the condition $R_1/R_4 = R_2/R_3$ is satisfied then the output voltage V_{out} will be zero, i.e. the bridge is balanced. A change in resistance R_1 will unbalance the bridge and produce a voltage across the output terminals.

If a similar change, in both magnitude and polarity occurs in an adjacent arm of the bridge, say R_4 , then the voltage V_{out} will remain zero and the bridge will remain in balance. If in adjacent arms the resistance changes occur of equal magnitude but opposite polarity then the voltage V_{out} will be twice that due to the resistance change in one arm. For strain gauge purposes the output equation for the bridge is:

$$V_{out} = \frac{K\epsilon N V_{in}}{4} \quad (2.3)$$

where

- K gauge factor
- V_{in} bridge volts
- ϵ strain
- N number of active arms of the bridge

The arms of the Wheatstone bridge can be made up from either strain gauges or resistors. However, the number of gauges used will depend on the application and accuracy required of the system. When a single gauge is used at the measurement point, it is termed a quarter bridge operation (Figure 2.20). When two gauges are used in adjacent arms of the bridge it is known as a half bridge system (Figure 2.21). For this to work one gauge must experience tension and the other compression. The full bridge uses gauges at all four arms of the bridge and is a logical extension of the half bridge and can be used to further increase the sensitivity of a measuring system. Putting two gauges on each side of the beam instead of one gives a value of $N = 4$ i.e. the output is four times that of a quarter bridge operation.

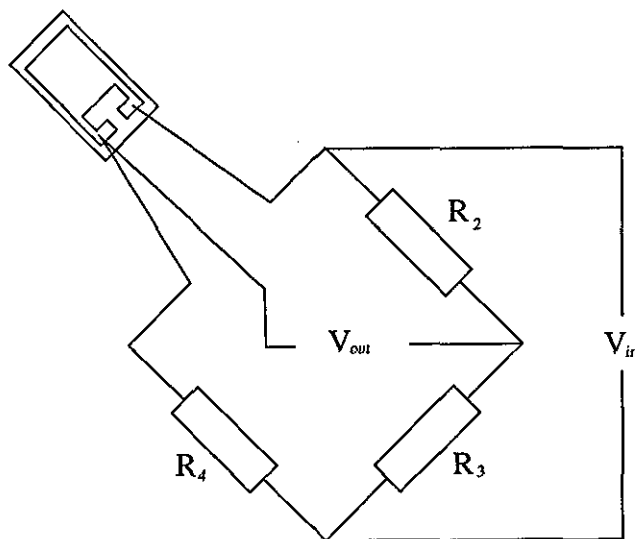


Figure 2.20. Quarter bridge circuit (adapted from Scott and Owens, 1992).

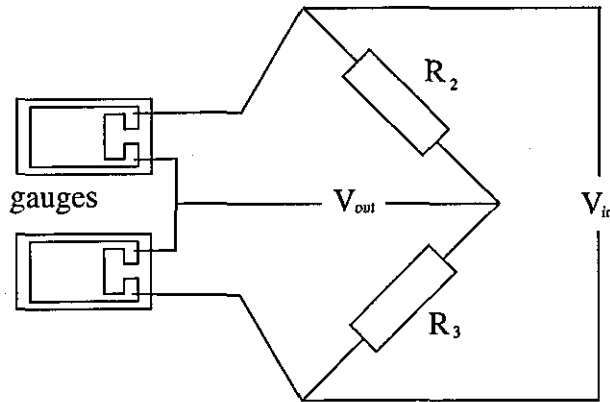


Figure 2.21. Half bridge circuit (adapted from Scott and Owens, 1992).

Once the appropriate bridge circuit has been selected and implemented it must be connected to an amplifier so that the output voltage from the bridge circuit can be amplified. The type of amplifier used is dictated by the nature of the task: that is, whether the task requires static or dynamic measurements (Scott and Owens, 1992). A signal that does not change in magnitude to any extent with time would be termed static, whereas a dynamic signal is likely to vary rapidly with time (Scott and Owens, 1992). When taking static measurements only one amplifier may be required. If more than one measurement point is needed, then a number of bridge circuits can be switched, feeding one at a time to the amplifier. In dynamic work simultaneous readings are often required. Therefore, one amplifier for every bridge circuit would be required.

The measurement of force has been carried out in a number of gymnastic disciplines using strain gauge technology. Gauges have been bonded to the parallel bars (Yessis, 1972), the asymmetric bars (Hay, Putnam and Wilson, 1979; Witten, Brown, Witten and Wells, 1996) and the high bar (Enchun, 1989; Gervais, 1993; Ishii and Komatsu, 1987; Kopp and Reid, 1980 and 1983). Load cells (objects with strain gauges bonded to them which have been pre-calibrated to output voltages equivalent to force units) have been connected in series with rings cables (Nissinen, 1983; Sale and Judd, 1974), and force platforms have been incorporated into the vaulting horse, pommel horse (Yessis, 1972), and the landing area to measure the forces experienced by gymnasts (McNitt-Gray, Yokoi and Millward, 1993 and 1994).

Ishii and Komatsu (1987) bonded four strain gauges to a metal bar which had the elastic properties similar to a competition gymnastics high bar. Two gauges were bonded close to each end of the bar in such a way that strain could be measured in the horizontal and vertical directions using half bridge circuits. For the vertical strain one gauge was bonded to the top side at one end of the bar and the second gauge was bonded to the bottom side of the opposite end (Figure 2.22). A similar arrangement was used for measuring strain in the horizontal direction (Figure 2.22). The bar was calibrated by

loading the bar with known weights at the middle and locations either side of the middle. With the gauges located as described it was possible to measure the force applied to the bar irrespective of the point of application. The signals from the bridge circuits were amplified and combined to give the resultant reaction force at the bar for gymnasts performing giant circles. Kopp and Reid (1980,83) used a similar arrangement of strain gauges bonded to the high bar. Calibration of the bar was carried out statically by applying known weights at different positions on the bar in the vertical and horizontal directions and known torques clockwise and anti-clockwise. It was found during the calibration that there was a highly linear force-voltage relationship. This might suggest that the force-deformation relationship of the bar was also linear. If this were so the bar would behave as a linear spring. There was also found to be no interaction between vertical and horizontal outputs during calibration. This was also found by Witten et al. (1996) in a similar study carried out on the asymmetric bars.

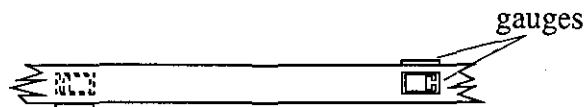


Figure 2.22. Strain gauge arrangement for measuring force on the high bar (Ishii and Komatsu, 1987).

In the previous studies the bar has been calibrated by applying known loads and measuring the deflection (Ishii and Komatsu 1987; Kopp and Reid, 1980). Neal, Kippers, Plooy and Forwood (1995) calibrated the bar in the horizontal direction by rotating the bar through 90° and loading it vertically. However, in order to calibrate the bar in the upwards vertical direction the bar would have to be turned over and calibrated in the downward vertical direction, unless the appropriate equipment was available. This may be better than assuming that the bar behaves the same in both vertical directions, but care must be taken when setting the bar up after it has been turned over.

In the outlined studies (Gervais, 1993; Ishii and Komatsu, 1987; Kopp and Reid, 1980, 1983; Enchun, 1989) the signal from the bridge circuits was sent to an amplifier before being recorded with a data logging device. The signal received by the data logger from the amplifier is an analogue signal. Whereas the data used in the analysis of the swinging skills is in general digital information (Gervais, 1993; Ishii and Komatsu, 1987; Kopp and Reid, 1980, 1983; Enchun, 1989). Therefore the analogue signal must be sampled at predefined rate. Enchun (1989) sampled at 50 Hz during one arm backward giant circles. With the giant circle lasting approximately two seconds this would have resulted in one hundred samples per circle studied. At this rate the gymnast would have rotated 3.6° on average between each sample. Through the lowest part of the giant circle the angle the gymnast would rotate through between samples may have been as large as

5.7° (assuming that peak angular velocity was 5.0 rad.s⁻¹). Ishii and Komatsu (1987) sampled at twice the rate of Enchun (1989) making readings at 100 Hz from an analogue recording. The ideal solution would be to sample at as high a rate as possible. This, however, leads to large amounts of data and increased processing time. Kopp and Reid (1980) sampled at 200 Hz for giant circles which lasted approximately two seconds. With a similar calculation the average angle of rotation between samples would have been approximately 0.9° with the largest angle of rotation between samples being approximately 1.4° (again assuming that peak angular velocity was 5.0 rad.s⁻¹). Gervais (1993) also sampled at 200 Hz but studied accelerated giant circles leading up to dismounts and release and regrasp skills. The higher angular velocity of the gymnasts during accelerated giant circles increased the average angle of rotation between samples to 1.2°. The general rule or sampling theorem states that "the process signal must be sampled at a frequency at least twice as high as the highest frequency present in the signal itself" (Winter, 1990). Sampling at a lower frequency would result in aliasing errors. For the backward giant circle it may be estimated that there will be no signal at a frequency higher than 50 Hz. However, unless the signal is sampled at a higher frequency there is no way of detecting noise frequencies which have been picked up through the instrumentation (e.g. the 50 Hz buzz of electrical circuitry).

Summary

Where possible full bridge circuits should be used to record the force applied to the high bar, since they are the most sensitive of the Wheatstone bridge configurations. When calibrating the strain gauge-bar system using known loads it is preferable to load the bar in both the horizontal and vertical directions. Having separate calibration curves means that no assumptions about the stiffness of the bar in the horizontal and vertical directions are made. The rate at which the strain data are sampled will depend upon the application. However, for swinging activities 200 Hz appears to be sufficient.

Isokinetic dynamometry and the Determination of muscle parameters

In section 2.3.1 the idea of driving a simulation model using either internal joint forces or joint angle time histories was presented. A simulation model which is driven by the internal joint forces or torques requires muscle models. The muscle model should reproduce the joint forces and torques that the subject is capable of producing. This may be achieved by using subject specific muscle parameters. Driving a simulation model using joint angle time histories also requires information that may be gained from a

subject specific muscle model. Yeadon (1993a) found that the techniques for producing twist did not require maximum effort therefore joint angle time histories were appropriate for the application. However, if the application in question may depend on reaching a state of maximum effort a knowledge of the individual's maximum joint torques for a given set of joint actions may be used to limit or restrict the simulation model to joint actions and/or joint angle time histories that are within the strength capabilities of the individual athlete.

This section reviews the literature related to obtaining subject specific muscle parameters using an isokinetic dynamometer.

An isokinetic dynamometer is a machine which is capable of measuring a force or a torque which is applied at a constant velocity. The term isokinetic refers to a muscular contraction where the angle at the joint centre, which the muscle is acting across, changes with a constant angular velocity. The term dynamometer refers to the device which measures the force. The device has usually been mounted with strain gauges and calibrated to measure force (as described in the section on strain gauges). When referring to isokinetic dynamometers the device which is used to measure the force is often called the load cell.

Isokinetic dynamometers are used to measure the force or torque applied to the load cell. The machine itself usually comprises a motor and gearing system onto which a crank arm is mounted. The motor and gearing system enable the crank arm to rotate in either direction (clockwise and anti-clockwise) at varying angular velocities. For the Kin-Com (one make of isokinetic dynamometer) the angular velocity of the crank arm may be selected from a range of $0^{\circ} \cdot s^{-1}$ to $\pm 250^{\circ} \cdot s^{-1}$ (approximately $0 \text{ rad} \cdot s^{-1}$ to $\pm 4.4 \text{ rad} \cdot s^{-1}$). However, some isokinetic dynamometers consist only of the gearing system and therefore rely on the subject to power the crank arm through the range of movement (Sapega, Nicholas, Sokolow and Saraniti, 1982; Winter, Wells and Orr, 1981). When the angular velocity of the crank arm is set to $0^{\circ} \cdot s^{-1}$ the isokinetic dynamometer is able to record isometric forces. An isometric contraction is one where the length of the muscle remains constant.

The load cell is mounted to the crank arm in order to measure the force. When a force is applied to the load cell a torque is created about the axis of rotation of the crank. This torque may be recorded through the data capture system of the isokinetic dynamometer and is approximately equal to the force applied to the load cell multiplied by the distance of the load cell to the axis of rotation of the crank arm. Some isokinetic dynamometers record force whilst others record torque. For human studies the joint centre of interest is aligned with the axis of the crank arm (Fuglevand, 1987; Herzog, 1988; Marshall, Mazur and Taylor, 1990; Winter et al., 1982; Perrine and Edgerton, 1978). Aligning the joint centre with the axis of the crank arm reduces the differences between crank and joint angles and moment arms.

Another feature of the isokinetic dynamometer is its ability to measure joint torques for both concentric and eccentric contractions (this is only possible for isokinetic dynamometers which are motor driven). A concentric contraction is where the points of insertion and origin of the muscle move closer together, i.e. the length of the muscle shortens. An example of a concentric contraction would be the biceps brachii shortening during a biceps curl. An eccentric contraction is where the points of insertion and origin move apart. In an eccentric contraction the force generated by the muscle acts to resist the lengthening of the muscle. An example of an eccentric contraction would be lowering of the forearm after performing the biceps curl. Studies have tended to collect data from concentric activities. The trials in these studies have consisted of concentric actions performed at a range of angular velocities. There is an argument for performing two repetitions of a concentric-eccentric protocol and using the middle eccentric and concentric phases (King et al., 1996; King 1998). This protocol ensures that the muscle is under full activation at the start and finish of the contractions of interest (King, 1998).

Isokinetic dynamometers have been used to determine the force-velocity relationships of muscles *in vivo* (Perrine and Edgerton, 1978). Several investigations have been interested in the relationships between the force and the velocity of shortening of the muscle (Perrine and Edgerton, 1978; Wichiewicz, Roy, Powell and Perrine, 1984; Froese and Houston, 1985). The relationship between force and velocity has been expressed as a hyperbolic function. This relationship was first established for *in-vitro* muscle fibres (Hill, 1970). Figure 2.23 shows the shape of the hyperbolic curve predicted from isolated animal muscles (Hill, 1970). Perrine and Edgerton (1978) recorded joint torque for knee extension, at an angle of 30° , for a range of angular velocities ($0^\circ.s^{-1}$ to $288^\circ.s^{-1}$). It was found that for the lower angular velocities the force-velocity curve obtained from the dynamometer differed from the hyperbolic curve predicted by Hill (1970). It was found that peak torques occurred during concentric contractions rather than during the isometric contractions.

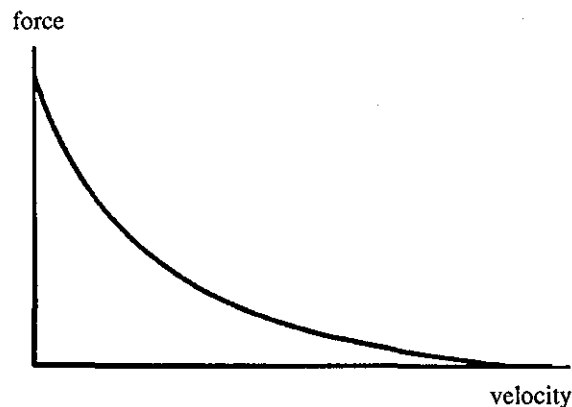


Figure 2.23. Force - velocity relationship found by Hill (1970).

Fuglevand (1987) recorded joint torque and angular displacement for maximal knee extension at various angular velocities (30 to 300°.s⁻¹ in steps of 10°.s⁻¹). The torque-velocity relationship was obtained for joint angles from 75° to 165° in steps 15°. It was found that for the smaller angles the torque-velocity curve followed a Hill type hyperbolic curve. As the angle increases the torque-velocity curve departed from the hyperbolic curve. The data appeared similar to the curves obtained by Perrine and Edgerton (1978). The author suggested that the phenomenon was related to the interaction between muscle length and the torque produced by the muscle. In a similar study Marshall et al. (1990) found that peak torque occurred at a velocity of 60°.s⁻¹ rather than 0°.s⁻¹ as predicted by the hyperbolic curve. Wickiewicz et al. (1984) also obtained torque-velocity curves which were biphasic.

Edman (1988) found that the force-velocity relationship was biphasic for individual muscle fibres from frogs (Figure 2.24). As the velocity of shortening dropped below one tenth of the maximum velocity of shortening the force produced by the muscle fibre was less than expected.

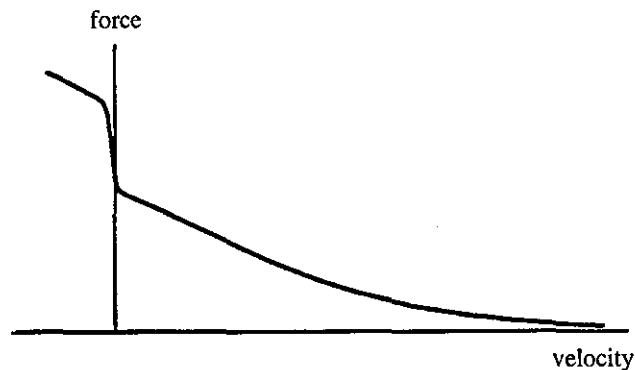


Figure 2.24. Force - velocity relationship found by Edman (1988).

A number of studies have used isokinetic dynamometers to obtain three dimensional surface plots of joint torque, angle and angular velocity (Marshall et al., 1990; Fuglevand, 1987; King et al., 1996; King, 1998). Fuglevand (1987) performed maximum knee extensions over a range of angular velocities (30°.s⁻¹ to 300°.s⁻¹) and plotted the joint torques against joint velocity and joint angle as three-dimensional surfaces. For any give joint angle and angular velocity the associated maximum joint torque could be determined. Marshall et al. (1990) obtained a similar set of three-dimensional plots for knee extension and plotted the muscle force against length and velocity. The three-dimensional plots obtained by Marshall et al. (1990) were similar to those obtained by Fuglevand (1987). King et al. (1996) outlined a method for fitting raw torque data as a function of joint angle and angular velocity data. Using a Kin-Com isokinetic dynamometer King et al. (1996) collected torque data at the ankle, knee, hip and shoulder from an elite male gymnast. In all cases the joint centre of the subject was lined up with

the axis of the dynamometer and the subject was secured with velcro straps. The subject performed two repetitions of concentric-eccentric muscle contractions at a range of different angular velocities (20, 50, 100, 150, 200 and 250 °.s⁻¹) at each joint centre. To create the three-dimensional surface fits of joint torque to angle and angular velocity two relationships were determined. Firstly an exponential relationship between the joint torque and angular velocity was obtained. The second relationship expressed the joint torque as a quadratic function of the joint angle. These two relationships were combined to express joint torque as a non-linear function of joint angle and angular velocity. The three-dimensional surface was defined using eighteen parameters.

When using an isokinetic dynamometer the operator must take into account the possible errors in the the data that are recorded. Many papers in the literature refer to errors created by "overshoot" (Sapega et al., 1982; Winter et al., 1981). The problem is associated primarily with dynamometers which are not motor driven. In order to move the arm of the dynamometer the subject must apply a force. The applied force initially accelerates the crank arm before the gearing of the dynamometer fixes the angular velocity. If the subject accelerates the arm beyond the predetermined isokinetic angular velocity the arm is decelerated by the gearing of the dynamometer. The deceleration of the arm leads to a peak in force/torque recorded by the data capture system (Sapega et al., 1982; Winter et al., 1981) which can lead to errors, especially if the purpose of the study is to determine peak force or time to peak force.

Overshoot is less of a problem for motor driven isokinetic dynamometers as it is the motor which accelerates the crank arm to the predetermined angular velocity. However, being driven by a motor has its own set of problems. During a concentric contraction the purpose of the motor is to accelerate the crank arm to the predetermined angular velocity and then maintain this angular velocity. If the concentric contraction is to precede an eccentric contraction the motor and gearing must bring the crank arm to rest then accelerate it in the opposite direction for the eccentric phase. These accelerations and decelerations lead to portions of the range of motion which are not isokinetic (Herzog, 1988; King et al., 1996). As the angular velocity of the trial increases, the range of movement which is isokinetic decreases (Herzog, 1988; Marshall et al., 1990; Perrine and Edgerton, 1978). To ensure the movement is isokinetic over the range of interest trials should be designed to allow for the acceleration and deceleration of the crank arm (Herzog, 1988; King, 1998).

Herzog (1988) presented a paper outlining the difficulties of obtaining true joint torques. The true joint torque was expressed as a function of several components. These included the torque recorded by the dynamometer and terms involving the weight and accelerations of the crank arm and the subject's limb. Depending on the orientation of the subject work must be done against gravity to lift both the limb and the crank arm. This means that the torque created by the weight of the limb and crank arm must be overcome

before the dynamometer could register a torque. By neglecting this factor the torque recorded by the dynamometer would tend to underestimate the joint torque (Herzog, 1988). Herzog (1988) found that the percentage differences between resultant joint moment recorded using the Cybex (an isokinetic dynamometer) associated with these terms reached maximum values of 17.2%, 11.7%, and 24.3% for the largest angles (the limb approaching the horizontal) at $0^{\circ} \cdot s^{-1}$, $120^{\circ} \cdot s^{-1}$ and $240^{\circ} \cdot s^{-1}$ respectively. If the joint action were to occur in the direction of gravity the converse would be true and the dynamometer would tend to overestimate the joint torque. King (1998) corrected the torque recorded by the dynamometer for the weight of the limb in order to obtain the joint torques.

The term relating to the acceleration of the arm proved to have negligible effect on the calculation of the joint torque during the mid-section of the exercise analysed, with a maximum magnitude at 0.3%. Therefore the assumption of constant angular velocity during the mid-section of the exercise was good even up to $240^{\circ}/s$ (even though the range where constant angular velocities of the Cybex arm can be expected to decrease with increasing angular velocities, Perrine and Edgerton, 1978). The error values created by the accelerations of the limb were larger than those for the dynamometer arm. Part of the reason for this was the larger moment of inertia of the limb segment compared with the Cybex arm. The larger error value obtained from the acceleration of the limb implied that even with the dynamometer arm moving at a constant angular velocity the limb may have considerable accelerations and thus the movement cannot be termed isokinetic (Herzog, 1988). King (1998) differentiated data collected from a goniometer in order to obtain the joint angular velocity and used this data (as opposed to the velocity recorded by the dynamometer) to determine when the joint actions were isokinetic.

The final source of error which Herzog (1988) looked at was how the axis of the knee moved relative to the axis of the dynamometer arm. If the axes were perfectly aligned throughout a trial the distance from the knee to the load cell should equal the distance from the axis of rotation of the crank to the load cell. By carefully aligning the joint centre with the crank and strapping the subject's limb to the dynamometer arm Herzog (1988) was able to keep the difference between the two distances to below 0.01 m. King (1998) collected data from a goniometer attached to the subject and corrected the torque for both joint angle and the moment arm of the subject.

Summary

The literature has shown that isokinetic dynamometers are useful machines for collecting information about the characteristics of intact muscles. These data may be fit with an appropriate function to form a three-dimensional surface of joint torque against

angular displacement and velocity. It has been shown that the hyperbolic function used to describe the force-velocity relationship does not always hold when recording joint torques from muscle groups. A function which is biphasic may be more appropriate to fit the concentric range of the data as shown by King (1998).

When using an isokinetic dynamometer care must be taken during the collection of data. The angle range over which the torque is recorded should be large enough to allow for the acceleration of the crank arm at the start and end of the isokinetic phase. Data should be corrected for gravity, limb weight and differences between crank and joint angle (King, 1998).

2.4.2 Segmental inertia parameters

The inertia parameters of an individual's body segments refer to their mass, mass centre locations and moments of inertia. Mass, or inertia, refers to how much matter a body, or segment, possesses and is a measure of its reluctance to alter its state of motion. The mass centre of a body, or segment, is the theoretical point where all the body's mass could be considered to be concentrated. Moment of inertia is the rotational equivalent of inertia. It is a measure of how the matter in a body is distributed about an axis. It is similar to inertia in that it determines how difficult it is to change a body's rotational motion. It is different to inertia because a body's moment of inertia will vary depending on its shape and the axis of rotation considered.

In the field of performance related sports biomechanics the researcher is interested in how the human moves. Since most human movements involve rotations about joint axes the moments of inertia of an athlete's limbs are of particular interest. Using a knowledge of the athlete's segmental moments of inertia and their angular velocities it is possible to determine segmental and whole body angular momenta.

The calculation of whole body mass, mass centre location, moments of inertia and subsequently angular momentum requires a knowledge of the individual segmental inertia parameters. In many applications it is desirable to have a set of parameters for the particular individual under investigation (Yeadon and Challis, 1994). Simulation models attempt to model the human form using rigid links (Morlock and Yeadon, 1988; Gatto and Neal, 1992; Dainis, 1968; Duck, 1980). To improve the external validity of the models the rigid links should have the inertia parameters corresponding to the segmental parameters of the individual who is being modelled. For example a three segment model used to simulate a gymnast circling the high bar may comprise an arm segment, a torso segment and a leg segment. It would therefore be appropriate for these three segments to have the same masses, mass centre locations and moments of inertia (in the sagittal plane) as the performer being modelled. Since any model should be evaluated against

experimentally obtained data it may be suggested that using individualised inertia parameters in both the experimental and theoretical analyses is both justifiable and likely to improve the accuracy and external validity of the results.

This section of the literature review outlines the methods for obtaining individualised inertia parameters for use with a simulation model and the kinematic analysis of the backward giant circle. The methods reviewed include experimental and theoretical techniques. The experimental techniques include cadaver studies and regression methods along with direct measures for obtaining inertia parameters in situ. The theoretical methods are based on geometric modelling using anthropometric measurements which have either been obtained directly or from photographic images.

Several methods have been presented for the determination of segmental parameters. Dempster (1955) calculated the mass of both cadaver segments and limbs in situ using the immersion technique. The segment of interest is lowered into a tank containing water. The volume of water displaced is equivalent to the volume of the segment. To find the mass of the segment Dempster (1955) assumed that its density was the same as water. However, for the segments of the eight cadavers used in the study it was possible to calculate their density from their measured mass. The mass centre locations of the cadaver segments were determined using a balance plate. A technique more commonly used is the moment table or reaction table (Nigg, 1994). If the weight of the segment is known the balance plate may be used to determine the mass centre location by taking moments about the pivot point. This method can only be used to locate the mass centre in one plane at a time. Hay (1994) used a reaction board to calculate the mass centre location for the whole body. Moments of inertia may be determined using the pendulum technique. The object/segment/body is suspended from a fixed point then set in motion. The moment of inertia is determined from the period of one oscillation. This method was used by Dempster (1955). Hatze (1975) presented a method for determining the mass centre location and moment of inertia of body segments in situ using passive oscillations. Hatze's (1975) method used the time period of oscillation and the decay in amplitude of the oscillation to determine the moment of inertia of the segment.

Gamma scanners have been used to determine the inertia parameters of segments. Brooks and Jacobs (1975) passed radiation from a cobalt-60 source through a leg of lamb. The mass calculated from the gamma scanning and from weighing differed by less than 1%. This method has been used on live subjects by Zatsiorsky and Seluyanov (1983). The entire body of 100 subjects was scanned and segmental masses determined. Nigg (1994) showed that the segmental masses expressed as a percentage of body weight obtained by Zatsiorsky and Seluyanov (1983) compared well with those obtained by Dempster (1955).

Inertia parameters have been determined using whole body mass, anthropometric

measurements and regression techniques (Hinrichs, 1985; Forwood, Neal and Wilson, 1985). Regression techniques for determining inertia parameters have relied on cadaver data. Hinrichs (1985) obtained regression equations based on the data of Chandler, Clauser, McConville, Reynolds and Young (1975) to predict moments of inertia based on anthropometric measurements. The author suggested that extrapolation using anthropometric measurements outside those of the cadaver sample should be done with care. This was due to the small number of cadavers used. Barter (1957) combined the data from three cadaver studies, including Dempster (1955), to express segmental mass as a linear function of whole body mass. The standard errors ranged from 0.3 kg to 2.9 kg for both feet and the head, neck and trunk respectively. The problem with regression techniques is that relatively few cadavers have been studied (fewer than fifty) which have largely consisted of adult caucasian males. Gymnasts tend not to have the physical dimensions of "average" people, therefore using regression equations will probably lead to errors caused by extrapolation. Morlock and Yeadon (1989) used non-linear regression equations and found them to be superior to the linear regression equations. It was also found that the non-linear regression equations gave reasonable estimates of the segmental inertia parameters even when the anthropometric measurements used lay outside the sample range of the cadaver data used (Chandler et al., 1975).

Mathematical models have been used to represent the human form as a specified number of rigid geometric solids (Whitsett, 1963; Hanavan, 1964; Jensen, 1976; Hatze, 1980; Yeadon, 1990b). By obtaining the volumes of the solids and assuming their density, which may be fixed (Yeadon, 1990b; Hanavan, 1964) or vary (Hatzé, 1980) throughout the solid, the mass, mass centre location and moment of inertia of the solid may be obtained using mathematical procedures. With the inertia parameters of the solids known the inertia parameters of the limbs/segments may be determined.

In general the mathematical models require the taking of anthropometric measurements from the subject to be modelled. The number of measurements taken depends on the number of solids that the model is constructed from. An alternative method for obtaining the dimensions of the solids is to digitise images of the subject from video or photographs (Jensen, 1978). Many of the mathematical models have also assumed fixed densities for the solids/segments. Ackland, Henson and Bailey (1988) found from the dissection of the left and right thigh of a cadaver that the cross-sectional density showed marked variations. The author predicted the volume of the segment using the inertia model of Jensen (1978) and computer tomography (CT). The mass of the segment was predicted using the calculated volumes and actual density values determined from the CT scans and from the uniform density values obtained from the cadaver studies of Dempster (1955). It was shown that the assumption of uniform density throughout the thigh segment would lead to only minor errors in the estimation of inertial parameters. Larger errors were obtained when the segment volume was inaccurately estimated. Since

the assumption of uniform density leads to only minor errors then a mathematical model which accurately estimates the segment volumes must be recommended. However, the question arises as to which density values to use. That is, the density values reported by either Dempster (1955) or Chandler et al. (1975) could be used. The most appropriate density values to use would be those that result in the estimation of whole body mass which is closest to the recorded mass.

Hanavan (1964) developed a 15 segment inertia model of the human form. The model was constructed from spheres, circular ellipsoid, elliptical cylinders and the frustra of right circular cones. The model required just 25 anthropometric measurements to define the segment volumes. The segment masses were calculated using the regression equations of Barter (1957). Barter (1957) obtained the regression equations based on cadaver data to express segmental weight as a linear function of body weight. Hanavan (1964) stated that a major limitation of the geometric model approach to obtaining segment volumes is that segment shapes cannot be duplicated by a geometric solid of revolution (Jensen, 1976).

Jensen (1976) modelled the body using 16 segments. Lateral and frontal photographs of an athlete were sectioned at 2 cm intervals. Each interval was reconstructed as an elliptical zone based on the radii of the section. The volume of the individual segments were calculated by summing the volumes of the zones. Masses were calculated for each zone using uniform density values. The density values were obtained using the same method as Hanavan (1964). The moments of inertia for each zone were calculated as the moment of inertia of an elliptical plate. The moment of inertia for the segments was calculated using the moments of inertia of the zones and the parallel axis theorem. The model was able to calculate whole body mass to within 2% of the measured mass.

Hatze (1980) developed a 17 segment inertia model. The 17 segments were divided into small mass elements of varying geometric shape. This enabled the close approximation to fluctuations in segment shape. Cross-sectional density values could be varied along with the density about the segment's longitudinal axis. Separate considerations were made when modelling the male and female with adjustments made to the density of certain segments based on the fat levels of the subject. The model required 242 separate anthropometric measurements. When results between predicted and measured whole body mass were compared for four subjects the model produced a maximum error of 0.52%. Moments of inertia predicted by the model also compared well with experimentally obtained values (maximum error 5%). Although the model has been shown to be accurate when predicting whole body mass, it should be pointed out that for use in performance related sports biomechanics with elite athletes the researcher does not always have the luxury of enough time to obtain 242 anthropometric measurements from their subject. This dilemma may be compounded if several inertia sets are required.

Yeadon (1990b) presented a mathematical model for use with predicting personalised inertia parameters. The body was modelled as 40 geometric solids (Figure 2.25). To obtain the volumes of the 40 solids 95 anthropometric measurements are required. These measurements comprise 34 lengths, 41 perimeter, 17 widths and three depths taken at specified levels on the body. The time to record these measurements is less than 25 mins for an experienced operator. Previous geometric models have used ellipses to model the cross-section of body segments (Hanavan, 1964; Jensen, 1976; Hatze, 1980). Yeadon (1990b) showed that these were poor shapes for the modelling of the torso segments. To improve on the ellipse Yeadon developed a "stadium" solid based on the perimeter and width measurements. The model assumed uniform density across each solid and used the density values of Dempster (1955). The model was able to calculate the inertia parameters for up to 20 body segments (Figure 2.25). The model predicted the whole body mass to within 2.5% for the three subjects used.

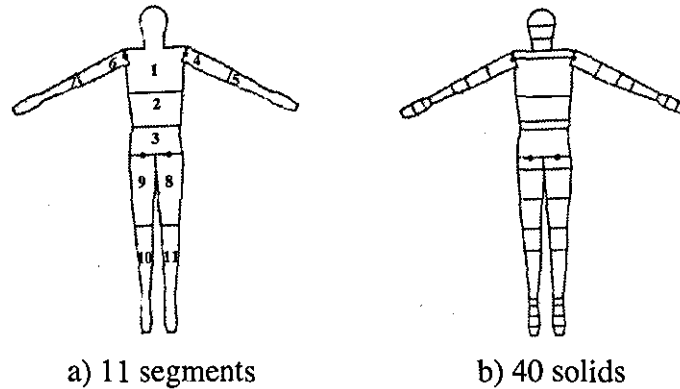


Figure 2.25. The inertia model of Yeadon (1990b) (adapted from Yeadon, 1990b)

The use of accurate subject specific inertia parameters is desirable whether it is to improve the external validity of a simulation model or to be used in the analysis of cine or video data. The geometric models reviewed allow the inertia parameters to be customised to the individual. The model of Yeadon (1990b) has been shown to be accurate at predicting the whole body mass of a subject and requires only 25 mins of contact time with the subject. Since access to the subject is permitted in the present study the model of Yeadon (1990b) will be used to obtain inertia parameters for both the simulation model and the three-dimensional analysis of the backward giant circle.

2.4.3 Three-dimensional analysis

In the field of performance related sports biomechanics the most common and versatile techniques of analysis are the visual techniques. The visual techniques include

cine and video recordings along with the appropriate analysis procedures.

The simplest approach is to assume that the movement occurs in two dimensions (i.e. planar motion). This method requires the use of only one camera. Further cameras may be used depending on the field of view required. By placing a calibration object in the plane of movement a scale factor may be determined. The scale factor is then used to transform the image co-ordinates from the digitised image into co-ordinates in the movement space (Yeadon and Challis, 1994; Winter, 1990; Miller and Nelson, 1973). This method works on the assumption that all movement occurs in the plane of progression or that the movements which do not are not important. The simplicity of this method is not without its shortcomings. Errors are produced when the focal axis of the camera is not in line with the movement (Miller and Nelson, 1973) and it is also common for important body landmarks to be obscured by other body parts when using only one camera. To avoid these errors and assumptions it is often better to perform a three-dimensional analysis even when the movement appears to be planar. The method of three-dimensional analysis requires the use of two or more cine or video cameras (Miller and Nelson, 1973; Yeadon and Challis, 1994).

Historically, cinefilm has been used in preference to video due to its superior resolution (Kennedy, Wright and Smith, 1989; Angulo and Dapena, 1992). However, recent developments in video cameras and video based digitising systems have reduced the difference in resolution. The use of more than one "charged coupled device" (CCD) chips in modern cameras produces a more colour refined picture than older one-chip systems (Tan, Kerwin and Yeadon, 1995). Recording formats have also improved with Hi8 tapes having 400 lines of resolution compared with the 240 lines associated with VHS. Kerwin and Challis (1994) produced data of equal accuracy to cine using a high resolution video digitising system (Prisma III based). This system had a maximum resolution of 1,536 x 1,150. Kerwin (1995) presented an improved video digitising system based on the Apex imager (Target). This system was capable of four times zoom, line interpolation to "smooth" the images and sub pixel cursor movement. The Target (Apex based) system has a resolution of 12,288 x 9,200. Tan et al. (1995) found the Apex based system to have better precision and accuracy when compared with the Prisma III based system used by Kerwin and Challis (1994).

Cine and video techniques require the manual digitisation of each field of movement. This can be a very time consuming task and a possible source of errors. This has led to the development of automatic motion analysis systems. The MacReflex system uses reflective markers attached to the athlete or object which are tracked by infrared cameras within a calibrated movement space. This method requires enough cameras so that the markers can always be seen by at least two of the infra red cameras at all times. Such a system reduces the process and analysis time considerably (Lindsay, 1996). However, for complicated skills as seen in gymnastics problems arise due to the

large volumes of movement space required and the obscuring or dislodging of the markers by other body parts. It should also be noted that the markers cannot be placed at the joint centres of the subject, therefore some correction/analysis would be required to locate the joint centres from the output.

In conclusion three-dimensional analysis should be preferred to a planar approach when investigating human movements. The advancement in video based analysis systems in terms of their accuracy and precision coupled with the flexibility they offer in terms of cost and processing time make them the ideal choice in performance related biomechanics. Although the automatic tracking systems would reduce the time for data analysis they still have their limitations. Two multi-chip video cameras will be used to collect data on an elite gymnast performing backward giant circles. The images will be digitised using the Target high resolution system.

Synchronisation of force and video data

Three-dimensional reconstruction of a single point requires image co-ordinates for that point simultaneously from at least two camera views (Yeadon and Challis, 1994). The images from the two cameras therefore need to be synchronised. Cine cameras and video cameras may be physically synchronised by phase-locking and gen-locking the cameras respectively.

When phase/gen-locking has not been available other methods have been used to synchronise the data sets. By placing a timing device within the fields of view the times for each frame/field may be determined. The data from each camera view can then be interpolated (Yeadon and Challis, 1994 cited Walton, 1981 and Dapena, 1979). Yeadon (1989) presented a method of synchronising camera views by identifying common events from the two camera views. Greig and Yeadon (1994) matched the events of foot contact from two cameras during the approach phase in high jump.

Aside from the three-dimensional reconstruction, film data is often required to be synchronised with force data (Cappozzo, Leo and Pedotti, 1975). When combining data from a video analysis and force data capture, errors in synchronisation can lead to further errors in the analysis. O'Connor, Yack and White (1995) demonstrated how an LED used to synchronise force and video could lead to an error in synchronisation of one whole video field. A method was presented for interpreting the video signal for improved synchronisation with force data collected from a force platform.

Brewin (1995) recorded the tension in one cable for a gymnast performing giant circles on rings whilst simultaneously recording video images from two cameras. The collection of the tension data was initiated using a trigger. The video and tension data were synchronised by an array of LED's connected to the trigger which was placed in

view of both cameras. Shapiro (1978) synchronised two cameras filming a golf ball falling under the acceleration of gravity by illuminating a flash bulb in the view of both cameras.

Where possible gen-locking should be used to synchronise multiple cameras recording the same event, since this reduces the additional analysis time required to synchronise the image data using an alternative method. O'Connor et al. (1995) and Cappozzo et al. (1975) highlighted the problem associated with errors in synchronising video and force data. Using an event to trigger the force data collection and to produce a visible record of when this event occurred would allow the force and video data to be synchronised to within half the time for one frame/field of the image recording. Such a system will be used when collecting force and video images of a gymnast performing backward giant circles on the high bar.

Three-dimensional reconstruction

Several techniques have been developed to calculate three-dimensional locations of landmarks from synchronised image co-ordinates (Abdel-Aziz and Karara, 1971; Chow, 1994; Bergemann, 1974). The most common technique used is the direct linear transformation (DLT) method outlined by Abdel-Aziz and Karara (1971). As with the other techniques a minimum of two cameras are required. A major advantage of DLT is that it was designed to be used with non-metric cameras. This allows the cameras to be placed in unknown locations (Van Gheluwe, 1978). The cost of this is that calibration of the movement space is required. The process of transforming comparator co-ordinates into object co-ordinates was usually performed in two stages (Abdel-Aziz and Karara, 1971). The comparator co-ordinates are first transformed into image co-ordinates and then from image co-ordinates into object space co-ordinates. However, these steps were not possible using non-metric cameras. Therefore, the method of Abdel-Aziz and Karara set out to solve the above transformations simultaneously.

The DLT method is based on the collinearity condition which relates the digitised co-ordinates to the spacial co-ordinates (Yeadon, 1996). Yeadon (1996) stated that for an ideal system a point P in space, the centre of the lens C and the image I are collinear (Figure 2.26).

From this condition a transformation which is defined by 11 parameters may be obtained. These parameters are related to the location and orientation of the camera and the characteristics of the digitising system. There are eleven parameters for each of the cameras. To calibrate the camera-digitiser system control points in the movement space, with known locations, must be filmed. Each control point corresponds to a pair of digitised co-ordinates (u,v) which gives rise to two equations for the 11 DLT parameters

(Yeadon, 1996). Therefore to solve for the 11 DLT parameters a minimum of six control points are required. This results in 12 equations in 11 unknowns. The 11 DLT parameters are then determined using a "least squares" formulation.

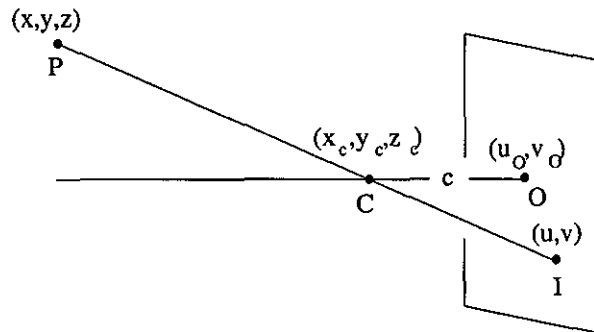


Figure 2.26. The collinearity condition.

To reconstruct the three-dimensional co-ordinates of unknown points the digitised co-ordinates from the two camera views are required (synchronised). Using the two sets of DLT parameters obtained from the calibration of the two cameras and the digitised co-ordinates four equations in the three unknown co-ordinates of the point (x, y, z) are obtained. The three-dimensional co-ordinates of the point are determined using a least squares solution.

Accuracy of reconstruction

Shapiro (1978) determined the accuracy of the 11 parameter DLT reconstruction by filming a calibration volume containing 48 control points. Only 20 of the points were used to calculate the 11 parameters. The remaining points were used to determine the accuracy of the reconstruction. For a 3m field of view the average error in reconstruction was 5 mm. To investigate the accuracy of filming a dynamic movement Shapiro filmed a golf ball in free flight falling through the calibrated movement space. The acceleration due to gravity was calculated from the reconstructed vertical displacement data. The error in the calculation of the acceleration due to gravity (9.8 m.s^{-2}) was found to be within 1% to 4%.

A number of studies have attempted to determine the effect that the number of control points has on reconstruction accuracy (Wood and Marshall, 1986; Hatze, 1988). The 11 parameter DLT requires a minimum of six control points; however it was found that the accuracy of reconstruction improved with the number of control points used (Wood and Marshall, 1986; Hatze, 1988; both studies used a maximum of 30 control points).

Studies have also been carried out to determine the accuracy of reconstruction outside the calibration volume (Challis, 1995; Wood and Marshall, 1986; Angulo and Dapena, 1992). All three studies showed that reconstruction accuracy was inferior for points outside the calibration volume. Wood and Marshall (1986) concluded that it would be better to have a smaller number of control points well distributed throughout the object space than to use extrapolation.

The DLT method of three-dimensional reconstruction is flexible in that it allows the cameras to be placed in arbitrary position. In order to reconstruct the digitised images into three-dimensional locations the 11 DLT parameters must be determined from known control points which make up the calibration volume. The best results in terms of reconstruction accuracy were obtained when the points to be reconstructed fell within the calibration volume. Using more than the six control points was also found to improve reconstruction accuracy. It is therefore suggested that when constructing a calibration volume effort should be made to incorporate the entire movement space of the activity to be reconstructed.

Curve fitting

A theoretical approach to the analysis of human movement requires a knowledge of the equations of motion which define the system. These equations of motion often contain terms relating to the linear and rotational displacement of body segments. It would also be necessary to obtain the first and second derivatives of these displacement-time data. Nearly all kinematic data is obtained through some measurement and data reduction system (Winter, Sidwall and Hobson, 1974). As a result the data will consist of two parts; the true signal and the noise which has been added to the true signal (Challis and Kerwin, 1988). Therefore a method is required to obtain the simplest representation of the data that adequately describes the true signal whilst eliminating the noise due to experimental errors (Wood, 1982). Such a process is referred to as either "curve fitting" or "data smoothing".

Data may be smoothed and differentiated using a number of techniques. The most commonly used techniques are a digital filter with numerical differentiation based on finite differences, a least squares polynomial fit with analytical differentiation, a Fourier analysis and polynomial splines.

Fourier analysis allows periodic data to be expressed as a weighted sum of sine and cosine terms of increasing frequency (Wood, 1982). Using a truncated Fourier series allows the frequencies associated with the noise signal to be eliminated.

A global polynomial fit uses all the available data points and attempts to fit a low order polynomial (less than seven) (Wood, 1982) using a least squares approach. While

a least squares approximating polynomial provides the same degree of accuracy over all data points, it should be noted that outside this interval the function departs to plus or minus infinity. For this reason it is often better to record additional data points outside the time interval of interest. The drawbacks to using a polynomial fit are that decisions must be made regarding the order of the polynomial and the number of data points to be included. Another shortcoming is the inability of global polynomial functions to adequately fit regions of varying complexity within one data series. The need for an approximating function that can fit data in different regions of time with varying curvature has led to the use of spline functions (Wood, 1982).

Spline functions may be defined as piecewise polynomials of some degree $2m-1$ joined at points called knots in such a manner as to give a continuous function having m continuous derivatives (Wood and Jennings, 1979). The condition by which the function has m continuous derivatives ensures that it is smooth itself but, unlike a global polynomial, its piecewise nature enables it to adapt quickly to changes in curvature (Wood, 1982).

The spline approximation procedure commonly employed is that of Reinsch (1967, 1971) which provides a natural spline function of degree $2m-1$ with knots at each data point (N). A set of $N-1$ polynomials of degree $2m-1$ are pieced together in such a way that the "smoothness integral" is minimised.

$$\int_{x_1}^{x_N} [g^{(m)}(x)]^2 dx \quad (2.4)$$

under the boundary condition that the fit is within the "accuracy measurement"

$$\sum_{i=1}^N \left(\frac{g(x_i) - y_i}{\delta y_i} \right)^2 \leq S \quad (2.5)$$

where

- δy_i standard errors of measurement
- S parameter that controls the extent of smoothing

Cubic splines have been commonly used in biomechanics for curve fitting. Zernicke, Caldwell and Roberts (1976) calculated the difference between the force determined from the second derivative of displacement-time data and those obtained from the force platform during a kicking activity. This procedure was used to compare the polynomial and cubic spline methods of curve fitting. The mean percentage difference

between the force recorded from the force plate and that derived from the fifth order polynomial fit was 10.27% (range 0.50% to 81.30%). The mean percentage difference for the cubic spline was 4.75% (range 0.04% to 11.43%). Zernicke et al. (1976) found that the spline was more flexible and was able to cope with rapid changes in the data, whereas the polynomial tended to over-smooth the data which lead to inaccuracies in the computation of force and accelerations. McLaughlin, Dillman and Lardner (1977) also found that the cubic spline was superior to the polynomial fit.

The first and last values of the second derivative of a cubic spline function will be zero; consequently, spurious acceleration data may be obtained close to the end-points. To cope with this problem Zernicke et al. (1976) and McLaughlin et al. (1977) suggested that additional data points should be collected at either end of the interval. A further weakness of a cubic spline is that the third derivative (jerk) has jump discontinuities, and to assume that forces acting within the body act in a non-smooth manner would seem to be inappropriate (Wood and Jennings, 1979).

Wood and Jennings (1979) overcame the problems of the cubic spline by using a quintic spline. Since the third derivative (jerk) of a quintic function is both continuous and smooth Wood and Jennings (1979) suggested that the quintic spline would be a more appropriate model for biomechanical data.

Challis and Kerwin (1988) compared the performance of a number of curve fitting techniques by generating mathematical functions and adding noise to them. This allowed the second derivative to be accurately determined prior to fitting the curve. The quintic splines produced superior results to the cubic splines. The cubic spline was inferior at the endpoints of the second derivative. Also the second differential of the cubic spline is piecewise-linear so does not approximate very well to a signal whose second differential is complex.

Summary

It is preferable to collect three-dimensional data rather than two-dimensional data even if the motion to be investigated appears to be planar. Using three-dimensional analysis no assumptions about the nature of the movements are made. The difference in resolution between cine based and video based analysis has decreased due to the improvement of both the video cameras and the video based digitising systems. It is therefore the choice of the researcher as to which format to use. The method of three-dimensional DLT has been proven. Care must be taken during calibration that the entire movement space is contained within the calibration volume. The smoothing of data will depend upon the individual application. However, if second derivative data is required a quintic spline would be most appropriate.

2.4.4 Simulation

The definition of a simulation model was given in section 2.3.1 and examples of such models used to simulate swinging on the high bar were given in section 2.3.3. Using a simulation model the researcher has complete control over the experiment being conducted and internal validity can be maximised. That is, changes to the independent variable may be made without effecting or changing other variables. This is not always the case when working with a live subject. Although simulation models have high internal validity it is the external validity which causes most concern. As stated in section 2.3.1 external validity refers to how well the results of an experiment relate to the real world. For a simulation model external validity is most often related to its complexity. To maximise the external validity the model should contain all the components relevant to the activity under investigation. This statement can be interpreted in two ways. The first is to take the statement literally and attempt to model the finest details. For example, Hatze (1981) presented a human body model which was used to simulate the long jump takeoff. The model comprised 17 segments and 46 muscle groups. These muscles required neural control time histories for activation. The advantage of such a complicated model is that it requires so much input information that there is an increased possibility of mimicking the activity under investigation (Yeadon and Challis, 1994). However, since the model is so complex interpretation of the results is far more difficult. Often a less complex model will yield a better understanding of the underlying mechanics than a more complex model. For the simulation of giant circles models containing one or more rigid links have been successful (Dainis, 1968; Jarle, Morlon and Canal, 1993; Morlock and Yeadon, 1988; Rustenburg, Figgen and Nicol, 1993).

Simulation models may be used to predict the movements of the sporting equipment. An example of this is the simulation of the javelin. Hubbard and Rust (1984) modelled the javelin as an aerodynamic rod and simulated flight (cited by Yeadon and Challis, 1994). Other models have been used to simulate the human body. For example Yeadon, Atha and Hales (1990) simulated aerial movements with an 11 segment simulation model. In the case of the high bar both the body and the equipment must be modelled. Gatto and Neal (1992) showed how the elastic properties of the high bar effect the reaction forces experienced at the gymnast's hands. Similarly the body must be adequately modelled. Gatto and Neal's model overestimated the reaction forces at the bar by nearly one bodyweight when compared with the work of Kopp and Reid (1980). This may be in part due to the stiffness of the spring used to model the bar; however, a single segment cannot model the effect that the gymnast's technique may have on the reaction force. Since actions are performed at the shoulders, hips and knees (Okamoto et al., 1987; Brüggemann et al., 1994) the minimum number of segments required for a two-dimensional model is four.

The external validity of the simulation model is determined by evaluation with experimentally obtained data. Yeadon (1984) compared the twist and somersault angles obtained from film analysis and the simulation of twisting somersaults and expressed the accuracy of the model in terms of the percentage angle difference between the simulated and actual performance. The accuracy of the model could then be expressed in these terms. For the high bar application, the optimum technique for increasing energy or rotation may be obtained using an optimisation algorithm (section 2.3.4); yet these optimal solutions would be meaningless without knowing the accuracy of the model.

2.4.5 Optimisation

The process of optimisation may be described as the search for the maximum or minimum value of a given function. The function, f , will usually depend on one or more independent variable. If the function is dependent on only one independent variable the process of optimisation is referred to as one-dimensional. If the function is dependent on more than one variable it is termed multi-dimensional. To optimise the function the values of the independent variables must be found where f takes on a maximum or minimum value (Press, Flannery, Teukolsky and Vetterling, 1988). From this definition the process of optimisation is the quest for either the largest value for the function f or the smallest value. Maxima or minima can be either global (truly the highest or lowest function value) or local (the highest or lowest function value in a neighbourhood).

To perform an optimisation requires numerous function evaluations along with some process of manipulating the function variables in such a way as to obtain the maximum or minimum value of the function. It is therefore practical to use a mathematical algorithm to solve this problem. When choosing an optimising routine/algorithm it is important to consider the computational costs. That is, how long the procedure will take to find the optimum value of f . This will be related to the complexity of the function and the method used by the optimising algorithm. A simple method for optimisation is the Golden section search. This process attempts to bracket the optimum using three points. It is assumed that the minimum value is within the interval defined by the outer two points. At each step one of the intervals is reduced until the interval is acceptably small. When this acceptably small interval is achieved the middle point of the triplet is the minimum or maximum value of the function.

If the behaviour of the function is known an appropriate method may be adopted. For example if the function is parabolic near the minimum then an algorithm which fits a parabola through any three points on the function would be an adequate algorithm to find the minimum. One such method is called inverse parabolic interpolation. Here, a parabola is drawn through three points on the function curve. The function is then

evaluated at the parabola's minimum. In the next step one of the initial three points is replaced by the value at the parabola's minimum and so the process continues (Press et al., 1988).

The two methods described above were for one-dimensional optimisations. The next two methods are for multi-dimensional functions where the function is dependent on N variables (where $N > 1$). The "downhill simplex method" as developed by Nelder and Mead (1965) is not considered to be efficient in terms of the number of function evaluations required. It is based on a geometric shape which comprises $N + 1$ points. The algorithm is started with an initial guess of the function variables. The algorithm then moves these points in such a way that the highest point is reflected through the opposite face to produce a lower point. By repeating this process the simplex "walks downhill". If the simplex enters a valley (possibly a local or the global minima) it is able to flow along the bottom of it. However, if this valley is a local minimum the simplex may not be able to escape as the vertices will remain within the valley. This is a common problem with many other optimisation algorithms. To avoid obtaining a local minimum it is suggested that the algorithm is used a number of times but from different starting positions (different starting values of the function variables). This may result in a number of different local minimums. If the process is repeated an adequate number of times the minimum which has the lowest function value may be accepted as the global minimum.

The second method is called "Simulated Annealing". This process is based on how liquids cool to form solids. If molten metal is allowed to cool slowly (anneal) the molecules within are able to line themselves up to form pure crystals. When the molecules form the pure crystals they are in a state of minimum energy. If however, the molten metal is cooled too quickly it is unable to reach this minimum energy state. The process is based on the idea that at a temperature T the system has its energy probabilistically distributed among all different energy states. Even when at a low temperature there is a chance that the system is in a high energy state (Press et al., 1988). Therefore the process does not give up this possibility and will continue to look for a possible escape from the local minimum in an attempt to find the global minimum. This is done by accepting uphill moves as well as the usual downhill moves. This is known as the Metropolis algorithm.

Corana et al. (1987) and Goffe et al. (1994) tested the Simulated Annealing algorithm on a number of test functions and compared the results with other minimisation algorithms (including the Simplex algorithm). Having a prior knowledge of the test functions local and global minima allowed the authors to evaluate the success of the algorithms. The process of Simulated Annealing was found costly in terms of function evaluations when compared with the Simplex algorithm and other Adaptive Random Search methods (Corana et al., 1987). However, it was able to find the global minimum in all but one case (a neural network function whose nature proved to be virtually

impossible for any method to find the global optimum, Goffe et al., 1994) when all the other methods failed. Even when the global optimum could not be found by the Simulated Annealing a better optimum was found than any of the other algorithms (Goffe et al., 1994).

It would seem that the cost, in terms of function evaluations, of the Simulated Annealing algorithm is outweighed by its robustness in its ability to find the global optimum even for functions with a large number of independent variables. In many cases the need to find the global optimum is more important than cost and therefore the Simulated Annealing algorithm should be used.

2.5 Summary

The research question posed in Chapter 1 will be addressed using a simulation model. The model will be simple enough to allow the mechanics of the backward giant circle to be determined, yet sophisticated enough to model the major contributions to technique.

Subject specific inertia and muscle data will be collected and used in the simulation model to increase its internal validity. The inertia data will be obtained using anthropometric measurements and the inertia model of Yeadon (1990b). The muscle data will be collected using an isokinetic dynamometer. Care will be taken to address the limitations which arise during data collection which have been highlighted in the literature.

Evaluation of the model will be carried out using kinetic and kinematic data. A gymnast performing giant circles will be videoed using two cameras so that a three-dimensional analysis may be performed. Reaction forces at the bar will be collected using strain gauge technology. Full Wheatstone bridge circuits will be used to maximise the sensitivity of the strain measurement system. For the evaluation the simulation model will be driven by the joint angle time histories obtained from the video analysis. These will be input to the model in the form of quintic splines. Quintic splines are chosen as their second derivatives are smooth.

The optimisation of the accelerated backward giant circle will be carried out using the simulation model in conjunction with the Simulated Annealing algorithm (Goffe, et al., 1994). Although this method may take longer than the Simplex algorithm its chances of reaching the global optimum are higher.

CHAPTER 3

DEVELOPMENT OF A FOUR SEGMENT MODEL

3.1 Introduction

Chapter 3 presents the development of a single segment simulation model and a four segment simulation model. In both cases the equations of motion are presented along with the method of their solution. The inputs to the models and the outputs obtained from them are also presented.

3.2 Development of a single segment simulation model of a gymnast swinging on an elastic high bar

3.2.1 Introduction

Some of the previous attempts to model a gymnast swinging on the high bar have assumed that the bar was rigid (Dainis, 1968; Yeadon and Morlock, 1988). Gatto and Neal (1992) used a simulation model to show that an elastic bar lead to a reduction in peak reaction force. Brüggemann et al. (1994) showed that during an accelerated giant circle the bar achieves a vertical displacement of approximately 0.10 m from its neutral resting position as the gymnast passes through the lowest part of the giant circle. Neglecting the elastic properties of the bar during simulations may lead to an over-estimation of the model's angular velocity through the lowest point. When using an elastic bar, the vertical displacement of the bar away from its neutral resting position will increase the model's moment of inertia about that point and hence reduce the angular velocity when compared with a rigid system.

This section presents a single segment simulation model of a gymnast swinging on the high bar. A damped linear spring will be used to model the elastic properties of the bar.

3.2.2 Methods

The model comprises a single rigid rod, constrained to move parallel to the sagittal plane, to represent the gymnast and a massless damped linear spring to represent the bar

(Figure 3.1). Friction at the hands and air resistance are assumed to be negligible. The free body diagram of the system is given in Figure 3.1.

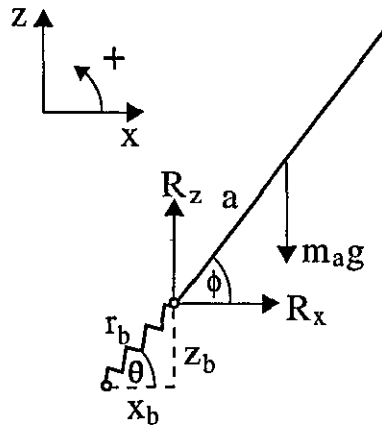


Figure 3.1. Free body diagram of the single segment model.

The nomenclature is given below:

- a : distance of mass centre from proximal end
- m_a : mass of segment
- I_a : moment of inertia of segment about its mass centre
- θ : angle between the spring and the horizontal
- ϕ : angle between segment and the horizontal
- $\dot{\phi}$: angular velocity of segment
- $\ddot{\phi}$: angular acceleration of segment
- x_b : horizontal displacement of the spring
- \dot{x}_b : horizontal velocity of high bar spring
- \ddot{x}_b : horizontal acceleration of the spring
- z_b : vertical displacement of the spring
- \dot{z}_b : vertical velocity of high bar spring
- \ddot{z}_b : vertical acceleration of the spring
- k : stiffness coefficient of the spring
- b : damping coefficient of the spring
- R_z : vertical reaction force
- R_x : horizontal reaction force
- r_b : length of the spring

Equations of motion

The equations of motion are obtained by resolving in the horizontal and vertical directions using Newton's Second Law and by taking moments about the neutral bar position (i.e. where the spring has zero length). The location of the mass centre relative to the neutral bar position is given by;

$$x = x_b + a \cos \phi \quad (3.1)$$

$$z = z_b + a \sin \phi \quad (3.2)$$

First and second derivatives of these equations yield the velocity and acceleration of the mass centre.

$$\dot{x} = \dot{x}_b - a \sin \phi \dot{\phi} \quad \dot{z} = \dot{z}_b + a \cos \phi \dot{\phi}$$

$$\ddot{x} = \ddot{x}_b - a \sin \phi \ddot{\phi} - a \cos \phi \dot{\phi}^2 \quad \ddot{z} = \ddot{z}_b + a \cos \phi \ddot{\phi} - a \sin \phi \dot{\phi}^2$$

The tension T in the spring may be calculated from the resultant of the forces R_x and R_z . The horizontal and vertical reaction forces may therefore be written as follows:

$$R_x = -T \cos \theta \quad (3.3)$$

$$R_z = -T \sin \theta \quad (3.4)$$

Hooke's Law states that the tension in a spring is equal to the product of extension and the coefficient of stiffness of the spring.

$$T = kl \quad (3.5)$$

where

k is the stiffness coefficient and l is the extension in the spring.

Substituting T from equation (3.5) into equations (3.3) and (3.4) allows the horizontal and vertical reaction forces to be written as follows:

$$R_x = -kr_b \cos \theta = -kx_b \quad (3.6)$$

$$R_z = -kr_b \sin \theta = -kz_b \quad (3.7)$$

The first equation of motion is obtained by resolving horizontally using Newton's Second Law:

$$R_x = m_a \ddot{x} \quad (3.8)$$

The horizontal reaction force, R_x , in equation (3.8) may be substituted using equation (3.6) to give the following expression:

$$-kx_b = m_a \ddot{x} \quad (3.9)$$

The second equation of motion is obtained by resolving vertically using Newton's Second Law:

$$R_z - m_a g = m_a \ddot{z} \quad (3.10)$$

Similarly the expression for the vertical reaction force obtained in equation (3.7) may be substituted into equation (3.10) to give equation (3.11).

$$-kz_b - m_a g = m_a \ddot{z}_a \quad (3.11)$$

Equation (3.5) is for a linear spring with zero damping. Equations (3.12) and (3.13) are for damped linear springs and include terms for the force due to damping. The damping force is proportional to the velocity of lengthening of the spring. The damping force is calculated by multiplying the lengthening velocity of the spring by the spring's coefficient of damping. When damping terms are introduced into equations (3.9) and (3.11) the following equations are obtained:

$$-kz_b - m_a g - b\dot{z}_b = m_a \ddot{z}_a \quad (3.12)$$

$$-kx_b - b\dot{x}_b = m_a \ddot{x}_a \quad (3.13)$$

The final equation of motion is obtained by taking moments about O, the neutral bar position. The angular momentum for the system is given in equation (3.14). The torque about the bar created by the model's weight is equal to the rate of change of angular momentum. Differentiation of equation (3.14) gives equation (3.15). The torque created by the weight of the model is the product of its mass, the horizontal displacement of the mass centre and the acceleration due to gravity (equation (3.16)). The moment equation is obtained by placing the torque created by the weight of the model equal to the rate of change of angular momentum (equation (3.16)).

$$h_o = m_a \dot{x}z - m_a \dot{z}x - I_a \dot{\phi} \quad (3.14)$$

$$\frac{d(h_o)}{dt} = m_a \ddot{x}z - m_a \ddot{z}x - I_a \ddot{\phi} \quad (3.15)$$

$$m_a g x = m_a \ddot{x}z - m_a \ddot{z}x - I_a \ddot{\phi} \quad (3.16)$$

Solution of equations

Equations (3.12), (3.13) and (3.16) are three equations in three unknowns. The unknowns are the accelerations of the spring (horizontal and vertical) and the angular acceleration of the rigid segment. The equations are solved as a set of simultaneous linear equations. Numerical integration is used to calculate the new length and velocities of the spring and the angular displacement and velocity of the body after a time interval (integration interval) using the three accelerations. At the start of each integration interval, equations (3.12), (3.13) and (3.16) are solved simultaneously for the three unknowns, accelerations of the bar and the angular acceleration of the model (all other variables are known at the start of the integration interval; these are known as the initial conditions). The accelerations are assumed to be constant over the integration interval. The new values for the displacements and velocities of the bar and segment then become the initial conditions for the next integration interval and so the process continues. This method for second order equations is similar to Euler's first order method which is the simplest form of numerical integration (Presse et al., 1986). The differential equation may be in the form given in equation (3.17). The next function value may be obtained by rearranging equation (3.17) and extrapolating over the integration interval, h , from the starting point (equation (3.18)).

$$f(x_n, y_n) = (y_{n+1} - y_n) / h \quad (3.17)$$

$$y_{n+1} = y_n + hf(x_n, y_n) \quad (3.18)$$

The assumption that the accelerations of the bar and the rotation angle will be constant throughout the integration interval will lead to systematic errors given that in reality they are constantly changing. To improve on this assumption a modified Euler method will be used. This will be explained in more detail in section 3.3.2.

A listing of the Fortran 77 code for the single segment model is given in Appendix 1a.

Input/Output

The input to the simulation model includes the inertia parameters of the gymnast to be modelled, the stiffness and damping coefficients of the bar, and the initial conditions. The initial conditions comprised the initial bar displacements and velocities and the initial angle and angular velocity of the body.

Time histories of the bar and segment displacements, velocities and accelerations are available as output. In addition the time histories of the reaction forces at the bar and the mechanical energy possessed by the model are output.

3.3 Development of a four segment elastic gymnast swinging on an elastic high bar

3.3.1 Introduction

Brüggemann et al. (1994) and Okamoto et al. (1987) showed that the major contributors to the technique of the backward giant circle came from actions at the hips, shoulders and knees. Gatto and Neal (1992) demonstrated the effect of introducing a linear spring to a rigid single segment model. However, Gatto and Neal (1992) found that merely using a spring that represented the stiffness and damping of the high bar and a single rigid segment was not sufficient to accurately model the gymnast-high bar system.

The literature indicates that the simplest model which could accurately model a gymnast swinging on the high bar must include the following components. The model must be able to perform movements at the shoulders, hips and knees. These movements would require a model with a minimum of four segments, one each for the arms, torso (including the head), thighs, and shank (including feet). As the major movements of the backward giant circle appear to occur in the sagittal plane, with the left and right sides of the body acting in symmetry, a two-dimensional model would be appropriate. The arm, thigh and shank segments would represent both arms, both thighs and both shanks respectively. In addition some provision for the elastic properties of the high bar and gymnast must be incorporated. Damped linear springs have been shown to be a simple and effective method of describing these phenomenon (Gatto and Neal, 1992).

This section outlines the development of a four segment, two spring simulation model of a gymnast swinging on the high bar. Using the initial conditions and the joint angle time histories the model calculates the rotation angle of the model, the reaction force produced at the bar and the angular momentum of the model about the neutral bar and the mass centre locations. The methods of determining and solving the equations of motion are presented. The evaluation of the model is undertaken in Chapter 7.

3.3.2 Methods

Nomenclature for the four segment simulation model

- a : distance of arm segment mass centre from proximal end
- b : distance of torso segment mass centre from proximal end
- c : distance of thigh segment mass centre from proximal end
- d : distance of shank segment mass centre from proximal end
- p : length of arm segment
- q : length of torso segment
- r : length of thigh segment
- m_a : mass of arm segment
- m_b : mass of torso segment
- m_c : mass of thigh segment
- m_d : mass of shank segment
- I_a : moment of inertia of arm segment about its mass centre
- I_b : moment of inertia of torso segment about its mass centre
- I_c : moment of inertia of thigh segment about its mass centre
- I_d : moment of inertia of shank segment about its mass centre
- ϕ : angle between arm segment and the horizontal
- $\dot{\phi}$: angular velocity of arm segment
- $\ddot{\phi}$: angular acceleration of arm segment
- ϕ_2 : angle between torso segment and the horizontal
- $\dot{\phi}_2$: angular velocity of the torso segment
- $\ddot{\phi}_2$: angular acceleration of the torso segment
- ϕ_3 : angle between thigh segment and the horizontal
- $\dot{\phi}_3$: angular velocity of the thigh segment
- $\ddot{\phi}_3$: angular acceleration of the thigh segment
- ϕ_4 : angle between shank and the horizontal
- $\dot{\phi}_4$: angular velocity of shank segment
- $\ddot{\phi}_4$: angular acceleration of shank segment

- α : angle between arm and torso segments (shoulder angle)
 $\dot{\alpha}$: angular velocity of shoulder angle
 $\ddot{\alpha}$: angular acceleration of shoulder angle
 β : angle between torso and thigh segments (hip angle)
 $\dot{\beta}$: angular velocity of shoulder angle
 $\ddot{\beta}$: angular acceleration of hip angle
 ψ : angle between thigh and shank segments
 $\dot{\psi}$: angular velocity of knee angle
 $\ddot{\psi}$: angular acceleration of knee angle
 x_{ba} : horizontal displacement of spring at the high bar
 \dot{x}_{ba} : horizontal velocity of high bar spring
 \ddot{x}_{ba} : horizontal acceleration of high bar spring
 z_{ba} : vertical displacement of high bar spring
 \dot{z}_{ba} : vertical velocity of high bar spring
 \ddot{z}_{ba} : vertical acceleration of high bar spring
 x_s : horizontal displacement of shoulder spring
 \dot{x}_s : horizontal velocity of shoulder spring
 \ddot{x}_s : horizontal acceleration of shoulder spring
 z_s : vertical displacement of shoulder spring
 \dot{z}_s : vertical velocity of shoulder spring
 \ddot{z}_s : vertical acceleration of shoulder spring
 k_{ba} : stiffness coefficient of high bar spring
 b_{ba} : damping coefficient of high bar spring
 k_s : stiffness coefficient of shoulder spring
 b_s : damping coefficient of shoulder spring
 T_1 : joint torque at the shoulders
 T_2 : joint torque at the hips
 T_3 : joint torque at the knees

The model comprises four rigid bodies representing the arms, the torso (including head), the thighs and the lower leg (including the foot), linked by three pin joints. The configuration of the system is defined by the angles shown in Figure 3.2. The system is fixed at point O and is restricted to movement in the sagittal plane. The elastic properties of the gymnast's shoulder structures are modelled using a massless damped linear spring. The bar is modelled as a damped linear spring with a known mass. It is assumed that there is no air resistance or friction between the hands and the bar.

The following relationships exist between the angles and their derivatives.

$$\begin{aligned}\phi_2 &= \alpha - (\pi - \phi) & \dot{\phi}_2 &= \dot{\alpha} + \dot{\phi} & \ddot{\phi}_2 &= \ddot{\alpha} + \ddot{\phi} \\ \phi_3 &= \alpha + \beta + \phi - 2\pi & \dot{\phi}_3 &= \dot{\alpha} + \dot{\beta} + \dot{\phi} & \ddot{\phi}_3 &= \ddot{\alpha} + \ddot{\beta} + \ddot{\phi} \\ \phi_4 &= \psi + \alpha + \beta + \phi - 3\pi & \dot{\phi}_4 &= \dot{\psi} + \dot{\alpha} + \dot{\beta} + \dot{\phi}\end{aligned}$$

The horizontal (x) and vertical (z) mass centre location, linear velocity and acceleration of the arm and torso segments are given below. The velocity and acceleration terms are obtained by twice differentiating the location of the segment mass centre with respect to time. Similar terms may be obtained for the thigh and lower leg segments (i.e. x_c, z_c, x_d, z_d and their first and second derivatives).

segment one

$$\begin{aligned}x_a &= x_{bA} + a \cos \phi & z_a &= z_{bA} + a \sin \phi \\ \dot{x}_a &= \dot{x}_{bA} - a \sin \phi \dot{\phi} & \dot{z}_a &= \dot{z}_{bA} + a \cos \phi \dot{\phi} \\ \ddot{x}_a &= \ddot{x}_{bA} - a \sin \phi \ddot{\phi} - a \cos \phi \dot{\phi}^2 & \ddot{z}_a &= \ddot{z}_{bA} + a \cos \phi \ddot{\phi} - a \sin \phi \dot{\phi}^2\end{aligned}$$

segment two

$$\begin{aligned}x_b &= x_{bA} + p \cos \phi + x_s + b \cos \phi_2 \\ \dot{x}_b &= \dot{x}_{bA} - p \sin \phi \dot{\phi} + \dot{x}_s - b \sin \phi_2 \dot{\phi}_2 \\ \ddot{x}_b &= \ddot{x}_{bA} - p \sin \phi \ddot{\phi} - p \cos \phi \dot{\phi}^2 + \ddot{x}_s - b \sin \phi_2 \ddot{\phi}_2 - b \cos \phi_2 \dot{\phi}_2^2 \\ z_b &= z_{bA} + p \sin \phi + z_s + b \sin \phi_2 \\ \dot{z}_b &= \dot{z}_{bA} + p \cos \phi \dot{\phi} + \dot{z}_s + b \cos \phi_2 \dot{\phi}_2 \\ \ddot{z}_b &= \ddot{z}_{bA} + p \cos \phi \ddot{\phi} - p \sin \phi \dot{\phi}^2 + \ddot{z}_s + b \cos \phi_2 \ddot{\phi}_2 - b \sin \phi_2 \dot{\phi}_2^2\end{aligned}$$

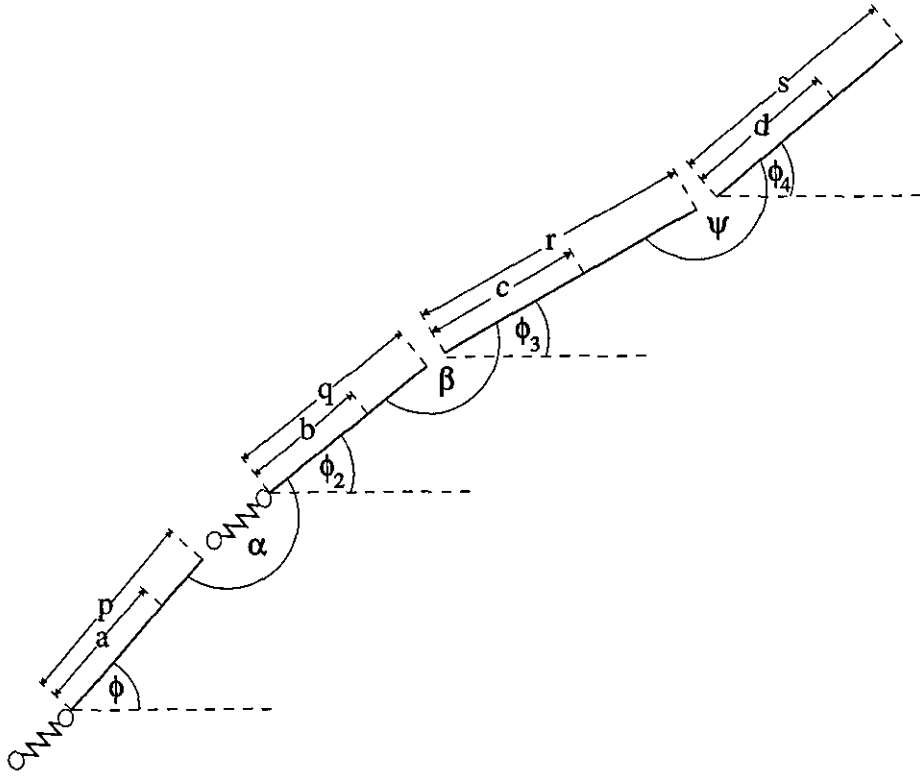


Figure 3.2. The angles defining the configuration of the four segment simulation model.

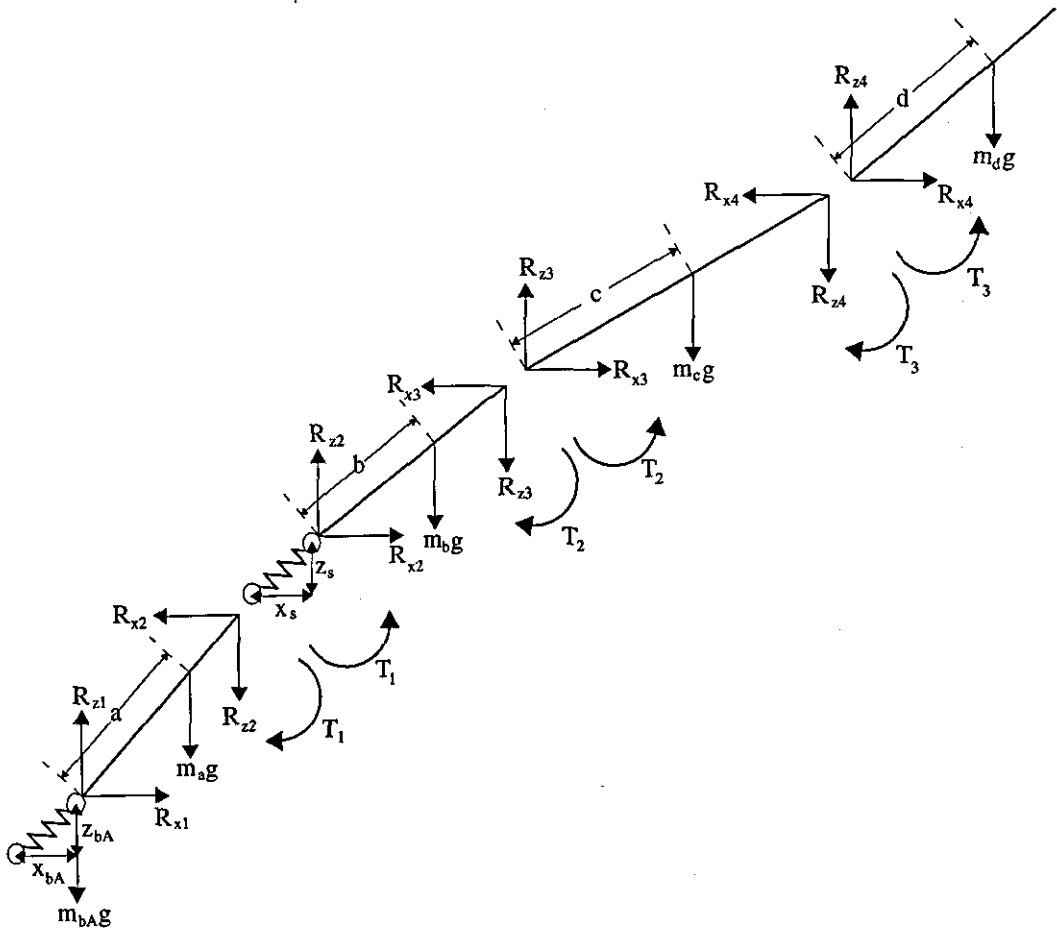


Figure 3.3. Free body diagram of the four segment model.

Equations of motion

The equations of motion are derived by resolving horizontally and vertically using Newton's Second Law of motion and by taking moments about the mass centre of each segment. The system of forces and torques is given in Figure 3.3.

Segment One : The arms.

Figure 3.4 shows the free body diagram of the arm segment. It can be seen that there are two forces acting due to the mass of the segment, m_a , and the mass of the bar, m_{bA} . The mass of the bar is included into the arm segment. That is, the mass of the bar is treated as a point mass positioned at the end of the arm segment. This gives rise to a new mass centre location and moment of inertia for the arm segment (Figure 3.5). Gatto and Neal (1992) assumed that this point mass was half that of the whole bar mass (4.7 kg). The bar that will be used in the analysis of the backward giant circles (Chapter 5) has a mass of 15 kg. A point mass of 5 kg is chosen for the present simulation model.

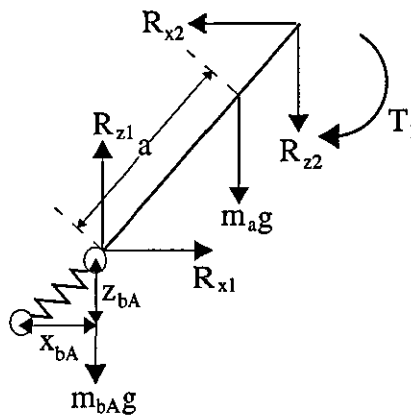


Figure 3.4. Free body diagram of the arm segment.

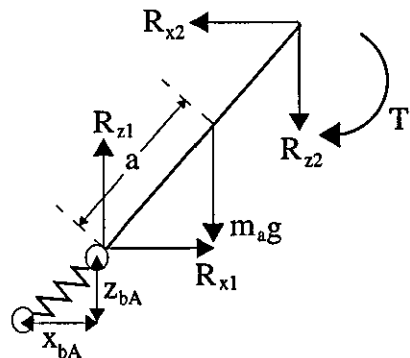


Figure 3.5. Amended free body diagram of the arm segment.

Resolving the forces vertically using Newton's Second Law for the arm segment gives:

$$R_{z1} - R_{z2} - m_a g = m_a \ddot{z}_a \quad (3.19)$$

As discussed in section 3.2 R_{z1} and R_{z2} are the vertical tensions in the bar and shoulder springs and may be replaced by the following terms:

$$R_{z1} = -k_{bA} z_{bA} \quad (3.20)$$

$$R_{z2} = -k_s z_s \quad (3.21)$$

where

k_{bA} stiffness coefficient of the bar spring

k_s stiffness coefficient of the shoulder spring

z_{bA} vertical displacement of the bar spring

z_s vertical displacement of the shoulder spring

Substituting these new terms into the first equation for R_{z1} and R_{z2} gives:

$$-k_{bA} z_{bA} + k_s z_s - m_a g = m_a \ddot{z}_a \quad (3.22)$$

However, the springs at the bar and shoulders are damped springs. A damping term for each spring must therefore be introduced into equation (3.22). The damping force is proportional to the rate of change in length of the spring. For an individual damped linear spring, suspended vertically from one end with a mass m at the other, the equation of motion can be written as follows:

$$-kz - b\dot{z} = m\ddot{z} \quad (3.23)$$

where

b damping coefficient of the spring

In equation (3.23) the damping coefficient of the spring is multiplied by the rate of change in length of the spring to give the damping force. Similar damping terms are introduced to equation (3.22) to give:

$$-k_{bA} z_{bA} - b_{bA} \dot{z}_{bA} + k_s z_s + b_s \dot{z}_s - m_a g = m_a \ddot{z}_a \quad (3.24)$$

Equation (3.24) is derived by resolving horizontally for the arm segment using Newton's Second Law.

$$R_{x1} - R_{x2} = m_a \ddot{x}_a \quad (3.25)$$

Similar to the treatment of R_{z1} and R_{z2} , R_{x1} and R_{x2} may be replaced by the formula for the damped linear spring.

$$R_{x1} = -k_{bA} x_{bA} \quad (3.26)$$

$$R_{x2} = -k_s x_s \quad (3.27)$$

where

x_{bA} horizontal displacement of the bar spring

x_s horizontal displacement of the shoulder

Again substituting for R_{x1} and R_{x2} and introducing damping terms into equation (3.25) gives equation (3.28).

$$-k_{bA} x_{bA} - b_{bA} \dot{x}_{bA} + k_s x_s + b_s \dot{x}_s = m_a \ddot{x}_a \quad (3.28)$$

At this point it is assumed that the high bar is equally stiff in the vertical and horizontal directions. Should this assumption be proved untrue individual stiffness coefficients for each direction will be used.

The third equation for the arm segment is obtained by taking moments about O, the neutral bar position. The net moment about the neutral bar position is equal to the rate of change of angular momentum of the segment as detailed below.

$$m_a g x_a + T_1 = \frac{d(h_o)}{dt}$$

$$\frac{d(h_o)}{dt} = m_a \ddot{x}_a z_a - m_a \ddot{z}_a x_a - I_a \ddot{\phi} \quad (3.29)$$

where

T_1 = joint torque at the shoulders.

Segment Two : The torso (including the head).

The free body diagram for the torso segment is given in Figure 3.6.

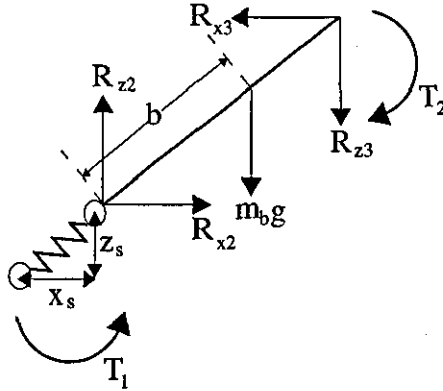


Figure 3.6. Free body diagram of the torso segment.

Resolving vertically for the torso segment gives:

$$R_{z2} - R_{z3} - m_b g = m_b \ddot{z}_b \quad (3.30)$$

$-k_s z_s$ is substituted for R_{z2} and the damping term is introduced to give equation (3.31).

$$-k_s z_s - b_s \dot{z}_s - R_{z3} - m_b g = m_b \ddot{z}_b \quad (3.31)$$

Resolving horizontally for the second segment gives:

$$R_{x2} - R_{x3} = m_b \ddot{x}_b \quad (3.32)$$

Substituting for R_{x2} and introducing the damping term gives:

$$-k_s x_s - b_s \dot{x}_s - R_{x3} = m_b \ddot{x}_b \quad (3.33)$$

Equation (3.34) is obtained by taking moments about the mass centre of the second segment.

$$T_1 - T_2 + R_{x2} b \sin \phi_2 + R_{x3} (q - b) \sin \phi_2 - R_{z2} b \cos \phi_2 - R_{z3} (q - b) \cos \phi_2 = I_b \ddot{\phi}_2 \quad (3.34)$$

Segment Three : The thighs.

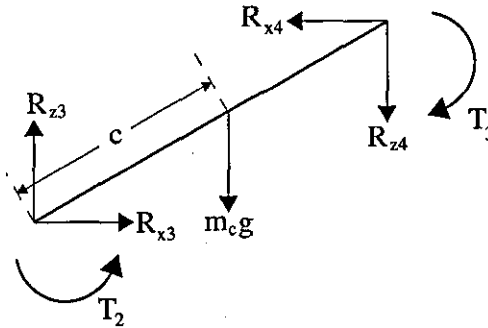


Figure 3.7. Free body diagram of the thigh segment.

Resolving vertically using Newton's Second Law for the thigh segment gives,

$$R_{z3} - R_{z4} - m_c g = m_c \ddot{z}_c \quad (3.35)$$

Resolving horizontally for the thigh segment gives:

$$R_{x3} - R_{x4} = m_c \ddot{x}_c \quad (3.36)$$

Taking moments about the mass centre of the thigh segment gives equation (3.37).

$$T_2 - T_3 + R_{x3} c \sin \phi_3 + R_{x4} (r - c) \sin \phi_3 - R_{z3} c \cos \phi_3 - R_{z4} (r - c) \cos \phi_3 = I_c \ddot{\phi}_3 \quad (3.37)$$

Segment Four : The lower leg (including the foot).

The free body diagram of the fourth segment, representing the shank, is given in Figure 3.8.

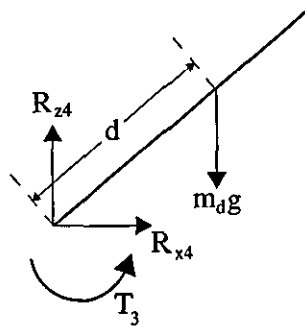


Figure 3.8. Free body diagram of the shank segment.

Resolving vertically:

$$R_{z4} - m_d g = m_d \ddot{z}_d \quad (3.38)$$

Resolving horizontally:

$$R_{x4} = m_d \ddot{x}_d \quad (3.39)$$

Taking moments about the mass centre of the fourth segment:

$$T_3 + R_{x4} d \sin \phi_4 - R_{z4} d \cos \phi_4 = I_d \ddot{\phi}_4 \quad (3.40)$$

The final three equations are obtained by resolving horizontally and vertically and by taking moments about O for the whole system using Newton's Second Law of motion. Resolving in the vertical direction gives:

$$R_{z1} - g(m_a + m_b + m_c + m_d) = m_a \ddot{z}_a + m_b \ddot{z}_b + m_c \ddot{z}_c + m_d \ddot{z}_d \quad (3.41)$$

Resolving in the horizontal direction for the whole system:

$$R_{x1} = m_a \ddot{x}_a + m_b \ddot{x}_b + m_c \ddot{x}_c + m_d \ddot{x}_d \quad (3.42)$$

Finally, differentiating the momentum equation (about the neutral bar position) with respect to time gives the moment equation for the whole system about the neutral bar position O.

$$\text{Torque} = \frac{d(h_o)}{dt}$$

$$\text{Torque} = -g(m_a x_a + m_b x_b + m_c x_c + m_d x_d)$$

$$\frac{d(h_o)}{dt} = m_a \ddot{x}_a z_a - m_a \ddot{z}_a x_a - I_a \ddot{\phi}$$

$$+ m_b \ddot{x}_b z_b - m_b \ddot{z}_b x_b - I_b \ddot{\phi}_2$$

$$+ m_c \ddot{x}_c z_c - m_c \ddot{z}_c x_c - I_c \ddot{\phi}_3$$

$$+ m_d \ddot{x}_d z_d - m_d \ddot{z}_d x_d - I_d \ddot{\phi}_4 \quad (3.43)$$

Solution of equations

In order to obtain all the internal joint forces and torques almost all the equations derived for each of the four segments will be required. However, the system may be reduced to five equations in five unknowns. The five equations which are required to solve the system are equations (3.24), (3.28), (3.41), (3.42) and (3.43).

Equation (3.24) :

$$-k_{bA}z_{bA} - b_{bA}\dot{z}_{bA} + k_s z_s + b_s \dot{z}_s - m_a g = m_a \ddot{z}_a$$

Equation (3.28) :

$$-k_{bA}x_{bA} - b_{bA}\dot{x}_{bA} + k_s x_s + b_s \dot{x}_s = m_a \ddot{x}_a$$

Equation (3.41) :

$$R_{z1} - g(m_a + m_b + m_c + m_d) = m_a \ddot{z}_a + m_b \ddot{z}_b + m_c \ddot{z}_c + m_d \ddot{z}_d$$

Equation (3.42) :

$$R_{x1} = m_a \ddot{x}_a + m_b \ddot{x}_b + m_c \ddot{x}_c + m_d \ddot{x}_d$$

Equation (3.43) :

$$\text{Torque} = \frac{d(h_o)}{dt}$$

$$\text{Torque} = -g(m_a x_a + m_b x_b + m_c x_c + m_d x_d)$$

$$\begin{aligned} \frac{d(h_o)}{dt} = & m_a \ddot{x}_a z_a - m_a \ddot{z}_a x_a - I_a \ddot{\phi} \\ & + m_b \ddot{x}_b z_b - m_b \ddot{z}_b x_b - I_b \ddot{\phi}_2 \\ & + m_c \ddot{x}_c z_c - m_c \ddot{z}_c x_c - I_c \ddot{\phi}_3 \\ & + m_d \ddot{x}_d z_d - m_d \ddot{z}_d x_d - I_d \ddot{\phi}_4 \end{aligned}$$

The five unknowns are the horizontal and vertical accelerations of the bar and shoulder springs and the angular acceleration of the arm segment. Numerical integration is used to calculate the new location of the model after small successive time intervals. This requires the solution of the above five equations using the following method.

At the start of the simulation process the initial conditions are known. These initial conditions comprise the configuration of the model, the initial angular velocity of the model, the displacements of the two springs and the velocities of the two springs. Therefore, the unknowns of the system are the angular accelerations of each segment and the accelerations of the two springs. From the relationships between the segment orientation angles (ϕ , ϕ_2 , ϕ_3 and ϕ_4) and their first and second derivatives, the unknowns are the angular acceleration of the arm segment, the second derivatives with respect to time of the joint angles α , β and ψ , and the accelerations of the springs.

The model is designed to accept joint angle time histories as input. These time histories are in the form of either piecewise quintic functions of time or quintic splines. From either option (spline or quintic function) the first and second derivatives of the joint angle time history may be obtained at all times during a simulation. This reduces the unknowns to the angular acceleration of the arm segment and the accelerations of the springs (a total of five unknowns).

To solve the system of five equations in five unknowns a linear equation solver is used (Stewart, 1973). The equation solver is used to solve a system of equations in the form:

$$Ax = b \quad (3.44)$$

where

- A is the 5 x 5 matrix containing the coefficients of the five equations
- x is the 5 x 1 matrix containing the unknowns
- b is the 5 x 1 matrix containing the the solutions to the five equations

The initial conditions and the solutions from the equation solver are then used to calculate the conditions at the end of the time interval (the time interval ranged between 0.001 s and 0.00001 s). The new angles, angular velocities, spring displacements and velocities are calculated using Newton's equations of motion. For example, the equations below are for calculating the angular displacement and velocity for the arm segment (equations (3.44) and (3.45)) and the horizontal displacement and velocity of the spring representing the bar (equations (3.46) and (3.47)).

$$\phi_1 = \phi_0 + \dot{\phi}_0 t + \frac{1}{2} \ddot{\phi}_0 t^2 \quad (3.44)$$

$$\dot{\phi}_1 = \dot{\phi}_0 + \ddot{\phi}_0 t \quad (3.45)$$

$$x_{ba_1} = x_{ba_0} + \dot{x}_{ba_0} t + \frac{1}{2} \ddot{x}_{ba_0} t^2 \quad (3.46)$$

$$\dot{x}_{ba_1} = \dot{x}_{ba_0} + \ddot{x}_{ba_0} t \quad (3.47)$$

where

t is the integration interval

It is assumed that the accelerations of the arm segment and the springs are constant over the integration interval. At the end of each time interval the new set of conditions become the initial conditions for the next time interval and so the process continues. This method of numerical integration is the equivalent of Euler's method (see equations (3.17) and (3.18)).

The problems with this method are that the accelerations calculated at the start of the integration interval are assumed to be constant throughout the interval. During the backward giant circle the angular acceleration of the gymnast and the linear accelerations of the springs are constantly changing. Assuming that the accelerations are constant over an integration interval will result in either an over or under-estimation of the calculated displacement and velocity data. A similar problem would arise if an inappropriate integration interval was selected. If the interval were too long the simulation model would not be sensitive to small changes in acceleration. The ideal solution would be to have as short an integration interval as possible. However, this would lead to excessive amounts of computer time to run simulations. Therefore a compromise is required.

The problem of the constant acceleration assumption was addressed by using an "average" estimate of the accelerations during the integration interval. The equations of motion are solved at the start of the integration interval. This provides the initial estimate of the accelerations of the arm segment and the springs. The initial accelerations are then used to obtain the displacements and velocities of the arm segment and springs at the end of the integration interval using equations (3.44) to (3.47).

The new displacements and velocities of the arm segment and springs are used to calculate the accelerations at the end of the integration interval. The initial and final accelerations are then averaged to give the "average" estimate of the accelerations during the integration interval.

The "average" accelerations are chosen to be a better estimate of the accelerations over the whole interval. Therefore, the "average" accelerations and the displacements and velocities of the arm segment and springs at the start of the interval are used to calculate

the displacements and velocities of the arm segment and springs at the end of the interval (using equations (3.44) to (3.47)). The method of using average accelerations is the same as a modified Euler method or a second order Runge Kutta. These methods use an initial step to find a point half way across the interval and then use the derivative at the mid-point to cross the whole interval (Press et al., 1986).

Variable step length

To avoid the problems of a fixed integration interval a variable step length may be used. This approach is designed to increase the length of the integration interval during periods of small change and reduce the integration interval during periods of rapid change. This is achieved using a by-product of the average acceleration routine described above. At the end of each integration interval a comparison is made between the initial estimates of the angular and linear displacements calculated from the first estimate of the arm segment and spring accelerations and the angular and linear displacements calculated using the average accelerations. If these differences exceed a tolerance level the length of the integration interval is either halved or doubled. If the difference is greater than the tolerance level the integration interval is halved. If the difference is less than the tolerance level the integration interval is doubled. However, if the difference is within the tolerance level the current length of the integration interval is maintained. Separate tolerance levels were set for the angular and the linear differences in displacements. For this reason priority was always given to reducing the integration interval.

Output

The time histories of the displacements and velocities of the segments and springs are known from the solution of the equations of motion and the integration using equations (3.44) to (3.47). With the system of the equations solved it is possible to calculate the internal joint forces and torques at each joint using equations (3.19) to (3.43). For the evaluation of the simulation model it is necessary to calculate the mass centre location and the whole body angle of rotation. For the optimisation of the accelerated backward giant circle the calculation of the angular momentum of the model about its mass centre is required. In addition, the energy within the system is calculated to demonstrate the effects of strain energy stored in the bar and the effects of actions performed at the hips and shoulder.

Calculation of the mass centre location and angle of rotation

For the evaluation of the simulation model the location of the mass centre and the angle through which the mass centre has rotated is required (see Chapter 7). At the end of each integration interval the horizontal and vertical displacements of the springs and the angle which each segment makes with the horizontal are known. The horizontal location of the mass centre from the neutral bar position is calculated by taking moments about the vertical axis and dividing by the sum of the segment masses.

$$x = \frac{\sum_{i=1}^4 (m_i x_i)}{\sum_{i=1}^4 (m_i)} \quad (3.48)$$

The vertical location of the mass centre is calculated in a similar way.

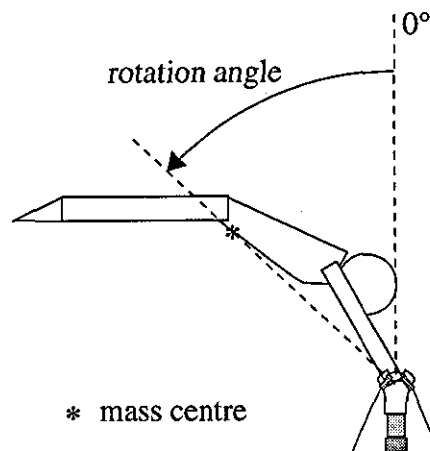


Figure 3.9. Definition of the rotation angle.

The rotation angle of the model is defined as the angle made by the line joining the mass centre to the neutral bar position and the vertical (Figure 3.9). Using the horizontal and vertical locations of the mass centre relative to the neutral bar position, the sine and cosine are used to find the rotation angle (Yeadon, 1990a). Anti-clockwise is taken as positive and a rotation angle of 0° refers to the model being in the vertical handstand position.

Calculation of angular momentum

The angular momentum of a rigid segment about a fixed point, S, is given by;

$$h_s = I\omega + m(x\dot{z} - z\dot{x}) \quad (3.49)$$

where

- h_s angular momentum about the point S
- I moment of inertia of the rigid segment about its mass centre
- ω angular velocity of the segment
- m mass of the segment
- x horizontal displacement of the segment mass centre relative to S
- z vertical displacement of the segment mass centre relative to S
- $\dot{}$ above the variable signifies the first derivative with respect to time

In the case of the four segment model the fixed point is chosen to be the neutral bar position O. The angular momentum is calculated by summing equation (3.49) for each of the segments (equation (3.50)). Therefore, the formula for the angular momentum about the neutral bar position may be written as:

$$h = \sum_{i=1}^4 (I_i \omega_i + m_i (x_i \dot{z}_i - z_i \dot{x}_i)) \quad (3.50)$$

From equation (3.50) it can be seen that the angular momentum of the four segment system is not only dependent on the angular velocity of the segments, but is also dependent on the linear velocities of the segment mass centres.

Equation (3.50) gives the angular momentum of the model about the neutral bar position. In certain applications it may be more appropriate to calculate the angular momentum about the mass centre of the model. The equation for calculating angular momentum about the mass centre is given in Equation (3.51). This equation is more appropriate if the application is to optimise the angular momentum possessed by the model prior to release for a double layout somersault dismount.

$$h = \sum_{i=1}^4 (I_i \omega_i + m_i (x_i \dot{z}_i - z_i \dot{x}_i)) \quad (3.51)$$

where

- h angular momentum about the mass centre
- I moment of inertia of the rigid segment about its mass centre
- ω angular velocity of the segment
- m mass of the segment
- x horizontal displacement of the segment mass centre relative to the mass centre of the model
- z vertical displacement of the segment mass centre relative to the mass centre

- above the variable signifies the first derivative with respect to time (in this case it refers to the velocity of the segment mass centers relative to the velocity of the mass centre of the model)

Calculation of the energy in the system

For a given set of conditions (i.e. when the damping coefficients of the springs are set to zero) all the models outlined should behave as conservative systems. From the description of the backward giant circle given in Chapter 2 the technique used by a gymnast may be related to the energy within the system. In order to test whether this is the case an energy calculation is required. The energy within the system will comprise the potential energy of each segment due to its mass centre location relative to a given reference level, the potential strain energy which is present in the springs of the system, and the linear and rotational kinetic energy possessed by each of the segments. The potential energy possessed by each segment is calculated from:

$$\text{potential energy} = m g h \quad (3.52)$$

where m is the mass of the segment, g is the acceleration due to gravity and h is the height of the segment's mass centre above the zero potential energy reference level. Therefore the potential energy of the whole system can be written as follows:

$$\text{potential energy} = \sum_{i=1}^4 (m_i g h_i) \quad (3.53)$$

The energy stored in a linear spring can analytically be shown to be:

$$\text{strain energy} = \frac{1}{2} k x^2 \quad (3.54)$$

where

- k stiffness coefficient of the spring
- x displacement in the spring

The strain energy for the whole system is obtained by summing the energy stored in each of the springs.

$$\text{strain energy} = \sum_{i=1}^2 (\frac{1}{2} k_i x_i^2) \quad (3.55)$$

The linear kinetic energy and rotational kinetic energy of a rigid segment may be written as:

$$\text{linear kinetic energy} = \frac{1}{2} m v^2 \quad (3.56)$$

$$\text{rotational kinetic energy} = \frac{1}{2} I \omega^2 \quad (3.57)$$

where

- m mass of the segment
- I moment of inertia of the segment about its mass centre
- v linear velocity of the segment's mass centre
- ω angular velocity of the segment's mass centre

The kinetic energy (linear plus rotational) of the system of segments may be expressed as:

$$\text{kinetic energy} = \sum_{i=1}^4 \left(\left(\frac{1}{2} m_i v_i^2 \right) + \left(\frac{1}{2} I_i \omega_i^2 \right) \right) \quad (3.58)$$

To obtain the total energy in the system the equations (3.53), (3.55) and (3.58) are summed.

Input

The solution of the above equations of motion requires the following input:

- i) inertia parameters
- ii) spring parameters
- iii) joint angle time histories

Inertia parameters

The model requires the masses, mass centre locations and moments of inertia about the mass centre of each segment. The inertia parameters are determined from anthropometric measurements taken from the subjects and the inertia model of Yeadon (1990b). The inertia data is also used in the data collection for the muscle parameters and the analysis of the backward giant circles (Chapters 4 and 5). The inertia data will be presented in the results chapter (Chapter 6). These results will include the modified inertia data which takes into account the mass of the high bar at the gymnast's hands (see Figures 3.4 and 3.5).

Spring parameters

The spring parameters comprise the stiffness and damping coefficients of both the bar and the shoulder springs. These parameters are determined using experimental and theoretical techniques which are presented in Chapter 5.

Joint angle time histories

Three versions of the four segment simulation model are used in the following chapters. Each version is used for a separate application of the simulation model.

In the first version the input to the model comprises the joint angle time histories obtained from the video analysis of the backward giant circles. This version will be used to evaluate the four segment simulation model (Chapter 7) and for obtaining the spring parameters (Chapter 5). The joint angles time histories are input in the form of spline coefficients obtained from the splined joint angle time histories of the hip, shoulder and knee joints. The spline fitting library of Jennings (1979) is used to evaluate the splines and calculate their first and second derivatives for each integration interval. The input to the model comprises the joint angle time histories and the initial displacements and velocities of the bar spring and the arm segment. The initial conditions of the bar and the rotation angle of the arm segment are input to the model as spline coefficients which are obtained from the video analysis. Initial displacements and velocities of the bar and arm segment are obtained from the spline evaluation subroutines of the Jennings library (1979). Using splines for the joint angle time histories and initial conditions meant that a simulation could be initiated from any point within the time interval containing the video data. The output from this version of the simulation model is the time history of the whole body angle of rotation, the horizontal and vertical bar displacements and the horizontal and vertical reaction forces at the bar. The displacements of the bar and the rotation angle obtained from the splines are also output so that comparisons between the estimated and measured output could be made.

The second version of the simulation model is used for running single simulations where the joint angle time histories are defined by the user. These may be the joint angle time histories for backward giant circles or any other high bar skill that may be considered to be two dimensional in nature. The joint angle time histories may be defined using one of two functions. Both have justifications for their implementation in the four segment model. A sensitivity analysis will be performed to determine which of the two functions is the most appropriate for defining joint angle time histories during swinging on the high bar (Chapter 8).

The first of the two functions was derived by Yeadon (1984) for use with his simulation model of aerial movements. Yeadon used the following quintic function $q(x)$ and its derivatives:

$$q(x) = x^3(6x^2 - 15x + 10) \quad (3.59)$$

$$\dot{q}(x) = 30x^2(x - 1)^2 \quad (3.60)$$

$$\ddot{q}(x) = 120x(x - \frac{1}{2})(x - 1) \quad (3.61)$$

The function $q(x)$ increases from 0 to 1 on the interval $[0, 1]$ and has zero first and second derivatives at the end-points (Figure 3.11, 3.12 and 3.13). This function $q(x)$ is therefore an appropriate function for modelling angle values since angular velocities and accelerations change smoothly. If the application requires that angle α changes from α_0 to α_1 in the time interval $[t_0, t_1]$, then angle α and its derivatives α' and α'' are defined by:

$$\alpha(t) = \alpha_0 + (\alpha_1 - \alpha_0).q(x) \quad (3.62)$$

$$\alpha(t)' = (\alpha_1 - \alpha_0).q'(x)/(t_1 - t_0) \quad (3.63)$$

$$\alpha(t)'' = (\alpha_1 - \alpha_0).q''(x)/(t_1 - t_0)^2 \quad (3.64)$$

where

$$x = (t - t_0)/(t_1 - t_0) \text{ (Yeadon, 1984).}$$

By using a succession of non-overlapping intervals it is possible to define the angles α , β and ψ and their derivatives at any time.

Using the quintic function above it may be seen from Figure 3.12 that the second derivative of the joint angle time history is at a maximum and/or minimum for only an instant. The implication of this is that the joint torque produced by such an acceleration curve will only be at a maximum level at this instant. During actual performances the gymnast may produce a peak joint torque which is maintained for a longer period whilst still changing the joint angle over a smooth curve. In order to model this situation the acceleration curve in Figure 3.15 was derived. It can be seen that the acceleration of the angle change is now either at some maximum level or at a minimum level. Unlike Figure 3.12 the gymnast has maximum acceleration for a longer duration.

The same principle used for the quintic function is used for the function which has the square wave acceleration curve. The function has first and second derivatives with zero end-points making it appropriate for modelling human angle changes. The duration of the angle change is standardised to increase over the interval $[0,1]$. Due to the nature of the acceleration curve two functions make up the curve in Figure 3.13. The following inequalities are used to define the angle and its first and second derivatives (Figures 3.13, 3.15 and 3.15).

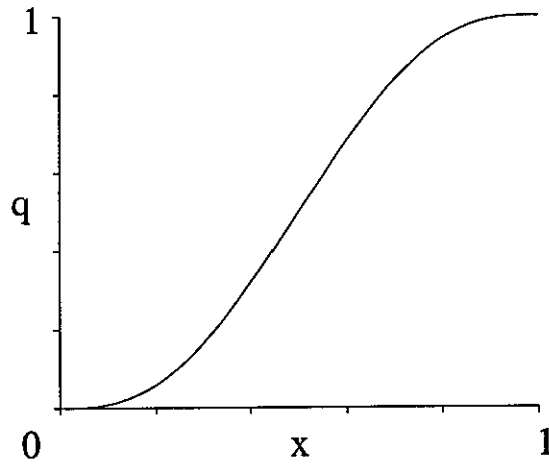


Figure 3.10. The quintic function $q(x)$ used for changing joint angles.

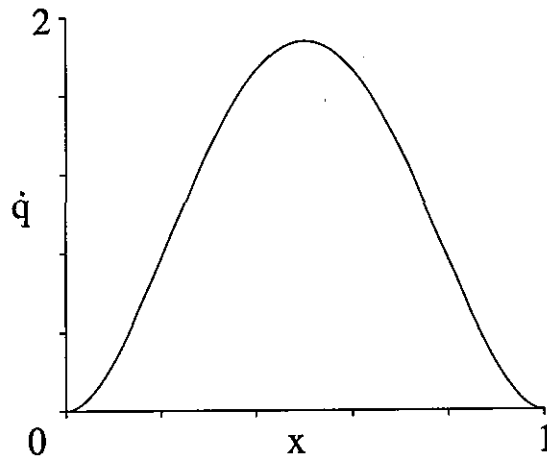


Figure 3.11. The first derivative of the quintic function $q(x)$ which defines the angular velocity of the angle change.

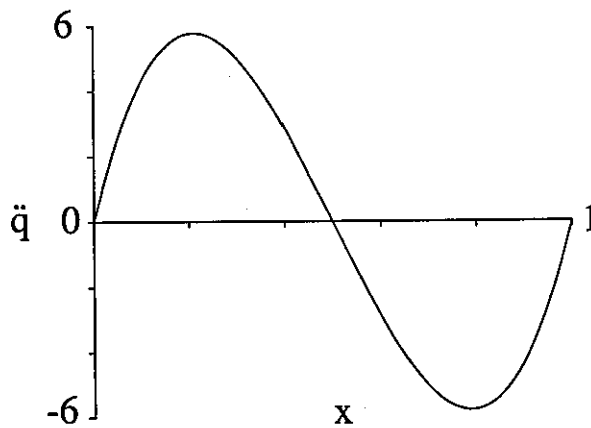


Figure 3.12. The second derivative of the quintic function $q(x)$ which defines the angular acceleration of the angle change.

For t in the interval $[0, \frac{1}{2}]$:

$$\alpha(t) = \alpha_0 + (\alpha_1 - \alpha_0) \cdot (2t^2) \quad (3.65)$$

$$\alpha(t)' = (\alpha_1 - \alpha_0) \cdot (4t) / (t_1 - t_0) \quad (3.66)$$

$$\alpha(t)'' = (\alpha_1 - \alpha_0) \cdot (4) / (t_1 - t_0)^2 \quad (3.67)$$

For t in the interval $(\frac{1}{2}, 1]$:

$$\alpha(t) = \alpha_0 + (\alpha_1 - \alpha_0) \cdot (1 - 2(t - 1)^2) \quad (3.68)$$

$$\alpha(t)' = (\alpha_1 - \alpha_0) \cdot (-4(t - 1)) / (t_1 - t_0) \quad (3.69)$$

$$\alpha(t)'' = (\alpha_1 - \alpha_0) \cdot (-4) / (t_1 - t_0)^2 \quad (3.70)$$

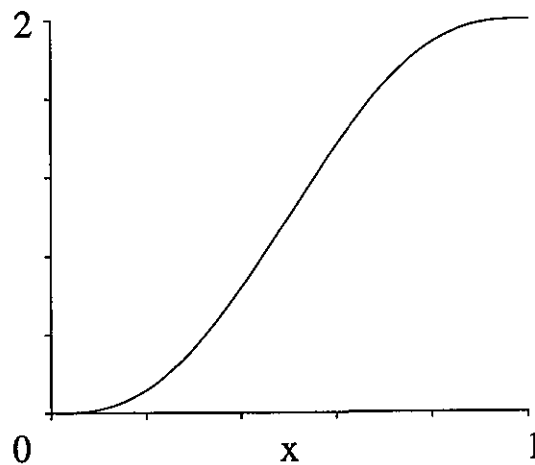


Figure 3.13. The curve used for changing joint angles with the square wave acceleration curve.

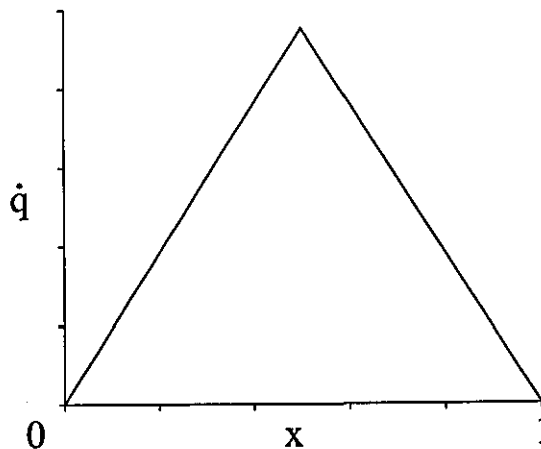


Figure 3.14. The first derivative of the change in angle curve, using the square wave acceleration curve, which defines the angular velocity of the angle change.

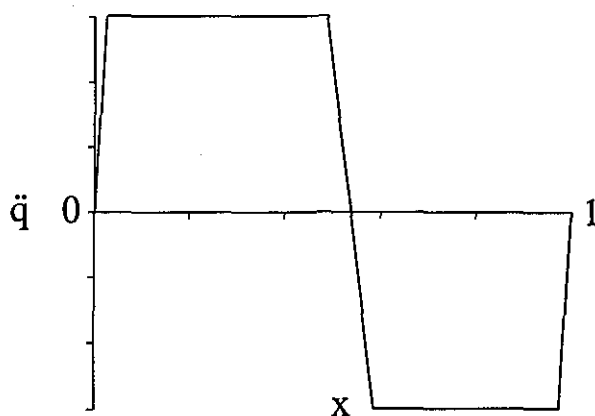


Figure 3.15. The square wave acceleration curve which defines the angular acceleration of the angle change.

The output for the second version of the model comprises any variable which would be included in an inverse dynamic analysis of the skill. This data may be output as a Comma Separated Variable (CSV) file which may subsequently be used to obtain graphics of the desired output parameters.

The third version of the simulation model is selected for the optimisation of the backward giant circle (Chapter 8). The program reads the initial conditions and joint angle time histories from a data file. The code for the simulation model is used with the Simulated Annealing algorithm to optimise the angular momentum about the model's mass centre produced by a set of joint angle time histories (see Chapter 8). The Annealing process is able to manipulate the joint angle time histories until the optimal solution is obtained.

Joint torque limit

When the third version of the simulation model is used the joint angle time histories are manipulated until the optimal solution is obtained. For a real performer the changes in joint angles are created by joint torques which are in turn created by the musculature surrounding the joints. It is probable that during the optimisation process the Annealing algorithm will develop a joint angle time history that exceeds the capabilities of the performer. Therefore, it is necessary to limit the range of possible joint actions to those which are humanly possible. Chapter 4 outlines the procedure undertaken to collect joint angle - angular velocity - torque data from an isokinetic dynamometer. Joint torques were recorded for a range of angles and angular velocities. These data were used to form a three-dimensional surface for each joint tested (shoulder and hip). For any given angle and angular velocity the maximum joint torque the gymnast can produce may be determined.

For each step of the numerical integration the joint torques produced by the model

are monitored. The torques created by the model are compared to the maximum joint torque produced by the gymnast for the given angle and angular velocity of model's joint centres. If during the Annealing process a torque created by the model exceeds the maximum torque produced by the gymnast, the simulation is terminated and given a score of zero. Since the Annealing process attempts to maximise the score of the simulation, only a backward giant circle performed within the limits of the gymnast's capability can be the optimal solution (see Chapter 8).

A comparison of the joint torques produced by the simulation model and the joint torques determined by the three-dimensional torque surface during the evaluation of the simulation model is given in Chapter 7.

3.4 Summary

The equations of motion for both the single and four segment simulation models are based on Newtonian mechanics. The elastic properties of the bar and the gymnast are modelled using damped linear springs. After the equations of motion have been solved numerical integration equivalent to a modified Euler second order method is used to progress the models to the next interval. The single segment model requires only the initial condition for each simulation that is to be performed. The four segment simulation model, however, is driven using joint angle time histories. These joint angle time histories may be in the form of quintic splines (obtained from video analysis) or a piecewise quintic function.

The single segment simulation model will be used to investigate the effects of bar elasticity on peak angular velocity and reaction force. By varying the stiffness of the spring used to represent the bar a comparison between an elastic bar and a rigid bar may be made. The model will also be used in the evaluation of the four segment simulation model. The four segment simulation model will be evaluated against experimental data as suggested by Yeadon and Challis (1994). The model will then be used to optimise the accelerated backward giant circle. These analyses will be carried out in Chapters 7 and 8.

CHAPTER 4

DETERMINATION OF MUSCLE PARAMETERS

4.1 Introduction

The four segment simulation model is driven by joint angle time histories. The requirement of the joint angle time histories is that they are continuous and have known first and second derivatives. These time histories may be obtained from either kinematic analysis of gymnastic performances or from mathematical formulae. The problem with the latter method is that time histories may be determined which do not take into consideration the gymnast's strength. It is therefore possible for the simulation model to perform joint actions which are humanly impossible.

The literature has identified that there exist relationships between the amount of torque a person can produce at a joint centre, the angle made by the moving limb and the angular velocity of the moving limb (King, 1998; Fugelvand, 1987; Marshall et al., 1990). These data have been collected using isokinetic dynamometers and subsequently presented as three-dimensional surface plots. Interpolation of the surface plots using angle and angular velocity may be used to obtain the joint torque produced by the subject.

This chapter outlines the method for obtaining muscle parameters from data collected using an isokinetic dynamometer (King, 1998). The muscle parameters define the relationship between torque, angle and angular velocity for a given joint. These data will be used to determine the strength limits of the gymnast during simulations using the four segment model. The output from the simulation model includes the joint angles, angular velocities and the joint torques for each time interval. The joint torques determined by the simulation model will be compared with the maximum torque given by the muscle parameters.

4.2 Methods

4.2.1 Data collection

The protocol used followed closely the methodology outlined by King (1998). Data were recorded simultaneously using an isokinetic dynamometer (Kin-Com 125E) and a twin axis goniometer (Penny and Giles M180). The isokinetic dynamometer was used to record forces applied to a load cell (based on a full bridge circuit) mounted on the crank

arm. At the same time the dynamometer recorded the angle and angular velocity of the crank arm. The angle of the crank arm was measured using a potentiometer, the output from which was converted into degrees. The angular velocity of the crank arm was measured using a tachometer which monitored the speed of the motor which drove the crank arm. A further check on the angular velocity was performed by comparing the recordings from the tachometer with the first derivative of the potentiometer data. All data from the dynamometer were recorded at 100 Hz to ASCII files using an IBM compatible computer.

The goniometer data were recorded using a charged amplifier (Penny and Giles K100), analogue to digital converter (CED 1401) and a personal computer (Acorn 5000). All goniometer data were recorded at 250 Hz. The goniometer data captures were triggered using a control switch with four seconds before and 16 s after the trigger being recorded.

Written consent

The subject signed the written consent form agreeing to take part in the study. The consent form allowed the subject to withdraw from the study at any time (Appendix 2a).

Calibration of the dynamometer

The dynamometer was initially calibrated using the protocol supplied by the operators manual. The dynamometer was further calibrated using a static load. The crank arm was raised until it was horizontal, using a spirit level. A load of 350 N was attached to the crank arm using chains so that it hung vertically. Data were collected using the dynamometer software so that a comparison between the load recorded and the load applied could be made.

Calibration of the goniometer

Before testing the goniometer was placed along a straight line and zeroed according to the manufacturers instructions. The goniometer was calibrated after testing. The calibration protocol involved data being collected with the goniometer positioned at known angles. The angles ranged from -180° to $+180^{\circ}$ with recordings taken every 22.5° . At each angle 20 s of data were recorded. The ADC counts recorded in each of the calibration trials were averaged over 5000 data points (20 s of data capture). The mean and standard deviations of the calibration data are presented in Appendix 2b. The mean ADC counts were then regressed against the known angles used in the calibration procedure. The rms difference between the predicted and the measured angles of the calibration was 2.6° . The predicted angles were calculated using the following regression equation:

$$\text{angle} = 237.26 - 0.027642 \times \text{ADCcount} \quad (4.1)$$

The calibration data did not appear to fall on a straight line (Figure 4.1). The data were split into those calibration recordings from 0° to $+180^\circ$ and those in the range 0° to -180° . The above calibration equation was used to convert all goniometer recordings obtained during dynamometer trials into degrees. It was found that the angle range for all trials (both hip and shoulder) fell within the calibration range of 45° to -135° . Since only 60% of the calibration points fell within the 45° to -135° range a second regression analysis was performed. A linear regression was performed on the calibration recordings in the range of 45° to -135° . The second regression analysis yielded the following calibration equation:

$$\text{angle} = 236.813 - 0.0275638 \times \text{ADCcount} \quad (4.2)$$

Calibration equation (4.2) reduced the rms difference between the predicted and measured calibration angles to 2.3° . This new calibration equation was used to convert all the ADC counts into degrees. The goniometer files were then transformed so that 180° corresponded to the joint being fully closed. This was done so that both the goniometer data and the crank angle time histories from the isokinetic dynamometer increased within the same range.

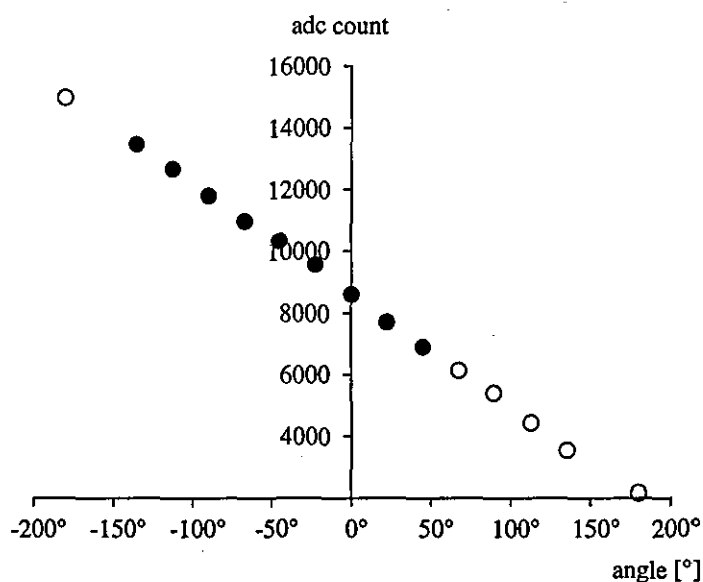


Figure 4.1. Mean ADC counts from calibration of the goniometer (filled circles used in the second linear regression).

Attaching the goniometer

As recommended by the manufacturers the goniometer was attached to the subject when the joint was straight and fully open. The goniometer was attached, in a straight position, across the joint being tested using double sided sticky tape. The goniometer and connecting cables were further secured using self-adhesive fabric tape.

Positioning of the subject

During testing of both the hip and the shoulder the subject was positioned on his back with the joint axis and crank axis aligned. Once positioned the subject was secured using Velcro straps to prevent excessive movement.

Exercise protocol

The same exercise protocol was used for both joints (hip and shoulder) and directions of movement (flexion and extension). The first and last two trials of the protocol comprised one repetition of concentric - eccentric exercise at $20^{\circ} \cdot s^{-1}$. Due to the slow angular velocity of these four trials the subject only worked maximally on the concentric phase of the first and penultimate trial. Similarly the subject only worked maximally on the eccentric phase of the second and the last trial. For the remainder of the trials the subject performed maximally for two repetitions of concentric - eccentric exercise at a pre-set angular velocity. The angular velocities ranged from $20^{\circ} \cdot s^{-1}$ to $250^{\circ} \cdot s^{-1}$ (maximum angular velocity of the dynamometer). The sequence of angular velocities was $20^{\circ} \cdot s^{-1}$, $20^{\circ} \cdot s^{-1}$, $50^{\circ} \cdot s^{-1}$, $100^{\circ} \cdot s^{-1}$, $150^{\circ} \cdot s^{-1}$, $200^{\circ} \cdot s^{-1}$, $250^{\circ} \cdot s^{-1}$, $250^{\circ} \cdot s^{-1}$, $250^{\circ} \cdot s^{-1}$, $20^{\circ} \cdot s^{-1}$ and $20^{\circ} \cdot s^{-1}$ (King, 1998).

The range of motion for each joint was determined from performances of accelerated backward giant circles. Where possible the range of motion was increased to allow for the accelerations of the crank arm (Herzog, 1988). Where the gymnast was unable to achieve the desired ranges of motion the largest possible, yet comfortable, range was used.

Each trial was started once the subject exceeded a 50 N force threshold. Verbal encouragement was given throughout the trial which was ended when the operator pressed the appropriate button on the computer. The goniometer data capture was initiated with the trigger which was operated manually once the dynamometer trial had started. Since four seconds of goniometer data before the trigger were recorded no data would be lost due to the reaction time of the operator. After testing both the dynamometer and goniometer data were copied onto floppy disk.

4.2.2 Data Analysis

Editing data files from the goniometer and dynamometer

The data files obtained from the dynamometer contained the time histories of the crank angle, angular velocity and force recorded from the load cell. All files were edited so that only the central eccentric - concentric phase of each trial remained (Figure 4.2). The isokinetic portions of this central eccentric - concentric phase were identified and the points p1 to p4 were determined for each trial (Figure 4.3).

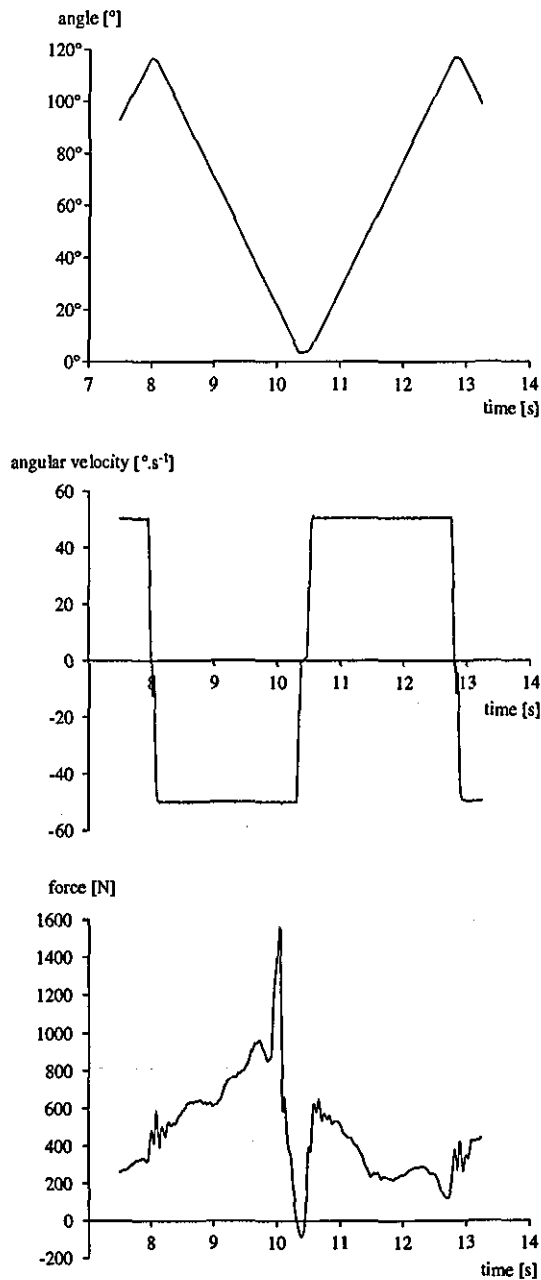


Figure 4.2. All files were edited to obtain the central eccentric - concentric portion of each trial.

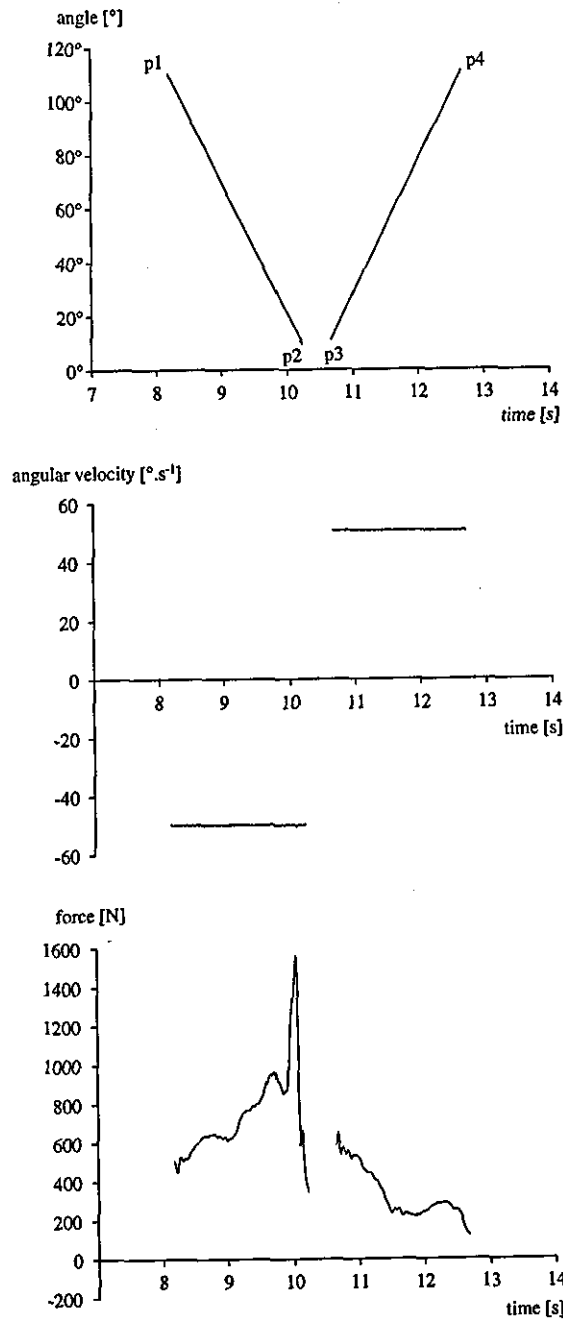


Figure 4.3. The start and finish of the eccentric and concentric portions of the trial were identified and labelled p1 to p4.

The goniometer files which had been converted into degrees were edited in a similar manner to obtain the central eccentric - concentric portions (Figure 4.4). For the trials performed at $20^{\circ}\cdot\text{s}^{-1}$ the concentric part of the first trial was combined with the eccentric part of the second trial to form a complete data set.

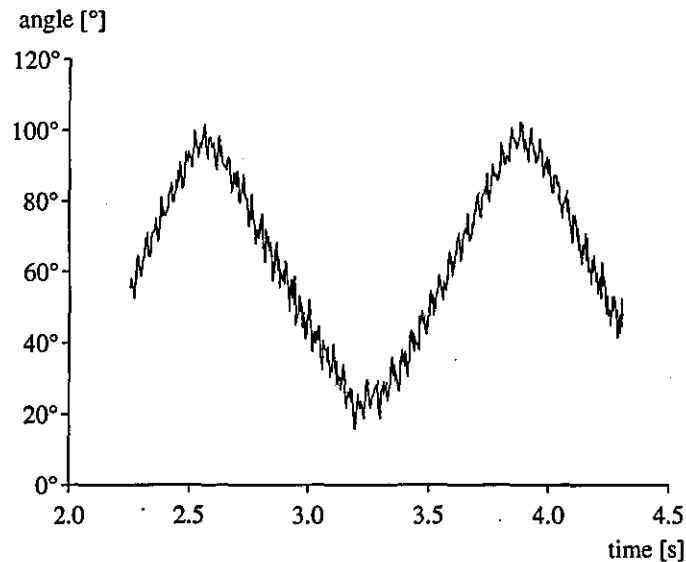


Figure 4.4. Example of a goniometer file which has been edited to obtain the central eccentric - concentric portion.

Synchronisation of the goniometer and dynamometer data files

An optimisation procedure was used to synchronise the edited crank angle and joint angle time histories. The procedure assumed that the turning points in the joint angle time histories occurred at the same time as the turning points in the crank angle time histories. The turning points occurred when the direction of the crank angular velocity changed. These corresponded to changing from the eccentric to the concentric portions of the trial and vice versa. This resulted in three turning points from each edited file (Figures 4.2).

Synchronisation of the crank and goniometer data required the data sets to be of equal length and frequency. Cubic splines (Reinsch, 1967) were fit to the crank and joint angle time histories. These splines were evaluated at 250 Hz over the greater interval between the crank and joint for each trial.

For the purpose of fitting the cubic spline to the crank angle time history the error estimate was calculated from the difference between the crank time history and a pseudo crank time history. The pseudo crank time history was obtained by averaging the crank angle values at adjacent times. The standard error estimate for each data point comprised 75% local error and 25% global error.

Linear regressions performed on portions of the joint angle time histories of the $20^{\circ} \cdot s^{-1}$ trial where the angular velocity appeared to be constant yielded standard errors of fit. The error estimates used for fitting the cubic spline to the joint angle time history to the trials of each joint action were determined by averaging the four standard errors obtained from each joint action.

Optimisation procedure

The joint angle time history and crank angle time histories were related by a transformation which mapped the joint angle time history onto the crank angle time history (King, 1998). The relationship between the crank and joint angle was expressed in terms of a horizontal translation, a translation which stretched the joint angle in the vertical direction and finally a translation of the joint angle in the vertical direction (equation (4.3)).

$$\phi_t(t) = x_2\phi(t + x_1) + x_3 \quad (4.3)$$

where

- $\phi_t(t)$ transformed joint angle at time t
- $\phi(t)$ joint angle at time t
- x_1 constant which allows the joint angle to be translated horizontally
- x_2 constant which stretches the joint angle vertically
- x_3 constant which translates the joint angle vertically

The Simplex (Nelder and Mead, 1965) and the Simulated Annealing (Goffe et al., 1994) algorithms were used to minimise the sum of squares difference between the crank angle and the transformed joint angle time histories. The Simplex algorithm was used to find a solution which was then confirmed or improved upon by the Simulated Annealing algorithm. The solution from the Simplex optimisation was used as the starting point for the Simulated Annealing optimisation.

In some cases the optimisation procedure failed to find a sensible solution to the synchronisation of the joint angle time histories. In these cases the trials were synchronised by plotting the two time histories and measuring the appropriate time translation factor. This factor was then fixed and the optimisation procedure repeated to determine the remaining parameters of the transformation.

Obtaining joint angle and joint angular velocity time histories

The synchronised joint angle was obtained from the known crank angle by rearranging equation (4.3) and replacing the transformed joint angle with the crank angle (equation (4.4), King, 1998). The angular velocity for each trial was calculated from the joint angle time history (equation (4.5)).

$$\phi(t) = \frac{(\phi_t(t) - x_3)}{x_2} \quad (4.4)$$

$$\omega(t) = \frac{(\phi(t) - \phi(t - 1))}{0.01} \quad (4.5)$$

Corrections to synchronised muscle data

Conversion of crank force to crank torque

The crank torque was calculated by multiplying the force recorded by the dynamometer by the moment arm of the crank. The moment arm was the perpendicular distance from the axis of the crank to the point where the force was measured. The moment arm of the crank was measured and recorded for each joint. The calculation is shown in equation (4.6).

$$T_c = Fd_c \quad (4.6)$$

where:

- T_c crank torque
- F force recorded by the dynamometer
- d_c recorded moment arm length

Segment weight correction

It was necessary to correct for the weight of the subject's limb (Winter et al., 1981). Depending on the direction of the joint action it was necessary to add or subtract the torque created by the weight of the subject's limb from the crank torque. The corrected crank torque was calculated using equation (4.7). The mass and mass centre location of the limb was determined using anthropometric measurements and the inertia model of Yeadon (1990b).

$$T_c = T_c \pm (Mgd_c \cos \theta) \quad (4.7)$$

where

- T_c crank torque
- M mass of limb
- d perpendicular distance from mass centre location to joint centre
- θ crank angle relative to the vertical

Conversion of crank torque to joint torque

The relationship between joint torque and crank torque was calculated as follows (King, 1998).

$$T_j = Fd_j \quad (4.8)$$

$$T_j = Fd_c \frac{d_j}{d_c} \quad (4.9)$$

$$T_j = T_c \frac{d_j}{d_c} \quad (4.10)$$

where

- T_c crank torque
- T_j joint torque
- F recorded force
- d_c crank moment arm
- d_j joint moment arm

The crank moment arm was constant throughout each trial. However, the joint moment arm was not constant and varied throughout each trial since there was some relative movement between the limb and the crank. To estimate the relationship between joint and crank moment arms a ratio of joint and crank angle was used (King, 1988).

Extrapolation of torque - angle relationship

The angle range of the crank arm was selected to be large enough to include the range of interest. It was necessary to collect data either side of the range of interest to allow for the accelerations of the crank. In certain cases the gymnast was unable to obtain motion through the desired range. When this occurred the gymnast performed over the greatest range possible. In addition the range of motion of the crank arm may not always be the same as the crank arm. In order to obtain the required joint angle ranges it was necessary to extend the torque - angle relationship.

King (1998) suggested three methods for extrapolation of the torque - angle relationship:

1. extrapolate with a constant torque value equal to the last known torque value
2. fit a spline to the torque - angle data and extrapolate outside the range
3. fit a least squares quadratic function through the torque - angle data

King (1998) found that the method of extrapolating from a spline fitted to the torque - angle data was dependent on the end-points of the data. Extrapolating using the quadratic fit over large angle ranges gave poor torque values (either too high or too low). It was found that the simplest approach, extrapolating using the last known torque value, was the most stable and robust and did not distort the torque - angle relationship. Therefore this method was used to extrapolate the torque - angle data where required.

4.2.3 Muscle model

The muscle model used a black box approach to fit the experimental angle, angular velocity and torque data to give a smooth surface of maximum torque as a function of angle and angular velocity (King, 1998). The following sections outline the methods used to fit the collected torque data so that maximum torque values can be obtained for use with the four segment simulation model.

Method - Six parameter double hyperbolic relationship

Hill (1970) found a hyperbolic relationship between force and velocity in whole muscle (Figure 4.5). However, Edman (1988) found a double hyperbolic function for the relationship between force and velocity for single muscle fibres (Figure 4.6). The muscle data collected in the present study showed a closer resemblance to the data of Edman than that of Hill. The characteristics of Edman's data were a plateau in the torque at high eccentric velocities, a steep drop in torque around zero velocity, a plateau in torque at low concentric velocities and a second drop in torque at high concentric velocities.

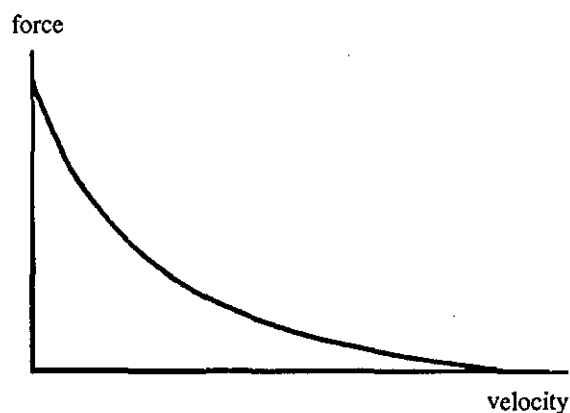


Figure 4.5. Force - velocity relationship found by Hill (1970).

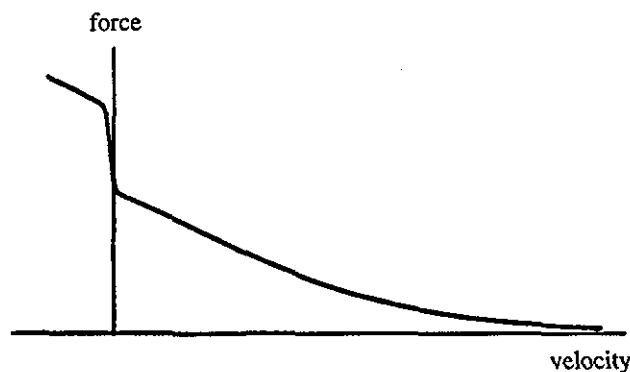


Figure 4.6. Force - velocity relationship found by Edman (1988).

To fit the torque - angular velocity data with a double hyperbolic function two exponential functions of four and two parameters were combined (King, 1998). The general shapes of the four, two and six parameter exponential functions are given in Figures 4.7, 4.8 and 4.9.

exponential function with four parameters:

$$T = \frac{a + be^{p\omega}}{1 + ce^{p\omega}} \quad (4.11)$$

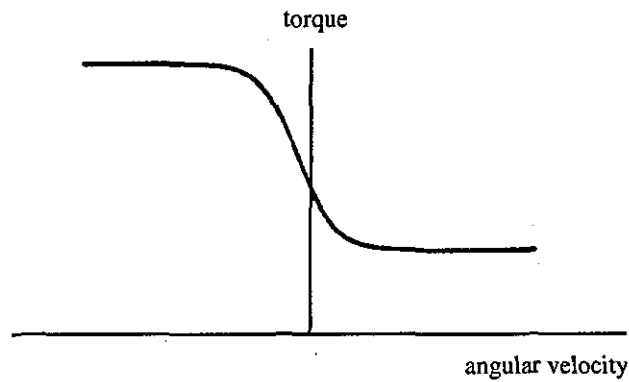


Figure 4.7. General shape of the four parameter exponential function.

exponential function with two parameters:

$$T = \frac{1}{1 + de^{q\omega}} \quad (4.12)$$

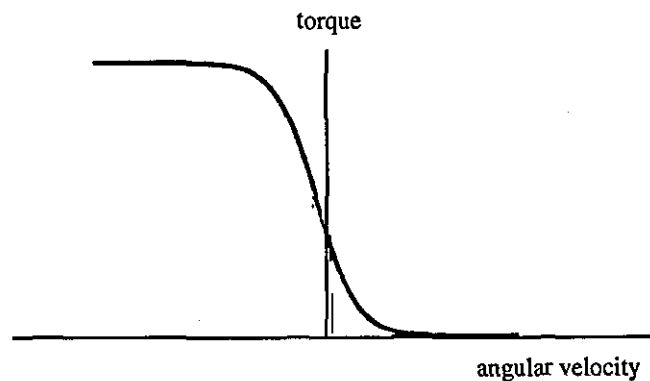


Figure 4.8. General shape of the two parameter exponential function.

six parameter exponential function:

$$T = \frac{a + be^{p\omega}}{(1 + ce^{p\omega})(1 + de^{q\omega})} \quad (4.13)$$

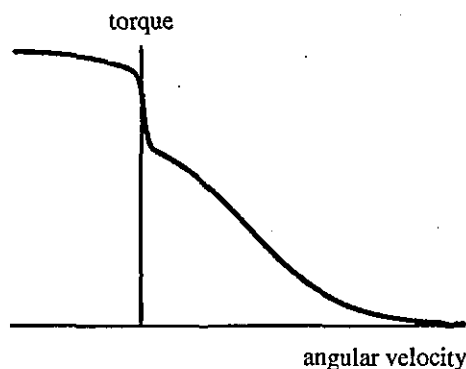


Figure 4.9. General shape of the six parameter exponential function.

The six parameter exponential function has the general shape of Edman's data with same characteristics outlined above. In addition the torque tends to zero at high concentric velocities. King (1998) presented a seven parameter exponential function and tested this along with the six parameter function by attempting to fit Edman's data (1988). The six parameter exponential function was found to offer greater stability when compared with the seven parameter function. The seven parameter function differed from the six parameter function in that it tended to a constant value at high concentric velocities instead of to zero. Since the six parameter function performed better it was chosen for fitting the data collected in the present study.

Extension of the torque - angular velocity relationship to include angle dependence

King (1998) found that a quadratic fit was sufficient to fit each parameter as a function of joint angle. Expressing each of the six parameters as a quadratic function of the joint angle increased the number at parameters to 18:

$$T = \frac{a + be^{p\omega}}{(1 + ce^{p\omega})(1 + de^{q\omega})} \quad (4.13)$$

with

$$a = x_1\theta^2 + x_2\theta + x_3 \quad (4.14)$$

$$b = x_4\theta^2 + x_5\theta + x_6 \quad (4.15)$$

$$c = x_7\theta^2 + x_8\theta + x_9 \quad (4.16)$$

$$d = x_{10}\theta^2 + x_{11}\theta + x_{12} \quad (4.17)$$

$$p = x_{13}\theta^2 + x_{14}\theta + x_{15} \quad (4.18)$$

$$q = x_{16}\theta^2 + x_{17}\theta + x_{18} \quad (4.19)$$

where

- $x_1 - x_{18}$ parameters
- ω joint angular velocity (radians/second)
- θ joint angle (radians)
- T torque

Optimisation procedure

A least squares optimisation method was used for each of the functions to fit the torque - angular velocity relationship to obtain the optimum set of coefficients. The optimisation procedure was performed with both the Simplex and Simulated Annealing algorithms. The solutions obtained from the Simplex algorithm were used as the starting point for the Simulated Annealing.

King (1998) found that in some cases the equations obtained with the 18 parameters became undefined due to the exponential function becoming too large. To prevent the function from being undefined two alternatives of the same function were used depending on the values of $p\omega$ and $q\omega$:

when $p\omega < 0$ and $q\omega < 0$

$$T = \frac{a + be^{p\omega}}{(1 + ce^{p\omega})(1 + de^{q\omega})} \quad (4.20)$$

when $p\omega > 0$ and $q\omega > 0$

$$T = \frac{ae^{-(p+q)\omega} + be^{-q\omega}}{(e^{p\omega} + c)(e^{-q\omega} + d)} \quad (4.21)$$

Range of data for the surface fit

The surface fits for each joint were optimised over different ranges of motion. Firstly over a range where there was no extrapolation of the torque - angle data for any trial (minimum range), secondly over the largest range (maximum range) and thirdly over a range of motion which used half real and half extrapolated data at the end points of each trial (average range).

Root mean squared (rms) differences were calculated between the raw torque data and the torques produced by the surface fit. The rms difference should be smallest when the surface is fit over the minimum angle range since none of the data will have been extrapolated. Depending on the rms value and the overall look of the surface fit the appropriate angle ranges were used (i.e. minimum, average or maximum). If the surface fits obtained do not appear to have been distorted by the use of extrapolated data the largest range will be used in the simulation model.

The surface function would be well-defined within the range of motion of the fitted data. However, King (1998) found that outside the range of motion used the function was not well-defined. To prevent the surface function from giving spurious torque values the function was constrained to a constant value outside the range.

4.3 Summary

Isokinetic joint torque data were collected from an elite male gymnast using an isokinetic dynamometer. Data were recorded from the hip and shoulder whilst performing flexion and extension actions over a range of angular velocities ($20^{\circ} \cdot s^{-1}$ to $250^{\circ} \cdot s^{-1}$). Each trial consisted of two repetitions of concentric - eccentric exercise. The middle eccentric - concentric portion of each trial (except trials at $20^{\circ} \cdot s^{-1}$) was used to ensure that the subject's muscles were "switched on" at the start and finish of the portion used.

Simultaneously data were recorded from a twin axis goniometer so that joint torques could be corrected for errors between the dynamometer crank angle and the angle of the subject's limb. The data were also corrected for segment weight and then converted from crank torque into joint torque.

At both joints and for each action (flexion/extension) the joint torque - angular velocity relationship was fitted using a six parameter exponential function developed by King (1998). For each joint action the data were combined using a quadratic fit to include the joint torque - angle relationship. Therefore, using 18 parameters a three-dimensional surface of joint torque, angle and angular velocity was obtained. These three-dimensional surfaces will allow the peak joint torque to be predicted based on a knowledge of joint angle and angular velocity. The peak joint torques will be used to limit the joint angle time histories used in the optimisation of the accelerated giant circles (Chapter 8).

CHAPTER 5

KINETIC ANALYSIS OF THE GIANT CIRCLE

5.1 Introduction

The majority of the experimental research which has been carried out on the backward giant circle has concentrated on the regular giant circle (Borms et al., 1975; Boone, 1977; Kopp and Reid, 1980; Okamoto et al., 1987). A small number of papers have looked at the accelerated giant circle (Cheetham, 1984; Gervais, 1993; Brüggemann et al., 1994). This chapter sets out to obtain kinetic and kinematic data from regular and accelerated giant circles. These data will provide a comparison between the two types of giant circle and provide the data required to evaluate the simulation models developed in Chapter 3.

5.2 Inertia parameters

5.2.1 Introduction

The inertia data is required for both the video analysis of the backward giant circles and the simulation models. The video analysis requires inertia data for 11 body segments whilst the simulation models require inertia parameters for one, three and four segments.

5.2.2 Methods

The 95 anthropometric measurements defined by Yeadon (1990b) were taken from two elite male gymnasts, subjects jb01 and tv01 (see Appendix 3a for data collection sheets). The anthropometry was performed by two experienced measurers, who had carried out the 95 measurements in excess of 50 times each. The anthropometric measurements were entered into the inertia model of Yeadon (1990b) to obtain the inertia characteristics of the subjects. The inertia model used the density parameters of Dempster (1955). The subject's masses were recorded and compared with the predicted mass obtained from the inertia model (Yeadon, 1990b).

The output from the inertia program, iseg90 (Yeadon, 1990b), was designed to

provide inertia data for an 11, four and three segment model. The simulation models were restricted to movements in the sagittal plane and therefore only the moments of inertia about the sagittal axis were required. For the four and three segment inertia sets the length and location of the mass centre data for the left and right sides of the body were averaged. The masses and moments of inertia were obtained by summing the values obtained for the left and right sides of the body. The inertia data for the single segment was obtained using the simulation program sim93 (Yeadon, 1984). The program is used to simulate the human during aerial movements. For each time interval of the simulation the program calculates the gymnast's whole body moment of inertia about the mass centre for the three principal axes of rotation. Using the 11 segment inertia parameters sim93 was used to simulate the gymnast with a fully extended body with the arms above the head. This body configuration was used as it approximated the shape of a gymnast during the downswing of a giant circle and could therefore be used for the one segment simulation model.

5.3 Video analysis

5.3.1 Introduction

The video analysis of the backward giant circles will provide a kinematic profile of both the accelerated and regular giant circle techniques. These kinematic data will be used to evaluate the simulation models developed in Chapter 3.

5.3.2 Data collection protocol

One senior male gymnast of international standard gave consent to perform several regular and accelerated backward giant circles on the high bar while force and video data were collected (see Appendix 3b for signed consent form). In total 12 trials were performed and recorded. These 12 trials were split into two groups depending on which type of giant circle was performed. The trials from the first group were the regular giant circles where the gymnast was requested to perform consecutive giant circles with good form. The trials from the second group were the accelerated giant circles, where the gymnast was requested to perform giant circles as if he were "winding up" for a double layout dismount. The high bar was erected inside a biomechanics laboratory. Due to the confines of the laboratory the gymnast wore canvas loops to prevent any loss of contact with the bar. The gymnast was allowed to rest between trials so that fatigue would not

develop and consequently lower the standard of his performance.

All trials were recorded using two video cameras, a Sony Hi8 Hyper HAD (EVW-300P) and a Sony Digital Handycam (DCR-VX1000E), both operating at 50 Hz. The cameras were genlocked in order to synchronise their shutters which were operating at 1/500 s and 1/600 s respectively. The two cameras were located approximately 1.6 m above the ground at a distance of 8.5 m from the centre of the high bar (Figure 5.1). The field of view was approximately 6 m wide and for calibration purposes contained 24 control points on eight calibration poles (Figure 5.2) which were placed in known locations within the movement space (Figure 5.3, see Appendix 3c for three-dimensional co-ordinates of the calibration markers). The markers on the poles were constructed from polystyrene balls (0.08 m in diameter) which had been drilled through their centres. In addition to the calibration poles four markers were placed on the uprights of the high bar (Figure 5.2). This gave a total of 28 control points distributed throughout the movement volume. The locations of the control points were chosen so that the subject would perform the giant circle within the calibration volume. This meant that no extrapolation outside the calibration volume was necessary. The calibration points were videoed prior to the subject performing the swinging trials.

In order to make use of the fact that the cameras were gen-locked a synchronisation unit was placed in the field of view of both cameras (Figure 5.1). The synchronisation unit comprised an array of 18 ultra bright light emitting diodes (LED), each LED was 0.01 m in diameter. The synchronisation unit was connected to a photocell attached to the upright of the high bar furthest away from the cameras (Figure 5.4). A reflective disc was placed on the upright nearest to the cameras facing the photocell and at the same height. Both the photocell and reflective disc were placed at a height so that the subject's hips would break the photocell beam as he passed through the uprights at the lowest point of each swing. The breaking of the beam acted as a switch which was used to light the synchronisation unit. Identifying this event from each camera view enabled the cameras to be synchronised.

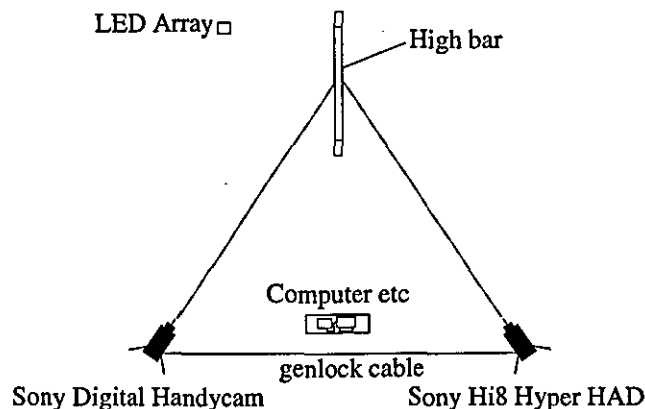


Figure 5.1. Arrangement of the video cameras and data capture system.

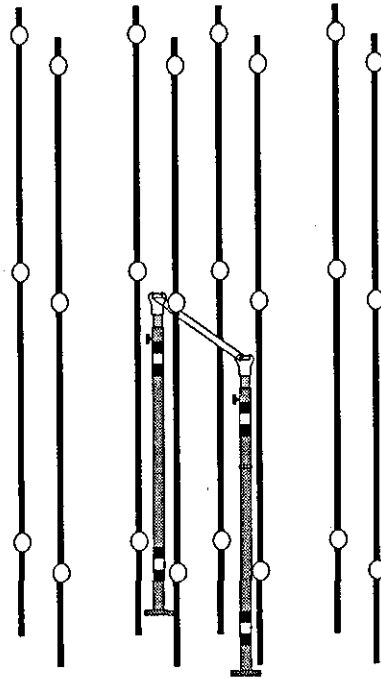


Figure 5.2. Arrangement of the calibration poles and markers.

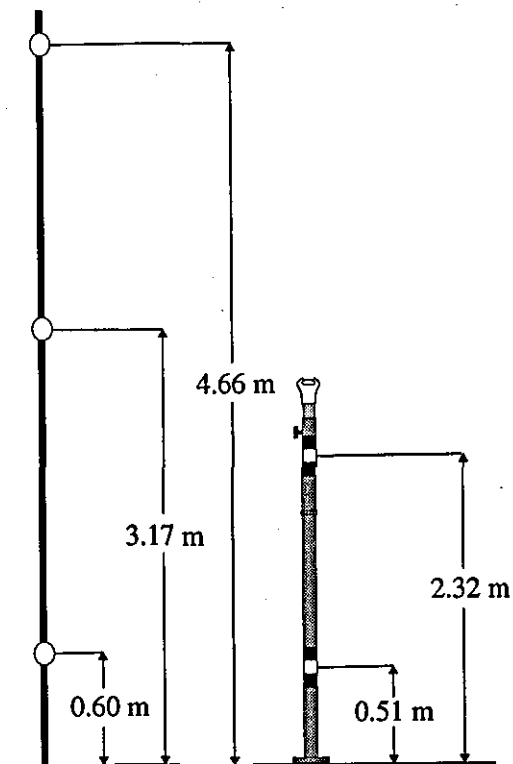


Figure 5.3. Heights of the calibration markers used in the calibration volume.

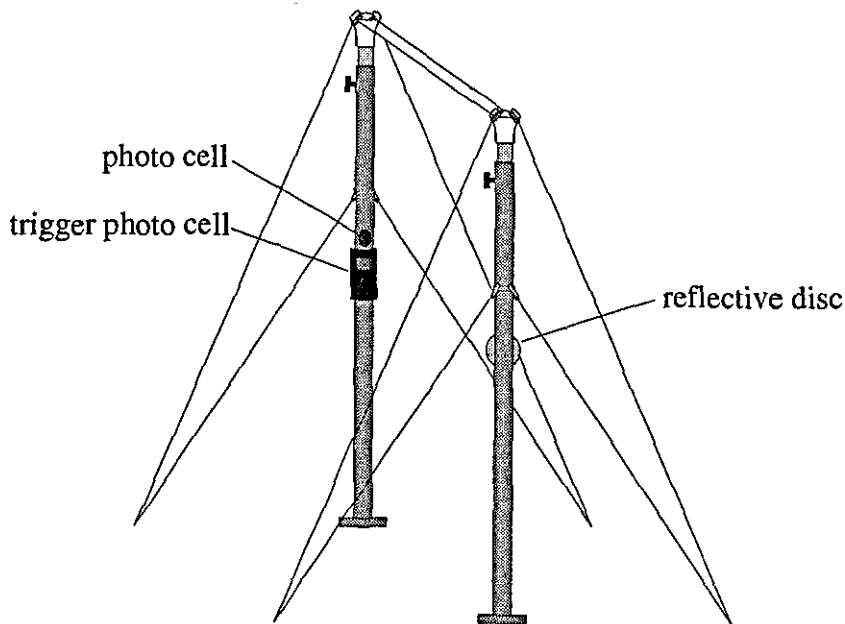


Figure 5.4. The photocell arrangement attached to uprights of the high bar.

5.3.3 Analysis of video data

Digitisation

The tapes from both video cameras were time-coded for use with the video digitiser system. All digitisation was carried out using the Target system (Kerwin, 1995). The zoom on the digitiser was set to x2 giving a resolution of 6144 x 4608.

Five images of the calibration volume were digitised prior to the movement data. From the measured three-dimensional locations of the 28 control points, together with the digitised locations, the 11 DLT camera parameters for each camera were determined using the method of Abdel-Aziz and Karara (1971). The calibration program produced root mean squared (rms) reconstruction errors for the calibration points in each of the three dimensions (x,y,z).

In each field of the movement phase the wrist, elbow, shoulder, hip, knee, ankle and toe of both sides of the body were digitised along with the head and the centre of the bar, giving a total of 16 landmarks per video field. A polystyrene ball of diameter 0.12 m, with a 0.028 m hole through its centre was positioned at the mid-point of the bar. This point was digitised as the centre of the bar. The views from both cameras were digitised for trial 10, trial 4 and trial 11. These trials contained three regular giant circles (trial 10) and two accelerated giant circles (trial 4 and trial 11). The two sets of digitised co-ordinates for each trial were synchronised by locating the common frame containing the illuminated synchronisation unit. The synchronised co-ordinates, 11 DLT parameters for

both cameras and the 11 segment inertia data were entered into the video analysis program film15h. The film program was adapted from the program film (Yeadon, 1984) to obtain the required output for the high bar application. Three dimensional co-ordinates of each digitised point were reconstructed using the method of Abdel-Aziz and Karara (1971). The video analysis program determined the rms values of the reconstructed points about the mean of each point for each field digitised. Rms values for all points were determined in each of the three dimensions (x,y,z).

The video analysis program calculated the three-dimensional co-ordinates of the mass centre location of the subject and the segment lengths for each video field. The segment lengths were compared with those obtained from the anthropometric measurements taken from the subject.

Orientation and joint angles were calculated for each frame of motion. The orientation angles (Yeadon, 1990a) refer to the somersault angle, defined as the angle created by the line joining the mass centre of the subject to the neutral bar position, the tilt and the twist angles. Although it was assumed that the majority of the movement occurred in the sagittal plane output of the tilt and twist angles will provide confirmation of this assumption. The angular velocity of the somersault angle was calculated by differentiating the somersault angle time history. This was done by evaluating the first derivative of the quintic spline which was fit to the somersault angle data (Jennings spline fitting library which fits splines using the method of Reinsch, 1967).

The joint angles output from the analysis program were the angle made by the arm segment and the horizontal, the pike angle at the hips, the elevation angle of the shoulders, and the angle at the knees (Yeadon, 1990a). The four segment simulation model required the time histories of the arm segment, hip, shoulder and knee angles along with their first and second derivatives. These data were fit using quintic splines. Before the splines were fit to the angle data, the angles obtained from the right and left side of the body were averaged. These averaged data were then splined using Jennings spline fitting library (1979). The spline coefficients of the somersault, arm, hip, shoulder and knee angle were output from the analysis program.

To determine the neutral resting location of the centre of the bar the polystyrene ball mounted at its centre was digitised with zero load applied to the bar. The polystyrene ball was digitised sixteen times in each of ten video fields from both camera views. The location of the centre of the bar was taken as the average of the one hundred and sixty reconstructed estimates. The horizontal and vertical displacements away from the neutral resting position of the bar were obtained by subtracting the resting position from the reconstructed three-dimensional co-ordinates obtained from the swinging trials. Quintic splines were fit to the horizontal and vertical bar displacements so that their linear velocities could be evaluated (Jennings spline fitting library). The coefficients of the bar displacement spline were output from the video analysis program.

5.4 Force measurement

5.4.1 Introduction

Reaction force data have been collected from gymnasts performing regular giant circles (Kopp and Reid, 1980) and also from gymnasts performing accelerated giant circles (Gervais, 1993). However, no results have been presented on force recorded from a gymnast performing both regular and accelerated giant circles. This section outlines the method for collecting force data which will be used to evaluate the simulation models developed in Chapter 3.

5.4.2 Calibration of the force measurement system

In order to measure force from a strain gauge device it is necessary to calibrate the system using known loads. When analysing the strain data these calibration curves may be used to convert the strain data into force.

Arrangement of strain gauges

To record the strain whilst the gymnast circled the high bar 16 strain gauges (CEA/09/280UW/120 linear strain gauges) were bonded to the surface of the bar (Figure 5.5). The gauges were arranged into two full wheatstone bridges at each end of the bar, one bridge to measure horizontal strain and one bridge to measure vertical strain. The arrangement of the bridges resulted in four channels of information. Due to the arrangement of the four wheatstone bridges the force applied to the bar could be recorded independently of the point of force application.

The bridges were connected to a six channel strain gauge amplifier (Model 2100, Measurement Group UK). The gain on the amplifier was set so that the output voltage would be in the range of ± 10 volts. This was the desired range of output so that the amplified signals could be passed through the analogue to digital converter (CED 1401). The analogue to digital converter sampled the amplified strain data at 200 Hz which was subsequently recorded on a PC (Acorn 5000). The arrangement of the strain data capture system is shown in Figure 5.6.

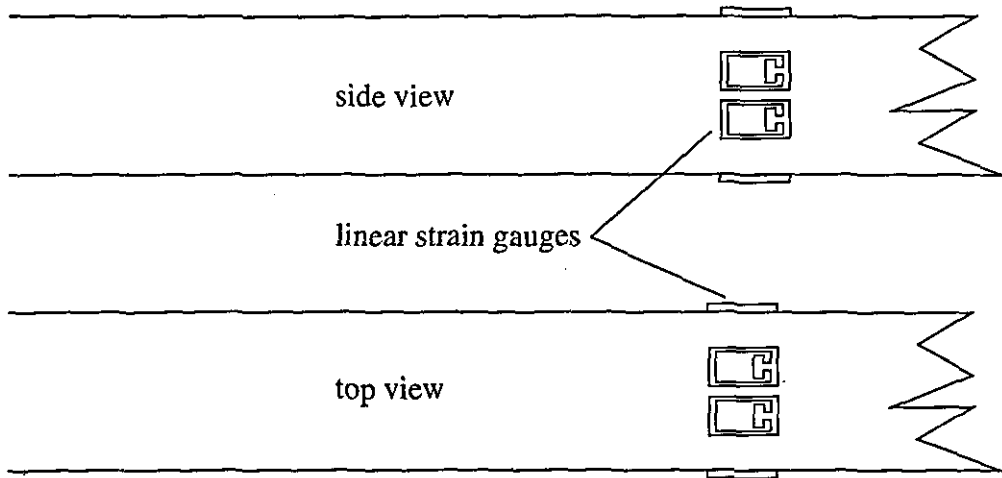


Figure 5.5. Arrangement of strain gauges bonded to each end of the high bar.

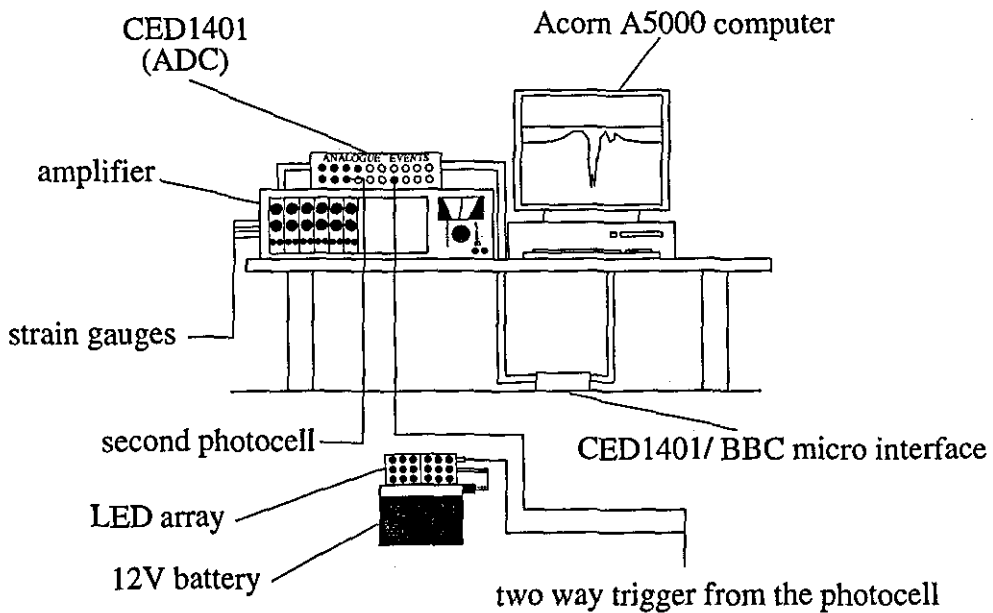


Figure 5.6. The data capture system used to collect strain data.

Methods

The bar was erected and the uprights were verticalised using spirit levels. Before testing with the gymnast it was necessary to calibrate the high bar so that the strain measured from the gauges could be converted into force. The gains on the vertical and horizontal channels of the strain gauge amplifier were set to 400. This allowed the full range of load to be recorded given the restriction of the ± 10 volts output required by the analogue to digital converter. The bar was then loaded vertically downwards at its centre

using chains and two cable tensioners. The cable tensioners were of the same type as those used to tighten the cables supporting uprights of the high bar. One end of the loading system was connected to the centre of the high bar using canvas loops. The other end was connected to a plate mounted in the floor directly under the centre of the bar (Figure 5.7). A load cell was placed within the chains of the loading system to measure the load applied to the bar (Figure 5.7).

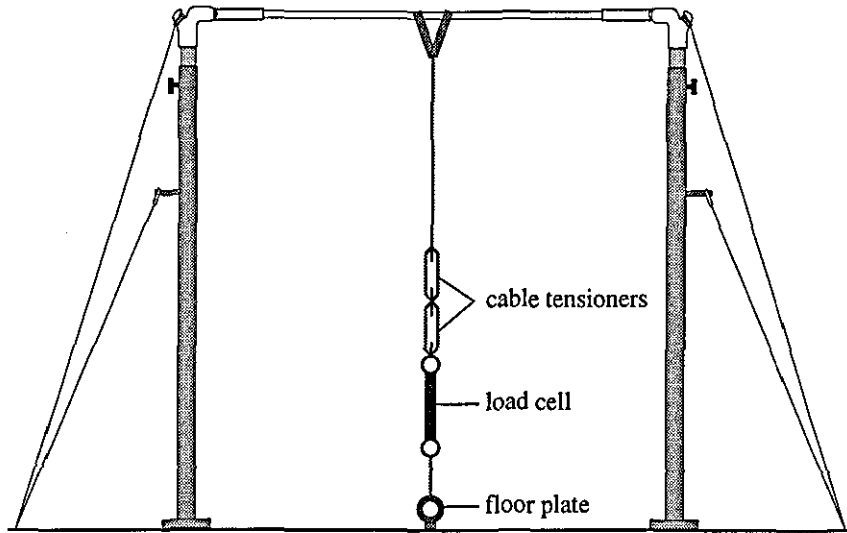


Figure 5.7. The load cell and loading system for vertical calibration.

The load cell was constructed from a length of steel with eye bolts mounted at each end (Figure 5.8). Two cross pair strain gauges were bonded to the load cell to form a full bridge circuit. The load cell was loaded to 8.0 kN in steps of 0.5 kN using an Instron hydraulic testing machine, model 8011 (see Appendix 3d for calibration of the load cell data). The output, in microstrain, from the load cell was recorded on a Tinsley Sovereign strain gauge amplifier.

The load cell was connected to a strain gauge amplifier (Tinsley Sovereign) which gave an analogue display of the strain. The bar was then loaded vertically to 3.0 kN in steps of 0.5 kN (see Appendix 3e for the data sheets). This was achieved by tightening the cable tensioners within the loading system. When the amplifier connected to the load cell gave the appropriate reading a recording from the high bar amplifier was taken. The reading (in ADC counts) was taken over a period of 7.5 s and was saved as both a comma separated variable file (CSV) and as a binary file. Average values from each calibration recording were made and entered into a separate file. By plotting the graph of load against amplifier reading it would be possible to convert any amplifier reading into force. In order to determine the interactions between channels (cross talk) data were recorded from all four channels during the calibration recordings, regardless of the direction of loading.

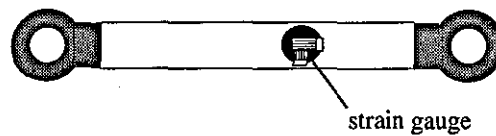


Figure 5.8. The calibrated load cell used in the calibration of the force measurement system.

To load the bar in the horizontal direction two eye bolts were mounted at bar level into the steel structure of the laboratory (Figure 5.9). The loading system was connected at one end to the high bar and to the eye bolts mounted in the wall at the other (Figure 5.9). The bar was loaded horizontally to 2.5 kN in steps of 0.5 kN (see Appendix 3f for data sheets).

The data from the horizontal and vertical strain gauges may be combined to obtain the resultant reaction force at any time during the swinging activity. Therefore, loading the bar at its centre may be justified. However when the gymnast circles the bar contact is made at two points (i.e. where the hands contact the bar). These points will be approximately shoulder width apart. In order to determine the effect of loading the bar at two points simultaneously a second bar was suspended under the high bar using two canvas loops (Figure 5.10). The second bar was then loaded at its centre using the loading system. The high bar was loaded in this manner up to 2.5 kN in steps of 0.5 kN as described previously (see Appendix 3g for data sheets).

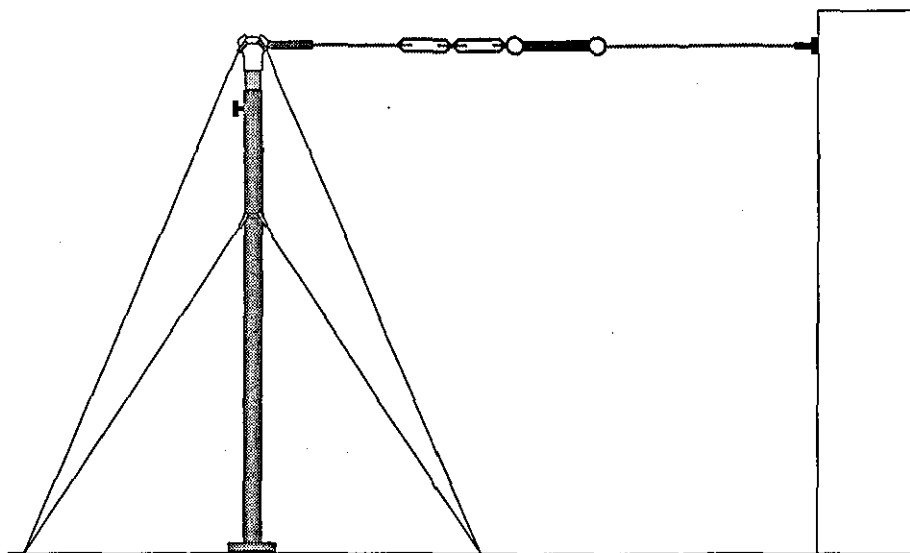


Figure 5.9. The load cell and loading system for horizontal calibration.

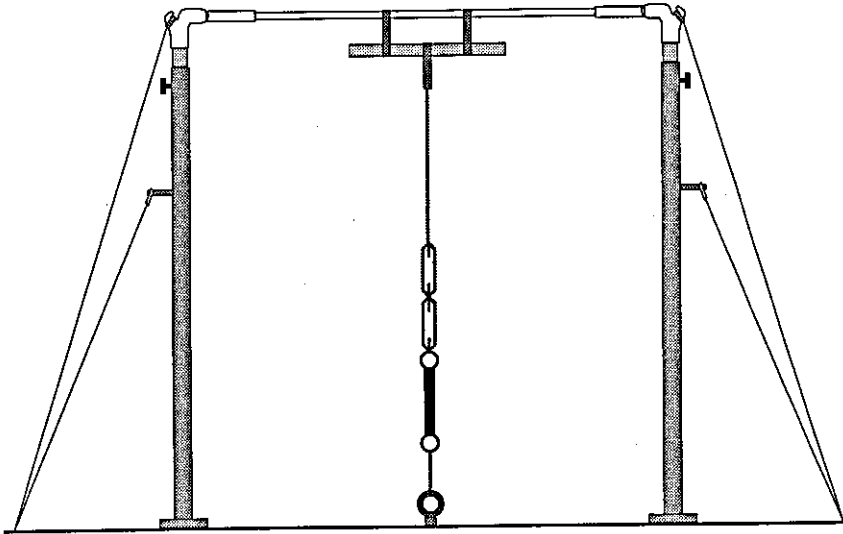


Figure 5.10. Arrangement of loops and chains for loading the bar at two points.

Analysis of the calibration data

The strain data from the two ends of the bar were combined. That is, the vertical strain data from channel one was added to the vertical strain data from channel four. The same was done for the horizontal strain data. This meant that the strain and subsequent force would be independent of point of application along the bar. Linear regressions were performed between the load applied to the bar and the recorded strain in both directions (i.e. vertical and horizontal). The recordings from the amplifier were defined as the dependent variables, whilst the known loads were used as the independent variables. The regressions were forced through the origin since all the amplifier channels had been zeroed with no force applied to the bar. All regressions were performed on the First statistics package. The output from the statistics package were the equation of the regression lines and the coefficient of correlation between the two variables.

5.4.3 Collection of force data

Data collection

The collection of the strain data was triggered using the photocell attached to the uprights of the high bar (Figure 5.4). This was the same photocell used to trigger the synchronisation unit (section 5.3.2). The photocell worked as a switch. As the gymnast passed through the lowest point on the first giant circle the breaking of the beam triggered the data collection. The software controlling the data recorder was designed to collect the

strain data one full second before the trigger was activated and 6.5 s after. This delayed trigger allowed the strain data to be recorded during the downswing of the first giant circle. All data were collected at 200 Hz and recorded using the same data collection system used in section 5.4.2.

5.4.4 Analysis of force data

The strain data were converted into force (Newtons) using the regression equations obtained in section 5.4.2. The error in the prediction of the force applied to the bar was calculated from the calibration and regression information. Peak reaction forces were determined for each giant circle. These data were expressed in Newtons and in terms of the gymnast's bodyweight. Force in bodyweights was calculated by dividing the force calculated in Newtons by the subject's mass and the acceleration due to gravity.

The force traces obtained from different giant circles were compared. The rms of the difference between the force trace of the three regular giant circle performed in trial 10 were obtained. All combinations of the three regular giant circles were compared. The trials for the accelerated giant circles were compared in the same way.

5.5 Synchronisation of force and video

5.5.1 Introduction

In Chapter 7 the four segment model will be evaluated by comparing the reaction forces produced by the model with those obtained from the force analysis of the backward giant circle. In order for these two force-time histories to correspond the simulation model will be driven using the joint angle time histories obtained from the video analysis. Therefore, the force and video data need to be synchronised so that the appropriated force recordings correspond to the movements of the subject.

5.5.2 Collection of force and synchronisation data

The force and video data were collected simultaneously. The force data were recorded at 200 Hz whilst the video data were recorded at 50 Hz. Therefore, for every field of video data recorded there were four recordings of force. The synchronisation unit allowed the force and video to be synchronised to the nearest video field. In order to

synchronise these data and obtain the force recordings corresponding to the video data it was necessary to collect some additional data.

A second photocell was attached to the furthest upright from the cameras. This was positioned as close to the first photocell as possible and was directed at the reflector attached to the nearest upright (Figure 5.4). The second photocell gave a voltage output of 10 volts when the beam was broken and zero volts when the beam was "made". This output was connected through the analogue to digital converter and recorded on a separate channel of the data recorder.

The second beam was broken as the gymnast's hips passed between the uprights on every giant circle. It was assumed that at the mid-point of the beam break the gymnast's hips were directly between the uprights. That is, the location of the mid-point of the hips (average location of the left and right hip locations) was in line with the two uprights. The time that the hips were in the middle of the beam break was determined by interpolating the hip location time history from the video data. Since the data from the beam break was recorded alongside the force recordings the event of the hips breaking the beam could be matched to the nearest force recording.

The force data obtained in section 5.4 were plotted against the rotation angle of the subject in order to determine where during the backward giant circle the peak force occurs. This would make it possible to determine whether features in the force traces correspond to the joint actions being performed by the subject.

5.6 Obtaining spring coefficients

5.6.1 Introduction

The four segment simulation model described in Chapter 3 requires stiffness and damping coefficients for the linear springs at the bar and shoulders. This section outlines how these coefficients were determined. The stiffness and damping coefficients of the bar were determined using two independent methods. The first method used static loading whereas the second method used dynamic data obtained from the force and video analysis of the backward giant circles. The spring coefficients for the shoulders were obtained in two stages. An initial estimate for the stiffness of the shoulder spring was determined from the extension which occurred in the shoulders during the backward giant circles. The four segment simulation model was then used to obtain a better estimate using an optimisation procedure. The same optimisation procedure was used with all spring coefficients. The spring coefficients obtained from the optimisation will be used in the four segment simulation model for both the evaluation of the model (Chapter 7) and

the optimisation of the backward giant circle (Chapter 8).

5.6.2 Stiffness and damping coefficients of the bar

Determination of stiffness coefficient via static loading

Data collection

The high bar used in sections 5.3 and 5.4 was videoed using a Sony Handycam Hi8 (CCD-VX1E) video camera, operating with a shutter speed of 1/300 s, positioned level with the height of the bar and 3.67 m in front (Figure 5.11). The location and zoom of the video camera gave a field of view of approximately 0.40 m wide. Three markers were placed on the bar - one on the centre line at the middle of the bar and one 0.05 m either side of the central marker (Figure 5.12). Two calibration poles were placed in the field of view and videoed prior to the loading to allow for calibration of the movement space (Figure 5.12). The markers on the poles were placed at known location so that a scale factor could be determined.

The bar was loaded in the vertical direction using weights of known mass suspended from the bar using chains and canvas loops (Figure 5.13). The bar was loaded to 2165 N in steps of approximately 228 N. At each each different load the bar was videoed. To increase the number of data points recordings were made as the bar was unloaded.

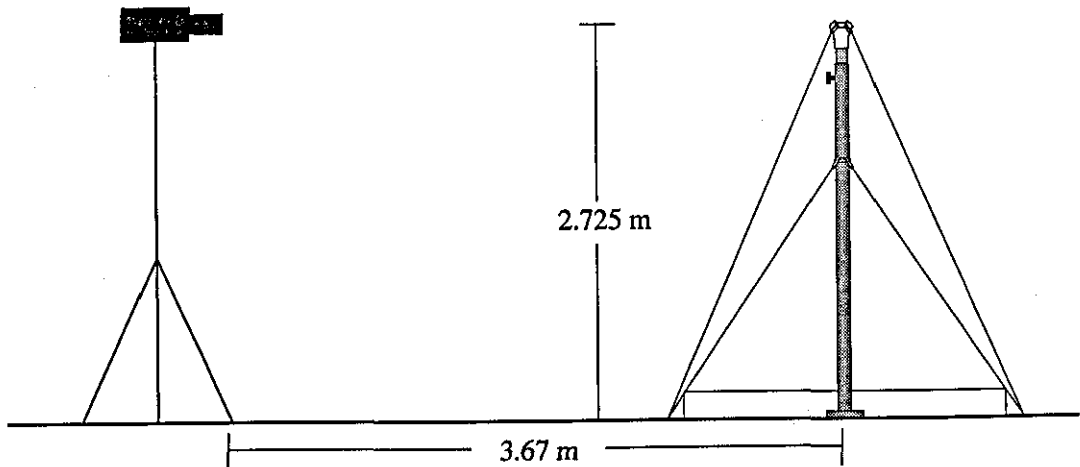


Figure 5.11. Location of the camera relative to the high bar during static loading.

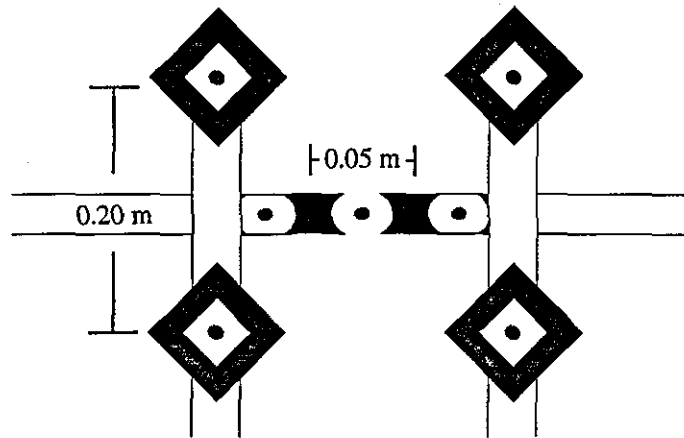


Figure 5.12. The calibration poles and markers placed in the field of view in order to determine the scale factor.

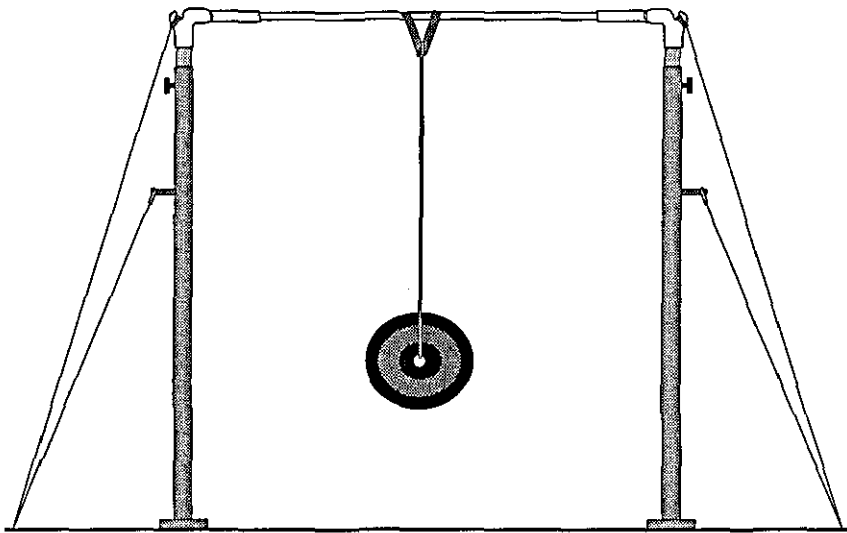


Figure 5.13. Method used to load the high bar.

Data analysis

Each of the video fields was digitised using the Target digitising system. The reference poles were digitised to calibrate the movement space. From the known co-ordinates and the digitisation of the reference markers the vertical displacement of the loaded bar from its neutral resting position was determined using a scale factor.

A linear regression was performed on the vertical bar displacement and the load applied to the bar. Since no vertical displacement occurred when zero load was applied to the bar, the regression was forced through the origin. Using Hooke's Law (equation 5.1) the gradient of the regression line may be used to determine the stiffness coefficient of the bar.

$$T = kx \quad (5.1)$$

where

- T tension in the spring
- x extension in the spring
- k stiffness coefficient of the spring

The stiffness coefficient obtained from the static loading was compared with that obtained from the kinetic and kinematic analysis of the backward giant circles.

Determination from kinetic and kinematic analysis

The horizontal and vertical displacements of the high bar about its neutral resting position were calculated. The horizontal and vertical coordinates of the centre of the bar in its neutral resting position were subtracted from the bar displacements obtained from the video analysis program.

Linear regressions were performed between the vertical bar displacement and the synchronised vertical force recordings for trial 10 circle one, circle two, and the combined data from circle one and two. The same regressions were performed in the horizontal direction. Similar regressions were performed on the data obtained from the accelerated giant circles performed in trial 4.

The gradient of the regression equations was defined as the stiffness coefficient of the bar (Hooke's Law). Using Hooke's Law the stiffness coefficient of the bar was used to calculate the estimated force. This was done by multiplying the stiffness coefficient with the bar displacement. Rms values, in the horizontal and vertical directions, were determined for the difference between the estimated and the recorded force. The same procedure was carried out to obtain rms difference values between estimated and recorded force using the stiffness coefficient obtained from the static loading of the bar.

The equation of motion for a damped linear spring was given in Chapter 3. The magnitude of the damping force is related to the damping coefficient and the rate of lengthening of the spring. To determine the damping coefficient of the bar a multiple regression was performed between the force recorded from the high bar, the displacement of the bar and the splined linear velocity of the bar obtained from the video analysis. The multiple regression yielded coefficients for the stiffness and the damping of the high bar. The multiple regressions were performed separately with the horizontal and vertical data. The estimated force was calculated using the stiffness and damping coefficients determined from the regression equations. The rms differences for the measured and estimated force using the stiffness and damping coefficients were calculated.

5.6.3 Stiffness and damping coefficients of the shoulder spring

Initial estimate of shoulder spring stiffness coefficient

The video analysis program calculated the lengths of the subjects limbs for each field of movement. It was hypothesised that the gymnast increased in length during the lowest part of the giant circle. It is thought that the majority of this extension occurs in the structures of the shoulders and the spine. In order to calculate the extension that occurs between the wrists and the hips, the video analysis program was modified to sum the average length of the arms to the length of the torso for each field of movement (section 5.3.3). Linear regressions were performed between the time history of the wrist to hip length and the resultant reaction force at the bar.

5.6.4 Optimisation of the spring parameters

The methods of obtaining the spring parameters outlined thus far have been dependent on regressions performed on the kinetic and kinematic data. Since no data has been collected on the internal joint forces at the shoulders and throughout the structures of the spine, any stiffness coefficient obtain from these results may be expected to be "ball park" at best. In addition no values for the damping coefficient for the shoulder spring have been determined. The current section outlines the method used to obtain stiffness and damping coefficients for the shoulder spring. The same method was also used to optimise the spring coefficients of the bar.

Methods

The four segment model outlined in Chapter 3 was used to obtain stiffness and damping coefficients for the shoulder spring using the Simulated Annealing optimisation routine. Splined joint angle time histories obtained from the video analysis were used to drive the simulation model. The optimisation procedure used a criterion based on a cost function. The cost function was derived from the whole body angle of rotation and the horizontal and vertical displacements of the bar. The rms difference between the simulated and the splined variables were calculated by the simulation program. The rotation angle obtained from the simulation model was called the "estimated" angle of rotation, whilst the angle of rotation obtained from the video analysis of the backward giant circles was called the "measured" angle of rotation. A similar notation was used for the horizontal and vertical bar displacements. The rms difference between the estimated

and measured variables were calculated for every integration interval of the simulation. At the end of the simulation the rms difference for each of the variables was produced for the whole simulation. The cost function contained the rms differences for the angle of rotation and the bar displacements with the appropriate weighting (see equation 5.2). Since the aim of the optimisation was to reduce the difference between the data obtained from the simulation model and the data obtained from the video analysis the cost function was minimised.

$$\text{Cost} = 1.0 * \text{RMS}_{\text{RA}} + 12.7 * \text{RMS}_{\text{HBD}} + 12.7 * \text{RMS}_{\text{VBD}} \quad (5.2)$$

where

- RMS_{RA} rms error in rotation angle [in radians]
- RMS_{HBD} rms error in horizontal bar displacement [in metres]
- RMS_{VBD} rms error in vertical bar displacement [in metres]

The weighting of the function is such that a 20° error in the rotation angle is equivalent to a 0.026 m error in the displacements of the bar. Using the stiffness coefficient of the bar obtained in section 5.6.2, a 0.026 m error in bar displacement would correspond to an error in the estimated reaction force of one bodyweight. The 0.026 m error in bar displacement therefore corresponds to approximately ¼ of the maximum force recorded during a backward giant circle. Similarly, multiplying the 20° error in rotation angle results in an unacceptably large difference between the simulation model and the video analysis. The weightings of the cost function were such that a 20° error in rotation angle and a 0.026 m error in each of the bar displacements would result in a score of 1.0.

The parameters varied in the optimisation were the stiffness and damping coefficients of the bar and shoulder springs. Upper and lower bounds were set to each of the parameters so that appropriate results could be obtained. The aim of the optimisation was not to find completely new spring coefficients but to test the sensitivity of the experimentally obtained values. The maximum number of function evaluations was set to 8000. That is, the Annealing process was given a maximum of 8000 simulations to vary the spring parameters within the upper and lower bounds to find the smallest value for the cost function.

The trial used to optimise the spring parameters was the third regular giant circle from trial 10. This giant circle was chosen since it was not used in section 5.6.2. In addition the evaluation of the four segment model will be carried out using the trials from the accelerated giant circles. Optimising the spring parameters using an accelerated giant circle may influence the results of the evaluation of the four segment model. It was therefore decided to use spring parameters obtained from a different movement.

The input to the simulation model were the initial estimates of the spring

parameters obtained from the regression equations performed on the experimental data (section 5.6.2), the spline coefficients for the joint angle time histories, the spline coefficients for the time history of the arm segment angle, the spline coefficients for the bar displacements and the rotation angle obtained from the video analysis. The initial velocities of the bar and the segments of the model were obtained from the evaluation of the first derivative of the spline data.

The optimisation performed using the regular giant circle was started from a rotation angle of 90° . It was found that the angular velocity during the rotation from 0° to 90° created problems with the simulation model. The gymnast initiated the giant circle from a near stationary position. The low angular velocity caused the rotation of the simulation model to deviate from the video data since the springs at the bar were prone to oscillations until sufficient angular velocity had been obtained.

The results of the optimisations would be used in the evaluation of the simulation models outlined in Chapter 3.

5.7 Summary

Chapter 5 has outlined the techniques used to collect three-dimensional coordinate data from a gymnast swinging on the high bar. Simultaneously force recordings from the bar were obtained and synchronised with the video data. The analysis of the video data will provide the necessary information to compare and contrast the regular and accelerated giant circles. The splined joint angle time histories will be used to drive the four segment simulation model. The force data will provide information relating to the loading of the high bar during both regular and accelerated giant circles. These data will also be used in the evaluation of the four segment simulation model.

Two techniques for obtaining spring parameters for the four segment simulation model were presented. The first used the synchronised force and video data, the second used the four segment simulation model and an optimisation algorithm. The results obtained from the first method may be used to answer the question as to whether the displacements of a calibrated high bar may be used as a force dynamometer. The results from the optimisation procedure will be used in the evaluation of the four segment simulation model (Chapter 7).

All results obtained from the methods presented in this chapter may be found in Chapter 6.

CHAPTER 6

RESULTS OF THE EXPERIMENTAL METHODS

6.1 Introduction

Chapter 6 contains the results from the methods outlined in Chapters 4 and 5. These include the data obtained from the isokinetic dynamometry and the kinetic and kinematic analysis of backward giant circles. The data presented in this chapter will be used in both the evaluation of the simulation models and the optimisation of the accelerated backward giant circle.

6.2 Muscle parameters

6.2.1 Introduction

A method for obtaining subject specific muscle parameters was outlined in Chapter 5. The method results in eighteen parameters which defines the relationship between the torque, angle and angular velocity of a joint. Since data were collected on four joint actions (flexion and extension at the hip and shoulder) four sets of the eighteen parameters were obtained. Each set of parameters defines the maximum joint torque the subject can produce given the angle and angular velocity at the joint. The muscle model is therefore a surface which represents the torque - angle - angular velocity relationship.

6.2.2 Calibration of the Kin-Com machine and goniometer

Estimate of accuracy

The average force measurement recorded by the dynamometer over a 5 s period with the crank arm in a horizontal position was within 1 N of the load hung from it. These errors are within the tolerance quoted by the manufacturers and of the same order of magnitude as the resolution of the machine. The resolution of the isokinetic dynamometer was therefore deemed acceptable.

The regression analysis performed on the goniometer calibration data yielded a standard deviation of 2.3°. Given the large angle ranges under investigation this was thought to be acceptable.

6.2.3 Raw joint torque data

Table 6.1 shows the chosen range of motion for the crank, the actual isokinetic range of motion of the crank and the isokinetic ranges of motion of the joint during hip flexion (similar tables for shoulder flexion and extension and hip extension may be found in Appendix 2c). In all cases (both direction and joint) the range of the crank angle was greater than that of the joint angle. This meant that the ranges of motion for which there were data were less than the ranges of motion that the subject was likely to use in performing accelerated giant circles. When fitting the surface to the raw data extrapolation of the torque - angle relationship was required on all joint ranges, except for when the minimum joint range was used.

Table 6.1. Ranges of motion during hip flexion

angle	from (°)	to (°)	range (°)
crank	3.0	116.0	113.0
isokinetic crank			
minimum	33.6	73.6	40.0
average	13.8	103.3	89.5
maximum	3.4	116.0	112.6
isokinetic joint			
minimum	40.5	69.8	29.3
average	28.9	90.4	61.5
maximum	11.3	107.9	96.6

The raw data were corrected for gravity and joint angle. In Figure 6.1 the raw data surface obtained from the average joint angle range for hip flexion is given. Since the average angle range is shown in Figure 6.1 some of the torque - angle data has been extrapolated using the last known torque value. The raw data for the average angle range from hip flexion and shoulder flexion and extension are shown in Figures 6.2, 6.3 and 6.4.

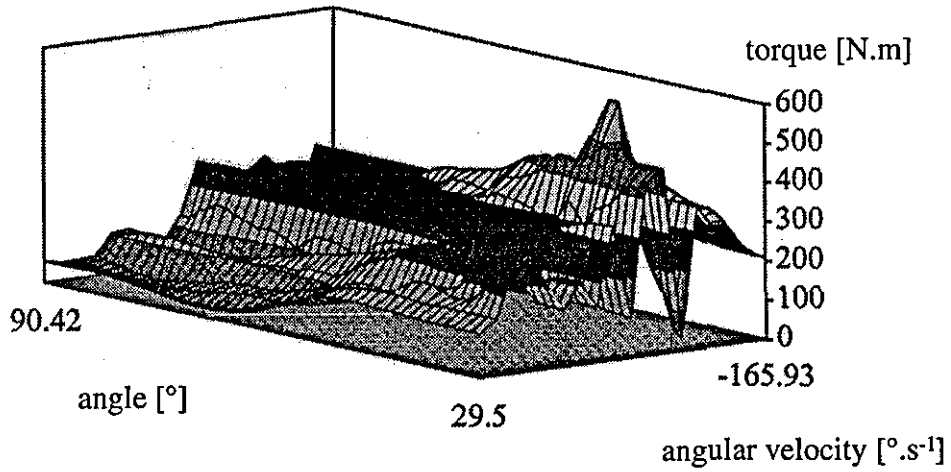


Figure 6.1. Raw data obtained using the average angle range for hip flexion.

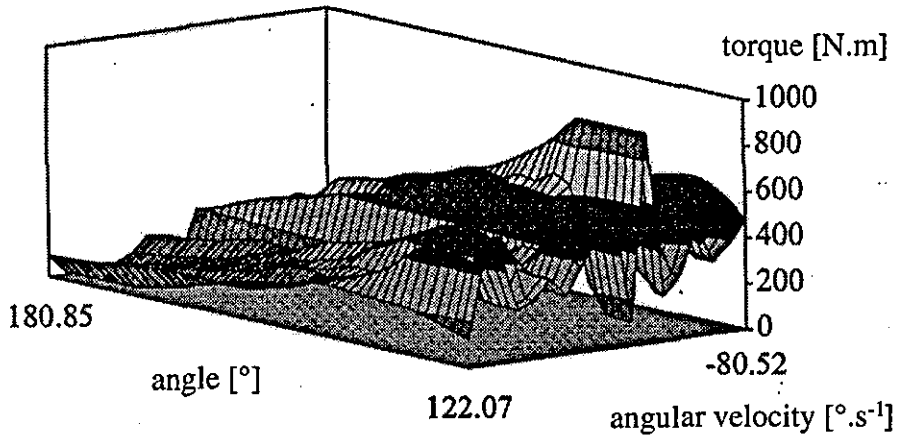


Figure 6.2. Raw data obtained using the average angle range for hip extension.

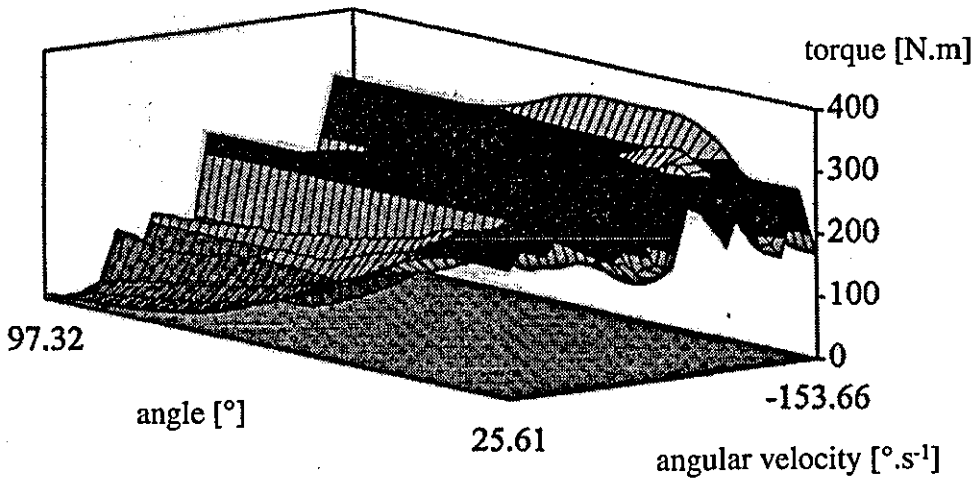


Figure 6.3. Raw data obtained using the average angle range for shoulder flexion.

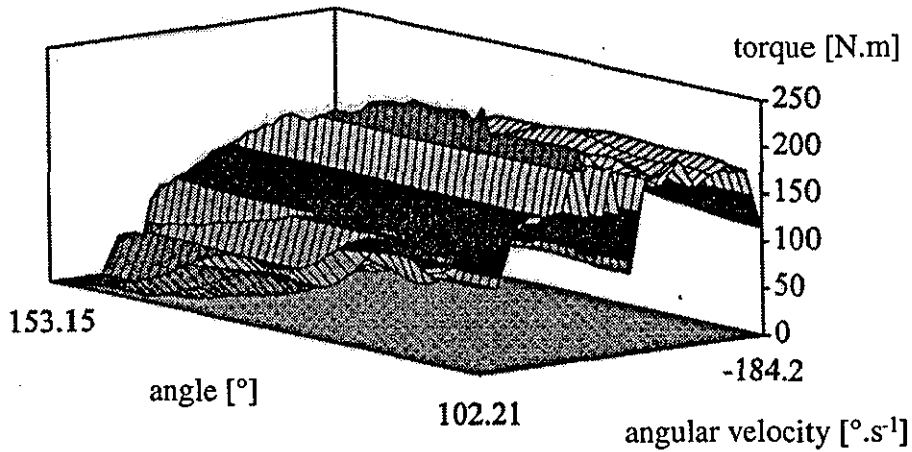


Figure 6.4. Raw data obtained using the average angle range for shoulder extension.

6.2.4 Smoothed 3-D joint torque surfaces

Estimate of accuracy

The rms difference between the raw and surface data were calculated for each of the joint angle ranges and for each joint action. These data are presented in Table 6.2. It might have been expected that the rms differences would have increased with increasing angle range since more extrapolated data would have been used.

Given the rms differences presented in Table 6.2, the joint angle ranges (see Table 6.1 and Appendix 2c) and the shape of the surface fits it was decided that the surfaces obtained using the average joint angle should be used in the simulation model. This gave a compromise between the angle range and the amount of extrapolated torque data. The surface fits for both of the hip and shoulder actions are shown in Figures 6.5, 6.6, 6.7 and 6.8.

Table 6.2. Rms differences between the raw data and the surface fits

action	rms difference over joint range [N.m]		
	minimum	average	maximum
shoulder flexion	26.4	30.8	38.9
shoulder extension	33.3	31.0	29.4
hip flexion	40.0	50.9	62.1
hip extension	182.7	102.1	121.9

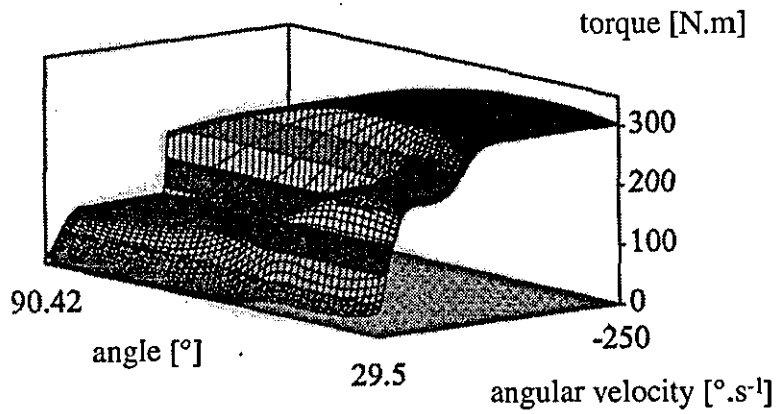


Figure 6.5. Surface fit using the average angle range for hip flexion.

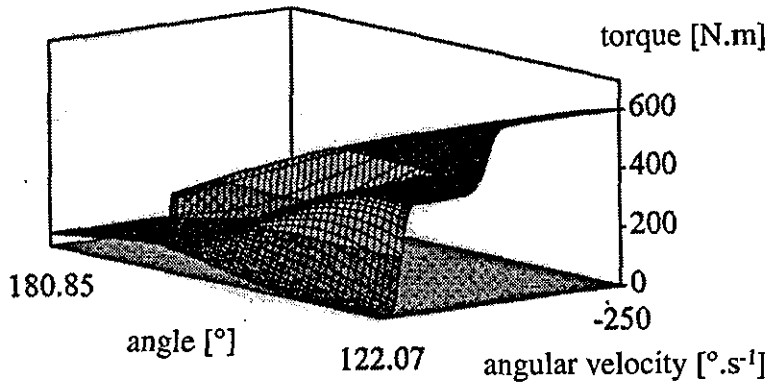


Figure 6.6. Surface fit using the average angle range for hip extension.

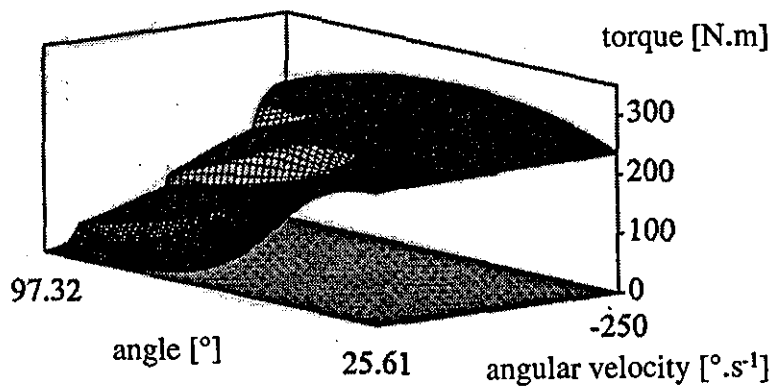


Figure 6.7. Surface fit using the average angle range for shoulder flexion.

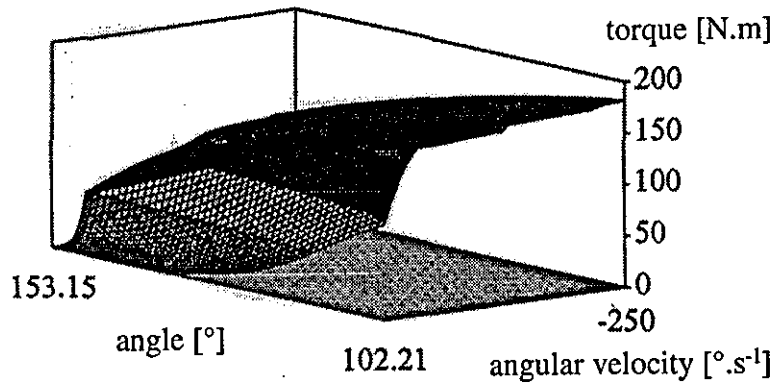


Figure 6.8. Surface fit using the average angle range for shoulder extension.

6.3 Kinematic analysis of the giant circle

6.3.1 Introduction

The following results were obtained from the methods presented in Chapter 5 from the collection and analysis of three-dimensional video data of the subject performing regular and accelerated giant circles. The results include the time histories of the path of the mass centre and the angular velocity of the whole body rotation angle, linear displacements of the bar, joint angle time histories and the segment lengths calculated from the video analysis program. Before the video analysis could be performed the inertia parameters of the subject used were required, therefore these results will be presented first.

6.3.2 Inertia parameters

The recorded masses of the two subject's were 62.8 kg and 65.0 kg for jb01 and tv01 respectively. The inertia model under-estimated the mass of subject jb01 by 0.75 kg, a difference of 1.2% when expressed as a percentage of the recorded whole body mass. The predicted mass for subject tv01 was over-estimated by 0.78 kg, a percentage difference of 1.2%. These percentage differences compare favourably with the results of Yeadon (1990b), Hatze (1980) and Hanavan (1978) who obtained mean values of 2.3%, 0.5% and 1.8% respectively.

The 11 segment inertia data are presented in Appendix 4a and 4b. The inertia data for the four, three and single segments are presented in Table 6.3 and Table 6.4 for the subjects jb01 and tv01, respectively.

Table 6.3. The four, three and single segment inertia data for subject jb01

segment	mass (kg)	length (m)	cmloc (m)	moment of inertia (kg.m ²)
arms	6.868	0.548	0.239	0.205
torso	33.566	0.435	0.337	1.610
thigh	14.074	0.374	0.151	0.173
l. leg	7.543	NA	0.227	0.164
legs	21.617	NA	0.308	1.329
whole body	62.050	NA	0.833	11.12

(where cmloc is the distance of the segment mass centre from the proximal joint centre and l. leg refers to the shank and foot)

Table 6.4. The four, three and single segment inertia data for subject tv01

segment	mass (kg)	length (m)	cmloc (m)	moment of inertia (kg.m ²)
arms	7.796	0.575	0.250	0.252
torso	34.450	0.466	0.351	1.617
thigh	15.412	0.403	0.171	0.212
l. leg	8.124	NA	0.228	0.199
legs	23.554	NA	0.330	1.539
whole body	65.780	NA	0.891	12.70

6.3.3 Estimation of accuracy

The overall rms error between the re-constructed co-ordinates and the known locations of the 28 markers in the calibration volume was 0.011 m. The rms error in each of the three directions were calculated. The largest rms error was in the direction parallel to the bar and was found to be 0.012 m. The smallest rms error was in the vertical direction and was found to be 0.008 m.

The average standard deviations for the reconstructed three-dimensional co-ordinates of the body points from a pseudo data was 0.009 m. The pseudo data set was created by averaging the data points in the two fields either side of the data point in

question. The average standard deviation gives an indication of the errors due to digitisation.

6.3.4 Obtaining model parameters

Regular giant circles

Path and velocity of the mass centre

During a regular backward giant circle the gymnast tries to maintain a straight body line. It might therefore be expected that the gymnast's mass centre will maintain a fixed distance from the axis of rotation. Figure 6.9 shows the vertical displacement of the mass centre against the horizontal displacement for the second giant circle of trial 10.

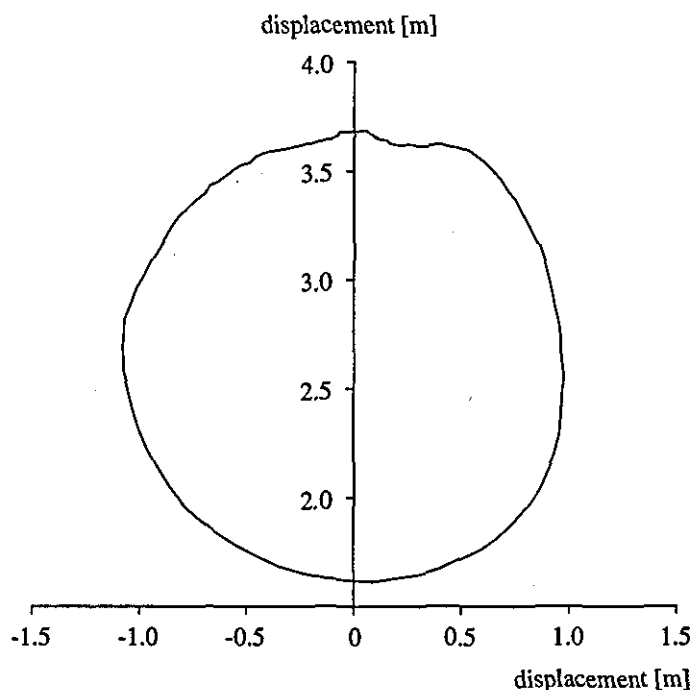


Figure 6.9. Path of the mass centre during one regular giant circle from trial 10.

In Figure 6.9 the gymnast circles in an anti-clockwise direction starting from the highest point. The path of the mass centre during the downswing is almost circular in nature. However, during the upswing the path of the mass centre appears to be squashed. As the subject swings from the handstand position he is accelerated by the torque created by his weight and its distance from the bar. The gymnast therefore tries to keep his mass centre as far away from the axis of rotation as possible during the downswing. On the upswing the torque created by his weight tends to accelerate him in the opposite direction to his swing. By moving the mass centre closer to the axis of rotation this torque and its

effect are reduced. The mass centre is brought closer to the bar by closing the angles at the hips and shoulders. At the end of the backward giant circle the gymnast extends by opening the angles at the hips and shoulders. This can be seen in Figure 6.9 where the mass centre starts and finishes the giant circle at the same height. The circular downswing followed by a squashed circular upswing shape for the path followed by the mass centre was found in the regular giant circles studied by Cheetham (1984).

The angular velocity of the rotation angle for one giant circle is shown in Figure 6.10. The angular velocity is graphed against rotation angle. Peak angular velocity occurred at a rotation angle of 167° and was approximately 5.0 rad.s^{-1} . Cheetham (1984) found a double peak in the angular velocity of the regular giant circles he studied. The first peak occurred before the gymnast had reach the lowest point of the giant circle and the second peak followed shortly afterwards. The second peak was associated with the closing of the hip and shoulder angles. It was found that the second peak was always greater than the first. The history of the angular velocity in the present study, Figure 6.10, also shows a double peak. However, the first peak is greater than the second. It may be that the subjects in Cheetham's study performed more vigorous "piking" actions than the subject in the current study.

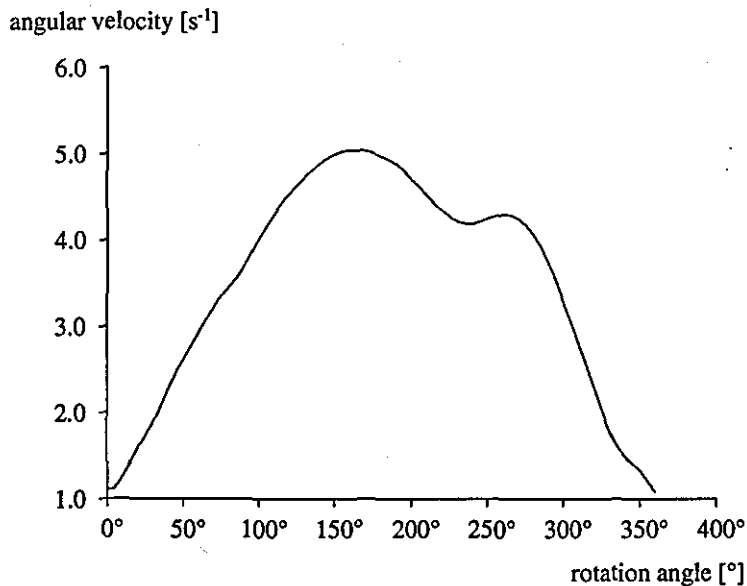


Figure 6.10. History of the angular velocity of the rotation angle during one regular giant circle from trial 10.

Table 6.5 shows the peak angular velocities and the angle at which these peaks occurred for all three regular giant circles analysed. The peak angular velocities in the present study compare well with those obtained by Cheetham (1984). Cheetham obtained peak angular velocities of between 5.1 rad.s^{-1} and 6.1 rad.s^{-1} for five subjects performing regular giant circles. The subject who achieved a peak angular velocity of 6.1 rad.s^{-1} for

the regular giant circle was only able to increase his angular velocity to 6.2 rad.s^{-1} when performing accelerated giant circles. Boone (1977) obtained a peak angular velocity of 4.8 rad.s^{-1} for regular backward giant circles.

Table 6.5. Peak angular velocities for regular giant circles (trial 10)

circle (trial 10)	peak angular velocity (rad.s^{-1})	rotation angle at peak ($^{\circ}$)
first	5.1	164.1
second	5.0	166.8
third	5.1	166.8

Bar displacements

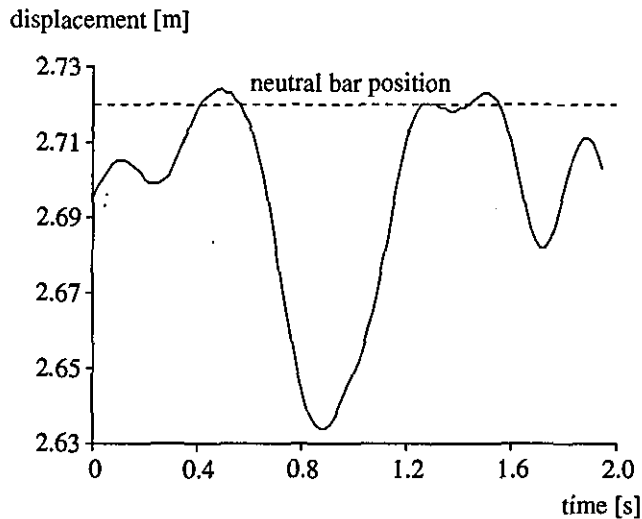


Figure 6.11. Time history of the vertical displacement of the centre of the bar for the first regular giant circle of trial 10.

For all trials the centre of the bar was digitised. Figures 6.11 and 6.12 show the vertical, horizontal and lateral displacement of the centre of the bar from the first giant circle of trial 10. So that data from the video analysis can be compared with the simulation model in subsequent chapters the sign of the horizontal displacement has been reversed so that a displacement from left to right is positive. The neutral resting position of the centre of the bar was at the three-dimensional co-ordinates (0,0.01,2.72). It can be seen that the bar moves in the range of $\pm 0.10 \text{ m}$ in the horizontal and vertical directions, as found by Brüggemann et al. (1994). In the lateral direction the movement of the bar is minimal as would be expected. The range of the lateral movement is mostly as a result of the errors due to digitisation.

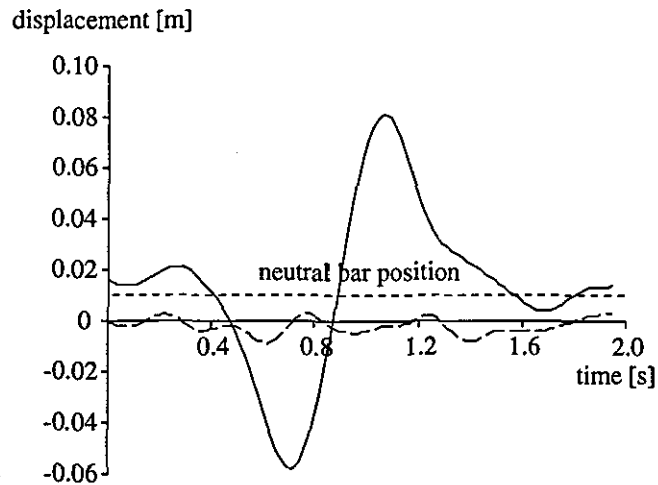


Figure 6.12. Time history of the horizontal and lateral displacement (dashed line) of the centre of the bar for the first regular giant circle of trial 10.

The range of the vertical and horizontal bar displacements for all three regular giant circles performed in trial 10 are presented in Table 6.6. The horizontal range of displacement was found to be larger than the vertical range. However, the peak absolute displacement of the bar from its neutral resting position was greater in the vertical direction. This occurs since there is a greater load on the bar in the vertical direction during regular giant circles. From Table 6.6 it can be seen that the ranges in bar displacements are very similar for each of the three giant circles performed in trial 10.

Table 6.6. The range of vertical and horizontal bar displacement during regular giant circles

circle (trial 10)	vertical displacement range (m)	horizontal displacement range (m)
first	0.091	0.143
second	0.091	0.145
third	0.095	0.150
mean	0.092	0.146

The rms difference between bar displacements of the three regular giant circles was calculated for both the horizontal and vertical directions and are presented in Table 6.7. The displacement of the bar appears to be very similar in all three regular giant circles. Since the displacement of the bar is related to the load applied to it, this may imply that the gymnast loads the bar using a similar technique for each of the three regular giant circles.

Table 6.7. Rms values for the difference in bar displacement (m) between regular giant circles from trial 10

circles compared	rms difference vertical (m)	rms difference horizontal (m)
first vs second	0.0041	0.0028
first vs third	0.0046	0.0044
second vs third	0.0025	0.0036

Figure 6.13 shows the horizontal and vertical displacements of the bar against rotation angle. The height of the bar has been subtracted from the vertical bar displacement so that it would fit on the same axes as the horizontal displacement. The peak vertical displacement occurred at a rotation angle of 175° when the gymnast is almost at the lowest point of the circle. The peak horizontal displacements occurred at rotation angles of 121° and 227° .

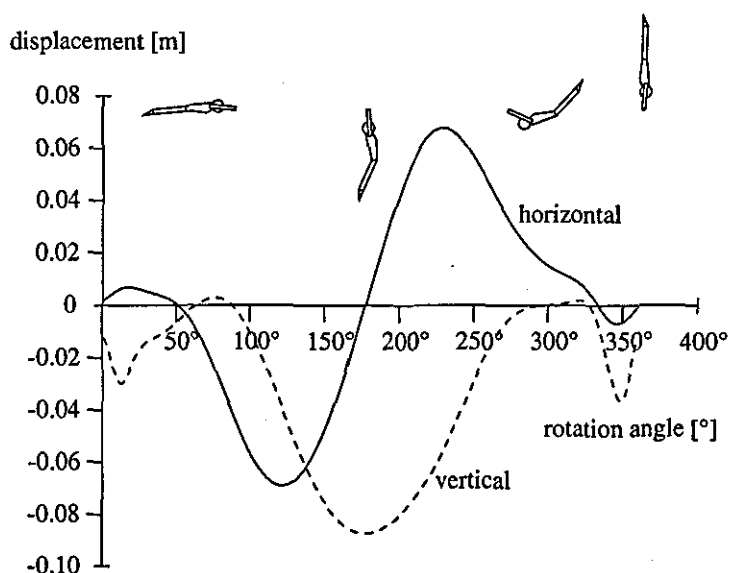


Figure 6.13. History of the horizontal and vertical displacement of the centre of the bar plotted against rotation angle for the second regular giant circle from trial 10.

Joint angle time histories

Throughout the simulation the tilt angle was minimal (less than $\pm 6^\circ$) and the twist angle was negligible (the largest twist angle was 7°). It may therefore be concluded that all major actions occurred in the sagittal plane. Hence the assumption made by using a two-dimensional model to simulate swinging movements is justified. The time history of the hip and shoulder angles for one regular giant circle are plotted against rotation angle

in Figures 6.14 and 6.15, respectively. These figures contain the raw data calculated from the reconstructed co-ordinate data which have not been splined. Pseudo joint angles for the hips, shoulders and knees were created by averaging the angles on both sides of the movement field in question. An error estimate for the joint angles was calculated by obtaining the standard deviation between the actual joint angle time histories and the pseudo joint angle time histories. The error estimates for the hip, shoulder, and knee angles as calculated by the film program were 0.8° , 2.0° and 1.3° respectively. The error for the rotation angle, which was calculated in the same way was found to be 0.3° .

The hips and shoulders are defined as being fully extended at an angle of 180° . For simplicity closing the shoulder angle is termed shoulder flexion and opening the shoulder angle is termed shoulder extension. Hyper-extension at the hips and shoulders therefore results in a joint angle less than 180° . Whereas, flexion at the hips and shoulders results in a joint angle greater than 180° .

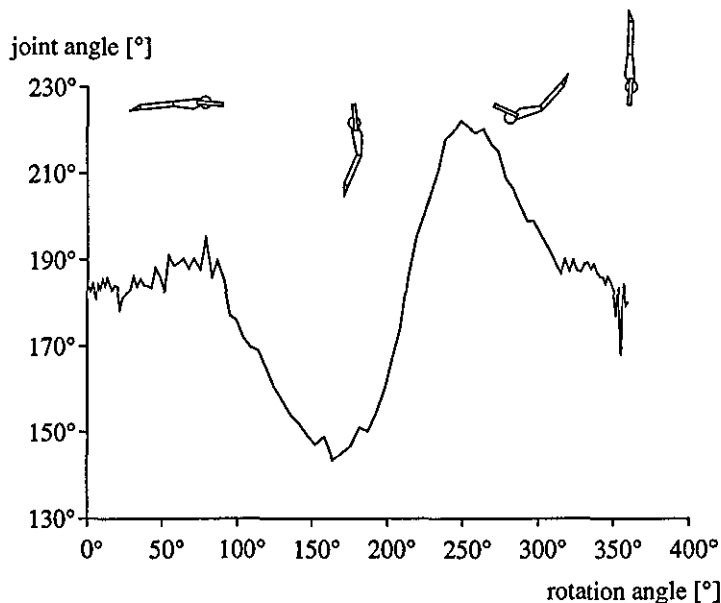


Figure 6.14. History of the hip angle against rotation angle for the third regular giant circle of trial 10.

During the first quadrant of the giant circle the hips are initially extended (Figure 6.14). On entering the second quadrant the hip joint starts to hyper-extend. At a rotation angle of approximately 160° a hyper-extension of 35° is achieved. As the subject nears the end of the second quadrant the hyper-extension of the hips is completed. The following flexion action is performed through the third quadrant, where the majority of the action occurs. The maximum flexion angle is approximately 40° for this giant circle (i.e. an angle of 220° at the hips). Before the end of the third quadrant is reached the hip angle starts to open as the gymnast extends. The extension is completed by the time the subject has reached a rotation angle of 360° . These actions are consistent with the

findings in the literature (Borms et al., 1975; Boone, 1977; Brüggemann et al., 1994; Cheetham, 1985; Okamoto et al., 1987). The joint angle time history of the shoulders is different to that of the hips (Figure 6.15). During the downswing the angle at the shoulder remained fixed. That is, no hyper-extension is performed in the first or second quadrants. This was also found by Okamoto et al. (1987). Once the subject had passed through the lowest point of the giant circle the shoulder angle was closed. This occurred entirely within the third quadrant. At the end of the third quadrant the shoulder angle had closed by approximately 40° . On entering the fourth quadrant the shoulder angle was opened, reaching full extension by the end of the giant circle.

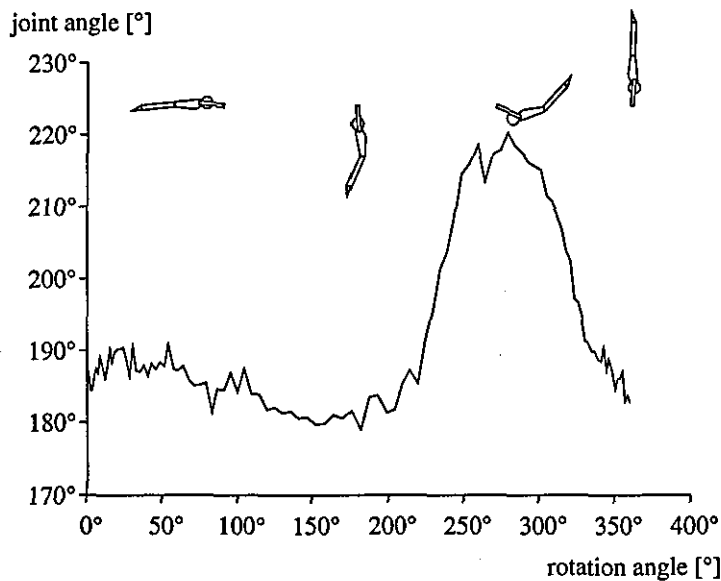


Figure 6.15. History of the shoulder angle against rotation angle for the third regular giant circle of trial 10.

Rms differences between the three regular giant circles of trial 10 were calculated for the hip and shoulder joint angle time histories (Table 6.8). The results are presented in degrees. In general the difference between the joint angle time histories of the regular giant circles was less than 10%. The rms differences for the hip and shoulder angles were small, approximately 6.7° and 3.0° respectively. The subject must therefore use the same technique when performing regular giant circles. It is possible that the rms differences would be less had the comparison been made after the joint angle time histories had been splined.

Table 6.8. Rms values for the difference in hip and shoulder joint angle time histories ($^{\circ}$) between the regular giant circles from trial 10

circles compared	rms difference hip joint ($^{\circ}$)	rms difference shoulder joint ($^{\circ}$)
first vs second	5.4 $^{\circ}$	2.4 $^{\circ}$
first vs third	9.4 $^{\circ}$	3.8 $^{\circ}$
second vs third	5.1 $^{\circ}$	2.8 $^{\circ}$

Accelerated giant circles

The accelerated giant circles under investigation comprise a wind up giant circle and a three quarter giant circle after which the gymnast would have released the bar for the dismount. The release would have occurred occur after approximately 622 $^{\circ}$ of rotation (Brüggemann et al., 1994). As the circle containing the release is dependent on the wind up giant circle both phases will be considered together.

Path and velocity of the mass centre

The path of the mass centre during an accelerated giant circle (Figure 6.16) is similar to that of the regular backward giant circle (Figure 6.5). On the downswing the subject is extended causing the mass centre to follow a what appears to be a circular path. The path of the mass centre is not completely circular during the downswing since at the start of the circle the gymnast has flexion angles at the hips and shoulders and also hyper-extends at the hips. On the upswing the subject reduced the distance between his mass centre and the axis of rotation by closing the hip and shoulder angles. However, unlike the regular giant circle the subject does not extend at the top of the circle. Instead the subject continues to reduce the distance of the mass centre from the axis of rotation. The subject does not appear to extend until he is well into the downswing of the second giant circle (Figure 6.16). Prior to release the subject reduces the distance between the mass centre and the axis of rotation. This reduction is greater than the reduction made in the previous giant circle. It must be noted that mass centre location includes the displacement of the bar from its resting position. Therefore, the increased reduction in the displacement of the mass centre from the axis of rotation seen in the giant circle containing the release may be due, in part, to the displacement of the bar as well as his body configuration.

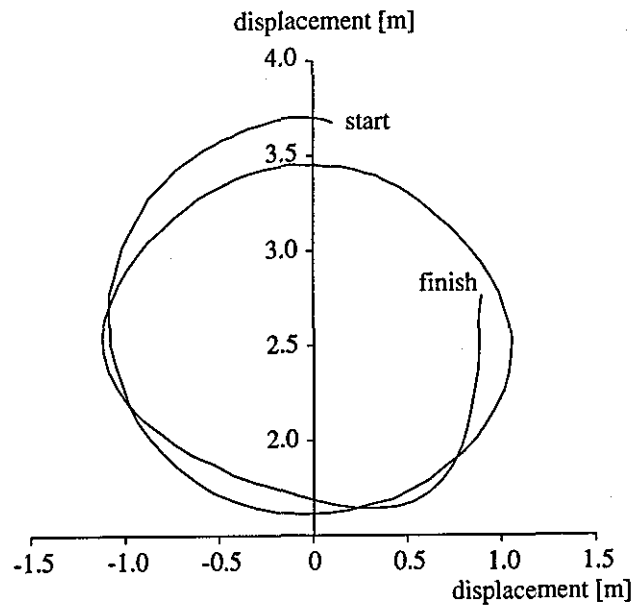


Figure 6.16. Path of the mass centre during an accelerated giant circle with release (trial 4).

The time history of the angular velocity of the rotation angle is given in Figure 6.17. The three major peaks correspond to the first and second time the subject passes through the lowest point and the point at which release would have occurred. These peak angular velocities are presented in Table 6.9. On the first giant circle the peak angular velocity occurred just before the lowest point of the circle.

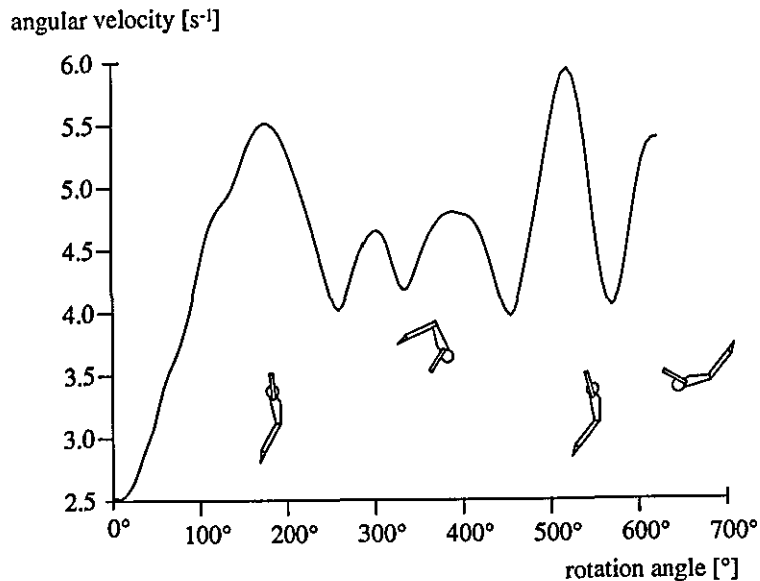


Figure 6.17. Time history of the angular velocity of the rotation angle (trial 4).

On the second giant circle the peak angular velocity occurred 20° before the lowest point. Like Cheetham (1987) the peaks in angular velocity increase with each giant circle. However, the double peak in angular velocity associated with closing the hip and shoulder angles found by Cheetham does not occur and the final angular velocity, at release, is less than the previous peak. It is possible that the gymnasts used in Cheetham's study used a different technique in the wind up giant circle prior to release. This may account for the differences in the time histories of the angular velocity. However, even though different techniques were used the peak angular velocities are comparable.

Table 6.9. Peak angular velocities for accelerated giant circles

trial	peak angular velocity (rad.s ⁻¹)	rotation angle at peak (°)
4	5.5	175.9°
	5.9	519.2°
	5.4	621.9°
11	5.4	177.3°
	6.0	520.0°
	5.6	623.7°

Bar displacements

The horizontal and vertical displacements of the centre of the bar during the wind up and release in trial 4 are given in Figures 6.18 and 6.19 respectively. The range of the vertical and horizontal displacements for trials 4 and 11 are given in Table 6.10. The ranges in displacement for the accelerated giant circles are larger when compared with the results obtained from the regular giant circles. Unlike the regular giant circles the peak absolute displacements about the bar's neutral resting position are equal in both the vertical and horizontal directions. Since the displacement of the bar was larger for the accelerated giant circles the load on the bar must also have been greater, when compared with the regular giant circles.

Table 6.10. The range in vertical and horizontal bar displacements during the accelerated giant circles

trial	vertical displacement range (m)	horizontal displacement range (m)
4	0.125	0.200
11	0.129	0.206
mean	0.127	0.203

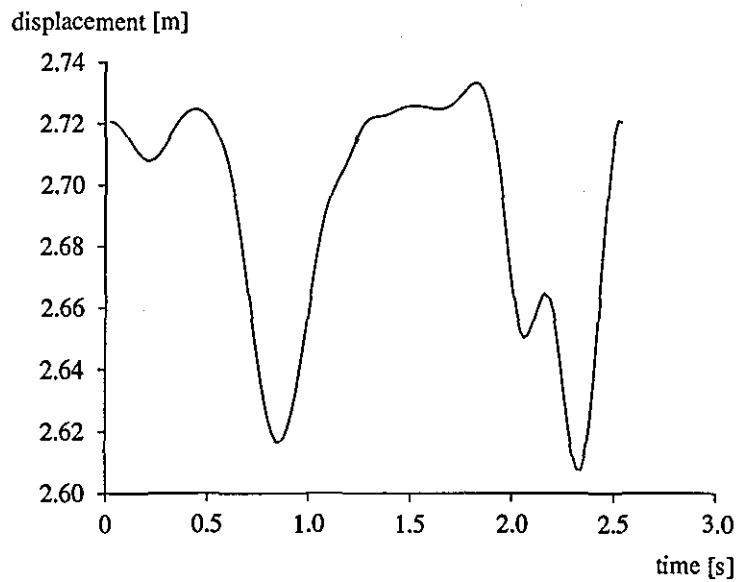


Figure 6.18. Time history of the vertical displacement of the centre of the bar during trial 4.

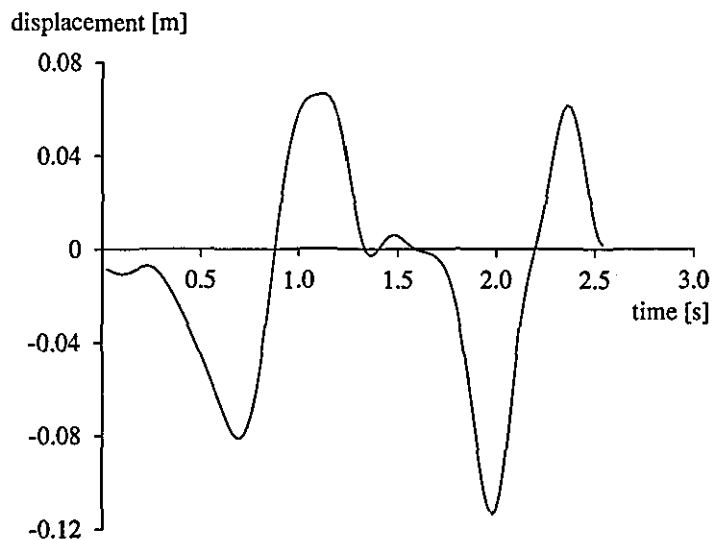


Figure 6.19. Time history of the horizontal displacement of the centre of the bar during trial 4.

The rms difference in the horizontal and vertical bar displacements between trial 4 and 11 are presented in Table 6.11. The rms differences for the two accelerated giant circle trials, like the regular giant circles, are small. It might therefore be assumed that the subject used a similar technique to load the bar in each trial. Note also that there is a double peak in vertical bar displacement during the release giant circle not seen in the regular giant circle trials (Figure 6.18).

Table 6.11. Rms values for the difference in bar displacement between the accelerated giant circle trials

trials compared	rms difference vertical (m)	rms difference horizontal (m)
4 vs 11	0.004	0.004

Figure 6.20 shows the horizontal and vertical displacements of the bar plotted against rotation angle. The neutral resting height of the bar has been subtracted from the vertical bar displacement so that it would fit on the same axes as the horizontal displacement. The first peak in vertical displacement occurs at a rotation angle of 173° , when the gymnast is almost at the lowest point of the circle. The second peak in vertical displacement was at a rotation angle of 569° . This corresponds to 30° past the lowest point of the giant circle. The small peak prior to this, as described earlier, occurred at a rotation angle of approximately 500° . The first two peaks in horizontal displacements occurred at rotation angles of 126° and 250° . Both of these angles correspond to the gymnast being in the lower half of the giant circle. The second two peaks occurred at 467° and 578° . The first of these two peaks occurs some 20° earlier than the same peak for the first giant circle. Similarly the second peak of the second giant occurred 30° earlier than in the previous giant circle. It appears that the technique the gymnast uses as he passes through the highest point alters the way that the bar is displaced during the release giant circle. The displacements are different both in terms of magnitude and timing. It is speculated that there may be a mechanical benefit from altering the loading of the bar when performing accelerated backward giant circles.

When comparing the displacements of the bar at 262° and 622° for the two accelerated trials the most striking thing is that at the release angle of 622° the vertical bar displacement was zero, compared with 0.02 m at the rotation angle of 262° . Similarly for the horizontal displacements, at 622° the bar had a positive horizontal displacement of less than 0.02 m compared with 0.08 m at a rotation angle of 262° . Figure 6.21 shows the horizontal and vertical velocities of the bar leading up to the point of release in trial 4. The velocities of the bar were obtained from evaluating the first derivative of a quintic spline which was fitted to the bar displacement data. At release the vertical bar velocity was very close to zero. That is, in the vertical direction, at or very close to release, the bar was stationary. This may have implications for the angular momentum the subject possessed at release. Clearly, if the hands were stationary at release the angular momentum about the subject's mass centre would be greater than if the bar were displaced vertically downwards with a positive vertical velocity. This idea will be explored further later in the thesis.

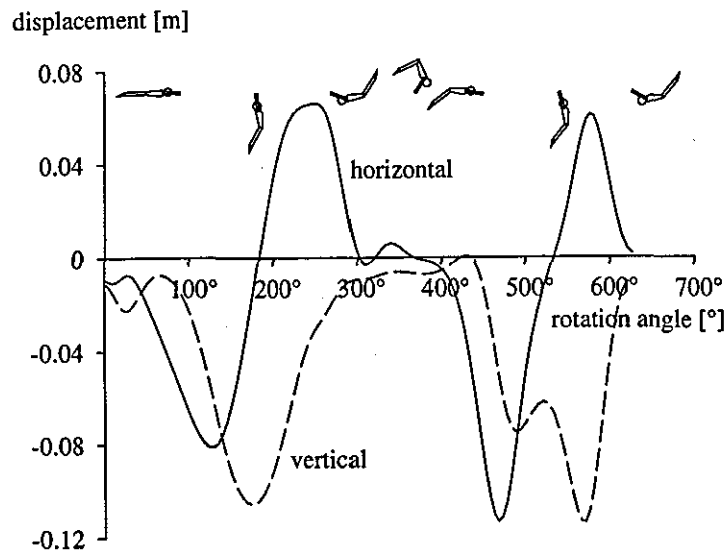


Figure 6.20. Histories of the horizontal and the vertical displacements of the bar (trial 4).

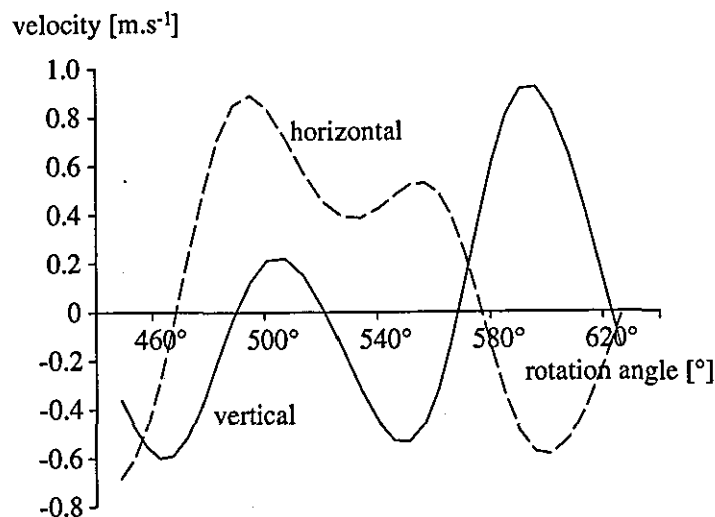


Figure 6.21. Histories of the horizontal and the vertical velocity of the bar (trial 4).

Joint angle time histories

The histories of the hip and shoulder angles for trial 4 are shown against rotation angle in Figures 6.22 and 6.23. Both figures show the joint angle histories for $1\frac{3}{4}$ giant circles.

At the start of the first quadrant of the circle the hip angle is fully extended (i.e. 180°). As with the regular giant circle this angle is maintained throughout the first quadrant. On entering the second quadrant the hips start to hyper-extend. This hyper-extension continues into the third quadrant reaching a maximum angle of between 35° and 40° . After passing a rotation angle of 200° the hips begin to flex. Remember, for the regular giant circles the flexion at the hips started before the subject had reached the

lowest point of the giant circle. The flexion action does not finish until the end of the fourth quadrant. On passing through the highest point the gymnast has a hip flexion angle of approximately 90° . At the same point during a regular giant circle the gymnast has already extended the hip and shoulder angles ready for the next circle. The extension of the hips is performed through the first and second quadrants of the circle containing the release. The hip angle passes through full extension during the second quadrant and continues to open until a hyper-extension angle of approximately 50° is achieved (Figure 6.22). This occurs before the end of the second quadrant. Upon reaching the maximum hyper-extension the hip angle is closed. Figure 6.20 shows the vertical bar displacement against rotation angle. The first smaller peak in vertical bar displacement occurs at the same instant that the hip stops hyper-extending and starts to flex. The flexion is initiated in the second quadrant and continues through and past the point of release, in the third quadrant.

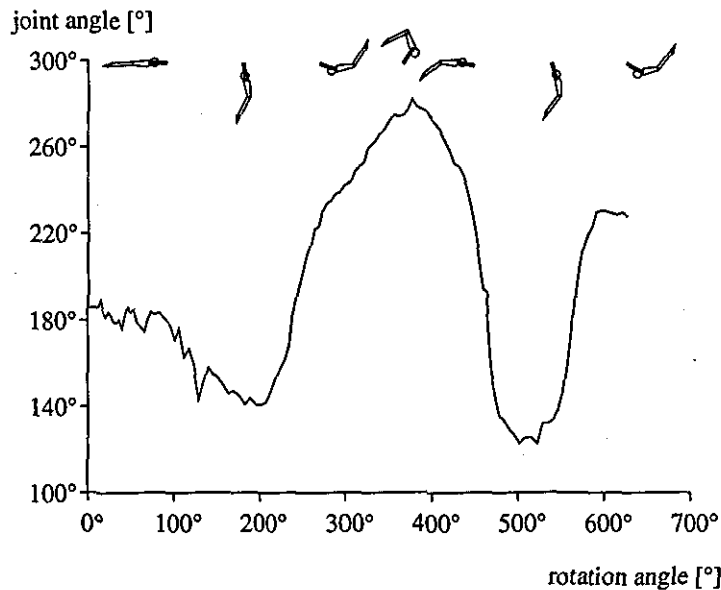


Figure 6.22. History of the hip angle against rotation angle from trial 4.

The joint angle time history of the shoulder (Figure 6.23) follows a similar phasing to that of the hip angle. This is in contrast to the joint angle time histories of the regular giant circles. However, the shoulder time history shows no hyper-extension in the first two quadrants. The maximum flexion angle of the shoulders is less than that of the hips, reaching a flexion angle of approximately 55° , compared with 90° for the hips. Similarly during the second downswing, leading to the release, the shoulder hyper-extension is less than that of the hips.

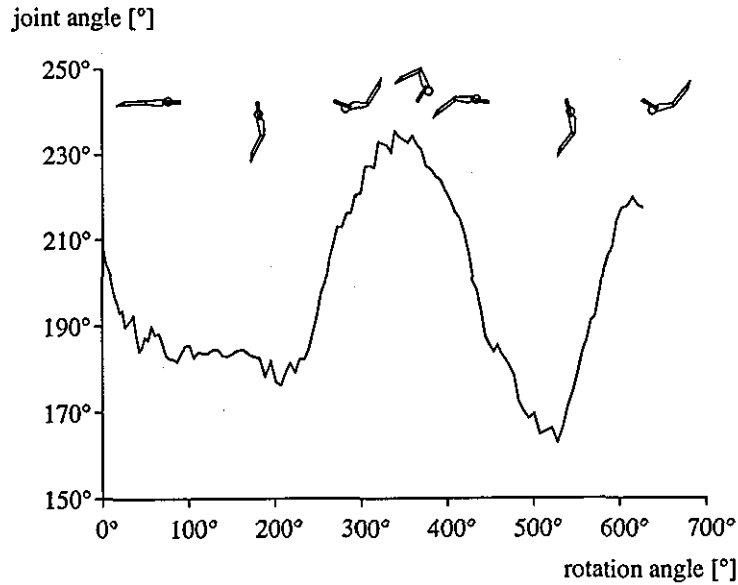


Figure 6.23. History of the shoulder angle against rotation angle from trial 4.

The joint angle time history of the knees is shown in Figure 6.24. Unlike the regular giant circle there is a definite flexion and extension action occurring during the second quarter of each phase of the giant circle. This must be a useful part of the gymnast's technique since the flexion angle is in excess of 35° and would therefore be clearly noticeable. Knee flexion and extension was also found during accelerated giant circles prior to release skills by Brüggemann et al. (1994). Note also that the maximum knee flexion occurred at the same rotation angle as the small peak in vertical bar displacement seen in Figure 6.18.

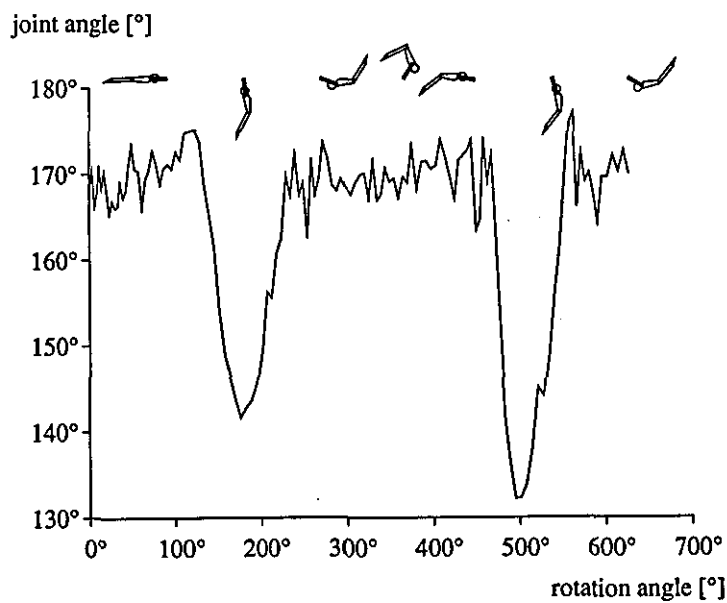


Figure 6.24. History of the knee angle against rotation angle from trial 4.

Rms differences were calculated for the joint angle time histories obtained from trial 4 and 11. The results are presented in Table 6.12. The rms differences are small ($< 5^\circ$) which implies that the subject used a similar technique each time he performed giant circles prior to the release for a double layout backward somersault dismount.

Table 6.12. Rms values for the difference in hip and shoulder joint angle time histories ($^\circ$) between accelerated giant circles from trials 4 and 11

trials compared	rms difference hip joint ($^\circ$)	rms difference shoulder joint ($^\circ$)	rms difference knee joint ($^\circ$)
4 vs 11	4.1 $^\circ$	5.0 $^\circ$	2.4 $^\circ$

Splined joint angle time histories

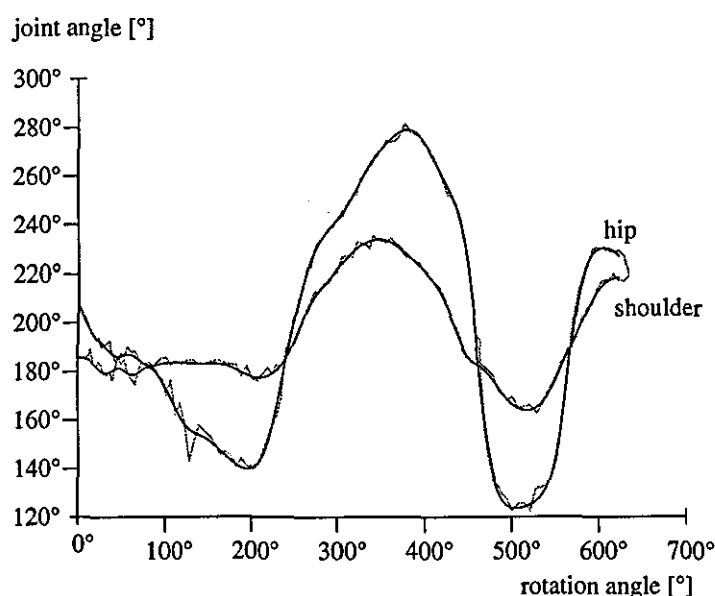


Figure 6.25. Splined and raw hip and shoulder angles from trial 4.

In order to evaluate the four segment simulation model the joint angle time histories of the hips, shoulders and knees are required. In addition the first and second derivatives of these joint angle time histories are required. All joint angle data were obtained using quintic splines as outlined in Chapter 5. Figure 6.25 shows the splined joint angle time histories of the hip and shoulder laid on top of the raw data for the accelerated giant circles from trial 4. The velocity and acceleration of the joint angles were evaluated using the Jennings spline fitting library (1979). The angular velocities of the hip and shoulder angles are graphed against rotation angle in Figure 6.26. These data are smooth as would be expected from the first derivative of a quintic spline. The shoulder joint angular velocity ranges from $-233^\circ.s^{-1}$ to $215^\circ.s^{-1}$. These angular velocities lie within the range of

angular velocities used when collecting the isokinetic muscle data. The range of the hip angular velocities determined from the spline data are greater than those obtained from the shoulder. The hip angular velocities range from $-784^{\circ} \cdot s^{-1}$ to $694^{\circ} \cdot s^{-1}$. At the limit of the hip joint angular velocity the velocity of the isokinetic data are exceeded by more than 275%. During these regions extrapolation will be required to obtain maximum joint torques from the 18 parameter torque data.

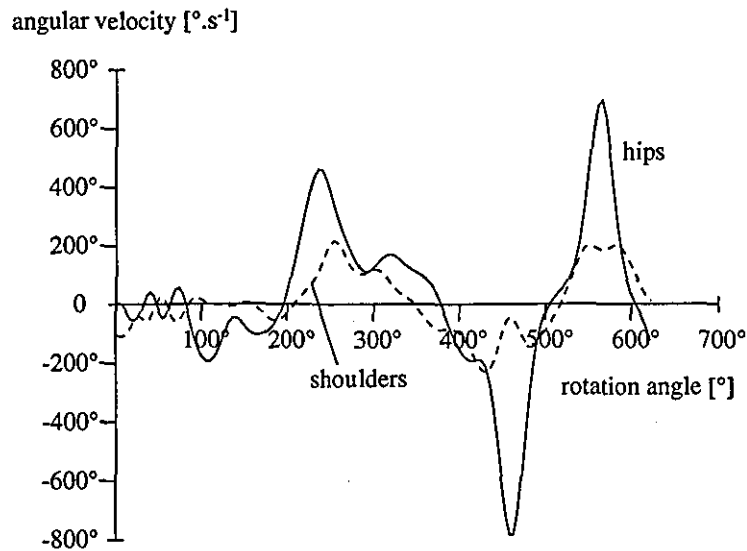


Figure 6.26. Angular velocities obtained from the evaluation of the splined joint angle histories of the hips and shoulders from trial 4.

The angular accelerations of the hip and shoulder are presented in Figure 6.27. Again the acceleration curves are smooth, and do not tend to infinity at the end points. The accelerations of the hip joint angle are greater than those obtained from the shoulder joint. Since the hip angle, during the accelerated giant circle, goes through a larger range than the shoulder angle during a similar time interval it would be expected that this would be the case. The greater acceleration suggests a greater torque is produced by the musculature surrounding the hip joint. This hypothesis will be examined in Chapter 7, the evaluation of the four segment simulation model.

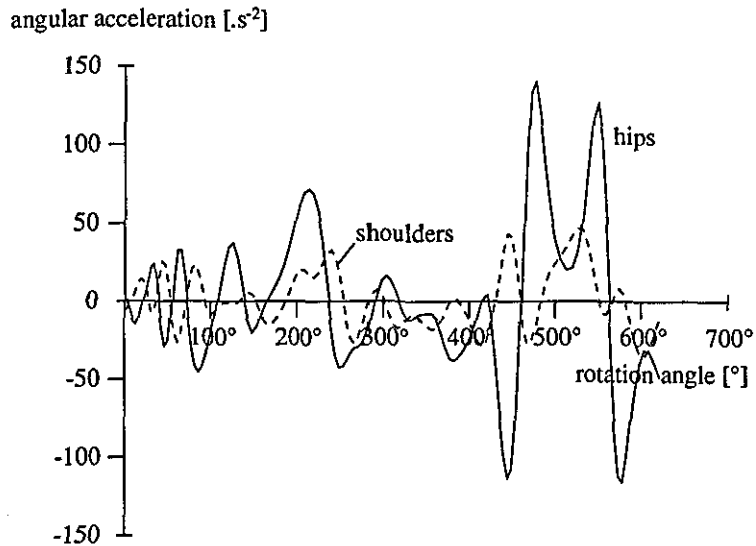


Figure 6.27. Angular accelerations obtained from the evaluation of the splined joint angle histories of the hips and shoulders from trial 4.

Segment lengths calculated from the reconstructed co-ordinates

The mean lengths of the limbs calculated from each field of trial 10 are presented with standard deviations in Table 6.13. The values of the left and right side of the body have been averaged. The calculated segment lengths of the legs compare well with the anthropometric measurements, yet the calculated arm and torso segment lengths appears to be considerably larger than the anthropometric measurements. The length of the gymnast from wrist to ankle has been calculated from both the anthropometric and video based measurements (Table 6.13). As well as the lengths of the arms and torso the wrist to ankle length of the gymnast obtained from the video analysis appears to be greater than the same value calculated from the anthropometric measurements. The difference is over 0.2 m. This difference may be in part due to the difficulty in locating the shoulder joint centre during digitisation. If the arm segment were calculated to be longer due to an error in digitising the shoulder joint centre one would expect the torso segment to be shorter due to the same error in locating the shoulder. Yet the mean values for the arm and torso segments are both larger than the anthropometric measurements. This is because when the arms are raised from the gymnast's sides to a position above the head, similar to the position adopted during swinging, the shoulder girdle experiences both elevation and upward rotation (Thompson, 1989).

Table 6.13. Segment lengths calculated from trial 10 (regular giant circles)

segment	anthropometric length (m)	mean digitised length (m)	range (m)
arms	0.477	0.537 ± 0.023	0.09
torso	0.435	0.621 ± 0.021	0.10
arm+torso	0.912	1.158 ± 0.036	0.15
thigh	0.374	0.360 ± 0.019	0.09
shank	0.403	0.409 ± 0.013	0.07
legs	0.776	0.773 ± 0.017	0.08
arm+torso +legs	1.688	1.931 ± 0.029	0.12

The time history of the arm segment and the torso segment lengths are presented in Figures 6.28 and 6.29, respectively. The minimum length of the arm segment appears to be 0.51 m (Figure 6.28), approximately 0.03 m longer than the anthropometric measurement. Similarly the minimum length of the torso segment appears to be 0.60 m (Figure 6.29). That is, the torso segment appears to be 0.165 m longer than it should be. This may be accounted for by the elevation and upward rotation that occurs in the shoulder girdle when the arms are elevated from the sides to above the subject's head. The length of the torso (Table 6.13) was based on the anthropometric measurement from the hip to the shoulder with the subject's arms by his sides. The length of the arm was taken from the same shoulder point to the wrist. When these two lengths are summed, to represent the distance from wrist to hip with arms above the head, no consideration is made for the elevation that occurs in the shoulder girdle.

To account for the elevation of the shoulder girdle the length of the torso segment will be increased from 0.44 m to 0.60 m. Similarly the length of the arm segment will be increased from 0.55 m to 0.58 m. Note that the length of the arm segment includes both the length of the arm from wrist to shoulder and the length of the hand from wrist to the centre of the bar. The length of the arm has therefore been increased by only 0.03 m. The increase in segment length alters the location of the segment mass centre relative to joint centre. The new segment lengths and mass centre locations for subject jb01 are given in Table 6.14. The second set of inertia values for the arm segment are those obtained when a mass of 5 kg, representing the bar is placed at the hands. It is the second set of arm inertia parameters that will be used in the four segment simulation model in Chapters 7 and 8.

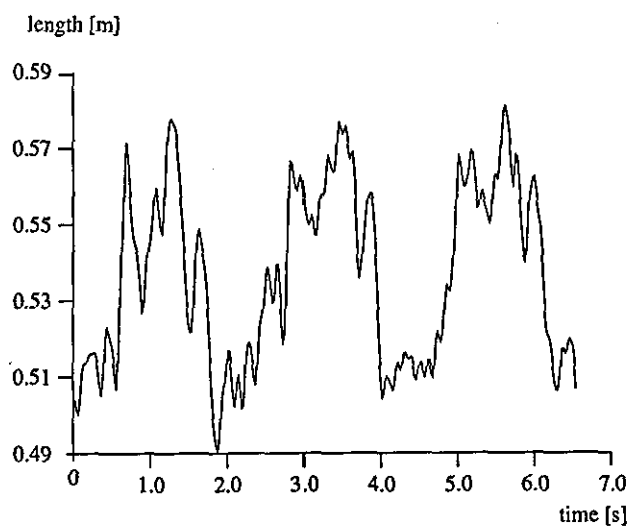


Figure 6.28. Arm length during trial 10.

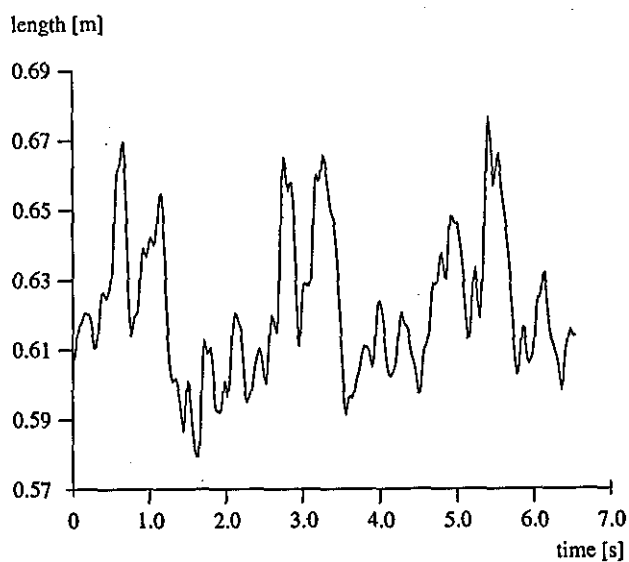


Figure 6.29. Torso length during trial 10.

Table 6.14. New inertia parameters for subject jb01

segment	mass (kg)	length (m)	cmloc (m)	moment of inertia (kg.m ²)
arms	6.868	0.548	0.239	0.205
arms + bar	11.868	0.582	0.403	0.481
torso	33.566	0.601	0.337	1.610
thigh	14.074	0.374	0.151	0.173
leg	7.543	NA	0.227	0.164

The fourth column of Table 6.13 contains the range of segment lengths. The largest range for a single segment belongs to the torso followed by the arms. When the length of the arms is added to the length of the torso the combined range is larger than the two individual ranges. Compare this to when the length of the thigh segment is added to the length of the shank segment. Both leg segments have similar ranges, approximately 0.08 m. When added together their combined range is also 0.08 m. This suggests that the change in length of the leg segments is random and due to errors in locating the joint centres of the hip, knee and ankle. For the torso and arm segments, however, the increase in combined range suggests that they are either lengthening and/or shortening at the same time.+

The time history of the wrist to ankle length obtained from the video analysis is shown in Figure 6.30. It appears that the subject's wrist to ankle length increases as he passes through the lower part of the giant circle. The increase in length is of the order of 0.10 m. The time history of the subject's length and the length from wrist to hip (i.e. length of arm plus torso segments) during one regular giant circle (from trial 10) is shown in Figure 6.31. The wrist to hip length also displays an increase in length through the lower part of the giant circle. The size of this increase is also in the region of 0.10 m. In the same figure (Figure 6.31) the time history of the subject's length has been overlaid. The increase in wrist to shoulder length follows reasonably closely the increase in wrist to ankle length.

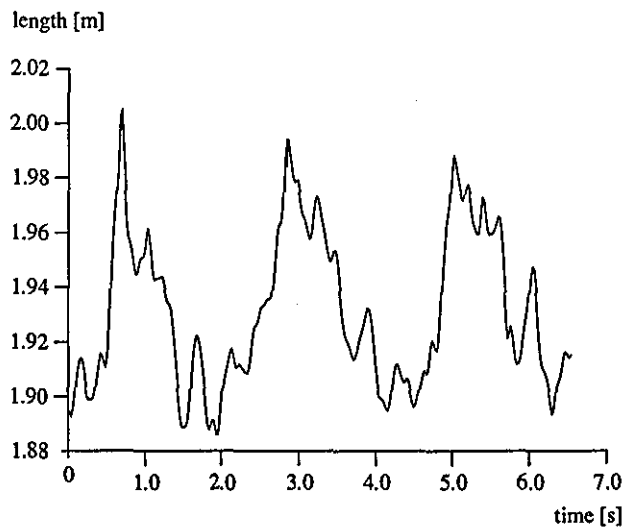


Figure 6.30. Sum of the arm, torso and leg segment lengths during trial 10.

Similar analyses were performed with the data from an accelerated giant circle. Again, the wrist to hip length increased as the subject passed through the lower part of the circle, and again the time history of the wrist to hip length closely followed that of the wrist to ankle time history. The wrist to hip and the wrist to ankle length both showed a

range of up to 0.14 m. Through the highest part of the giant circle these lengths were at their shortest, whilst through the lower parts of the circle they were at their longest.

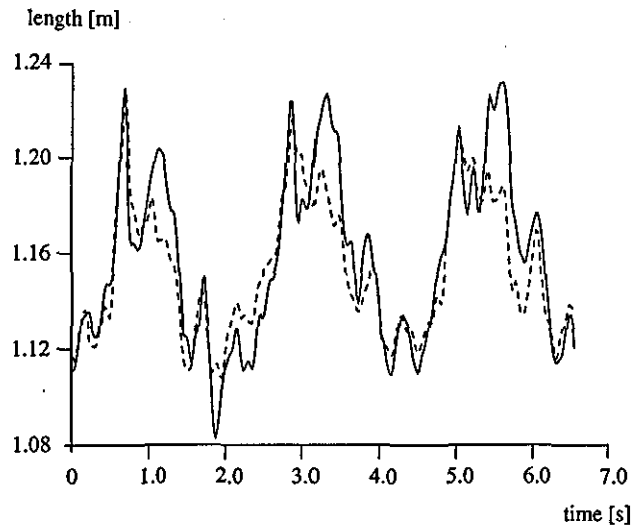


Figure 6.31. Sum of the arm and torso segment lengths during trial 10 (dashed line is the sum of the arm, torso and leg lengths overlaid).

The majority of the lengthening and shortening of the gymnast appears to occur in the region from the wrists to the hips. It is possible that the lengthening occurs due to the elastic properties/structures of the joints within that region. Since the increases in length occur with increasing reaction force at the bar (Kopp and Reid, 1980), it is suggested that the joints at the elbow, shoulder and spine act as springs which are able to extend and recoil under the fluctuating load.

6.3.5 Summary

The path of the mass centre and the angular velocity of the rotation angle for both regular and accelerated giant circles compared well with similar results in the literature (Cheetham, 1984). It was shown that in general the gymnast attempts to keep his mass centre away from the axis of rotation during the downswing. On the upswing the gymnast reduced this distance, by changing body shape so as to reduce the effect of the torque created by his weight. The peak angular velocity for the accelerated giant circles was greater than the peak value for the regular giant circles, and approached $6.0 \text{ rad}\cdot\text{s}^{-1}$. Cheetham (1984) obtained peak angular velocities of between $5.6 \text{ rad}\cdot\text{s}^{-1}$ and $6.3 \text{ rad}\cdot\text{s}^{-1}$ for accelerated giant circles.

The displacements of the bar for the regular giant circles were in the region of $\pm 0.10 \text{ m}$ in both the horizontal and vertical directions. This agreed with previous data

presented in the literature (Brüggemann et al., 1994). The bar displacements for the accelerated giant circles were greater than those for the regular giant circles. When the bar displacements were compared between trials/circles they were found to be very similar. That is, when the bar displacements for two regular giant or two accelerated circles were compared the differences between them were small.

The major joint actions performed during the regular giant circle occurred at the hips and the shoulders, with a small contribution from the knees. The timing of the joint actions at the hips and the shoulders for the regular giant circles confirmed the findings in the literature (Cheetham, 1984; Brüggemann et al., 1994; Okamoto et al., 1987). The size of the flexion angles at the hips and shoulders were larger for the accelerated giant circles compared with the regular giant circles. It was also found that the timing of the flexion and extension actions were slightly different for the accelerated giant circles. The flexion at the hips started later and lasted longer (in terms of body angle rotated through). Similarly the extension at the hips started later and finished later. It is speculated that this altered action may be used to affect the loading of the bar which results in increased angular momentum at release.

It was found that during giant circles the gymnast increases in length between 0.05 and 0.14 m. The majority of this increase occurred between the wrists and the hips. It is suggested that the increase is a result of extensions in the shoulder and spine structures of the gymnast. Since the increase in gymnast length occurred through the lower part of the giant circle it is speculated that part of this extension is as a result of the elastic properties of the shoulders and spine. In addition it was found that the length of the gymnast's torso was greater when the arms were elevated than when they were by his sides. This is due to the elevation in the shoulder girdle and therefore the length of the torso segment used in the four segment simulation model will be 0.60 m instead of 0.435 m .

Fitting splines to the joint angle time histories removed excess noise from the raw joint angle data. Evaluation of the spline coefficients using Jennings spline fitting library (1979) revealed smooth first and second derivatives of the joint angle data. These data will be used in the evaluation chapter (Chapter 7) to drive the four segment simulation model. Spline coefficients were also obtained for the bar displacements and angle of rotation. These too will be used in the four segment simulation model.

6.4 Kinetic analysis of the giant circle

6.4.1 Introduction

The following results were obtained from the methods described in Chapter 5. The section covers the results obtained from calibrating the high bar and converting the strain data recorded whilst the subject performed regular and accelerated giant circles into force.

6.4.2 Calibration of the force measurement system

The load cell

The error in the load applied to the load cell by the Instron hydraulic testing machine was ± 5 N. Over the range of zero to 3.0 kN this would result in an average error of less than one third of a percent. The strain recordings from the strain gauge amplifier were plotted against the load applied by the Instron testing machine (Figure 6.32). It can be seen that when the data points are connected they do not fall on a straight line. The difference between the readings on the amplifier correspond to the increase in microstrain when the load is increased by 0.5 kN. For perfect linearity it would be expected that the increase in microstrain would be proportional to the increase in load. The non-linearity was a result of the resolution of the recordings taken from the strain gauge amplifier. The amplifier readings were made to the nearest whole number (i.e. no decimal places were recorded). Therefore the resolution of the amplifier was half a microstrain.

Since the amplifier reading was used when calibrating the high bar, the resolution would lead to errors in the exact load applied to the bar. The bar was loaded using the cable tensioners. It was assumed that the load applied to the bar corresponded to the load applied to the load cell. This load was determined from the amplifier reading and the load cell calibration data. It was calculated that the maximum error in the load applied to the bar, due to the resolution of the strain gauge amplifier readings was ± 21 N. Over the range of 0 to 3.0 kN this results in a "most probable" fractional error of 0.53%, or an average error of 1.36% (Topping, 1962).

Cross talk

Figure 6.33 shows the vertical strain plotted against the load applied to the bar in the vertical direction (circles joined by solid lines). On the same graph the horizontal strain, recorded simultaneously, is plotted against the load applied in the vertical direction (squares joined by dashed lines). The horizontal and vertical strain data appear to be

reasonably linear in nature. The horizontal strain is minimal, approximately 1% of the strain recorded in the vertical direction. Observation of the strain data recorded with zero load applied to the bar revealed that there was a horizontal and vertical offset in the data recorded. The channels on the amplifier were "zeroed" before the bar was loaded. However, when the strain was recorded with zero load applied to the bar a strain equivalent to approximately 30 N was obtained in the horizontal direction and a strain equivalent to 3 N was recorded in the vertical direction. To correct for this error the appropriate amount of strain was subtracted from all data points and subsequently all strain recordings during the giant circle activities. The data used in Figure 6.33 has been corrected for the horizontal and vertical offsets and is plotted in Figure 6.34. Having corrected for the offset the cross talk was found to be minimal. This was also found to be true by Kopp and Reid (1980) and Witten et al. (1996).

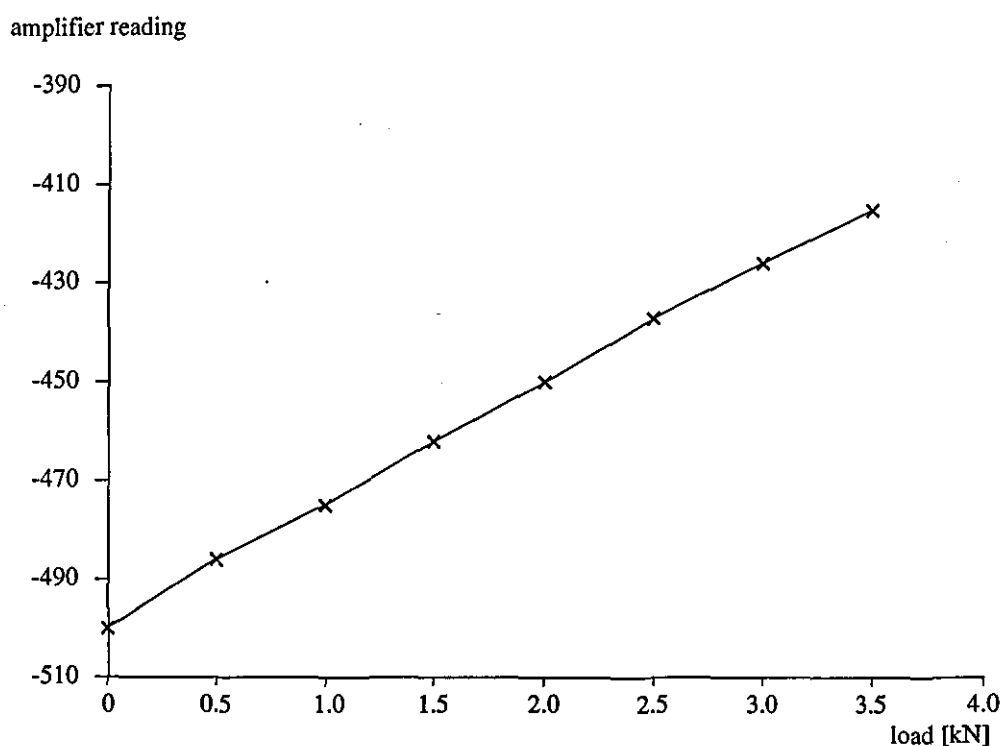


Figure 6.32. Data points obtained during the calibration of the load cell.

Regression/Calibration equations

The ADC (analogue to digital converter) counts recorded from the strain gauges attached to the bar were regressed against the load applied to the bar. The results of the linear regressions are presented in Table 6.15. In Table 6.15 the coefficient of the regression line is given along with its standard error. Table 6.15 contains the data obtained from the regressions performed in the vertical direction (using one and two points of force application) and the horizontal direction. The correlation coefficient between the load applied and the recorded strain data are also presented.

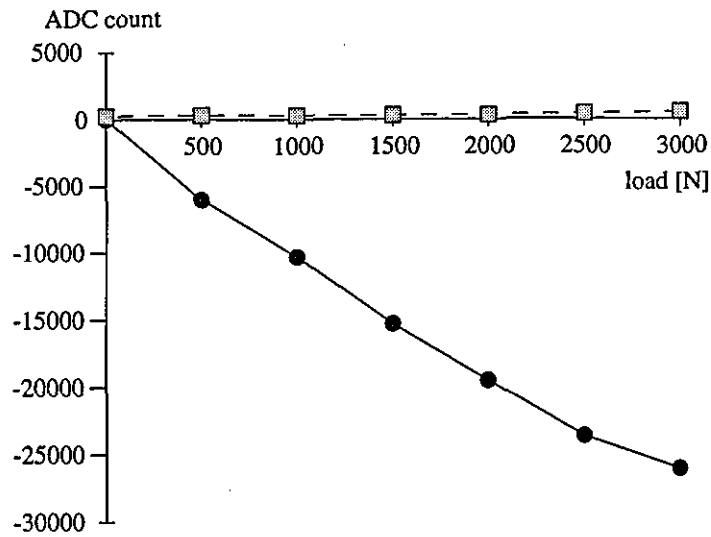


Figure 6.33. Strain recorded in the vertical direction (filled circles) plot against vertical load with strain recorded simultaneously in the horizontal direction (filled squares).

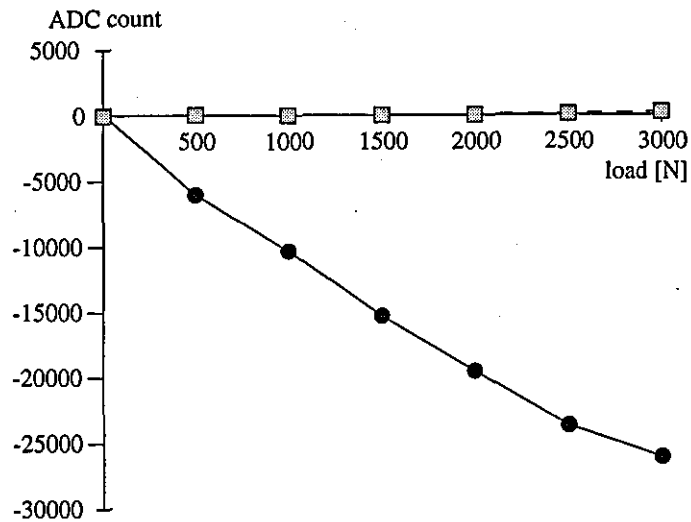


Figure 6.34. Strain recorded in the vertical direction plotted against vertical load with strain recorded simultaneously in the horizontal direction after correcting for the offset.

Table 6.15. Results of linear regressions forced through the origin

direction of load	correlation coefficient	gradient
vertical	0.997	-9.30 ± 0.11
vertical (at 2 points)	0.997	-9.82 ± 0.18
horizontal	0.997	10.00 ± 0.12

The linear regressions between the recorded strain and the load applied to the bar are displayed in Figures 6.35, 6.36 and 6.37. In these Figures it can be seen that the loads applied to the bar follow the same pattern as those seen in the calibration curve of the load cell (Figure 6.32). In Figure 6.35 (vertical load) it could be suggested that the bar is becoming stiffer as the load increases. However, if the loadings continued to follow the pattern of the load cell calibration curve this would not be the case.

If the first loading and unloading of the bar in the vertical direction were plotted (Figure 6.35) then it can be seen that the recordings from the strain gauges are different for loading and unloading. That is, the regression line drawn through the points obtained for loading would be different from the regression line obtained from the unloading. This may be as a result of a hysteresis effect. However, by performing the regression through all points the best average result is obtained. During an accelerated giant circle followed by a dismount the bar is likely to be loaded to over 3.0 kN and then unloaded. This loading and unloading will occur twice, once for the wind up giant circle and once for the giant circle containing the release. A regression which takes into account both the loading and the unloading of the bar would therefore be more appropriate.

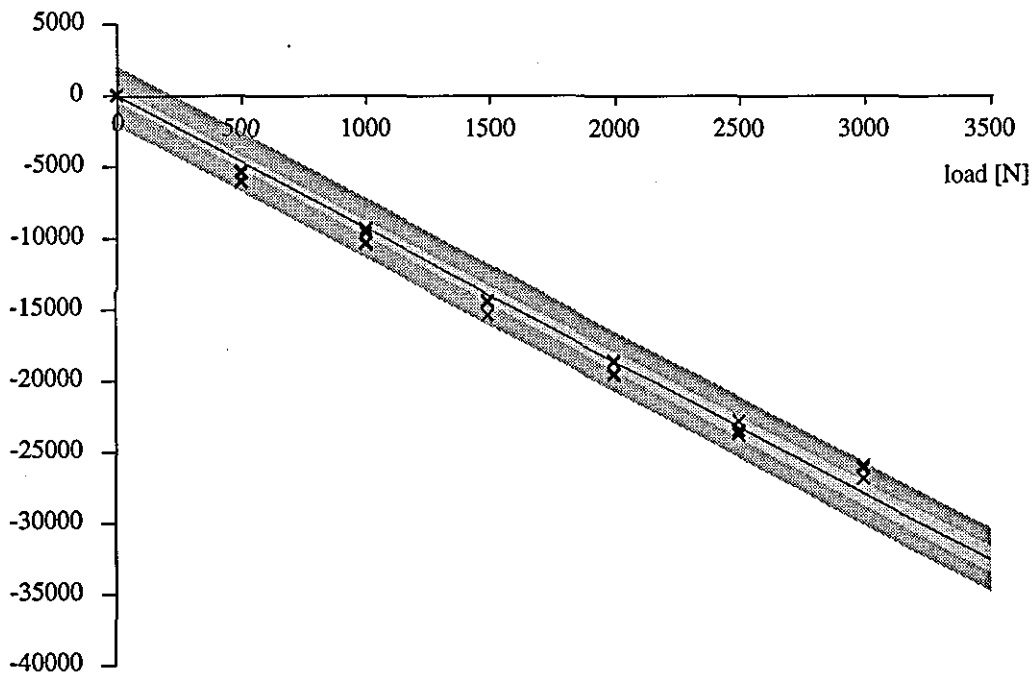


Figure 6.35. Linear regression between the load applied to the bar and the strain recorded in the vertical direction.

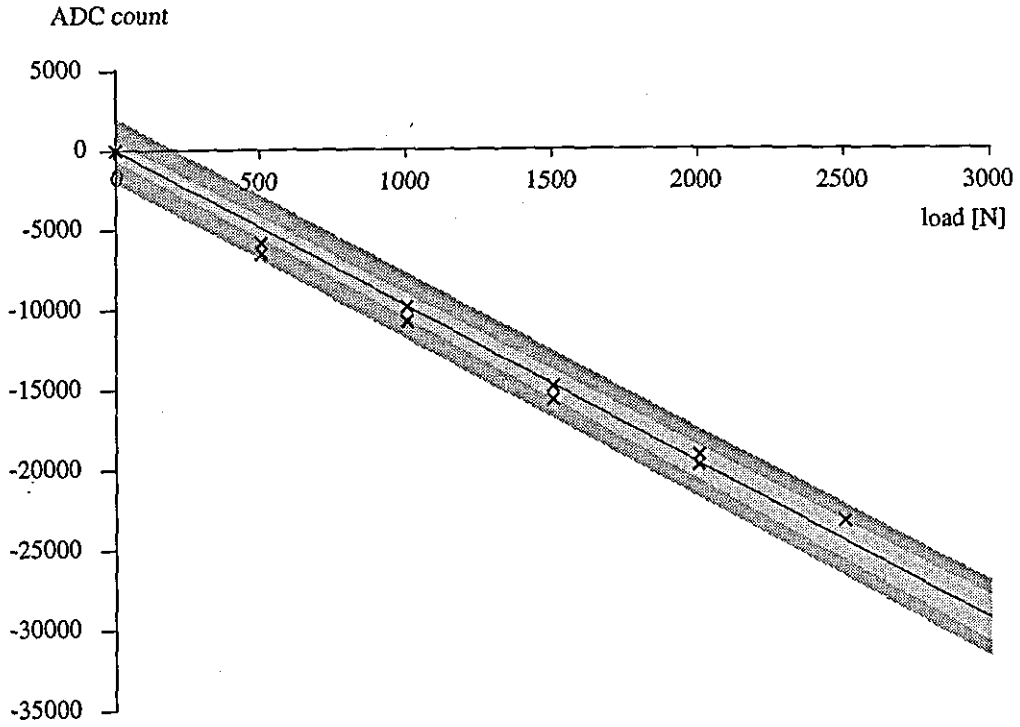


Figure 6.36. Linear regression between the load applied to the bar and the strain recorded in the vertical direction when loading at two points.

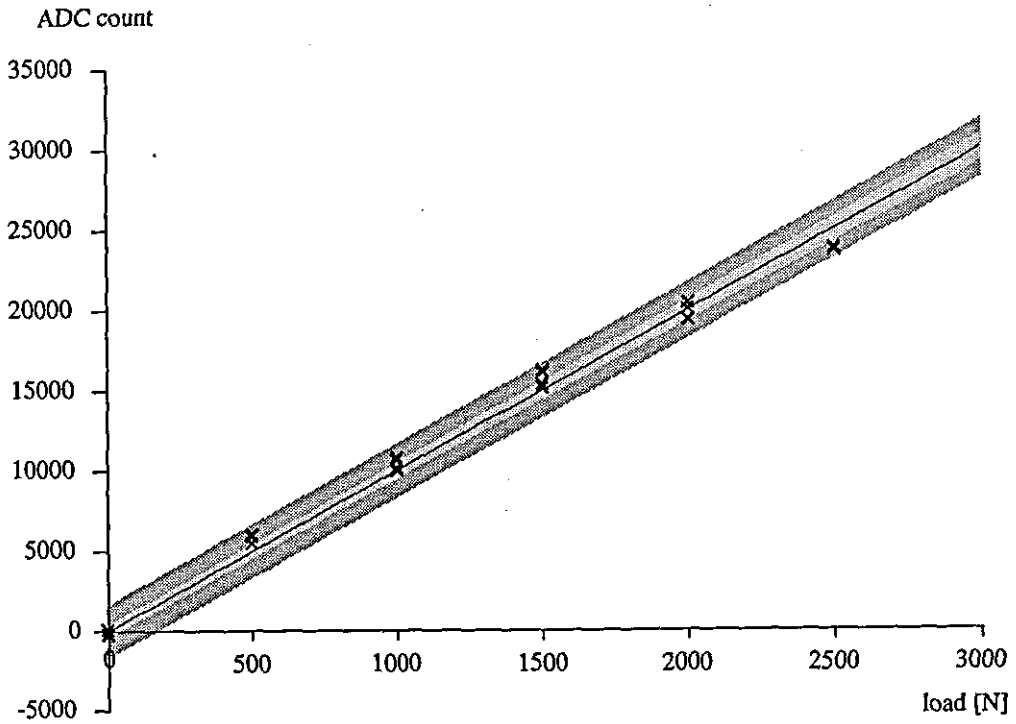


Figure 6.37. Linear regression between the load applied to the bar and the strain recorded in the horizontal direction.

The regressions performed on the data obtained from loading using one point of support appeared to be different to that obtained from loading using two points of support (Table 6.15). Although no statistics were used to determine whether the results obtained from the regressions were significantly different it was decided that they were close enough given the errors in the calibration procedure. Hence, the regression data obtained from loading using one point of support would be used to convert the strain data into force since the range of the calibration data was larger.

6.4.3 Converting strain data into force

The horizontal and vertical strain data from the trials where the gymnast circled the bar were converted into force using the following equations, based on the regressions performed with the calibration data.

$$\text{vertical force} = \text{ADC counts} / -9.30$$

$$\text{horizontal force} = \text{ADC counts} / 10.00$$

Estimate of accuracy

The regression equations obtained from the calibration data were used to convert the ADC amplifier counts into force. The standard errors of the calibration data about the regression line were 0.11 and 0.12 for the vertical and horizontal directions respectively (Table 6.15). This was calculated to be 1.2% when expressed as a percentage error in the gradient of the regression line. The standard error is the average estimate of the error for all points about the regression line. The standard error therefore incorporates all the errors accumulated during the loading of the bar (i.e. the error in the calibration of the load cell and the error resulting from the resolution of the strain gauge amplifier used to load the bar). When using the regression equations to convert the ADC counts into force the error in the recorded force will be $\pm 1.2\%$.

Using the calibration equations outlined above the strain data were converted into force. Figure 6.38 shows the vertical force trace for the first regular giant circle recorded from trial 10. The two dashed lines in Figure 6.38 represent the possible error in the calculation of the force. That is, the true force applied to the bar lies within the two sets of dashed lines. Only at the extremes of the force recorded do the solid and the dotted lines diverge. The data presented in Figure 6.38 was sampled at 50 Hz from the recorded force. Only a quarter of the data recorded for the giant circle is presented in this figure. The force curve even at this sample frequency is smooth and free from random noise.

Since this was the case for all recorded trials the data were not smoothed. Figure 6.39 is the corresponding force trace in the horizontal direction for the same giant circle (with the $\pm 1.2\%$ interval plotted as dashed lines).

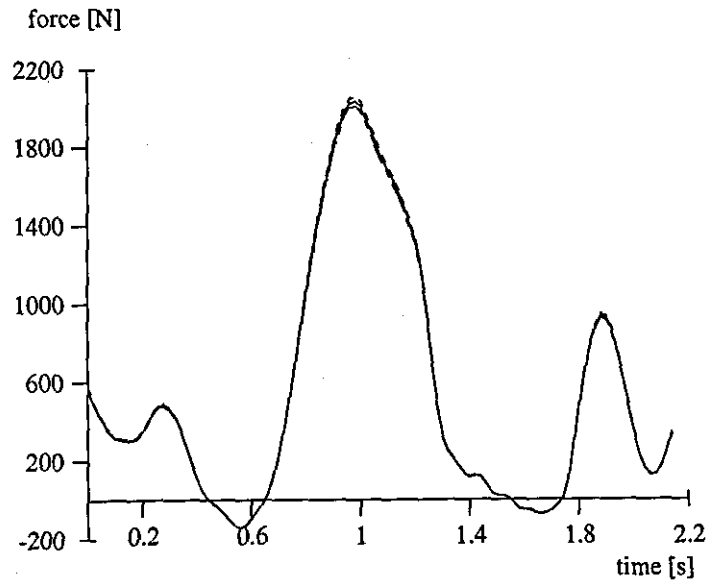


Figure 6.38. Vertical force trace with error estimates (the dashed lines) for a regular giant circle.

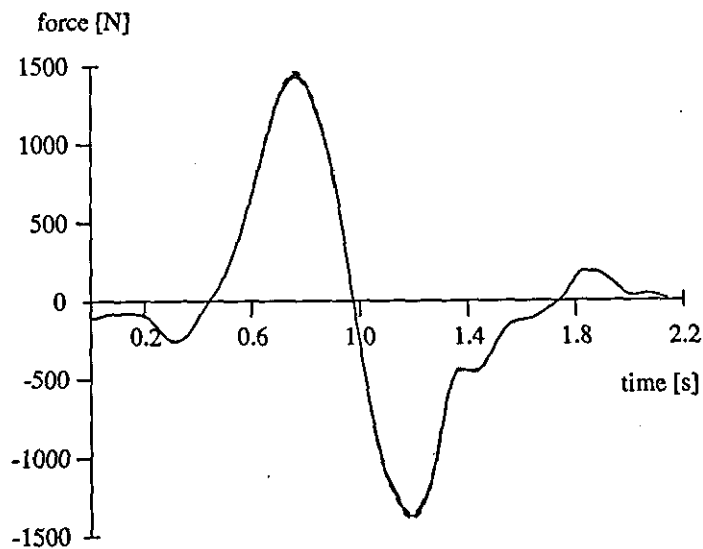


Figure 6.39. Horizontal force trace for a regular giant circle.

Calibration data were recorded for loading the bar vertically using one and two points of force application. The results are presented in Table 6.15. The rms difference between the force calculated when using both calibration equations for all three giant circles of trial 10 was 44.6 N (2.0% when expressed as a percent of the total range of force). Since more calibration data were collected when loading at one point of support and since the rms difference between the two loading conditions was small, the

calibration data obtained when using one point of support was used to convert all the strain data into force. In the literature resultant reaction forces as high as 3200 N have been recorded (Gervais, 1993). Further, the force data will be used in the evaluation of the simulation model. The model is two-dimensional and therefore has only one point of support during swinging. The data obtained when loading at one point will therefore be more appropriate.

Comparison of the force produced during different trials/swings

Regular giant circles

For the three giant circles performed during trial 10 the peak force in the vertical, and horizontal directions were obtained. Table 6.16 contains these peak forces expressed both in Newtons and in bodyweights. The third column of Table 6.16 contains the peak resultant force for trial 10. The results compare well with those obtained by Kopp and Reid (1980) and with the forces recorded by Enchun (1989) for one arm giant circles.

Table 6.16. Peak forces expressed in Newtons and bodyweights for trial 10

circle (trial 10)	vertical peak force (N, (BW))	horizontal peak force (N, (BW))	resultant peak force (N, (BW))
first	2036.42 (3.31)	1440.84 (2.34)	2037.60 (3.31)
second	2036.42 (3.31)	1501.63 (2.44)	2047.58 (3.33)
third	2110.43 (3.43)	1484.03 (2.41)	2110.99 (3.43)
mean	2061.09 (3.35)	1475.50 (2.40)	2065.39 (3.36)

The force traces for the three regular giant circles performed in trial 10 were compared. Circle one was compared with circle two and three and then circle two was compared with circle three. The rms values for the difference between vertical, horizontal, and resultant force were calculated. These rms values were expressed as a percentage of the range of force recorded in each case. Table 6.17 contains the results of the rms calculations. In all cases the rms differences were less than one fifth of a bodyweight. Figures 6.40 and 6.41 show the vertical and horizontal force trace of circle two and circle three (trial 10) overlaid. The results show that the forces produced in the three regular giant circles analysed were very similar. It is likely that the gymnast used a similar technique for each giant circle and did not attempt to increase his rate of rotation with each successive giant circle.

Table 6.17. Rms values for the difference in force between regular giant circles from trial 10 (also expressed as a percentage of the range of force)

circles compared	rms difference vertical (%)	rms difference horizontal (%)	rms difference resultant (%)
first vs second	93.89 (4.3%)	45.38 (1.6%)	101.03 (4.9%)
first vs third	100.54 (4.5%)	65.48 (2.2%)	104.66 (5.0%)
second vs third	47.45 (2.1%)	52.52 (1.8%)	45.11 (2.1%)

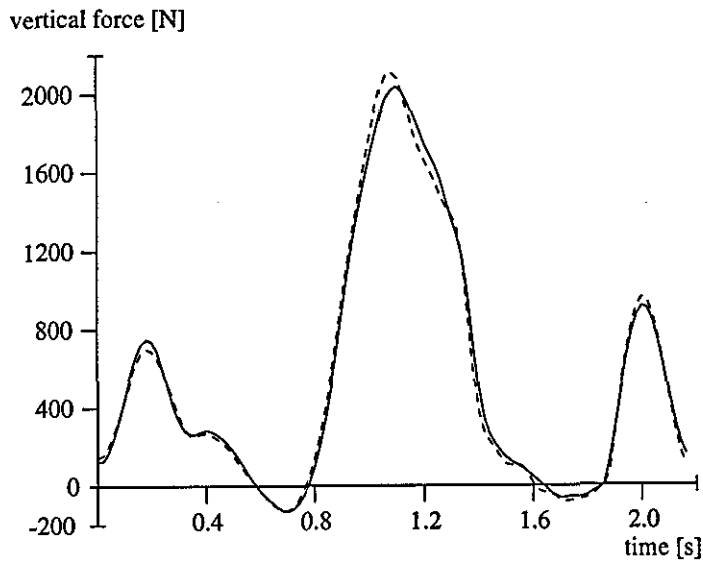


Figure 6.40. Vertical force trace for two regular giant circles.

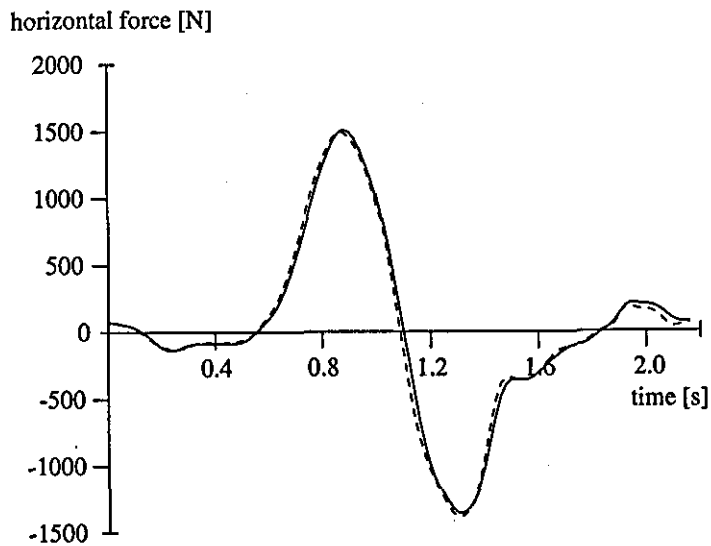


Figure 6.41. Horizontal force trace for two regular giant circles.

Accelerated giant circles (including the release giant)

The accelerated giant circles contained one complete circle and a further three-quarter circle after which the gymnast would normally release the bar. All peak forces were found to occur in the final three-quarter circle leading up to the release. The peak forces for the accelerated giant circles in trials 4 and 11 are given in Table 6.18. These results compare well with those obtained by Gervais (1993) for a giant circle leading into a double somersault dismount. The mean peak resultant force was found to be 50% larger than the mean peak resultant force of the regular giant circles. Note that the peak horizontal force for the accelerated giant circles exceeds the peak vertical force obtained during the regular giant circles.

Table 6.18. Peak forces expressed in Newtons and bodyweights for trials 4 and 11

circle (trial)	vertical peak force (N, (BW))	horizontal peak force (N, (BW))	resultant peak force (N, (BW))
4	2656.07 (4.31)	2498.35 (4.06)	3050.01 (4.95)
11	2792.05 (4.53)	2431.12 (3.95)	3134.46 (5.09)
mean	2724.06 (4.42)	2464.74 (4.01)	3092.24 (5.02)

Table 6.19 shows the peak forces obtained if the final three-quarter giant circle containing the release for the dismount had been ignored. The mean peak resultant force for the giant circle performed before the three-quarter release giant is 24% smaller than the peak resultant force obtained from the three-quarter release circle. It may be speculated that the technique used in the giant circle prior to the release giant must result in the larger forces obtained in the release giant circle.

Table 6.19. Peak forces for the giant circle performed before the three-quarter circle containing the release for trials 4 and 11

circle (trial)	vertical peak force (N, (BW))	horizontal peak force (N, (BW))	resultant peak force (N, (BW))
4	2396.16 (3.89)	1622.92 (2.64)	2413.91 (3.92)
11	2289.44 (3.72)	1645.32 (2.67)	2313.44 (3.76)
mean	2342.80 (3.81)	1643.12 (2.66)	2363.68 (3.84)

The force traces for the giant circle prior to and the giant circle containing the release for trials 4 and 11 were compared. The rms values for the difference between vertical, horizontal, and resultant force were calculated as for the regular giant circles. These rms values were expressed as a percentage of the range of force in each case. Table 6.20 contains the results of the rms calculations. Figure 6.42 and Figure 6.43 show the vertical and horizontal force traces from trial four 4 and 11 overlaid. The two accelerated giant circles appear to be very similar with only a 3.4% difference in the resultant force. Again, it is likely that the gymnast uses the same technique each time he performs accelerated giant circles prior to a double layout dismount.

When comparing the trace obtained from the regular and accelerated giant circles (especially the portion containing the release circle) there appear to be obvious differences. The vertical reaction force for the accelerated giant circle has two peaks (Figure 6.42) compared with the single peak for the regular giant circle (Figure 6.40). As in the vertical bar displacements of the accelerated giant circles (section 6.3.4) the first of the double peaks corresponded to the gymnast's maximum hip hyper-extension and maximum knee flexion angle. This first peak in force may be used as a timing mechanism by the gymnast. Once the gymnast feels the force increase the hyper-extension of the hips is reduced in order to initiate the flexion of the hip joint.

Table 6.20. Rms values for the difference in force between two accelerated giant circle trials (also expressed as a percentage of the range of force)

trials compared	rms difference vertical (%)	rms difference horizontal (%)	rms difference resultant (%)
4 vs 11	98.92 (3.1%)	53.88 (1.3%)	91.91 (3.4%)

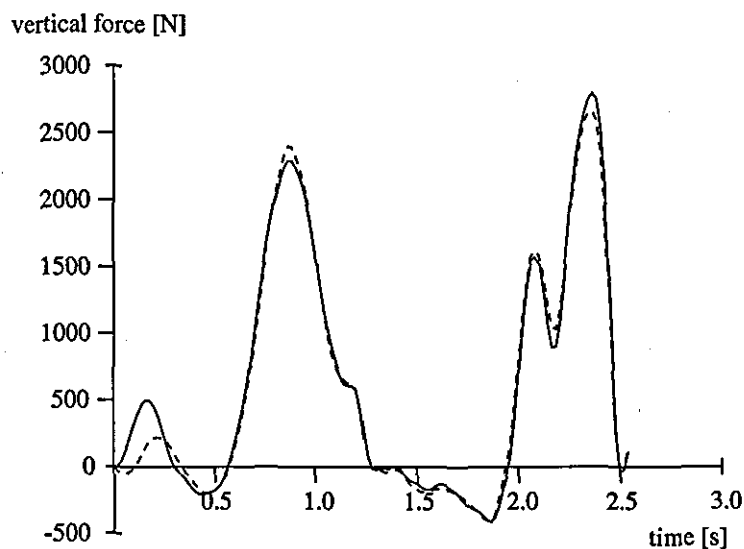


Figure 6.42. Vertical force trace for two accelerated giant circles.

It has been shown that the force traces obtained from two accelerated giant circles are very similar. It may be generalised that for this subject a similar force trace would be obtained every time a wind up prior to release for a double layout somersault dismount was requested. Therefore, the technique the gymnast used must produce the characteristic double peak in the force trace.

The force trace in Figure 6.42 shows the vertical force up until the point where the gymnast would release the bar for a double layout backward somersault dismount. This would occur at a rotation angle of approximately 622° . At this point the force in the vertical and horizontal directions (Figures 6.42 and 6.43, respectively) drops near to zero. Had this been a wind up giant circle the vertical reaction force would be closer to one bodyweight in the vertical direction and 2.5 bodyweights in the horizontal direction. Is the vertical and horizontal force dropping to zero at release a coincidence or is there some mechanical benefit to this when performing a double layout backward somersault dismount. Again this cannot be answered using the force trace alone.

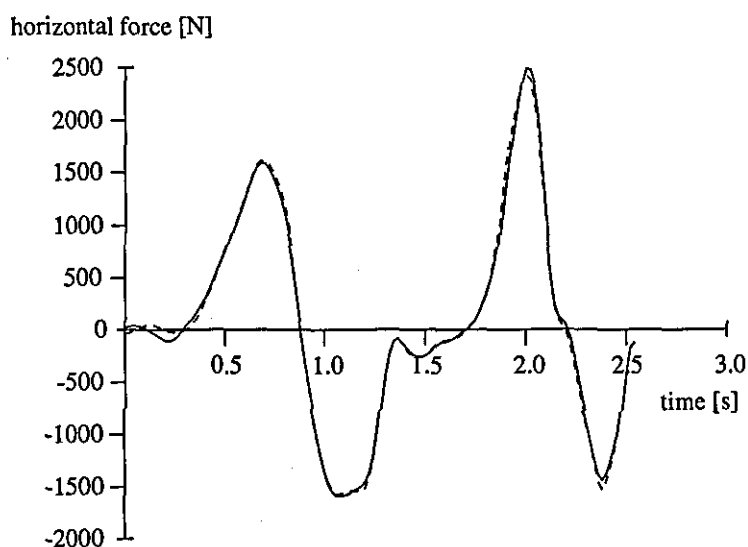


Figure 6.43. Horizontal force trace for two accelerated giant circles.

6.4.4 Summary

The regressions performed on the calibration data enabled the strain recorded from the bar to be converted into force to within $\pm 1.2\%$. The coefficients obtained in the vertical and horizontal directions were found to be different. It is likely that the bar is less stiff in the horizontal direction, based on this result. Using the regression equations the strain data were converted to force.

The peak resultant reaction force for the regular giant circles was approximately 2065.4 N (Table 6.16). This was equivalent of 3.4 bodyweights. For a similar study

Kopp and Reid (1980) obtained a peak reaction force of 2208 N, or 3.6 bodyweights, which compares well with the results of this study. The reaction forces for the accelerated giant circles were found to be larger than those obtained from the regular giant circles. The peak resultant reaction force was 3092.2 N (5.0 bodyweights). This peak value lay just outside the maximum load applied during the calibration of the high bar (3.0 kN). However, the peak horizontal and vertical components of force were 2464.7 and 2724.1 N respectively. These peak values were both within the range of the horizontal and vertical calibrations.

The force traces were compared between circles and trials. It was found when comparing two regular giant circles or two accelerated giant circles that the time histories of the force were very similar. It was suggested, as in section 6.3.4 that the gymnast used the same technique each time to load the bar.

6.5 Synchronisation of force and video

6.5.1 Introduction

In order to evaluate the simulation model it will be necessary to relate the reaction forces recorded at the bar to both the whole body angle of rotation and the joint angle time histories at the shoulder, hip and knee joints. For this reason the kinetic and kinematic data was synchronised.

6.5.2 Synchronised data

Estimate of accuracy

Since the synchronisation of the video cameras and the trigger for the force data occurred simultaneously the accuracy of the synchronisation could be at best to the nearest video field. The force and the video data were therefore synchronised to within 0.01 s, half the sampling frequency of the video camera. Although, interpolation of the video data were performed to locate the time at which the hips passed through the photocell beam the overall accuracy of the synchronisation was dependent on the sampling frequency of the video cameras.

Regular giant circles

Figure 6.44 shows the vertical and horizontal force traces plotted against the rotation angle for trial 10. The peak vertical force for each of the three regular giant circles performed in trial 10 occurred at a mean rotation angle of 178.0° . That is, just before the lowest point of the giant circle. In the horizontal direction the mean peak forces for this trial occurred at 118.5° and 233.4° . Figure 6.45 shows the resultant force plotted against rotation angle for trial 10. The peak resultant force occurred at a rotation angle of 176.1° . These coincide with the peak horizontal and vertical bar displacements. However, the peak angular velocity of the rotation angle occurred earlier at 167° (Table 6.21).

Table 6.21. Rotation angle at peak horizontal and vertical reaction forces (trial 4)

peak	rotation angle at vertical peak ($^\circ$)	rotation angle at horizontal peak ($^\circ$)
first	177°	124°
second	496°	235°
third	576°	473°
fourth	NA	581°

Kopp and Reid (1980) found that the resultant peak force occurred at a rotation angle of 210° . This means that the peak force occurred after the gymnast had passed through the lowest point. In the present study the peak force was recorded just before the gymnast passed through the lowest point. This may have occurred as a result of the subjects using a slightly different technique. From Figure 6.45 it can be seen that when the resultant force is at its highest there appears to be a flattening of the force time curve. A similar effect was seen in the data of Kopp and Reid (1980). The gymnasts in the 1980 study may therefore have used a slightly different technique to the one used in the current study which lead to the peak resultant reaction force occurring at a slightly different point.

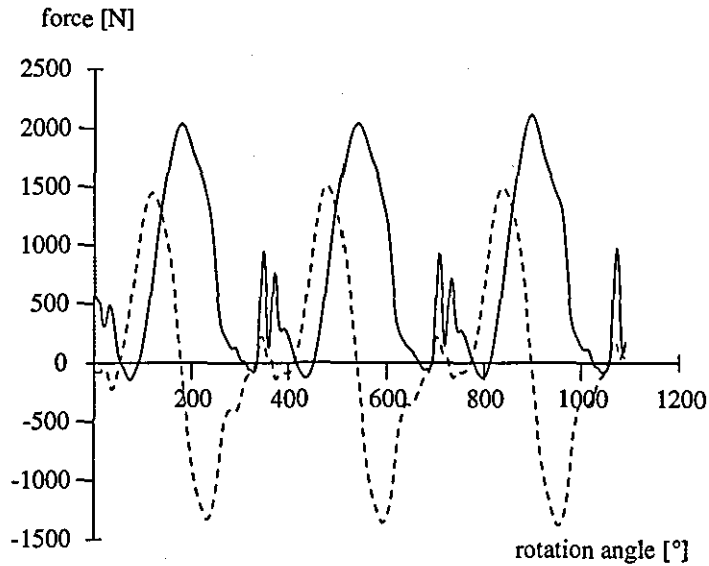


Figure 6.44. The vertical and horizontal force recorded in trial 10 plot against rotation angle.

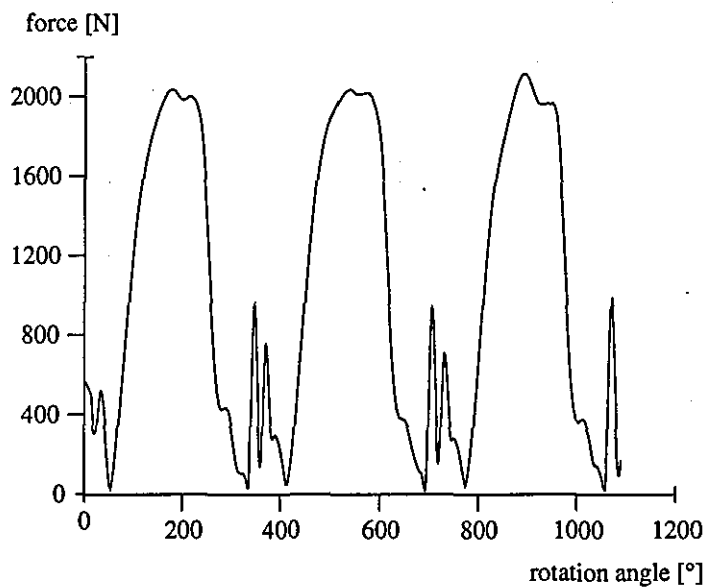


Figure 6.45. The resultant force recorded in trial 10 plotted against rotation angle.

Accelerated giant circles

The horizontal and vertical reaction forces recorded during trial 4 are plot against the angle of rotation in Figure 6.46. The rotation angles at which the peak forces occur are presented in Table 6.21. The peak vertical reaction force for the first accelerated giant circle occurred at a rotation angle of 177° . For the accelerated giant circle containing the release, the peak reaction force occurs at a rotation angle of 576° . This is approximately 36° after passing through the lowest point. The subject has therefore loaded the bar differently on passing through the lowest point for the second time. Just

before the second peak there is a smaller peak in the vertical reaction force (similar to that seen in the vertical bar displacement in section 6.3.4). This smaller peak occurs at 496° . The four peaks in horizontal reaction force occurred at rotation angles of 124° , 235° , 473° and 581° respectively. The corresponding peaks in linear bar displacements for trial 4 are given in Table 6.22. The differences between the rotation angle at the peak bar displacements and reaction forces are small with a mean of less than 7° . The mean would be less than 4° except for the difference between the second peak in the horizontal bar displacement and reaction force. On inspection of Figure 6.46 it can be seen that there is a plateau where the second peak in horizontal reaction force occurs. The range of this plateau contains the rotation angle at which the horizontal bar displacement is also at a peak. It is apparent from these results (Table 6.21 and Table 6.22) that the peaks in reaction force occur at or very near to the peaks in the bar displacements. This is further evidence of the relationship between the two sets of data.

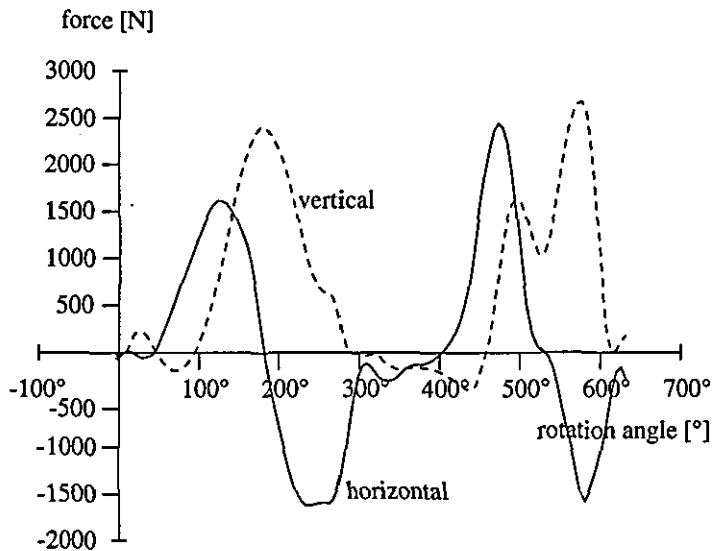


Figure 6.46. Horizontal and vertical reaction forces plot against rotation angle (trial 4).

Table 6.22. Rotation angle at peak horizontal and vertical bar displacements (trial 4)

peak	rotation angle at vertical peak ($^\circ$)	rotation angle at horizontal peak ($^\circ$)
first	176°	126°
second	489°	259°
third	571°	470°
fourth	NA	578°

6.6 Spring parameters

6.6.1 Introduction

Spring parameters are among the required input to the four segment simulation model. Section 6.6 outlines how these values were obtained using the data obtained from the kinetic and kinematic analysis of the backward giant circles.

6.6.2 Stiffness and damping coefficients of the bar

Determination via static loading

The reference frames were repeatedly digitised so that an estimation of the accuracy of the digitisation could be made. Average root mean square values, of the difference between the digitised and repeat digitised data sets, of 0.128 mm and 0.095 mm were found in the vertical and horizontal directions respectively. The rms values were small due to the size of the field of view.

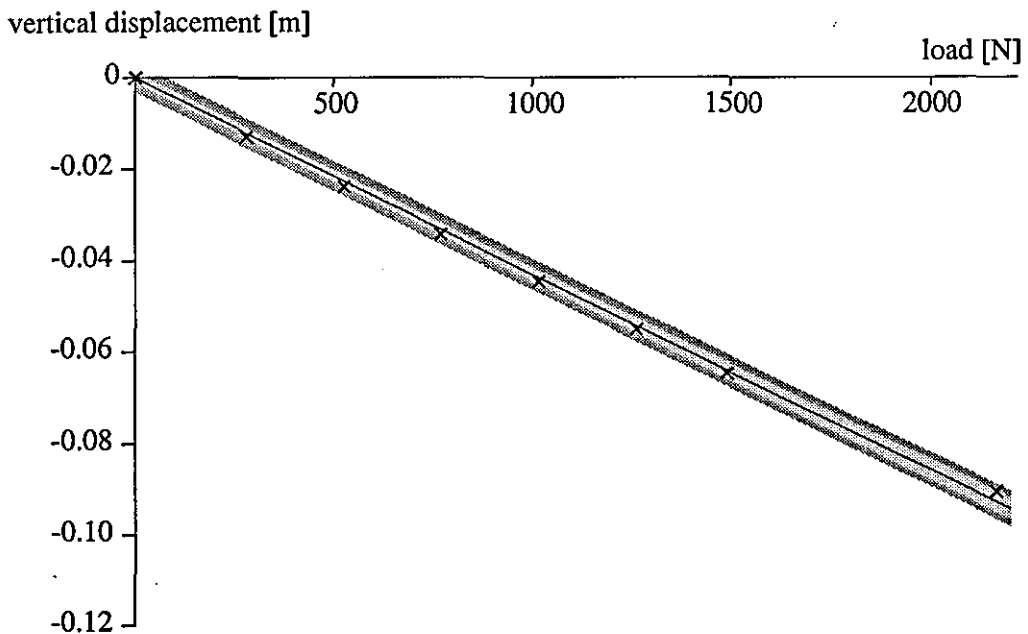


Figure 6.47. Regression line and single points for load against vertical bar displacement.

Figure 6.47 shows the vertical bar displacement plotted on the vertical axis against the load applied to the bar. It appears that the relationship between load and vertical displacement is linear. The linear regression produced a stiffness coefficient of

$-23305.9 \pm 210.0 \text{ N.m}^{-1}$. The standard error for the regression was 29.2 N. This means that the average error in predicting the reaction force using the bar displacement was 29.2 N. This is the equivalent of 0.05 of a body weight, or 1% when expressed as a percentage of the range of force applied to the bar. The correlation coefficient between load and bar displacement was 0.999.

The FIG manual of measures dimensions and forms states that the high bar must produce a "sag" of $0.10 \pm 0.01 \text{ m}$ under a load of 2200 N. Therefore, the bar may have a stiffness coefficient of between 20000.0 and 24444.4 N.m^{-1} (using Hooke's law and the FIG regulations). It would appear that the bar calibrated in this study was within the range required by the governing body.

Continental Sports (supplier of the tested high bar) perform a number of tests on the equipment it supplies, one of which is to load the high bar with 2200 N and measure its vertical displacement. In the Norms-testing manual supplied by Continental Sports a vertical displacement of 0.08 - 0.10 m was reported. This would yield a stiffness coefficient of between 22000 and 27500 N.m^{-1} . The value obtained in this investigation lies within this range.

Determination from force analysis of the giant circle

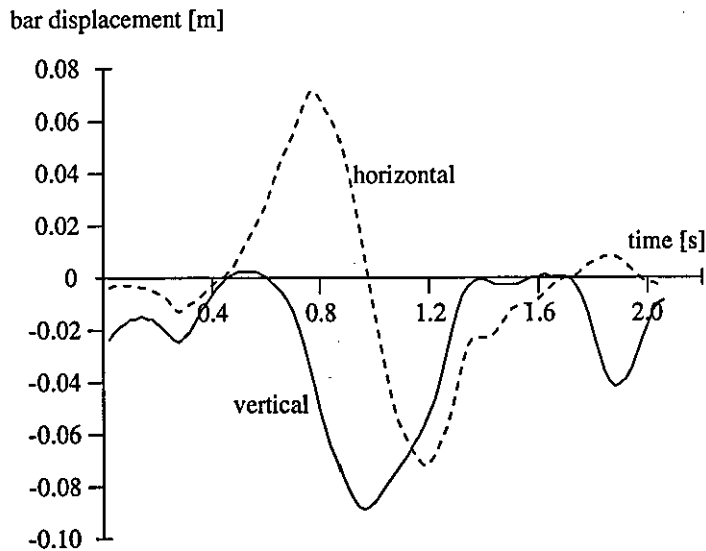


Figure 6.48. Vertical and horizontal bar displacements for regular giant circle one of trial 10.

The location of the centre of the bar was found to be at co-ordinates (-0.011, 2.721). These values were subtracted from the reconstructed three-dimensional co-ordinates. Figure 6.48 has the vertical and horizontal bar displacements plotted against time for circle one of trial 10. Note that the shape of the vertical force trace in Figure 6.40 is almost a reflection of Figure 6.11, vertical bar displacement, in the horizontal axis.

Table 6.23 contains the peak horizontal and vertical bar displacements for the regular giant circles performed in trial 10. Similar results for the accelerated giant circle performed in trials 4 and 11 are given in Table 6.24. The bar displacements were larger for the accelerated giant circles when compared with the regular giant circles. The values obtained are consistent with those obtained by Brüggemann et al. (1994) for the bar displacements during the giant circle prior to release. For the regular giant circles the peak vertical bar displacement was larger than the peak horizontal bar displacement. However, during the accelerated giant circles the peak bar displacements in the horizontal and vertical directions were similar.

Table 6.23. Peak bar displacements in the horizontal and vertical directions for trail 10

circle (trial 10)	peak vertical bar displacement (m)	peak horizontal bar displacement (m)
first	- 0.089	0.072
second	- 0.089	0.074
third	- 0.093	0.077
mean	- 0.090	0.074

Table 6.24. Peak bar displacements in the horizontal and vertical directions for trails 4 and 11

circle (trial)	peak vertical bar displacement (m)	peak horizontal bar displacement (m)
4	- 0.114	0.116
11	- 0.118	0.118
mean	- 0.116	0.117

The results of the linear regressions performed between the vertical bar displacements and the vertical force recordings for giant circles one and two of trial 10 are given in Table 6.25. The regressions were not forced through the origin since the data being regressed were obtained during dynamic conditions. When the bar has zero displacement it does not follow that there will be zero force applied to the bar. If the bar has a velocity when there is zero displacement there may be a force due to the damping of the bar. This damping would be due to the characteristics of the material the bar was constructed from. The damping force is calculated as the product of the spring velocity and the damping coefficient of the spring. Therefore, in Table 6.25 the stiffness of the bar is determined

from the coefficient of the regression line and the constant term indicates that the regression line does not pass through the origin. The value for the constant is less than 2% of the force recorded in the vertical direction for the regular giant circles. However, when expressed as an error in the displacement data the constant obtained from the regressions in the vertical direction correspond to less than 0.002 m. This value is less than the rms value of the reconstructed three-dimensional co-ordinates (approximately 0.011 m). The standard error for the regressions are displayed in the fifth column of Table 6.25. The mean rms difference for the regular giant circles was 60.1. The regression line was therefore able to predict the reaction force in the bar from the bar displacement with an average error of 60.1 N. This corresponds to an average error of 0.10 bodyweights. The stiffness coefficients determined from the regression of the force and displacement data were not significantly different from the coefficient obtained from the static loading experiment.

Table 6.25 also contains the results of the regression performed on the data from trial 4 (accelerated giant circle). The stiffness coefficient is not significantly different from those obtained from the regular giant circle data. It may therefore be inferred that the bar has a constant stiffness which does not change with increasing load. However, the standard error for the regression performed using the data from trial 4 was considerably larger than the standard errors obtained from the regular giant circles (Table 6.25).

Table 6.25. Results of linear regressions between vertical bar displacement and force

giant circles (trial 10)	correlation coefficient	gradient	constant	standard error
first	0.990	- 23409.9 ± 231.9	- 35.3 ± 8.6	63.8
second	0.992	- 23461.5 ± 204.9	- 36.8 ± 7.6	56.6
first & second	0.991	- 23435.8 ± 153.7	- 36.0 ± 5.7	59.9
trial 4	0.972	- 23221.8 ± 353.2	- 54.9 ± 16.9	152.0

The horizontal data were regressed in the same way as the vertical data. The results are presented in Table 6.26. The constant coefficient is less than 1% of the force recorded in the horizontal direction. Which again corresponds to a displacement error of less than 0.001 m. The gradient of the regression lines are significantly different from those obtained in the vertical direction. It may be inferred that the bar is less stiff in the horizontal direction. Table 6.18 (peak horizontal and vertical forces) indicated that the peak vertical forces during the accelerated giant circles were larger than those in the horizontal direction. However, Table 6.24 (peak bar displacements) shows that the bar was displaced similar amounts in both the horizontal and vertical directions. Using

Hooke's law it would therefore be expected that the bar is more stiff in the vertical direction. This difference in stiffness may be explained by the way the bar is mounted to the uprights. In the vertical direction the bar may pivot about two pins which pass through the middle of the bar mountings. In the horizontal direction the mounting is designed so that it can twist about its vertical axis. The twisting allows the bar to be displaced in the horizontal direction with less force.

The standard errors for the regressions in Table 6.26 for the regular giant circles have a mean of 48.2 N. Like the standard error for the regressions in the vertical direction this corresponds to a standard error of 0.10 bodyweights. The standard error for the regression performed on the data from trial 4 is considerably larger than those obtained for the regular giant circles (Table 6.26).

Table 6.26. Results of linear regressions between horizontal bar displacement and force

giant circles (trial 10)	correlation coefficient	gradient	constant	standard error
first	0.990	- 20359.0 ± 152.5	- 20.9 ± 5.0	50.4
second	0.992	- 20456.0 ± 137.3	- 13.3 ± 4.5	46.1
first & second	0.991	- 20407.3 ± 102.3	- 17.1 ± 3.3	48.2
trial 4	0.972	- 20069.3 ± 181.0	- 59.0 ± 9.1	103.0

Figure 6.49 shows a plot of the vertical force against the vertical bar displacement, for regular giant circle three, trial 10 (dashed line). The force data is sampled at 50 Hz, since it has been synchronised with the video data. The solid line is the force estimated using the regression equation below;

$$\text{estimated vertical force} = \text{vertical bar displacement} \times \text{gradient from regression line}$$

In Figure 6.49 the gradient of the solid line was -23409.9, the stiffness coefficient obtained from the regression using the data from the first giant circle of trial 10. The rms difference between the recorded force and the force calculated using the above equation is 68.8 N. This is equivalent of a 3.1% difference when expressed as a percent of the range of vertical force. The same analyses were performed using the stiffness values obtained from the static loading of the bar and from the regressions using the dynamic data. The process was repeated using the force and bar displacement data obtained from trial 11 (accelerated backward giant circle). The results are presented for the rms differences in the vertical and horizontal directions in Tables 6.27 and 6.28, respectively.

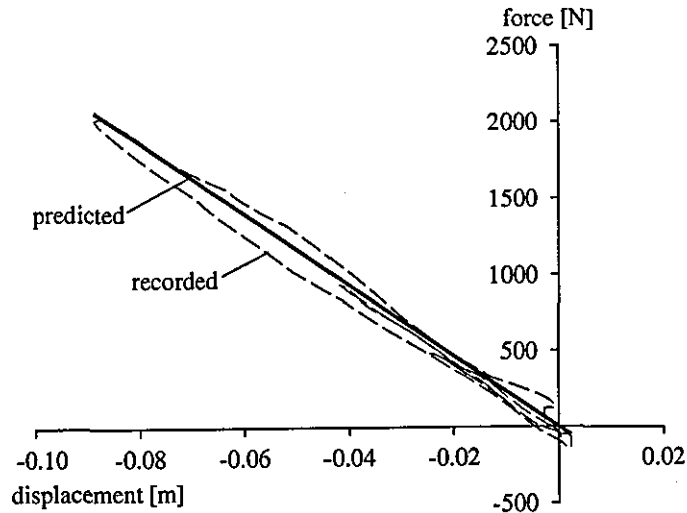


Figure 6.49. Estimated force and recorded force against vertical bar displacement.

Table 6.27. Rms difference between estimated and recorded vertical force

stiffness coefficient (N.m ⁻¹)	circle 3 (trial 10) rms difference (N, %)	trial 4 rms difference (N, %)
-23305.9	67.5 (3.0%)	168.6 (5.5%)
-23409.9	68.8 (3.1%)	169.9 (5.6%)
-23461.5	69.4 (3.1%)	170.5 (5.6%)
-23435.8	69.1 (3.1%)	170.2 (5.6%)

Table 6.28. Rms difference between estimated and recorded horizontal force

stiffness coefficient (N.m ⁻¹)	circle 3 (trial 10) rms difference (N, %)	trial 4 rms difference (N, %)
-20359.0	53.2 (1.7%)	125.8 (3.1%)
-20456.0	53.9 (1.8%)	126.6 (3.1%)
-20407.3	53.5 (1.8%)	126.2 (3.1%)

The stiffness coefficients obtained from the static loading and the regression analyses were successfully able to predict the vertical reaction for the regular and accelerated giant circles. Rms difference values of between 67.5 N and 69.4 N were obtained when comparing estimated and recorded vertical reaction forces for the regular giant circle. The rms difference compares well with the standard errors obtained from the linear regressions in Table 6.25 (regression results table). This was approximately 3%

when expressed as a percentage of the range of vertical force. Larger rms differences were obtained when the stiffness coefficients were used to predict the vertical force during an accelerated giant circle (approximately 170 N, 5.6%). However, the standard error obtained from the linear regression using the data from the accelerated giant circle was also considerably larger than those which used the data from the regular giant circles.

In the horizontal direction the rms differences between the recorded and the estimated force were slightly less when compared with the results obtained in the vertical direction (Table 6.26). The rms difference when estimating the horizontal force for the regular giant circle was approximately 54.0 N (approximately 2% when expressed as a percent of the range of horizontal force). When estimating the horizontal force for the accelerated giant circle the rms difference with the recorded force was approximately 126.0 N (3%).

To investigate the hypothesis that a relationship exists between the recorded force, bar displacement and bar velocity stepwise regressions were performed using these data. The results of the regressions performed on the vertical data are given in Table 6.29. The stiffness coefficients are largely unchanged by introducing a second coefficient (Table 6.25). From the regressions the damping coefficient lies within the range of 193.0 to 234.9 $\text{N}\cdot\text{s}^2\cdot\text{m}^{-1}$ for the regular giant circles. The damping coefficient for the accelerated giant circle is considerably larger at 412.5 $\text{N}\cdot\text{s}^2\cdot\text{m}^{-1}$. Introducing the damping coefficient also improved the correlation coefficients in all cases. Similarly the standard errors obtained for these regressions (Table 6.29) are smaller than those obtained for the regressions which did not account for the velocity of the bar. The mean standard error was reduced from 60.1 to 48.5 for the regular giant circles. The standard error for the regression performed on the accelerated giant circle data was reduced by 47% by introducing the damping coefficient.

Stepwise regressions were also performed for the horizontal force and bar displacement data. In order to obtain a damping coefficient the second coefficient, i.e. the damping term, had to be forced into the regression. When forced into the regression the correlation coefficient increased and the standard error of the regressions were reduced, Table 6.30. The stiffness coefficients are largely unchanged from the regression performed without the damping term. This is because, for the regular giant circles, the damping term does not really improve the regression (Table 6.26 and Table 6.30). It can also be seen that the standard deviations for the damping coefficients are large. In the case of the accelerated giant circle the the damping coefficient is large, when compared with the regular giant circles (Table 6.30). Introduction of the damping term improved the standard error by 50%. It may be inferred from this result that the damping of the bar has greater effect on the reaction force when the bar has greater displacements and velocities.

Table 6.29. Results of linear regressions between vertical bar displacement and velocity and vertical force

giant circles (trial 10)	correlation coefficient	stiffness coefficient	damping coefficient	constant	standard error
first	0.995	- 23426.2 ± 172.4	234.9 ± 25.8	- 37.4 ± 6.4	47.4
second	0.994	- 23455.6 ± 179.2	152.7 ± 26.5	- 36.3 ± 6.6	49.5
first & second	0.994	- 23438.8 ± 125.0	193.0 ± 18.6	- 36.6 ± 4.6	48.7
trial 4	0.992	- 23213.9 ± 190.9	412.5 ± 23.7	- 54.3 ± 9.1	81.0

Table 6.30. Results of linear regressions between horizontal bar displacement and velocity and horizontal force

giant circles (trial 10)	correlation coefficient	stiffness coefficient	damping coefficient	constant	standard error
first	0.994	- 20359.3 ± 152.2	28.0 ± 23.3	- 20.9 ± 5.0	50.3
second	0.995	- 20456.1 ± 136.3	34.1 ± 21.0	- 13.2 ± 4.4	45.7
first & second	0.995	- 20407.5 ± 101.6	31.1 ± 15.6	- 17.0 ± 3.3	47.9
trial 4	0.997	- 20071.4 ± 95.3	228.0 ± 12.6	- 58.0 ± 4.8	51.6

The regression equations including the term for damping were used to estimate the force in one regular giant and one accelerated giant circle. None of the data from these trials were used to obtain the regression equations. The force was estimated using the following formula:

$$\text{Force} = \text{bar displacement} \times \text{stiffness coefficient} + \text{bar velocity} \times \text{damping coefficient}$$

Figure 6.50 a) shows the recorded vertical force plot against vertical bar displacement. Figure 6.50 b) shows the estimated vertical force plot against vertical bar displacement. The introduction of the damping term into the formula used to estimate the force produces a force trace which is more representative of the actual recorded force. The rms difference between the recorded and estimated force was calculated. The results are presented in Tables 6.31 and 6.32 (vertical and horizontal data, respectively). Introducing the damping coefficient reduced the rms difference in all cases when compared with rms differences obtained with no damping term. The rms differences were largest when using the coefficients obtained from the regular giant circles to estimate the reaction forces during trial 4. However, in all cases, regular and accelerated, the rms differences are all less than a quarter of a bodyweight.

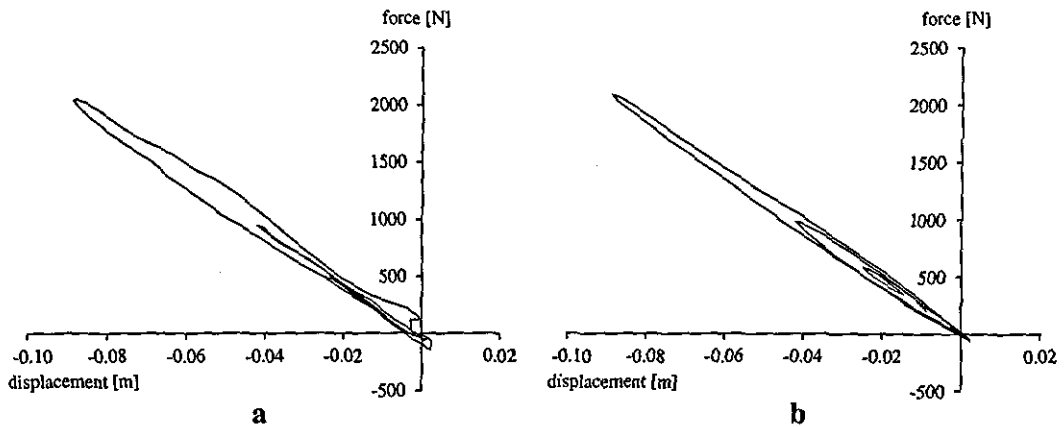


Figure 6.50. Recorded force (a) and estimated force (b) against vertical bar displacement.

Table 6.31. Rms difference between estimated and recorded vertical force

stiffness coefficient (N.m^{-1})	damping coefficient (N.m)	circle 3 (trial 10) rms difference ($\text{N}, \%$)	trial 4 rms difference ($\text{N}, \%$)
- 23426.2	234.9	65.0 (2.9%)	119.1 (3.9%)
- 23455.6	152.7	63.9 (2.8%)	134.4 (4.4%)
- 23438.8	193.0	64.0 (2.8%)	126.4 (4.1%)

Table 6.32. Rms difference between estimated and recorded horizontal force

stiffness coefficient (N.m^{-1})	damping coefficient (N.m)	circle 3 (trial 10) rms difference ($\text{N}, \%$)	trial 4 rms difference ($\text{N}, \%$)
- 20359.3	28.0	52.1 (1.7%)	133.8 (3.3%)
- 20456.1	34.1	52.8 (1.7%)	136.5 (3.3%)
- 20407.5	31.1	52.4 (1.7%)	135.1 (3.3%)
- 20071.4	228.0	64.7 (2.2%)	202.1 (5.0%)

6.6.3 Stiffness coefficient of the shoulders

Estimate obtained from displacement time history of the shoulders

The results of the regressions performed on the resultant reaction force and the displacement in the subject's shoulders are given in Table 6.33. The regressions yielded stiffness coefficients for the shoulders of between 12500 N.m^{-1} and 16500 N.m^{-1} . The

large constant values in Table 6.33 refer to where the regression line crosses the vertical axis. This is a theoretical value since the arm and torso segments have a minimum length greater than zero. The correlation coefficients imply that the wrist to hip length increases with increasing reaction force at the bar. However the standard errors for the regressions are large, corresponding to an average error of nearly one bodyweight when using the wrist to hip length to estimate the reaction force at the bar. These results may lead to the conclusion that the extension that occurs between the gymnast's wrist and hips is not best modelled using a linear spring. The increase in length may be better modelled using a more complex system or possibly a non-linear spring. Since the regressions revealed that there is a relationship between the increase in length of the subject and the increase in reaction force the assumption of a linear spring will be maintained. The optimisation of all the spring parameters may yield a more appropriated stiffness and damping coefficient for the shoulder spring. Since the damping coefficient of the shoulder could not be determined from the above regressions it may be speculated that any spring at the shoulders would require considerable damping (when compared with the high bar).

Table 6.33. Results of the regressions performed on the wrist to hip length and the resultant reaction force at the bar

giant circles (trial 10)	correlation coefficient	gradient	constant	standard error
first	0.400	12816 ± 1561	- 13908 ± 1796	540.4
second	0.464	13059 ± 1362	- 14338 ± 1581	511.9
first & second	0.422	12634 ± 1023	- 13774 ± 1182	528.7
trial 4	0.579	16467 ± 1257	- 17966 ± 1461	605.2

6.6.4 Damping coefficient of the bar and shoulder springs

Initial estimates

The initial spring parameters used in the Annealing process are presented in Table 6.34. The bar coefficient were taken from the regression performed on the data from the first two regular giant circles of trial 10. The initial stiffness coefficient of the shoulder spring was taken as a "ball park" figure based on the results of the regressions performed in section 6.6.3.

Table 6.34. Initial spring parameters used in the optimisation procedure

spring coefficients	stiffness (N.m ⁻¹)	damping
bar. horiz.	20407.5	31.1
bar. vert.	23438.8	193.0
shoulder	16000.0	0.0

The initial value of the cost function based on the initial parameter values in Table 6.34 was 0.86. This corresponded to a rms difference of 13.5° in rotation angle, 0.033 m in horizontal bar displacement, and 0.016 m in vertical bar displacement.

After 8000 evaluations the final value of the cost function was 0.54. The value of the cost function corresponded to a rms difference of 4.17° in rotation angle, 0.012 m in horizontal bar displacement, and 0.009 m in vertical bar displacement. All three contributions to the cost function show an improvement on the initial evaluation of the cost function based on the spring parameters in Table 6.34. The final values for the spring parameters obtained after the optimisation are given in Table 6.35.

Table 6.35. Final spring parameters obtained from the optimisation procedure

spring coefficients	stiffness (N.m ⁻¹)	damping
bar. horiz.	22236.0	540.8
bar. vert.	26784.0	325.9
shoulder	124.5	18418.0

On comparison of the two sets of spring parameters in Tables 6.34 and 6.35 there are certain similarities and some marked differences. Both before and after the optimisation the stiffness in the vertical direction is greater than that in the horizontal direction. However, both the bar stiffness coefficients are greater after the optimisation than the values estimated by the regression analyses carried out in section 6.6.2. The damping coefficients are also larger than those estimated by the regression analysis on the data obtained from the regular giant circles. Instead, the damping coefficients compare better with the damping coefficients obtained from the regressions performed on the data obtained from the accelerated giant circles.

The most significant difference between the two sets of spring parameters are the stiffness and damping coefficients of the shoulder spring. It appears as though the shoulder spring has minimal stiffness and large damping when compared with the bar

coefficients. It is likely that these spring coefficients would prevent the extension in the shoulders behaving like the data obtained from the video analysis (Figure 6.31). The spring would probably increase in length initially, but when it would be expected to "re-coil" the lack of stiffness in the spring would prevent this. Yet the data from section 6.2.2 (Figure 6.31) showed that there was a definite increase followed by a decrease in the distance from the subject's wrists to hips during the backward giant circles.

The theory behind the Simulated Annealing algorithm is based on the theory of cooling liquids and finding a state of minimum energy. Each time the Annealing changes temperature the current optimum value of the cost function is output along with the function parameters. In Figure 6.51 the value of the cost function at each temperature change has been plotted. Almost immediately a plateau in the function was obtained. A likely explanation is that the algorithm had found a local optimum. However, the algorithm continued to search for a better value of the cost function and eventually departs from the plateau. Figure 6.52 shows the history of the horizontal and vertical stiffness coefficients of the bar during the optimisation. Compared with the history of the shoulder stiffness and damping coefficients, Figures 6.52 and 6.53 respectively, the bar stiffness and damping coefficients remain fairly constant (Figures 6.52 and 6.54). Similarly after the initial plateau the damping coefficient of the shoulder spring remains constant (Figure 6.53). The initial plateau in the shoulder stiffness occurred at a value of 12086.0 N.m^{-1} . This shoulder stiffness value compares with those obtained from the regression analysis in section 6.5.2 (Table 6.33). With such a stiffness coefficient the shoulders are more likely to behave as a spring capable of re-coiling after extension.

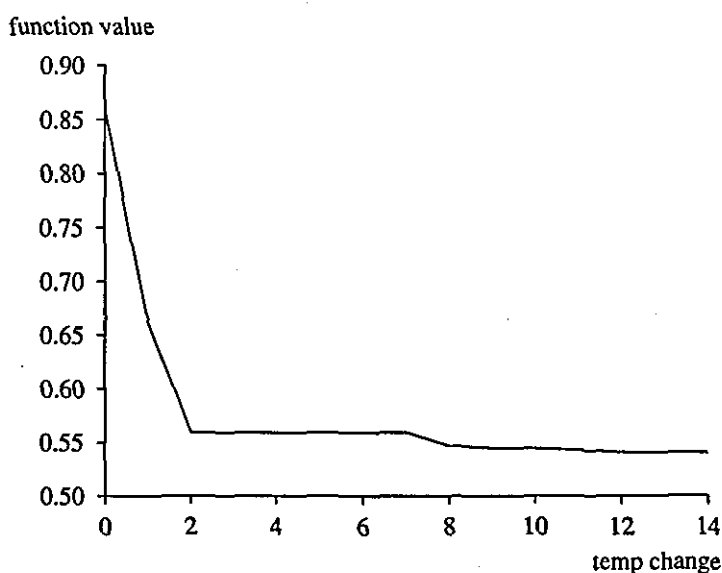


Figure 6.51. History of the cost function value.

It is, therefore, hypothesised that had the extension in the shoulders been included into the cost function the initial plateau may have been the global optimum rather than a

local optimum. However, it is the strength of the Annealing algorithm that it is able to distinguish between local and global optima.

The value of the cost function at the initial plateau was 0.56. This corresponded to a rms difference of 4.90° in rotation angle, 0.012 m in horizontal bar displacement, and 0.009 m in vertical bar displacement. These rms values are only marginally different from those obtained at the end of the optimisation procedure. The spring coefficients obtained at the initial plateau are given in Table 6.36. The spring parameters in Table 6.36 will be used in the evaluation of the four segment simulation model.

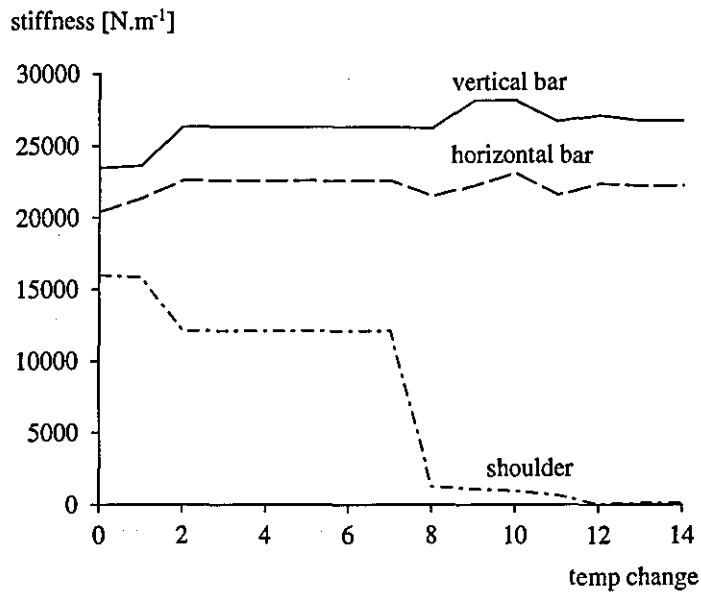


Figure 6.52. History of the stiffness coefficients.

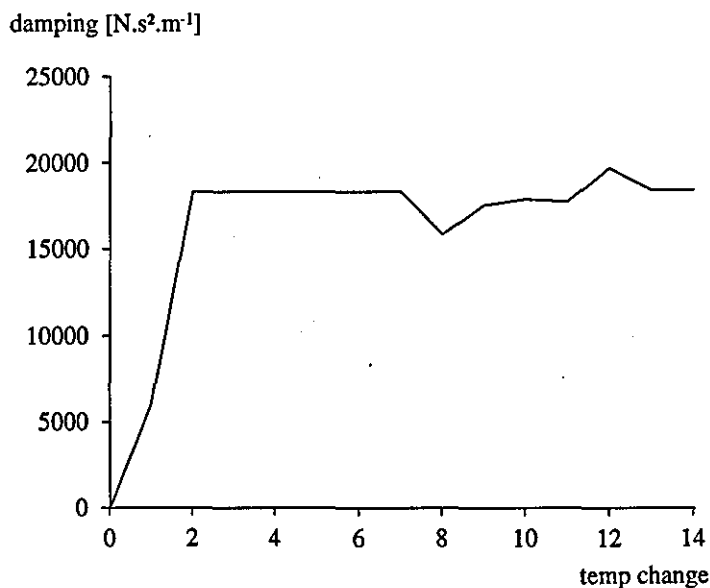


Figure 6.53. History of the shoulder damping coefficient.

Table 6.36. Spring parameters obtained from the initial plateau in cost function

spring coefficients	stiffness (N.m ⁻¹)	damping (N.s ² .m ⁻¹)
bar. horiz.	22560.0	419.6
bar. vert.	26297.0	379.4
shoulder	12086.0	18309.0

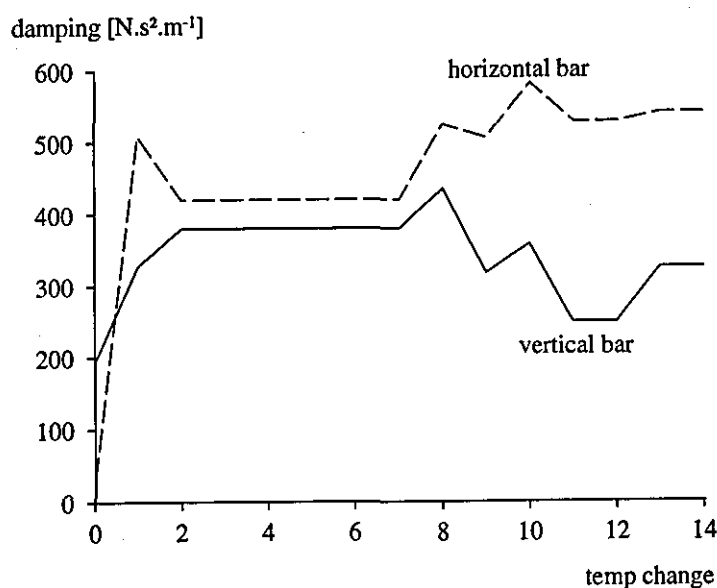


Figure 6.54. History of the bar damping coefficients.

6.7 Summary

The data collected from the isokinetic dynamometer was expressed in two relationships between torque and joint angle and torque and joint angular velocity. These two relationships were combined to form a three-dimensional surface. Given a joint angle and angular velocity it will be possible to estimate the peak joint torque the subject can produce. As stated earlier, these muscle model surfaces will be used to limit the joint torques at the hip and shoulder joints during the optimisation of the accelerated backward giant circles.

The kinetic and kinematic data compared well with similar results obtained in the literature. For the comparisons with the literature see the summary sections 6.3.5 and 6.4.4. The force and the video data were synchronised to within 0.01 s, to the nearest half of a video field. The synchronised data were then used to estimate the stiffness and

damping coefficients of the high bar. Reaction forces recorded during regular and accelerated giant circles were regressed against the displacements of the bar for the same trials. The gradient of the regression line being the stiffness coefficient of the high bar. These data were compared with a stiffness coefficient obtained from a static loading of the bar, which compared favourably. It was found that the standard deviation between the data points and the regression line improved when the velocities of the bar were included in the regressions. The coefficient relating to the velocities of the bar was the damping coefficient. The stiffness and damping coefficients obtained in the regressions were then used to estimate the reaction forces during different trials of giant circles on the high bar. For the regular giant circle the reaction forces were estimated to within 65 N (0.11 BW). For the accelerated giant circles the reaction forces were estimated to within 136 N (0.22 BW). Therefore, if the stiffness and damping coefficients of the bar are known the reaction forces at the bar can be estimated with reasonable accuracy based purely on the displacement and velocity of the bar.

The coefficients obtained from the experimental data were used with the four segment simulation model to obtain optimised stiffness and damping coefficients which will be used in the evaluation and optimisation of the accelerated backward giant circles.

CHAPTER 7

EVALUATION OF THE SIMULATION MODELS

7.1 Introduction

The development of the single segment and four segment models was dealt with in Chapter 3. Yeadon and Challis (1994) described the need to evaluate theoretical predictions by comparing the results with experimental data. This chapter outlines the method used to determine the external validity of the models by using a combination of simulations and data obtained from the analysis of the backward giant circle.

The process of evaluating the models has been broken down into four sections. The first three of these sections are used to evaluate the assumptions made in the development of the simulation models and to determine whether there are any errors in the computer code.

Section 7.2 tests the assumption that the bar may be modelled as a linear spring. Simulations are performed to determine the peak angular velocity and reaction force during the downswing of a backward giant circle. The results of these are compared with data obtained from the video and force analyses of the backward giant circle.

Section 7.3 is used to check the computer code of the four segment model. If the four segment model is constrained to behave like the single segment model a similar set of results to section 7.2 should be obtained. In addition section 7.3 tests the assumption that a spring may be used to model the extension in the gymnast's shoulders.

The third section (7.4) investigates the use of joint angle time histories. A simplification of the four segment model will be used to demonstrate the use of the functions used to define the joint angle time histories. A three segment model which assumes rigid structures for the bar and gymnast will be used.

The final section (7.5) performs a complete kinetic and kinematic evaluation of the four segment simulation model. The joint angle time histories from the video analysis are used to drive the simulation model. A comparison between various output from the model are made with data obtained from the video and force analysis. An overall estimation of the accuracy of the four segment model will be determined from these results. An evaluation of the joint torques predicted by the model and those obtained from the muscle model will be made.

7.2 One segment model vs. kinetic and kinematic analysis

7.2.1 Introduction

Previous attempts to model a gymnast swinging on high bar have assumed that the bar was rigid (Dainis, 1968; Morlock and Yeadon, 1988). The analysis of the accelerated giant circle has shown that the bar achieves a vertical displacement of approximately 0.10 m as the gymnast passes through the lowest point. Neglecting the elastic properties of the bar during simulations may lead to an over-estimation of the model's angular velocity through the lowest point.

The purpose of this section is to determine the effect of an elastic bar on angular velocity and reaction force during a giant circle.

7.2.2 Methods

The equations of motion and their solution for the single segment model were dealt with in Chapter 3. The single segment inertia data of subject jb01 was used for all simulations (Table 7.1). The stiffness and damping coefficients for the spring representing the bar were those obtained from the analysis of the backward giant circle (Table 7.2). It was assumed that the bar was equally stiff in the horizontal and vertical directions.

Table 7.1. Inertia data used in the single segment simulation model (jb01)

segment	mass (kg)	length (m)	cmloc (m)	moment of inertia (kg.m ²)
whole body	62.050	NA	0.833	11.12

Three simulations were run, one where the bar was modelled as a rigid structure, one where the bar was modelled as a linear spring and one where the bar was modelled as a damped linear spring. For the purposes of modelling the bar as a rigid structure the stiffness coefficient was set to a value of 999999.0 N.m⁻¹ and the damping was set to zero. To model the bar as a linear spring with no damping the damping coefficient was set to zero. In each case the simulation was started with the model in the vertical handstand position with an initial angular velocity of 2.5 rad.s⁻¹. This was the angular velocity of the rotation angle as the subject through the handstand position at the beginning of the first giant circle of trial 4. The spring was given an initial length and velocity corresponding to those obtained from trial 4 as the gymnast passed through the

handstand position. The initial displacements and velocities of the bar are given in Table 7.3.

The outputs from the model comprised the peak angular velocity, reaction force, bar displacements and the energy possessed within the single segment system.

Table 7.2. Stiffness and damping coefficients used in the single segment model

bar	stiffness coefficient [N.m ⁻¹]	damping coefficient [N.s ² .m ⁻¹]
rigid	99999999.0	0.0
spring	26297.0	0.0
spring damped	26297.0	379.4

Table 7.3. Initial bar displacements and velocities obtained from the video analysis of the accelerated giant circle

direction	bar displacement [m]	bar velocity [m.s ⁻¹]
horizontal	0.0019	-0.0416
vertical	-0.0002	-0.0264

7.2.3 Results and Discussion

Figure 7.1 shows the energy during the simulation where the bar was modelled as a linear spring with no damping. The total energy is the sum of the potential, strain (stored in the bar) and kinetic energy. The model was designed and behaves as a conservative system, with no energy being lost during the simulation of one giant circle.

The peak angular velocity and reaction force (measured in bodyweights) for the three simulations and the results from the video analysis are presented in Table 7.4. Introducing an elastic bar reduced the peak angular velocity from 6.59 to 5.86 rad.s⁻¹, a reduction of 11%, and reduced the peak reaction force from 4.69 to 4.37 bodyweights, a reduction of 7%. However, the peak angular velocity obtained from the simulations where the bar was modelled as an elastic structure was still 6% greater than that obtained from the video analysis.

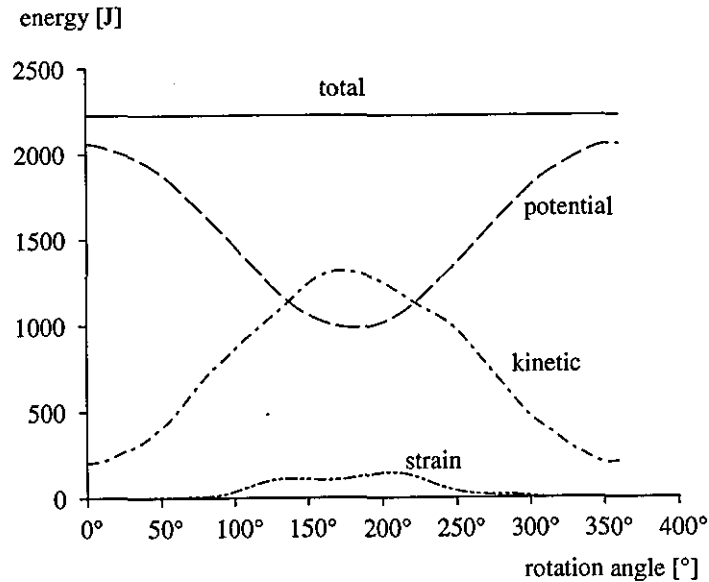


Figure 7.1. Total energy in the system and its components when the bar is modelled as a linear spring with no damping.

Table 7.4. Results obtained from the simulations using the single segment model and those obtained from the video analysis

	video analysis	rigid	spring	spring damped	
peak angular velocity	5.52	6.59	6.01	5.84	[s ⁻¹]
reaction force	3.97	4.69	4.55	4.37	[BW]

The reduction in the peak angular velocity may be accounted for in the following way. Figure 7.2 shows the kinetic energies (linear and rotational) and strain energy for the simulation where the bar was modelled as a linear spring without damping. Had the bar been modelled as a rigid structure the linear and rotational energy would have been greater, as the strain energy would have been distributed between them. As a consequence the peak angular velocity would be decreased when modelling the bar as an elastic structure. To determine the contribution of the strain energy to the reduction of peak angular velocity, the strain energy (133.0 J) stored in the bar at the lowest point of the giant circle was distributed proportionally between the linear and rotational energy. It was found that the strain energy accounted for 6% of the reduction in peak angular velocity.

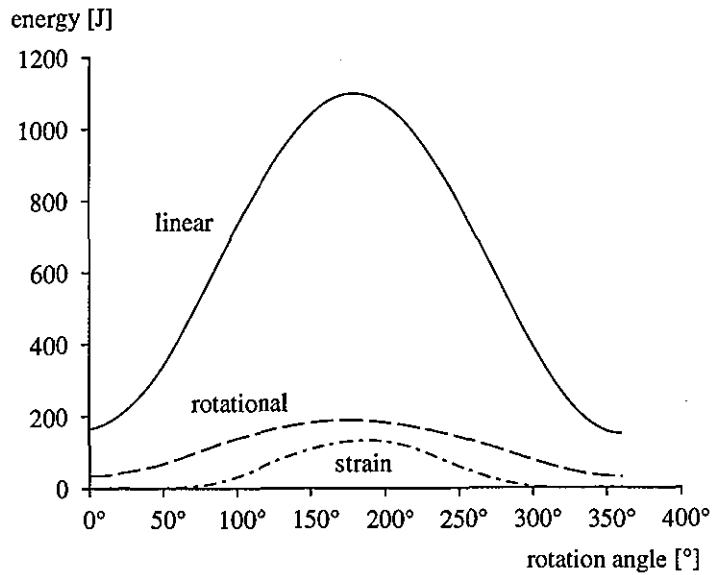


Figure 7.2. Contributions of the kinetic energies (linear and rotational) and strain energy to the total energy when the bar is modelled as a linear spring with no damping.

At the lowest point the bar became vertically displaced by 0.099 m (Figure 7.3). This in effect increases the moment of inertia of the model about the neutral bar position. Comparing this with results using a rigid bar model shows that the increase in moment of inertia reduces the peak angular velocity by 5%. Similarly the reduction in reaction force between the rigid and elastic models could be accounted for. It was found that the strain energy accounted for 1% and the increase in moment of inertia accounted for 4% of the reduction in reaction force.

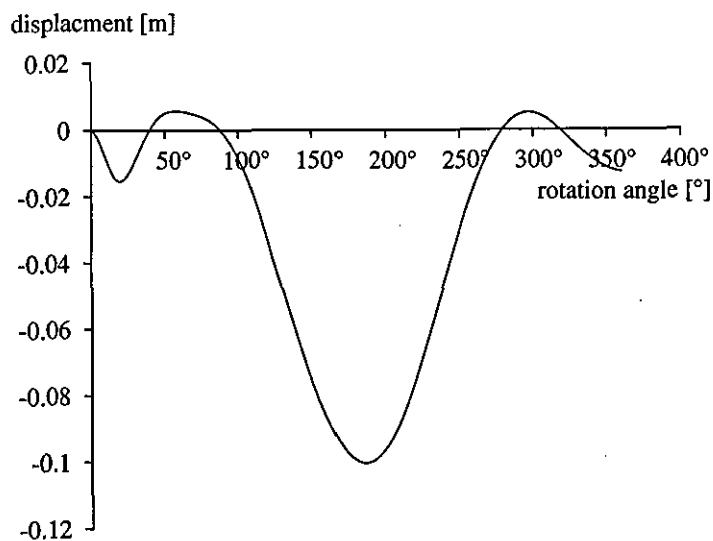


Figure 7.3. Vertical bar displacement when the bar is modelled as a linear spring with no damping.

7.2.4 Conclusions

The aim of this section was to determine the effect of bar elasticity on angular velocity and reaction force. It was found that the introduction of bar elasticity reduced the peak angular velocity by 11% and the reaction force by 7%. The reduction in peak angular velocity and reaction force could be explained in terms of the strain energy stored in the bar and the increase in moment of inertia of the model about the neutral bar position. When comparing the simulation model with the video analysis, the model overestimated the peak angular velocity by 6%, indicating that a single segment model which models the elasticity of the bar is close to representing a gymnast during the downswing phase of the giant circle. To reduce the differences in peak angular velocity and reaction force, obtained from the model and the video analysis, will require a more sophisticated model. In Chapter 6 it was found that the distance from the gymnast's wrist to hips varied during the backward giant circle, with the largest increase occurring as the gymnast passed through the lower part of the circle. This may lead to a further increase in the moment of inertia of the gymnast and to a possible storage of energy, similar to that seen in the bar. It was also found that the bar was less stiff in the horizontal direction than in the vertical direction. It is therefore suggested that when modelling a gymnast swinging on the high bar, both the elastic properties of the bar and of the gymnast are taken into consideration.

7.3 One segment model vs. four segment model

7.3.1 Introduction

The obvious limitation of the one segment model is its inability to simulate the techniques used by the gymnasts. However, it may be used to check the mechanics and programming of the more complex four segment model. If the four segment model is constrained to swing with a fully extended body shape, and the spring at the shoulders is made extremely stiff, it should behave as a single segment model. A comparison between the four segment and the single segment model would then be possible.

In section 7.2.4 it was hypothesised that the remaining difference in peak angular velocity obtained by the single segment model and that from the video analysis may be due to the extension in the shoulder region of the gymnast (Chapter 6). By introducing the correct spring parameters for the shoulder spring this hypothesis may be tested.

7.3.2 Methods

The same stiffness and damping coefficients were used for the single and four segment model. These were the same as those used in section 7.2 when the bar was model as a damped linear spring (Table 7.2). The inertia data from subject jb01 was used for both the single and four segment models (Tables 7.1 and 7.5). Since the one segment model did not account for the shoulder elevation found in Chapter 6 the inertia data in Table 7.5 was used. This inertia data has the segment lengths based on the anthropometric measurements taken from the subject and does not account for the elevation in the shoulder girdle. Similarly, so that a comparison between the single and four segment models can be made the bar was assumed to be massless in both cases.

Table 7.5. Inertia data used in the four segment simulation model (jb01)

segment	mass (kg)	length (m)	cmloc (m)	moment of inertia (kg.m ²)
arms	6.868	0.548	0.239	0.205
torso	33.566	0.435	0.337	1.610
thigh	14.074	0.374	0.151	0.173
l. leg	7.543	NA	0.227	0.164

For the purposes of comparing the four segment model and the single segment model the stiffness and damping coefficients of the shoulder spring were set to 999999.0 N.m⁻¹ and zero, respectively. To test whether the four segment model behaved as a conservative system a simulation was run with the damping coefficient of the bar spring set to zero.

The stiffness of the shoulder spring was reduced to test the hypothesis that a closer agreement to the video data may be obtained by introducing a spring at the shoulders. For this simulation the stiffness and damping coefficients of the shoulder spring were set to 12086.0 N.m⁻¹ and 18309.0 N.s².m⁻¹, respectively (Chapter 6). For all simulations the four segment model maintained a rigid and fully extended body shape.

Each simulation was started from the vertical handstand with an initial angular velocity of 2.5 rad.s⁻¹. The initial spring lengths and velocities are given in Table 7.3.

The outputs from the model comprised the peak angular velocity, reaction force, bar displacement, extension in shoulders and the energy possessed within the single and four segment systems.

7.3.3 Results and Discussion

Figure 7.4 shows the energy during the four segment simulation where the bar was modelled as a linear spring with no damping and the shoulders were modelled as a stiff structure. The total energy remained constant during the simulation of one giant circle, indicating that the model behaves as a conservative system. When the four segment model was compared with the single segment model the total energy in the system differed by less than 2%. This difference was most likely due to small differences in the whole body moment of inertia about the neutral bar position.

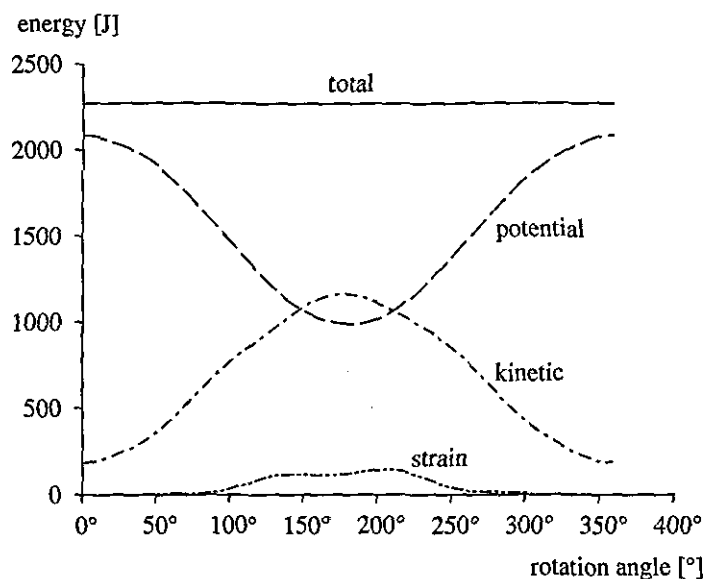


Figure 7.4. Total energy in the four segment system and its components when the bar is modelled as a linear spring with no damping.

The peak angular velocity and reaction force (measured in bodyweights) for the simulations and the results from the video analysis are presented in Table 7.6. When the four segment model is constrained to behave as a single segment model with rigid shoulders the appropriate results are obtained. Minor differences may occur due to the assumption that using a high stiffness coefficient results in a perfectly rigid structure and/or small differences in the whole body moment of inertia. However, the results of the single segment model and the constrained four segment model are practically identical. The introduction of the elastic shoulder structure caused a reduction in both peak angular velocity and peak reaction force. This small reduction will be due to the strain energy stored in the shoulder spring and the increase in moment of inertia about the neutral bar position caused by the lengthening of the shoulder spring. The peak strain energy increased from 133 J to 140 J with the introduction of the elastic shoulder structure. This corresponded to an increase in length at the shoulders of approximately 0.05 m.

Table 7.6. Results obtained from the simulations using the single and four segment model and those obtained from the video analysis

	video analysis	1 seg	4 seg	4 seg 2 springs	
peak angular velocity	5.52	5.84	5.83	5.78	[s ⁻¹]
reaction force	3.97	4.37	4.38	4.33	[BW]

Since the reductions in peak angular velocity and reaction force are only small when compared with the results of the single segment simulation model it may be speculated that the difference between the simulation model and the video analysis is due to the assumptions made in the models. Increasing the length of the torso to account for the elevation found in the shoulder girdle would increase the moment of inertia about the neutral bar position leading to a further reduction in peak angular velocity and reaction force as described in section 7.2. Similarly in Chapter 6 it was found that the bar was less stiff in the horizontal direction than in the vertical. With a less stiff bar the model would have a greater displacement about the neutral bar position, again increasing the moment of inertia of the model about the neutral bar position. The third explanation for the difference in peak angular velocities and reaction forces is the techniques adopted by the gymnast as he circles the bar. In Chapter 6 it was shown that during the downswing the gymnast performed actions at both the hips and shoulders.

The peak vertical displacements of the bar are given in Table 7.7 for the video analysis and the simulations. In all cases the displacements compare well. The closest agreement with the displacement obtained from the video analysis was when the shoulders were modelled as an elastic structure.

Table 7.7. Vertical bar displacements obtained from the simulations using the single and four segment model and those obtained from the video analysis

vertical displacement	video analysis	1 seg	4 seg	4 seg 2 springs	
bar	-0.11	-0.10	-0.10	-0.11	[m]

7.3.4 Conclusions

The aim of this section was to see if the four segment model would behave like the single segment model and to see whether the introduction of the spring at the shoulders improved the comparison between the video analysis and simulation. It was found that

the four segment model compared well with the single segment model, both in terms of peak angular velocity and reaction force. The single and four segment models were found to differ from the video analysis by 6% and 11% for peak angular velocity and reaction force. The introduction of the spring at the shoulders reduced the difference between video and simulation to 5% and 9%. The reduction in peak angular velocity and reaction force could be explained in terms of the strain energy stored in the shoulders and the increase in moment of inertia of the model about the neutral bar position. The vertical displacement of the bar and shoulders at the lowest point for the simulation and video compared well. It may be inferred that the use of springs to model the movements of the bar and shoulder structures is appropriate in this situation.

To reduce the differences in peak angular velocity and reaction force, obtained from the model and the video analysis, will require a more sophisticated model. Although the gymnast appears to be fully extended during the downswing phase of the backward giant circle this is not entirely the case. From Chapter 6 it was shown that the gymnast performs actions at the shoulders, hips and knees during the downswing. It is therefore suggested that in order to model the gymnast during the downswing, or during any part of the giant circle, the model must be capable of performing actions at least at the hips and shoulders and must also model the elastic properties of the bar and gymnast.

7.4 Three segment model

7.4.1 Introduction

Section 7.3 showed how linear springs improved estimates of peak angular velocity and reaction force when compared with data obtained from video analysis. In order to improve on these results and increase the number of applications the models are appropriate for use with, it is necessary that they are capable of performing actions at the shoulders, hips and to some extent the knees.

From sections 7.2 and 7.3 it could be argued that a three segment model assuming a rigid bar and gymnast is limited. However, this assumption reduces the complexity of the model so that a more clear understanding of the mechanics behind the techniques used on the high bar may be obtained without being complicated by the transfer of energy to and from the high bar.

Two simulations will be performed to demonstrate the use of the quintic function for defining joint angle time histories. The same method for defining joint angle time histories will be the proposed method in the optimisation of the accelerated giant circle, Chapter 8. In Chapter 3 a function was proposed which used a square acceleration

function for the angle changes. The application and implementation of this function is the same as the quintic function. The function with the square acceleration curve will be evaluated against the quintic function in Chapter 8. The three segment model will optimise a backward giant circle using both the quintic and square acceleration function.

7.4.2 Methods

The inertia parameters of subject jb01 were used in the three segment simulation model (Table 7.8). The three segments represent the arms, torso and leg segments of a gymnast. The model assumed that the bar and the gymnast's shoulders were rigid structures. Since there are no damped springs the system is designed to behave as a conservative system provided the configuration of the model is maintained. Two simulations were performed to evaluate the use of the two functions (described in Chapter 3) which are used to define the joint angle time histories of the model.

Table 7.8. Inertia data used in the three segment simulation model (jb01)

segment	mass (kg)	length (m)	cmloc (m)	moment of inertia (kg.m ²)
arms	6.868	0.584	0.239	0.205
torso	33.566	0.601	0.337	1.610
legs	21.617	NA	0.308	1.329

The first simulation was initiated with the model hanging in a stationary position vertically under the bar. Initially both the hip and shoulder angles were fully extended. After one second the shoulder angle was closed by 20°. This joint action took 0.3 s to complete. Once the joint action was complete the angle at the shoulder was maintained. The joint action was performed using the quintic function. Although the action has been termed "closing" the shoulder angle, due to the definition of the simulation model the angle at the shoulder will increase from 180° (fully extended) to 200°, a change of 20°.

The second simulation was initiated from the handstand position with both the hip and shoulders fully extended. The model had an initial angular velocity of 1.0 rad.s⁻¹. The model was allowed to swing to the lowest point (rotation angle of 180°) with both joints fully extended. After a rotation angle of 180° the hip angle was closed by 20°. This action also took 0.3 s to complete. After the joint action had been performed the angle at the hip was maintained. The joint angle time history was defined using the quintic function.

The output from the simulation models comprised time histories of the joint angles, whole body rotation angles, angular velocities, energy, reaction forces at the bar and internal joint torques.

7.4.3 Results and Discussion

The joint angle time history of the shoulder joint for the first simulation is shown in Figure 7.5. The joint angle was initially at 180° and increased to 200° in 0.3 s as defined by the quintic function. The path of the mass centre during the simulation is given in Figure 7.6. Initially the mass centre is directly beneath the bar, as would be expected if the model were hanging in a stationary position. As the joint action at the shoulders is initiated the mass centre is displaced both upwards and backwards. After the joint action was completed the mass centre began to move in a circular path. Displacing the mass centre in the horizontal direction created a torque due the model's weight about the bar. This torque in turn created an angular acceleration of the model about the bar and hence the model started to swing. The vertical reaction force at the bar is shown in Figure 7.7. Since the mass centre was displaced upwards one would expect the force curve obtained in Figure 7.7.

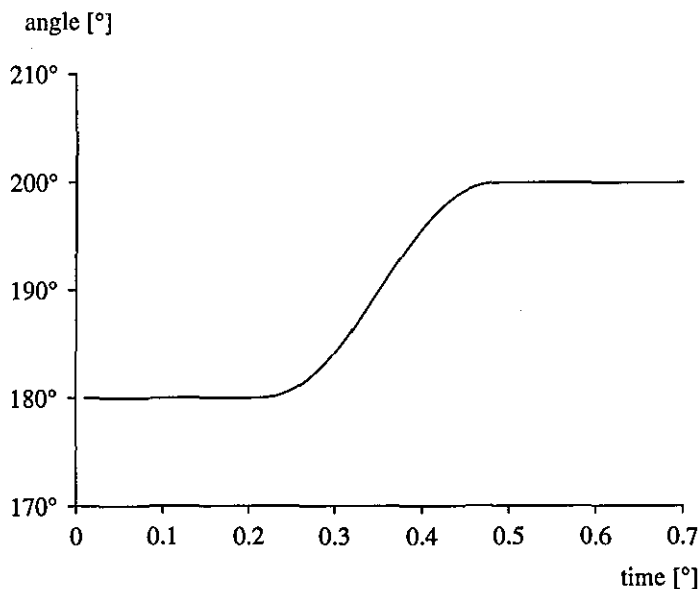


Figure 7.5. Joint angle time history of the shoulder joint from simulation one.

The angular velocity and acceleration of the change in the shoulder joint angle are presented in Figure 7.8. Both the angular velocity and acceleration start and finish at zero as defined by the quintic function. The torque required to produce the joint action is presented in Figure 7.9. The torque represents the muscular force produced by the

muscles surrounding the shoulder joint. The joint torque is initially zero since no muscular force is required to maintain the joint angle in the hanging position. During the joint action the torque follows a similar shape as the acceleration of the joint angle (Figure 7.8). The similarity between the joint torque and acceleration may not be as well defined in the second simulation due to the torques required to maintain the joint angles during the swing. The torque required to perform the joint action is positive, as would be expected. At the end of the joint action the torque does not return to zero (Figure 7.9). The joint torque is required to maintain the new joint angle as it swings about the bar. The sign of the torque remains positive, indicating that a joint torque that tends to close the shoulder angle is required to maintain the joint angle.

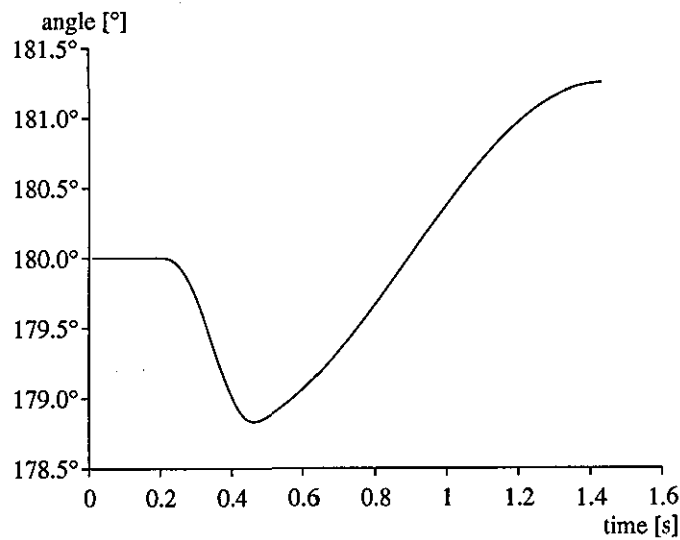


Figure 7.6. Time history of the rotation angle during simulation one.

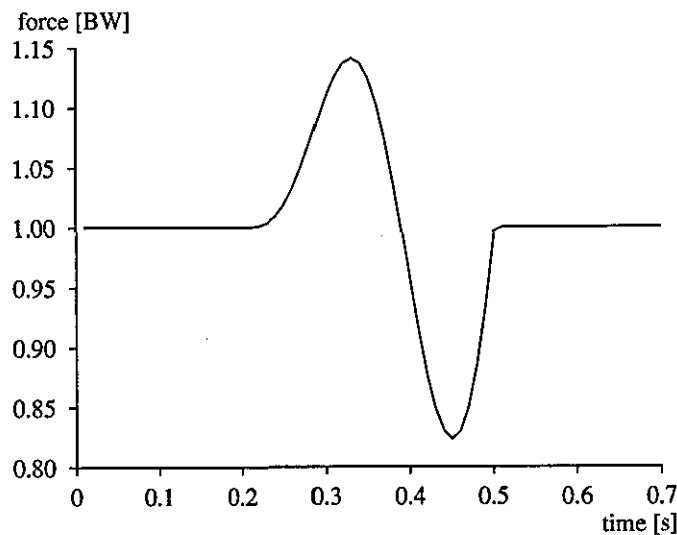


Figure 7.7. Time history of the vertical reaction force during simulation one.

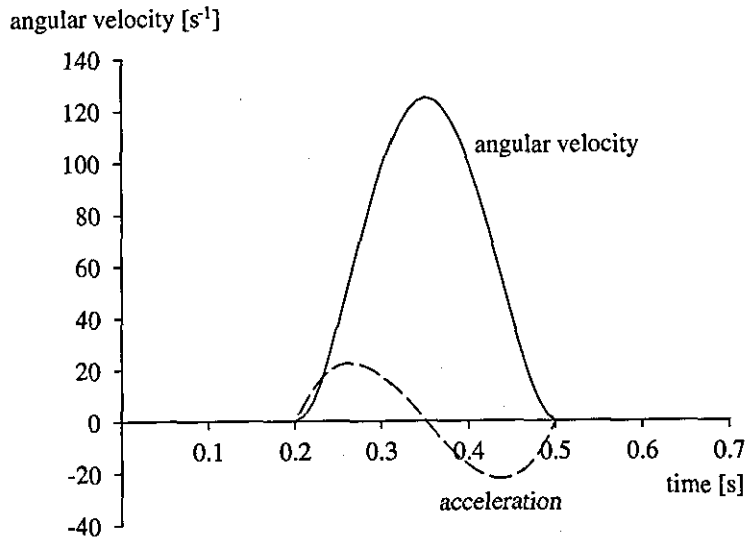


Figure 7.8. Time history of the shoulder joint angular velocity (solid line) and acceleration (dashed line, in $.s^{-2}$) from simulation one.

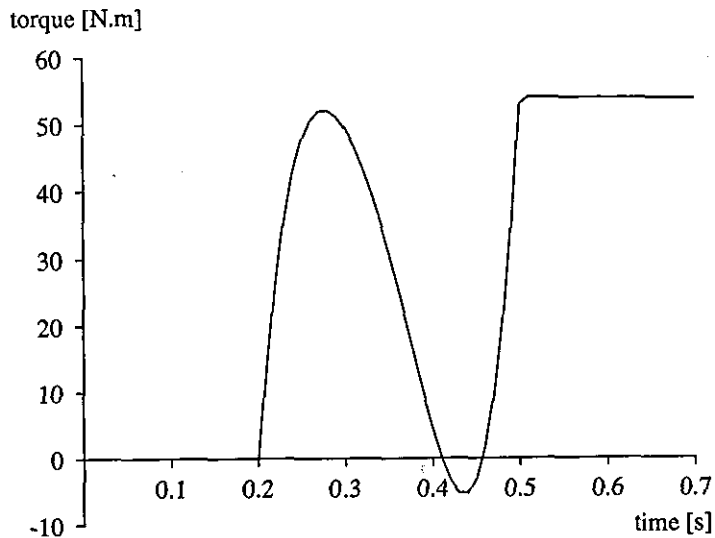


Figure 7.9. Time history of the shoulder torque during simulation one.

During the joint action the mass centre was displaced vertically. Raising the mass centre would lead to an increase in potential energy. The joint action, if performed by a gymnast, would be created by the muscles surrounding the shoulder structure. The action is performed using muscular energy which is transformed in mechanical energy. It would therefore be expected that closing the joint angle would lead to an increase in energy in the system. Figure 7.10 shows the *time history* of the energy during the first simulation. Initially the energy is zero as the model hangs beneath the bar. As the joint action occurs the energy in the system is increased. At the end of the simulation the model has more energy than at the start.

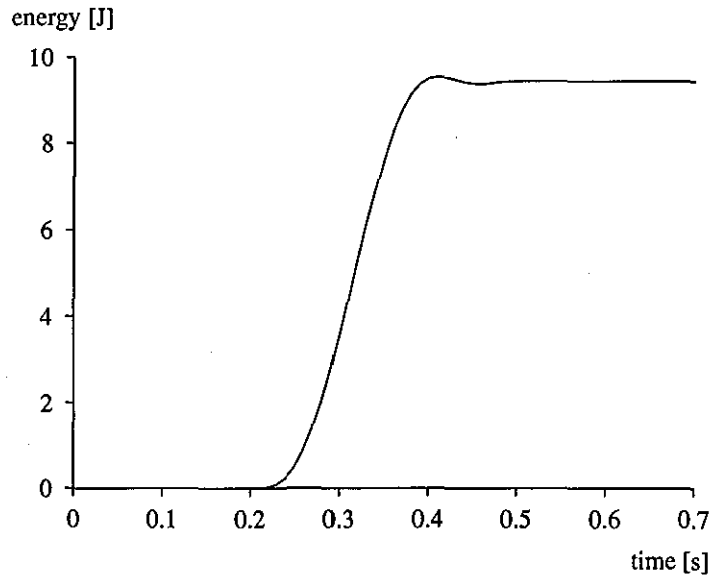


Figure 7.10. Time history of the energy during simulation one.

The joint angle time history of the hip joint from the second simulation is plot against rotation angle in Figure 7.11 a) and against time in Figure 7.11 b). The hip angle is maintained until a rotation angle of 180° is achieved. Thereafter the hip angle increases by 20° as defined by the quintic function. The shape of the graph in Figure 7.11 b) is identical to the graph in Figure 7.5. This would be expected since both the hip and shoulder angles were changed by the same amount in the same time period. Similarly the angular velocity and acceleration of the hip joint angle is shown in Figure 7.12 a) and b) against rotation angle and time respectively. Again Figure 7.12 b) is identical to Figure 7.8 as would be expected.

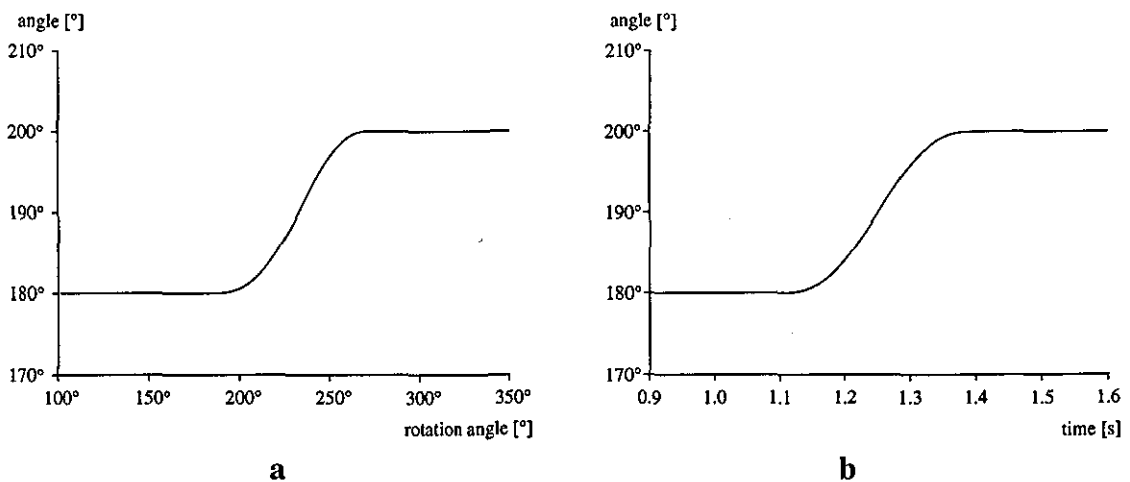


Figure 7.11. Angle at the hip during simulation two.

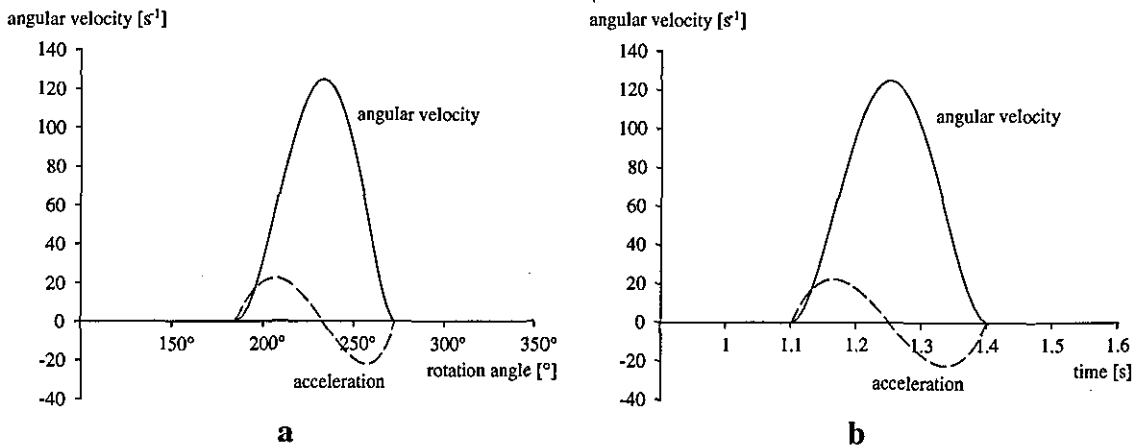


Figure 7.12. Time history of the shoulder joint angular velocity (solid line) and acceleration (dashed line, in $.s^{-2}$) from simulation two.

The joint torque at the hips for the second simulation is shown in Figure 7.13. The torque has been graphed against rotation angle. During the downswing the torque at the hips increases to 28 Nm then decreases back to zero as the rotation angle reaches 180°. In the first simulation it was shown that no torque at the shoulders was required to hang beneath the bar. Similarly, if the model were in a stationary handstand above the bar the same would be true. During the downswing a torque tending to close the hip angle is produced. If, therefore, at the start of the downswing the torque was set to zero, and maintained at zero, the hip angle would open as the model circled the bar. That is, the model would hyper-extend at the hips. These results were also obtained by Morlock and Yeadon (1988). Figure 7.13 shows the joint torque obtained from the second simulation with the torque at the hips had the joint action not occurred overlaid (dashed line). Had the joint action not occurred the torque at the hips would have changed from positive to negative as the model passed through the lowest point of the giant circle. To maintain a 180° angle at the hips during the upswing a negative joint torque is required (Figure 7.13). That is, a torque tending to open/hyper-extend the hip angle. If at the lowest point the joint torque at the hips was set to zero and maintained at zero the hip angle would close during the upswing performing a flexion action.

The total energy in the system is graphed against rotation angle in Figure 7.14. As in the first simulation the joint action at the hip increased the energy in the system. The most noticeable difference between Figure 7.14 and Figure 7.10 is the initial drop in energy prior to the increase. The initial drop in energy is due to the torque required to perform the angle change. As explained above, as the the model passes through the lowest point the torque required to maintain the extended body shape changes from a torque which tends close the hip angle to one which tends to open the hip angle. Therefore, if at the lowest point the torque at the hip were set to zero the hip angle would close by itself. If, however, the model were made to perform a flexion action at the

lowest point which resulted in an angle change slower than if the joint torque were set to zero, eccentric work would be performed. This would therefore result in a loss of energy from the system. The angle change in this simulation starts slowly, hence the small drop in energy. It is therefore feasible that a hip flexion could be performed that would result in an overall loss in energy.

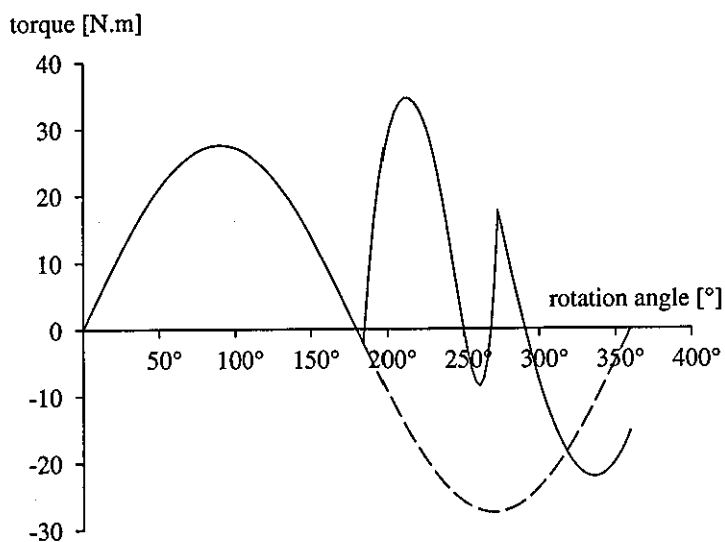


Figure 7.13. Torque at the hip during simulation two (solid line) along with the torque at the hip had the angle change not occurred.

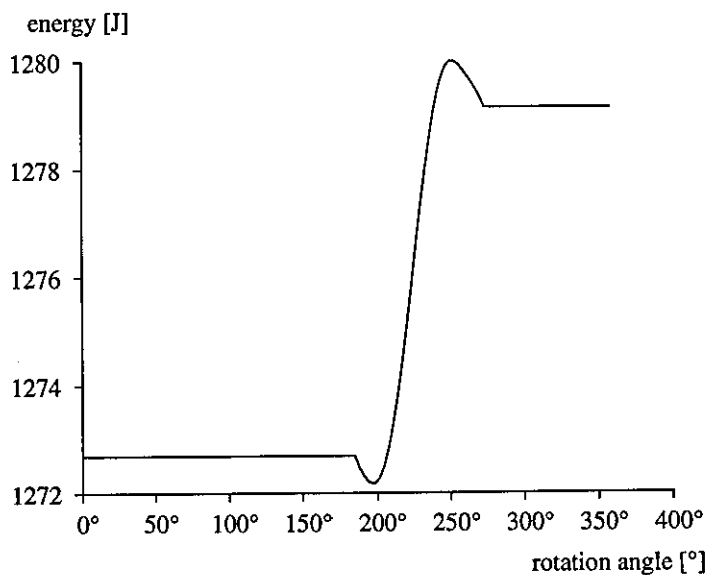


Figure 7.14. Energy during simulation two.

7.4.4 Conclusions

It has been shown that the quintic function can be used to change joint angles during simulations whether the model is stationary or swinging. The second simulation confirmed the findings of Morlock and Yeadon (1988) and Okamoto et al. (1987) that torques tending to close the angles at the hip and shoulder joints are required to maintain the extended body shape during the downswing. Similarly on the upswing it was found that torques tending to open the hip and shoulder angles are required to maintain a fully extended shape. In both simulations it was shown that closing the hip or shoulder angle lead to an increase in energy. In simulation one the increase in energy would be mainly due to the increase in potential energy caused by raising the mass centre. In simulation two the increase would be due to raising the mass centre, and also due to the reduction in moment of inertia of the model about the bar which leads to a proportional increase in the angular velocity and also, therefore, to $\frac{1}{2}I\omega^2$.

The use of the flexion action to increase the energy in the system is common knowledge. However, it has been shown that it would be possible to perform a flexion action through the bottom of the giant circle that would result in a loss of energy. This is due to the joint torques required to perform the action. If the action were such that eccentric work was required then energy would be lost.

7.5 Four segment model vs. kinetic and kinematic analysis

7.5.1 Introduction

In the previous three sections an evaluation of the concepts behind the four segment model have been evaluated. It has been shown that modelling the movements of the bar and extension in the gymnast's shoulders using springs improves the comparison between simulated and experimental results. Section 7.4 has shown that the actions at the hips and shoulders may be performed using a quintic function.

This section compares the output from the four segment simulation model with the video and force data collected in Chapter 5. The results of the comparisons will give an indication as to the accuracy of the four segment model.

7.5.2 Methods

The four segment simulation model was evaluated by comparing the output with

the results from the analysis of the backward giant circles (Chapter 6). The simulation model was used to simulate the accelerated giant circles from trials 4 and 11. The input to the simulation model comprised the inertia data for the subject who performed the trials analysed in Chapters 5 (Table 6.14), the eighteen muscle parameters for each joint (Appendix 2d), the bar and shoulder spring coefficients (Table 6.36) and the spline coefficients for the bar displacements, joint angle time histories of the hips, shoulders and knees, the angle time history of the arm segment and the rotation angle.

The initial conditions for the body configuration and orientation were obtained from evaluating the splined joint angle time history data and the arm segment orientation data. The first and second derivatives of these angles were also obtained by evaluating the first and second derivatives of the spline data. Similarly the initial bar displacements and velocities were obtained from spline data. Both simulations were started from a rotation angle of 90° and finished at a rotation angle of approximately 630° . To test the sensitivity of the angle at which the simulations were started an additional two simulations were performed with an initial rotation angle of 0° .

The output from the model comprised the whole body angle of rotation from both the simulation model and the splined equivalent, the time histories of the bar displacements, the time histories of the joint torques and the horizontal and vertical reaction forces at the bar.

Rms differences between the recorded (data from the force and video analysis) and the simulated rotation angle, bar displacements and reaction forces at the bar were calculated. The percentage differences between the maximum joint torques produced using the 18 parameter muscle models and those produced by the simulation model were calculated. The comparisons between recorded and simulated output were carried out for both trials.

7.5.3 Results and Discussion

The rms differences between simulated and recorded rotation angle for the both trials are presented in Table 7.9. The rms differences in rotation angle indicates by how much on average the simulations differed from the video data. In the same table the peak absolute errors in rotation angle for both trials are presented. The peak absolute errors are also expressed as a percentage of the whole angle rotated through in the trial. In both trials the rms differences in rotation angle are less than 5° . This corresponds to a difference of less than 0.02 revolutions. In Figure 7.15 the simulated and recorded rotation angle from trial 4 are plot against time. The two curves lie very close to one another. From Table 7.9 the maximum deviation of the two curves seen in Figure 7.15 is 6.9° . Both simulations were started from a rotation angle of 90° . This angle was chosen

to be the same as the start angle used in the optimisation of the spring parameters (Chapter 5). To test the sensitivity of the simulation model both simulations were repeated at an initial rotation angle of 0° . For trial 4 the rms difference was reduced from 4.2° to 4.0° when starting from the handstand position. However, for trial 11 the rms difference increased from 2.2° to 9.5° . The rms difference of 9.5° still corresponds to an error in rotation of less than 0.03 revolutions and less than 2% when expressed as a percentage of the angle rotated through. It appears as though the model is sensitive to the angle at which the simulation is initiated from. For trial 11 the rms difference has been shown to range from 2.2° to 9.5° . Based on the four simulations the model is able on average to predict the rotation angle to within 5° at any point during the simulation of the accelerated giant circles.

Table 7.9. Maximum and rms differences between simulated and recorded rotation angles

trial	rms difference ($^\circ$, revs, %)	max difference ($^\circ$, revs, %)
4	4.21, 0.01, 0.8%	6.87, 0.02, 1.3%
11	2.21, 0.01, 0.4%	3.97, 0.01, 0.7%

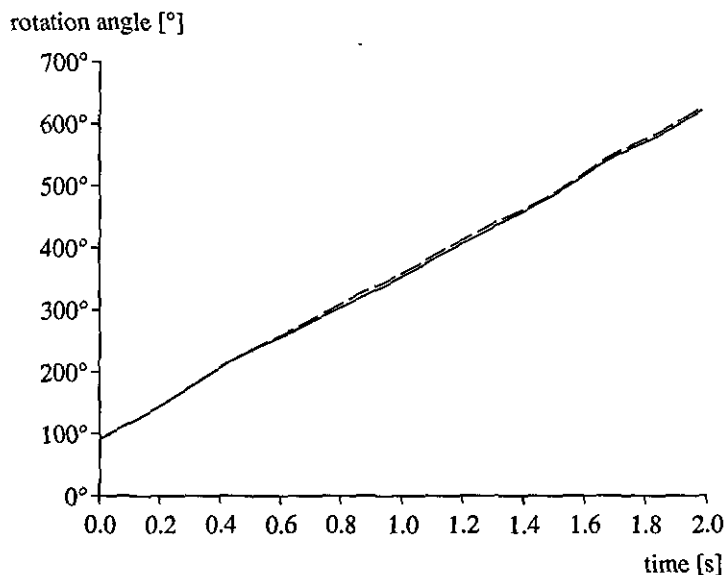


Figure 7.15. The simulated (solid line) and recorded (dashed line) time history of the rotation angle from trial 4.

The rms differences for the bar displacements are given in Table 7.10. The rms differences are slightly larger in the horizontal direction than in the vertical direction. On average the rms differences of the bar displacements is 0.011 m. This is of the same

magnitude as the error that was found in the reconstruction of the three-dimensional coordinates in the video analysis (Chapter 6). The bar displacements from the simulation model compare well with those obtained from the video analysis. The horizontal displacement of the bar during the simulated trial 4 and the the horizontal displacements from the video analysis are shown in Figure 7.16. The equivalent diagram for the vertical displacements is shown in Figure 7.17. In Figures 7.16 and 7.17 the simulated and recorded bar displacements are very similar. However, in both the horizontal and vertical directions the maximum difference between the two sets of data is over 0.02 m (Table 7.10). In both trials the simulation model produced peak bar displacements which were greater than those from the video analysis. Since the force recorded at the bar has been shown to be closely related to the displacement in the bar it might be expected that the simulation model will also over-estimate the forces at the bar.

Table 7.10. Maximum and rms differences between simulated and recorded bar displacements

trial	rms difference (m)		max difference (m)	
	horiz.	vert.	horiz.	vert.
4	0.011	0.008	0.031	0.021
11	0.015	0.010	0.037	0.025

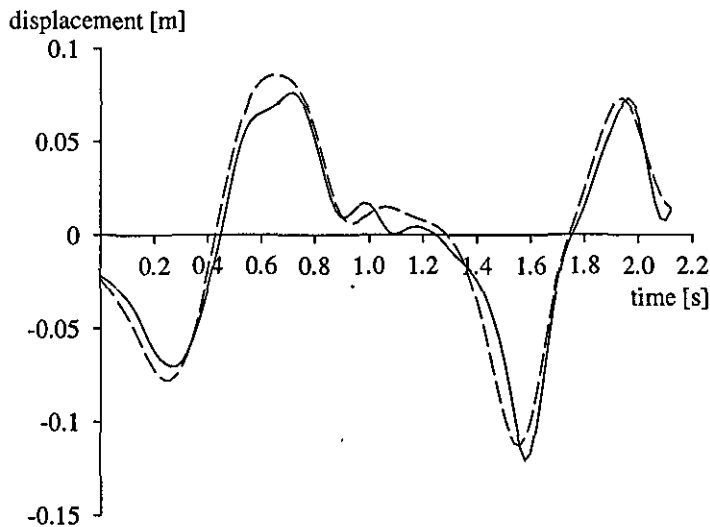


Figure 7.16. The simulated (solid line) and recorded (dashed line) time history of the horizontal bar displacements trial 11.

The rms differences for the simulated and recorded force in both the horizontal and vertical directions are presented in Table 7.11. In the horizontal direction the simulation

model was able to predict the force at the bar on average to within a third of a body-weight. As expected from the bar displacement the peak force in the horizontal direction predicted by the model is greater than the peak recorded horizontal force. At worst the largest difference between simulated and recorded horizontal force was 0.62 body-weights. It must be noted that this is the largest error in the horizontal direction and that on average the model was able to predict the horizontal force to within a third of a bodyweight (Figure 7.18).

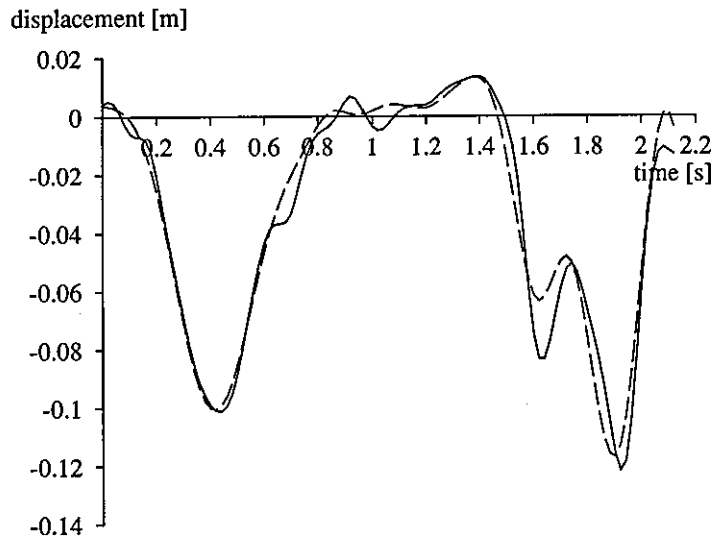


Figure 7.17. The simulated (solid line) and recorded (dashed line) time history of the vertical bar displacements from trial 11.

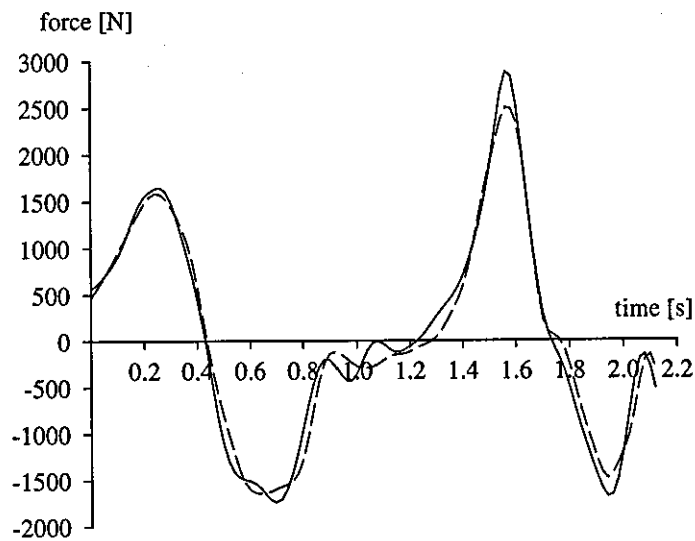


Figure 7.18. The simulated (solid line) and recorded (dashed line) time history of the horizontal force at the bar from trial 11.

Table 7.11. Maximum and rms differences between simulated and recorded forces

trial	rms difference (BW)		max difference (BW)	
	horiz.	vert.	horiz.	vert.
4	0.291	0.457	0.824	1.245
11	0.262	0.472	0.615	1.345

The simulated and recorded forces in the vertical direction are shown Figure 7.19. In the vertical direction the simulation model was able to predict the force at the bar to within half a body weight. Like the simulated force in the horizontal direction, the peak force in the vertical direction estimated by the model is greater than the peak recorded vertical force. At worst the largest difference between estimated and recorded horizontal force was 1.35 bodyweights. It again must be noted that this is the largest error in the vertical direction and that on average the model was able to predict the horizontal force to within a half a bodyweight during a simulation lasting over 2 s and passing through a rotation angle of 630° (Figure 7.19).

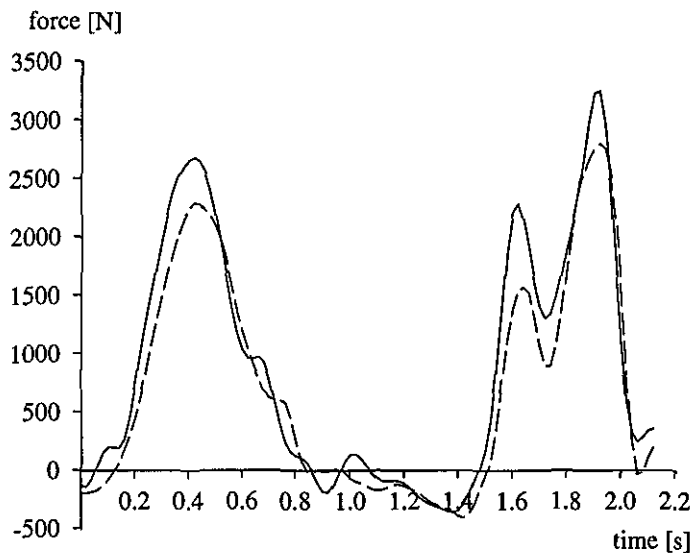


Figure 7.19. The simulated (solid line) and recorded (dashed line) time history of the vertical force at the bar from trial 11.

The time histories of the joint torques obtained from the simulation model and the maximum joint torques given by the three-dimensional muscle surfaces are given in Figures 7.20 and 7.21 (shoulders and hips respectively). In Figure 7.20 it can be seen that the joint torque at the shoulders obtained from the simulation model never exceeds the maximum joint torques given by the muscle surfaces. By expressing the shoulder torque as a percentage of the maximum torque obtained from the muscle surface fits it was found

that on average the gymnast required only 20% of the joint torque available to perform the accelerated giant circles.

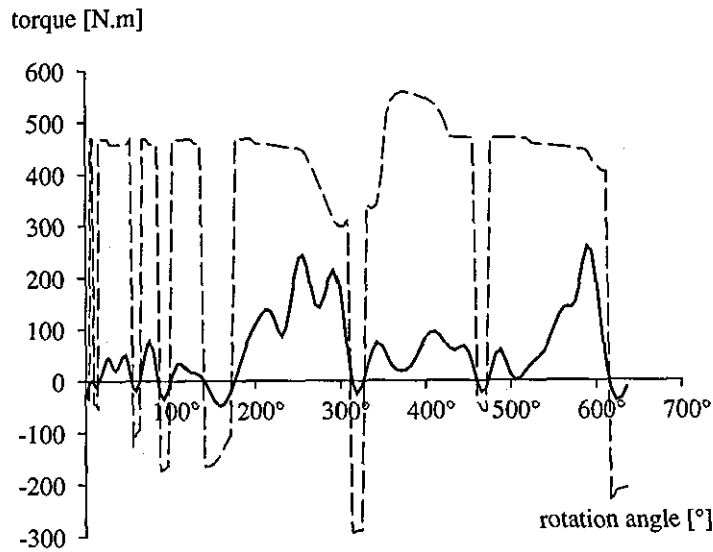


Figure 7.20. Joint torques at the shoulders obtained from the simulation model (solid line) and the maximum joint torques estimated by the 3D muscle surface fits (dashed line) during trial 11.

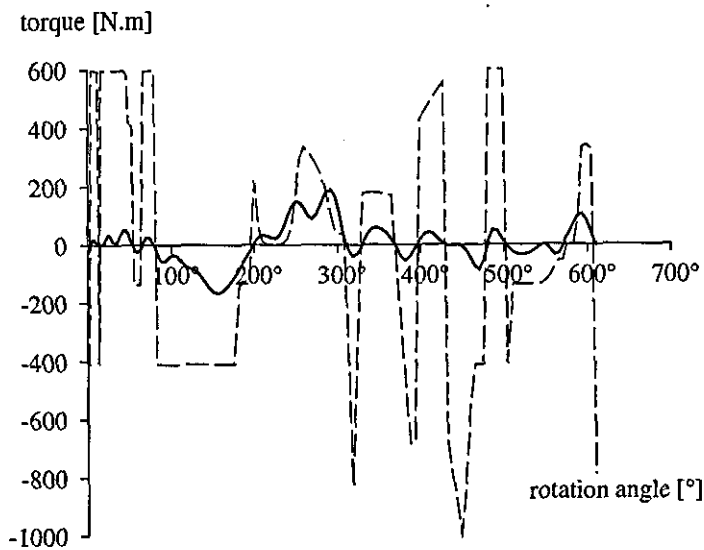


Figure 7.21. Joint torques at the hips obtained from the simulation model (solid line) and the maximum joint torques estimated by the 3D muscle surface fits (dashed line) during trial 11.

In Figure 7.21 there are three points where the hip torque obtained from the simulation model exceeds that given by the muscle surface fits. The first two occur between the rotation angles of 200° and 300° and the third occurs between the rotation angles of 575° and 590° . In all three cases this occurs when there is a large angular

velocity at the hip (Figure 7.22). That is, when the angle at the hip is changing rapidly the muscle surface predicts that the gymnast was unable to produce sufficient torque to perform the accelerated giant circle. However, at all three points that the maximum joint torque is exceeded the actual torque used by the simulation model is small (between 0 and 190 Nm). Also at the high angular velocities, in excess of $250\text{ }^{\circ}\cdot\text{s}^{-1}$ no isokinetic data were recorded. Therefore, the muscle surfaces rely on the surface fit to predict the joint torques at these high angular velocities. Given these considerations the muscle models behave well and will be used in the optimisation of the accelerated giant circles.

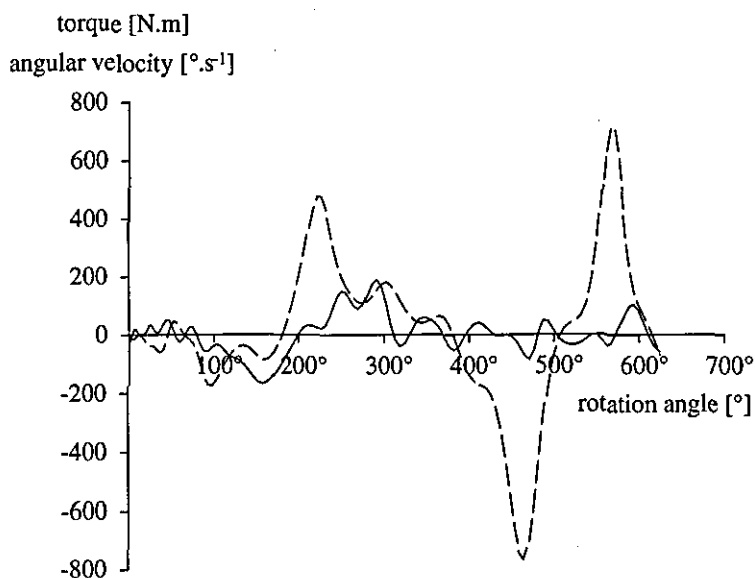


Figure 7.22. Joint torques at the hips obtained from the simulation model (solid line) and the angular velocity of the hip joint (dashed line) during trial 11.

7.5.4 Conclusions

The simulation model is able to predict the rotation angle on average to within 5° at any point during the simulations. This is during a simulation lasting almost one and three quarter revolutions. The four segment model is able to successfully simulate a gymnast performing accelerated giant circles on the high bar. The bar displacements estimated by the simulation model also compare well with the data obtained from the video analysis. The average difference between the simulated and measured bar displacements was approximately 0.011 m.

In the horizontal direction the simulation model estimated the reaction force to within a third of a bodyweight. The same value in the vertical direction was less than half a bodyweight. Although the comparisons between the estimated and recorded reaction forces were good (Figures 7.18 and 7.19) the peak force estimated by the simulation

model was greater than the peak force recorded during the analysis of the accelerated backward giant circles.

For the accelerated giant circle the shoulder joint torques obtained from the simulation model were on average 20% less than the maximum torques predicted by the muscle surfaces. On three occasions the hips torques predicted by the simulation model were greater than the maximum torques predicted by the muscle surfaces. The hip torque required by the simulation model were relatively small and given that at the high angular velocities the muscle model relies of the shape of the surface fit, since no data were available in that range, the muscle models performed well.

7.6 Summary

In section 7.2 it was shown that a damped linear spring representing the elastic properties of the high bar reduced the peak angular velocity and reaction force of a single segment model. These reductions were accounted for by the strain energy stored in the bar and the increase in moment of inertia about the neutral bar position caused by the displacement of the linear spring. When compared with the results from the video analysis of the backward giant circles the single segment model was able to successfully simulate the downswing. Peak angular velocity estimated by the single segment model was only 6% greater than that obtained from the video analysis.

In section 7.3 the four segment model was shown to behave like the single segment model when it was forced to maintain a fully extended configuration and assume a rigid structure for the shoulders. The shoulders were made rigid by the use of a large stiffness coefficient for the shoulder spring. This result confirmed that the model behaved as it was designed to. Introducing elasticity into the shoulders further reduced the peak angular velocity and reaction force. Again these reductions could be explained in terms of the energy stored in the bar and shoulders and the increase in moment of inertia about the neutral bar position. This second reduction was not sufficient to reduce the difference between simulated and recorded peak angular velocity below 5%. It was speculated that further reduction would probably occur as a result of the actions performed at the hips, shoulders and knees.

The quintic function described in Chapter 3 was used in a three segment simulation model to demonstrate its use in defining joint angle time histories. Using two simulations it was shown that performing a flexion action at the hips or shoulders during the lower part of the giant circle would lead to an increase in energy. It was also shown that for a gymnast to swing from handstand to handstand with an extended configuration, torques at the hips and shoulders tending to close the joint angles would be required during the

downswing and torques tending to open the joint angles would be required during the upswing.

The evaluation of the four segment model using force and video data was carried out in section 7.5. The model was able to estimate rotation angle to within 0.015 of a revolution during a simulation covering a range of 630°. Reaction forces also compared well within the experimental data with horizontal and vertical reaction forces being estimated to with one third and one half of a bodyweight respectively.

It is therefore concluded that the four segment simulation model is sufficiently accurate to be applied to the task of optimising the accelerated giant circles prior to release for a double layout backward somersault dismount.

CHAPTER 8

OPTIMISATION OF THE ACCELERATED BACKWARD GIANT CIRCLE

8.1 Introduction

The simulation models developed in Chapter 3 were evaluated in Chapter 7. With the accuracy of the models known it is now possible to apply them to specific tasks. The task chosen for this thesis is the optimisation of the accelerated backward giant circle.

The optimisation of the giant circle will first be carried out using the three segment simulation model introduced in Chapter 7. Then the four segment simulation model will be used to optimise the backward giant circle prior to release for a double layout backward somersault dismount.

The aim of the optimisations is to obtain techniques which may be used by all gymnasts. For this reason sensitivity analyses will be performed to determine the effects of varying the model parameters.

8.2 Three segment simulation model

8.2.1 Introduction

Although the external validity of the model is less than that of the four segment model, useful information regarding the mechanics of swinging may be obtained. The underlying mechanics of swinging will be determined from the three segment model which can then be applied to the results obtained from the four segment model. Since the four segment model is more complex these underlying principles may not be observed so easily.

8.2.2 Methods

The three segment simulation model used in Chapter 7 to evaluate the piecewise quintic function as a method of defining joint angle time histories was used to optimise the backward giant circle. It was assumed that the bar and the gymnast were rigid structures. The inertia data of both subjects, jb01 and tv01, were used in the three

segment model (Table 8.1). The centre of mass location (cmloc) is measured from the proximal joint centre and the moments of inertia are about the mass centre of each segment. For the application of optimising the backward giant circle the computer code of the three segment model was implemented with the Simulated Annealing algorithm (Goffe et al., 1994).

The criteria for the optimisation was to maximise the rotation possessed by the model after rotating through an angle of 450° . All simulations performed in the optimisation were started at a rotation angle of 0° (the handstand position). At the end of each simulation the model will have passed through $1\frac{1}{4}$ rotations. Within each simulation the model was required to perform a flexion and extension action at the hips and shoulders (Figure 8.1). In all simulations the angles at the hips and shoulders were initially extended (180°). It was decided that the model should also finish the simulation in the fully extended shape. Simulations not finishing in the extended shape were given a score of zero. Since the model would finish each simulation at the same rotation angle and in the same shape the angular velocity of the model was a sufficient indicator of the angular momentum it possessed.

Table 8.1. Inertia data used in the three segment optimisation of the backward giant circle

subject	segment	mass (kg)	length (m)	cmloc (m)	moment of inertia (kg.m ²)
jb01	arms	6.868	0.548	0.239	0.205
	torso	33.566	0.435	0.337	1.610
	legs	21.617	NA	0.308	1.329
tv01	arms	6.796	0.575	0.250	0.252
	torso	34.450	0.466	0.351	1.617
	legs	23.554	NA	0.330	1.539

Three restrictions were placed on the flexion and extension actions. Firstly the flexion had to be performed before the extension. This meant that the model would not simulate the hyper-extension at the hips seen in the giant circles analysed in Chapter 5. Secondly the hip and shoulder angles were closed and opened simultaneously and by the same amount. Finally the duration of the flexion and extension movements were forced to last longer than 0.01 s. With the integration interval used with the three segment model, 0.0001 s, this would result in a minimum of 100 integrations being performed for each flexion or extension movement.

Two initial optimisations were performed using the inertia data of subject jb01. The simulations performed within the optimisation were started from a rotation angle of 0° with an initial angular velocity of $1.0 \text{ rad}\cdot\text{s}^{-1}$. During the flexion movement the hip and shoulder angles were closed by 40° (Figure 8.1). During the extension movement the hip and shoulder joints were therefore opened by 40° . The joint angle time histories were defined using the piecewise quintic function. The initial angular velocity and size of the joint angle changes were chosen from the analysis of the backward giant circles in Chapter 5. The first optimisation was performed without a joint torque limit. The second optimisation was performed using a joint torque limit of 250 Nm at the shoulder joint. The shoulder torque was chosen to be limited since it was more likely that this limit would be exceeded when compared with the hip torque of a real gymnast. If during the second optimisation the joint torque at the shoulders exceeded 250 Nm the simulation was given a score of zero.

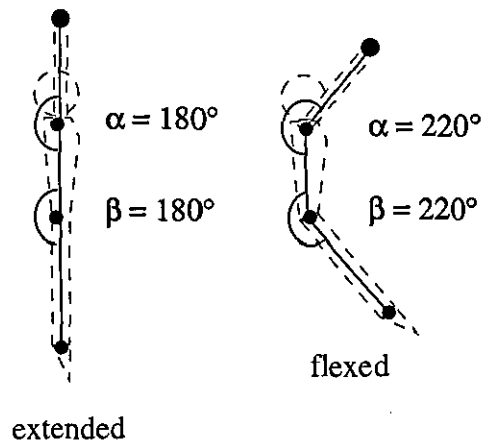


Figure 8.1. Angles at the hips and shoulders.

The above optimisations were repeated so as to perform a sensitivity analysis on the inertia parameters and the function used to define the joint angle time histories. The initial two optimisations were performed using the three segment inertia parameters of subject jb01 (Table 8.1) and the piecewise quintic function to define the joint angle time histories. The second pair of optimisations were performed using the square acceleration function and the inertia parameters of subject jb01. The third pair of optimisations were performed using the inertia data of subject tv01 (Table 8.1) and the piecewise quintic function.

8.2.3 Results and discussion

Without joint torque limit

The optimal solution for optimisation with no torque limit is given in Table 8.2. The table displays the rotation angle at the initiation of the joint angle changes during the flexion and extension phases of the giant circle. It can be seen that the flexion was initiated before the model had reached the lowest point of the circle (Figure 8.2).

Table 8.2. The optimum accelerated giant circle (without joint torque limit)

phase	body angle		joint angles	
	start	finish	start	finish
flexion	127°	191°	180°	220°
extension	334°	347°	220°	180°

For simplicity the backward giant circle has been broken down into the flexion and extension actions. Figure 8.3 shows the angular velocity of the model at a rotation angle of 270° plot against the rotation angle at the mid point of the flexion action. The curve is that of the optimum duration with each circle representing a single simulation. It can be seen that the optimal flexion occurs with a mid-point of 160°. However, the curve is shallow. This shows that the optimal solution is not very sensitive to where the flexion action is started. That is, the flexion may be started from a wide range of angles without a great difference in final angular velocity.

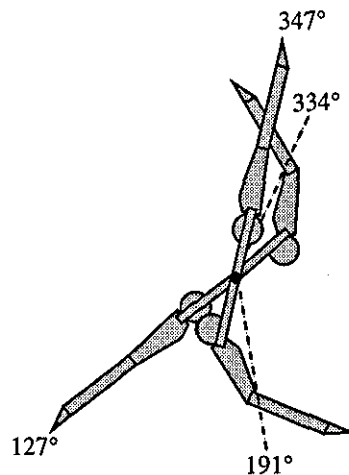


Figure 8.2. Optimal solution with no joint torque limit.

To explain the mechanics behind the flexion and why it was initiated before the lowest point of the giant circle, consider the giant circle as four separate quadrants (Figure 8.4). Using these quadrants (Figure 8.4) the majority of the flexion occurred in the second quadrant. The purpose of the flexion is to increase the energy in the system by increasing both the potential and rotational energy. If the flexion were to occur in the first or fourth quadrant the rotational energy possessed by the model would increase but the potential energy would decrease. It would therefore be expected that the flexion should occur in either the second or third quadrant.

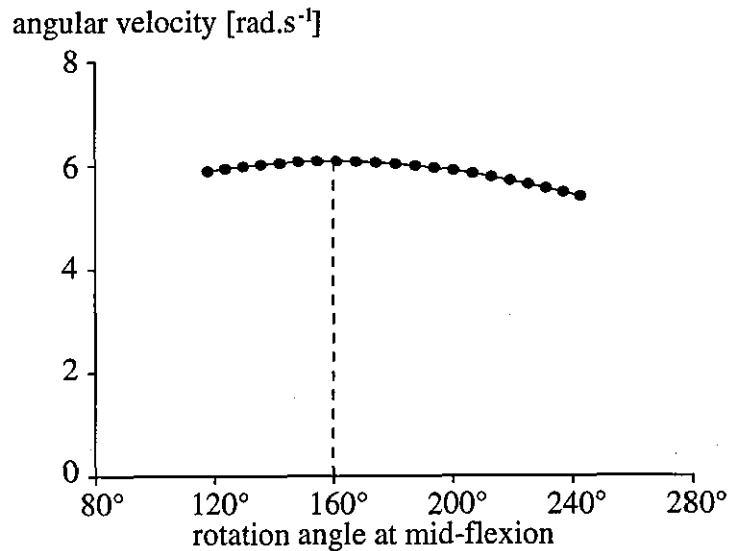


Figure 8.3. Angular velocity at a rotation angle of 270° against rotation angle at mid-flexion.

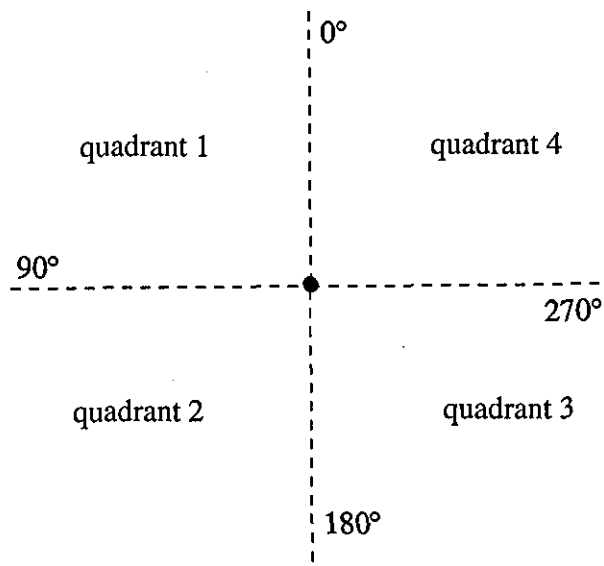


Figure 8.4. The four quadrants of the giant circle.

During the downswing phase of the giant circle, where the model swings from 0° to 180° , it has been shown that if the torques at the hips and shoulders were set to zero the model would perform an arching action, that is, the hip and shoulder angles would open (Chapter 7; Morlock and Yeadon, 1988). Therefore during the downswing phase torques tending to close the hip and shoulder angles must be exerted in order to maintain the extended configuration. Once the model has passed through the lowest point of the giant circle it commences the upswing (defined as swinging from 180° to 360°). If during the upswing the torques at the hip and shoulder joints were set to zero the model would perform a piking action, i.e. the hip and shoulder angles would close. Therefore, if a gymnast were to swing from handstand to handstand with a straight body, torques tending to close the hip and shoulder angles must be exerted on the downswing whilst torques tending to open these angles must be exerted during the upswing (Figure 8.5).

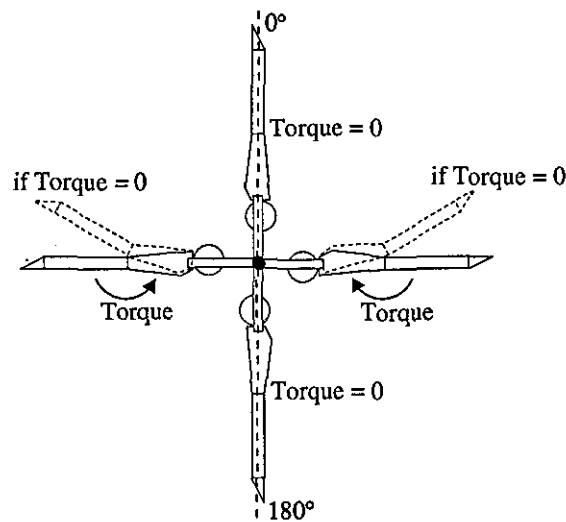


Figure 8.5. Torques required to maintain a straight body during a backward giant circle.

Consider two flexions, one performed either side of the lowest point of the giant circle (Figure 8.6), with the same change in hip angle and performed over the same duration. For the two flexions described above the flexion performed in the second quadrant will require a larger torque than the flexion performed in the third quadrant. Therefore more concentric work is done and the increase in energy is more. This is because in the third quadrant the model would tend to close the joint angles if the torques at those joints were set to zero. Therefore less work is required to produce the angle change. This was demonstrated in Chapter 7. Energy could be dissipated by performing a slow flexion after passing through the lowest point of the giant circle. If the torques required to produce the angle changes are negative, eccentric work would be done. This dissipates energy from the system. The eccentric work is the equivalent of work being done to prevent the angle change from occurring too rapidly. Therefore, in order to

maximise the increase in energy during the flexion it is of benefit to start the flexion before the lowest point of the giant circle. This is because the torques required to close the hip and shoulder angles during the downswing phase are concentric contractions which increase the energy in the system.

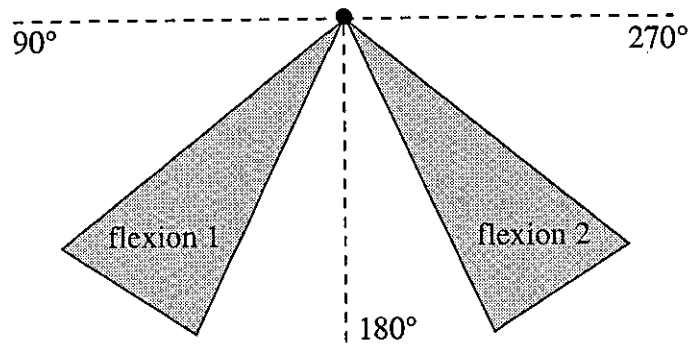


Figure 8.6. Two flexion actions performed either side of the lowest point.

A similar explanation to performing the flexion before the lowest point may be applied to performing the extension before the highest point. The angles at which the optimum extension started and finished are given in Table 8.2. When the extension occurs there is an increase in potential energy and a decrease in rotational energy due to the lengthening of the model. This would suggest that the optimum time to extend would be instantaneously at the vertical. However, by again examining the torque required to perform the extension it may be explained why the extension occurs in the fourth quadrant (Figure 8.4).

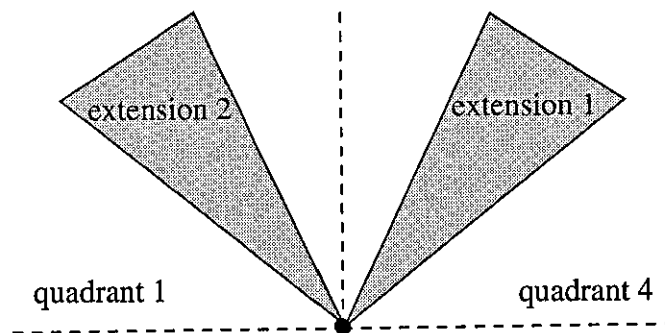


Figure 8.7. Two extensions performed either side of the highest point.

Consider two extensions, one performed either side of the vertical handstand position (360° , Figure 8.7), with the same change in hip angle and performed over the same duration. In the fourth quadrant the torques at the hip and shoulder joints are extensor torques, whilst in the first quadrant they are flexor torques. By extending in the fourth quadrant (to extend before the vertical) the energy in the system is increased more than if the extension occurs in the first quadrant.

With joint torque limit

Introducing the joint torque limit reduced the final angular velocity of the optimal simulation from 5.6 rad.s^{-1} to 5.4 rad.s^{-1} . This is a reduction in final angular velocity of only 4%. The results of the optimisation using a shoulder joint torque limit of 250 Nm are shown in Table 8.3. A graphical display is given in Figures 8.8 and 8.9.

Table 8.3. The optimum accelerated giant circle with torque limit

torque limit	phase	body angle		joint angles	
		start	finish	start	finish
without	flexion	127°	191°	180°	220°
	extension	334°	347°	220°	180°
with	flexion	136°	269°	180°	220°
	extension	304°	377°	220°	180°

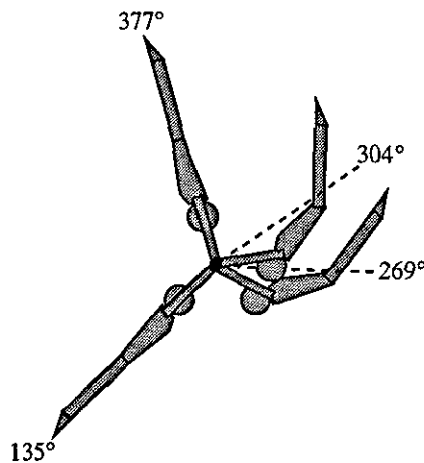


Figure 8.8. Optimal solution with 250 Nm joint torque limit at the shoulders.

When the torque limit is used more of the flexion action is performed after the lowest point and full extension occurs after passing through the highest point. This is closer to the technique used by gymnasts when compared with the optimisation performed with no torque limit (Figure 8.3). Figure 8.10 shows the peak shoulder joint torque plotted against the rotation angle at the point of mid-flexion (each triangle represents a simulation) for the optimal duration (0.4 s). The dotted line represents the torque limit which was used during the optimisation procedure. Only those triangles which are filled in would have received a score during the optimisation. Whereas the unfilled triangles would have received a score of zero as they have clearly exceeded the torque limit.

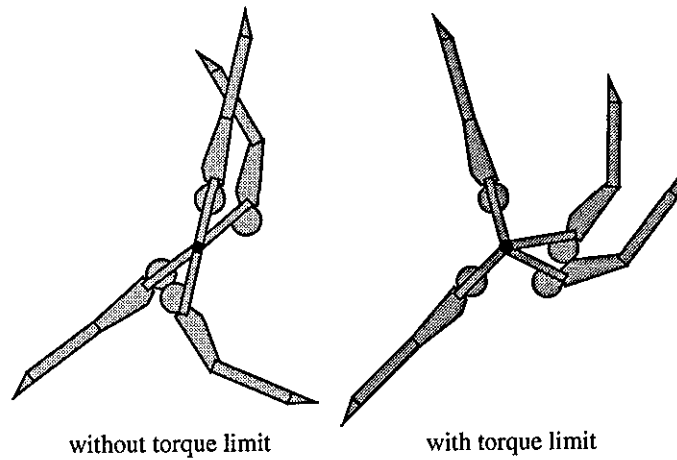


Figure 8.9. The effect of joint torque limit on the optimal solution using the three segment simulation model.

The torque limit had two major effects on the optimal solution. The first was the effect on the duration of the flexion and extension actions. When using the torque limit the optimal duration for the flexion was increased from 0.2 s to 0.4 s and for the extension 0.03 s to 0.30 s. It is clear that the shorter the duration the greater the torque required to perform that action. The second effect was to change where the action occurred. For the unlimited solution the mid-point of the optimal flexion was at approximately 160° (Figure 8.3). When the torque limit was introduced this angle was increased to approximately 202° (Figure 8.10).

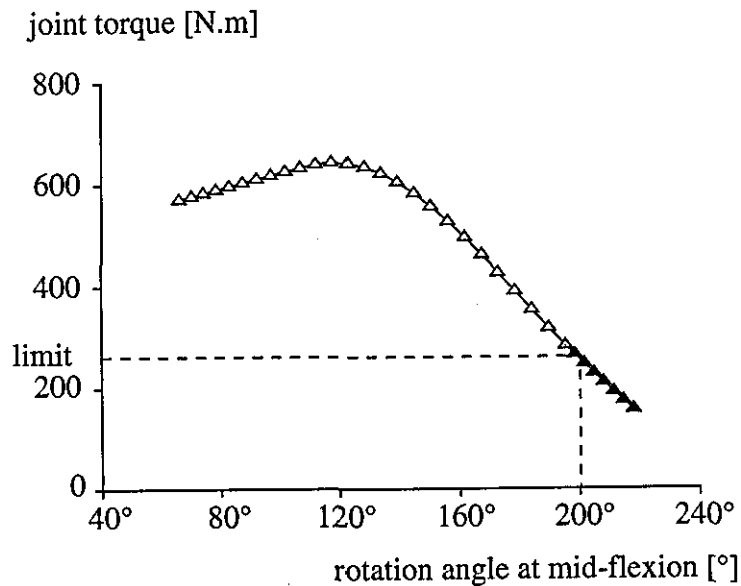


Figure 8.10. Peak shoulder joint torque against rotation angle at mid-flexion.

Although the flexion is initiated before the lowest point in both optimisations (Table 8.3) the effect of the torque limit would be more clearly seen if the simulations were performed in real time. For the solution with no torque limit the flexion occurred in 0.2 s, to an observer the action would appear as though it had occurred at the lowest point. However, due to the torque limit the duration for the flexion was increased to 0.4 s. To the observer it would appear that the majority of the flexion occurred after the lowest point.

Sensitivity analysis/additional optimisations

Varying the function used to define the joint angle time history

The first sensitivity analysis was performed on the function used to define the joint angle time histories of the hips and shoulders. The optimal simulation where the joint angle time histories were defined using the function with a square acceleration curve and where there was no torque limit produced a final angular velocity of 5.6 rad.s^{-1} . Compared with the same result using the quintic function there is a difference in peak angular velocity in only the third decimal place. The use of the function with the square acceleration curve did not result in a better performance when compared with the quintic function. When the torque limit at the shoulders was introduced the final angular velocity of the optimal simulation was 5.2 rad.s^{-1} which was less than the final angular velocity obtained using the quintic function (5.4 rad.s^{-1}). However, this represents a difference of less than 4%. It could therefore be argued that both functions used to define the joint angle time histories perform equally well.

Table 8.4 shows the rotation angles at which the flexion and extension actions started and finished in the optimal solutions using the square acceleration functions. A graphical display of these results is given in Figure 8.11. Introducing the torque limit increased the time over which the flexion and extensions occurred. The duration of the flexion was increased from 0.2 s to 0.7 s whilst the duration of the extension was increased from 0.03 s to 0.3 s.

The joint angle time histories of the optimal solutions obtained using the two different functions to define the joint angle time histories without a torque limit are shown in Figure 8.12. It can be seen that the time histories are practically identical. A larger difference in joint angle time histories is found when the joint torque limit is introduced (Tables 8.3 and 8.4). Although the flexion and extension actions in these two optimisations started and finished at different rotation angles, the joint angle time histories are still very similar in terms of the phasing of these actions (Figure 8.13).

Table 8.4. The optimum accelerated giant circle using the function with a square acceleration curve

torque limit	phase	body angle		joint angles	
		start	finish	start	finish
without	flexion	128°	189°	180°	220°
	extension	330°	343°	220°	180°
with	flexion	97°	315°	180°	220°
	extension	317°	376°	220°	180°

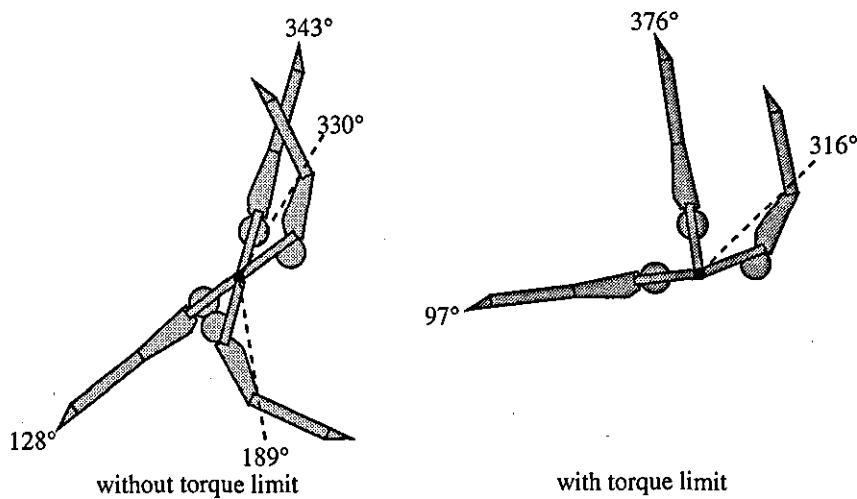


Figure 8.11. Optimal solutions obtained using the function with the square acceleration curve to define the joint angle time histories.

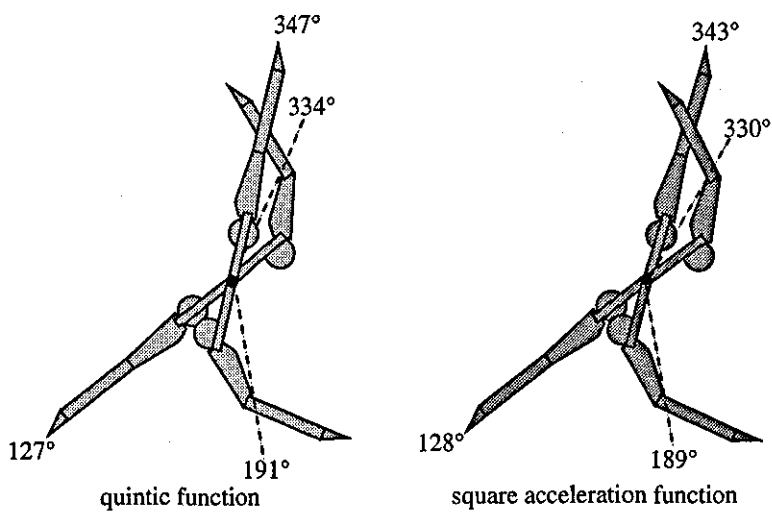


Figure 8.12. Optimal solutions obtained using the quintic function and the function with the square acceleration curve to define the joint angle time histories when no joint torque limit is used.

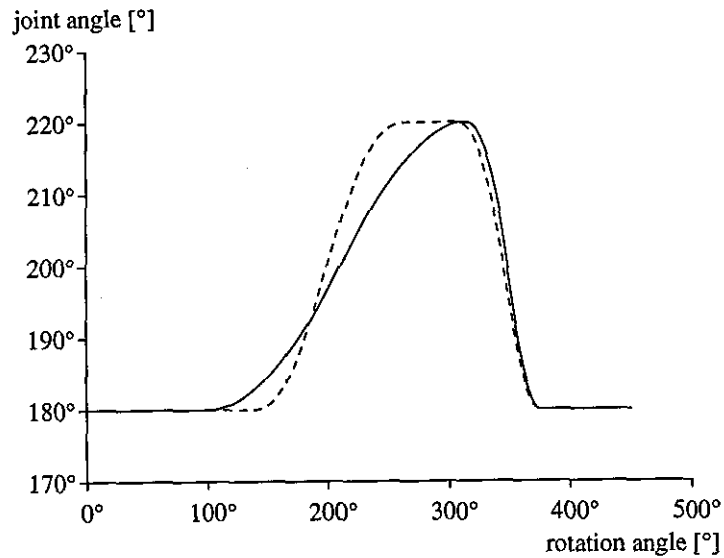


Figure 8.13. Histories of the joint angle from the optimum simulations using the 250 Nm torque limit where the joint angles were defined using the function with the square acceleration curve (solid line) and the quintic function (dashed line).

Varying the inertia data

For the third set of optimisations the inertia data of subject tv01 (Table 8.1) and the quintic function were used. The backward giant circle was again optimised with and without the joint torque limit at the shoulders. The final angular velocities for the two optimisations were 5.5 rad.s^{-1} (without torque limit) and 5.1 rad.s^{-1} (with torque limit). The two angular velocities are similar to those obtained using the inertia data of subject jb01. This differences in final angular velocity between the two sets of inertia were 2% and 6% without and with the torque limit (respectively). In both cases the the normalised angular momentum of subject jb01 was slightly larger than that of subject tv01.

Table 8.5. The optimum accelerated giant circle with and without torque limit using the inertia data tv01

torque limit	phase	body angle		joint angles	
		start	finish	start	finish
without	flexion	126°	196°	180°	220°
	extension	332°	345°	220°	180°
with	flexion	145°	285°	180°	220°
	extension	306°	381°	220°	180°

The results from the third set of optimisations are shown in Table 8.5. Despite the difference in final angular momentum the phasing of the flexion and extension actions are almost identical to those obtained from the original optimisations (Table 8.3). The optimal solutions using no torque limit for both inertia sets are shown in Figure 8.14. Similarly the results obtained using the joint torque limits are shown in Figure 8.15. Although the final solution obtained when using a different inertia sets are not identical the phasing of the flexion and extension actions are very similar. In Figures 8.14 and 8.15 the only noticeable difference is at the start and finish of the flexion action when the joint torque limit is used (Figure 8.15). The start and finish of the flexion action occurs later for subject tv01 when compared with subject jb01 (Figure 8.15). Subject tv01 had a greater body mass and larger moments of inertia than subject jb01 (Table 8.1). It might therefore be expected that subject tv01 would require larger joint torques to perform the same actions as subject jb01. Even though the rotation angle at the start and finish of the flexion action in Figure 8.15 appear to be different, on inspection of the joint angle time histories (Figure 8.16) this difference is small.

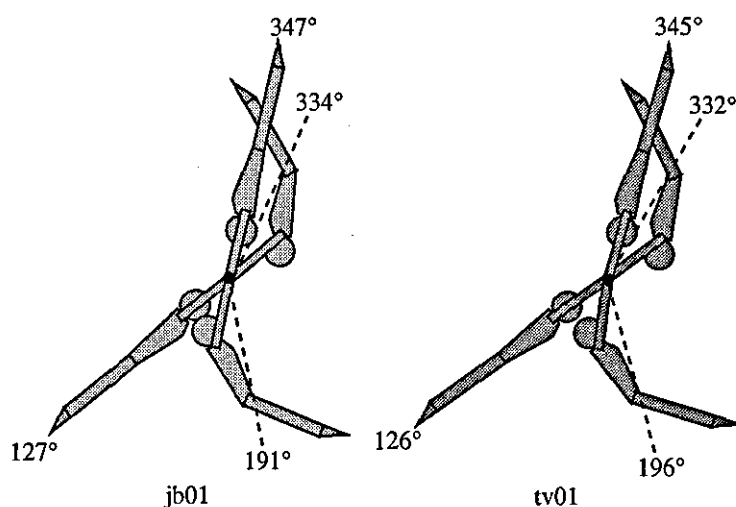


Figure 8.14. The effect of using different inertia data on the optimal solution obtained using no joint torque limit.

8.2.4 Conclusion

It was found that with no joint torque limit the optimum times to perform the flexion and extension actions were before the lowest point and before the highest point respectively. This optimum solution for accelerated giant circles differed from the technique used by elite gymnasts who generally perform the flexion after the lowest point and the extension whilst passing through the highest point. It was demonstrated that performing the flexion before the lowest point and the extension before the highest point

would result in more work being done by the gymnast and therefore a greater increase in energy.

With the introduction of a shoulder joint torque limit it was found that the majority of the flexion was performed after the lowest point and the extension was started before the highest point and finished after the highest point. This solution was a closer representation of the technique used by gymnasts. It is therefore concluded that the phasing of the flexion and extension actions are dependent on the joint torque limits. However, the introduction of the joint torque limit reduced the final angular velocity of the optimal solution by 4%. This difference corresponded to 0.2 rad.s^{-1} which is less than $12^\circ.\text{s}^{-1}$.

In Chapter 3 it was speculated that an improved performance may be obtained by using the function with the square acceleration curve to define the joint angle time histories. When no joint torque limit was used the optimisation produced a solution which was practically identical to that obtained when the quintic function was used to define the joint angle time histories (5.6 rad.s^{-1}). It was found that both the final angular velocities and joint angle time histories were very similar (Figure 8.12). When the joint torque limit was introduced the final angular velocities dropped to 5.4 rad.s^{-1} and 5.2 rad.s^{-1} for the quintic and square acceleration functions, respectively. Although the quintic function performed better than the function with the square acceleration curve the difference in final angular velocity was only 4%. For the optimisations in section 8.3 the quintic function will be used since its third derivative is smooth.

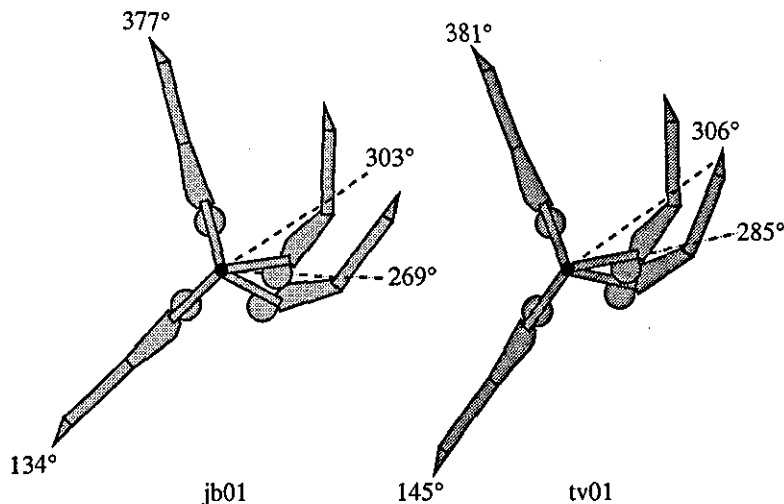


Figure 8.15. The effect of using different inertia data on the optimal solution obtained using a 250 Nm joint torque limit at the shoulders.

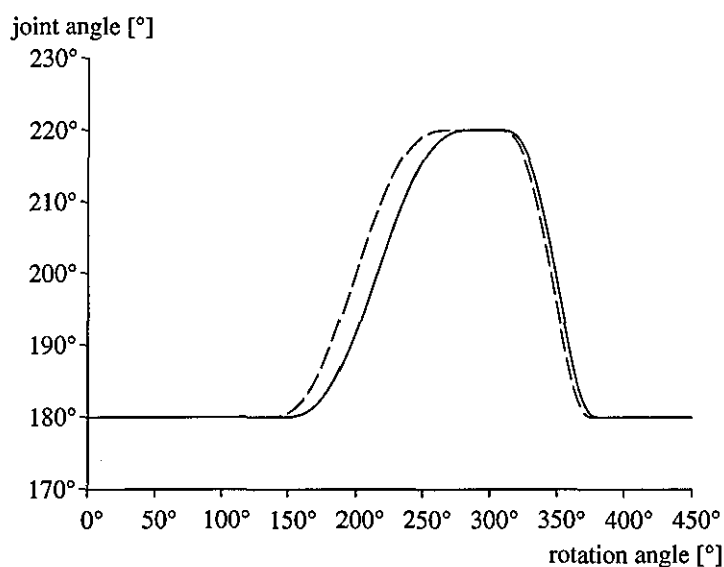


Figure 8.16. Histories of the joint angle from the optimum simulations using the quintic function and the inertia data of tv01 (solid line) and jb01 (dashed line) and the joint torque limit.

Varying the inertia data used in the optimisation did not appear to greatly effect the phasing of the flexion and extension actions whether or not the joint torque limit was used. Only small differences in the joint angle time histories were found when using the different inertia sets and the joint torque limit. Subject tv01 had a greater mass and larger moments of inertia than subject jb01. It is therefore likely that the differences were due to the torque limit. Given the same joint angle time histories, the larger moments of inertia would have resulted in requiring larger joint torques. Even though the phasing of the flexion and extension actions were not greatly different for the two sets of inertia used the subject who had the larger mass and moments of inertia (tv01) possessed less angular momentum at the end of the optimum simulation. It is therefore possible that there exists an optimal technique that may be used for any gymnast given the appropriate strength characteristics.

It has been found that the phasing of the flexion and extension actions is dependent on the limits placed on the joint torques. However, introducing a joint torque limit reduced the final angular velocity by 4%. Varying the function used to define the joint angle time history and the inertia data did not appear to have a large effect on the phasing of the flexion and extension actions. This may point the way to a common technique for all gymnasts. These results have been obtained using a simulation model that assumed a rigid bar and rigid gymnast. From the analysis of the backward giant circle in Chapters 5 and 6 the structure of the bar and gymnast are known to exhibit elastic properties. Therefore the accelerated giant circle will be optimised using the four segment simulation model in the next section (section 8.3). However, the mechanics of swinging that have been identified in the current section will still be valid in the next section.

8.3 Four segment simulation model

8.3.1 Introduction

The results of the optimisations using the three segment simulation model showed that the phasing of the flexion and extension actions were not greatly altered by varying the inertia parameters of the model or the function used to define the joint angle time histories. However, the introduction of a joint torque limit did alter the phasing of the hip and shoulder actions.

The major actions performed during backward giant circles occur at the hips and shoulders (Chapter 6; Brüggemann et al., 1994; Okamoto et al., 1987; Gervais & Tally, 1993). These actions were found to be independent of one-another (Chapter 6; Borms et al., 1977; Brüggemann et al., 1994; Okamoto et al., 1987; Gervais & Tally, 1993) both in terms of the timing and the angles through which the actions were performed. For this reason it is necessary that the joint angle time histories are independent of one-another during the optimisation (this was not the case for the optimisation with the three segment model).

In Chapter 2 it was proposed that the accelerated giant circle should be optimised for the individual skill which it precedes. For example the release conditions for the Tkatchov are considerably different to those of the double layout backward somersault dismount (Brüggemann et al., 1994). Therefore, one might expect the optimum technique for the accelerated backward giant circle prior to these two skills to be different.

Of all the dismounts that have been analysed in the literature, the double layout backward somersault dismount requires the greatest angular momentum in flight (Brüggemann et al., 1994; Kerwin et al., 1990). Since the angular momentum during flight is determined at release the only way it can be accumulated is during the accelerated giant circles prior to the release. Therefore, the accelerated backward giant circle and the giant circle prior to release for the double layout backward somersault dismount will be optimised in order to maximise the angular momentum about the gymnast's mass centre at the point of release.

The four segment simulation model developed in Chapter 3 will be used to optimise the accelerated giant circles prior to release. This includes one complete accelerated giant circle and the following giant circle containing the release. During the optimisation the joint angle time histories which are used to define the giant circles will be manipulated in order to maximise the model's angular momentum about its mass centre at release. In addition further optimisations will be performed to test the sensitivity of the optimal solution.

8.3.2 Methods

The four segment simulation model was implemented with the Simulated Annealing algorithm (Goffe et al., 1994). In all simulations the four segment inertia data of subject jb01 was used (Table 8.6). The spring parameters obtained in Chapter 6 for the bar and shoulder springs were also used in all simulations (Table 8.7). The aim of the optimisation was to maximise the angular momentum about the gymnast's mass centre after performing one accelerated giant circle and the giant circle containing release.

Table 8.6. Inertia parameters for subject jb01

segment	mass (kg)	length (m)	cmloc (m)	moment of inertia (kg.m ²)
arms	6.868	0.548	0.239	0.205
arms + bar	11.868	0.582	0.403	0.481
torso	33.566	0.601	0.337	1.610
thigh	14.074	0.374	0.151	0.173
leg	7.543	NA	0.227	0.164

Table 8.7. Spring parameters used in the optimisation

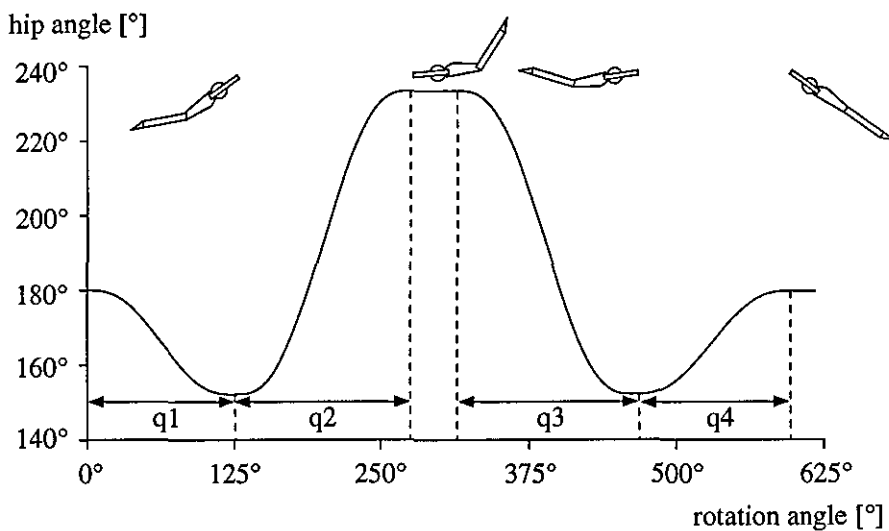
spring coefficients	stiffness (N.m ⁻¹)	damping
bar (horiz)	22560	419.6
bar (vert)	26297	379.4
shoulder	12086	18309.0

All simulations performed within the optimisation were initiated from a rotation angle of zero degrees (the vertical handstand position) with the model in a fully extended configuration. The initial angular velocity of the model for each simulation was 2.24 rad.s⁻¹. This value was obtained from the video analysis of the accelerated backward giant circles. Similarly the initial displacements and velocities of the bar were obtained from the video analysis (Table 8.8). Each simulation ended after the model had rotated through a rotation angle of 622°. The rotation angle at the end of each simulation corresponded to a possible release angle for the double layout somersault dismount (Brüggemann et al., 1994). Brüggemann et al. (1994) reported a mean angle at release of 8° below the horizontal for four double layout somersault dismounts.

Table 8.8. Initial bar displacements and velocities obtained from the video analysis of the accelerated giant circles

direction	bar displacement [m]	bar velocity [m.s ⁻¹]
horizontal	0.0033	- 0.0173
vertical	- 0.0033	- 0.1055

The joint angle time histories at each joint were defined using four non-overlapping quintic functions (Figure 8.17). Each of the quintic functions used to make up the joint angle time histories required four pieces of information. These were the start and finish angles and the start and finish times of the joint action. Since the model started each simulation with angles of 180° at the hips and shoulders and since the four joint actions were non-overlapping, 12 parameters were required to define each joint angle time history (i.e. 24 parameters to define both joint angle time histories).



8.17. The joint angle time history comprised four non-overlapping quintic functions.

The Simulated Annealing algorithm was used to manipulate the parameters which defined the joint angle time histories of the hips and shoulders. The 12 parameters for each angle were defined as follows:

- 1 magnitude of the first change in joint angle
- 2 duration from the start of the simulation to the first joint action
- 3 duration of the first joint action
- 4 magnitude of the second joint action
- 5 duration from the finish of the first joint action to the start of the second joint action

- 6 duration of the second joint action
- 7 magnitude of the third joint action
- 8 duration from the finish of the second joint action to the start of the third joint action
- 9 duration of the third joint action
- 10 magnitude of the fourth joint action
- 11 duration from the finish of the third joint action to the start of the fourth joint action
- 12 duration of the fourth joint action

Certain restrictions were placed on the joint angle time histories. It was decided that the model should not be able to hyper-extend by more than 50° at either joint. This restriction was used to represent the possible ranges of motion of the gymnast. Similarly the flexion angles at the hips and shoulders were restricted to a maximum flexion angle of 180° . For the hip joint a flexion angle of 180° would correspond the gymnast having his knees touching his nose. If either of the joint angle limits were exceeded during the optimisation the simulation was given a score of zero.

The joint torques produced by the simulation model during the optimisation procedure were limited using the three-dimensional surface muscle models obtained in Chapter 5. During a simulation at each step of the integration the joint angle and angular velocity of the hip and shoulder joints were used to obtain maximum joint torque values from the muscle models. If these values were exceeded by the torques produced by the simulation model the simulation was given a score of zero.

A final restriction was placed on the horizontal velocity of the mass centre at release. For a safe performance of a double layout somersault dismount the gymnast must not contact the bar during the flight phase. This may be achieved by forcing the horizontal velocity of the model's mass centre to be positive (in the direction away from the bar). To enable the optimisation to consider simulations which result in negative horizontal velocities at release a cost function which penalised a negative horizontal velocity was used. Since small negative horizontal velocities may pose a great problem the cost function was as follows:

If horizontal velocity at release > 0 then

Cost function = angular momentum about the model's mass centre

If horizontal velocity at release < 0 then

Cost function = angular momentum + $100 \times$ horizontal velocity of the mass centre

The value for the angular momentum about the model's mass centre will be in the region of 120 units. Therefore, if the mass centre of the model has a velocity of 0.1 m.s^{-1} towards the bar at release a deduction of 10 units would be made from the simulation's score. This means that only small deductions are made for small horizontal velocities at release.

Two preliminary optimisations were performed on the first accelerated giant circle and the giant circle containing the release so that a suitable starting point for the complete optimisation could be obtained. The results of the two preliminary optimisations were combined and used as the initial guess for the Annealing process. The optimisation procedure was given 12000 simulations to find the optimum solution. This resulted in 2400 simulations per drop in temperature. Since the optimisation was started from the results of the preliminary optimisations the initial temperature was reduced.

Output from the simulation driven by the optimal joint angle time histories included the time histories of the bar displacements, reaction forces at the bar, joint torques produced by the simulation model and those estimated by the muscle models, total energy and its components, angular momentum about the model's mass centre, rotation angle, mass centre location and mass centre velocity. The angular momentum at release was normalised to the number of straight somersaults the model would be capable of performing during the flight phase of the dismount (Yeadon et al., 1990). The flight time was calculated from the point of release until the mass was a fixed level above the landing surface which was used to represent the height of the mass centre at landing (0.82 m).

Sensitivity Analyses

In order to test the sensitivity of the optimal solution a further set of simulations and optimisations were performed.

Varying the strength of the muscle models

Since a gymnast's conditioning is specific to the skills he performs it is possible that a gymnast may be able to produce slightly larger joint torques whilst performing accelerated giant circles compared with similar performances (in terms of joint angle and angular velocity) on the isokinetic dynamometer. To see whether this would have an effect on the optimal solution an optimisation was performed where the peak joint torques given by the muscle models were increased by 10%. Similarly an optimisation was performed where the strength of the gymnast was decreased by 10%. The results of this optimisation could provide an insight into the effect the level of conditioning of a gymnast has on performance.

Varying the inertia parameters

To test the effect of varying the inertia parameters on the optimal performance the joint angle time histories from the initial optimisation were used with the four segment inertia data of tv01 (Table 8.9). In addition the backward giant circle and the giant circle containing release were optimised with the tv01 inertia set (Table 8.9). The initial simulation of the optimisation used the optimal joint angle time histories from the initial optimisation. The initial temperature and range of the upper and lower bounds were reduced so that a reduced number of simulations would be required to find a solution.

Table 8.9. Inertia parameters for subject tv01

segment	mass (kg)	length (m)	cmloc (m)	moment of inertia (kg.m ²)
arms	7.796	0.575	0.250	0.252
arms + bar	12.796	0.609	0.390	0.644
torso	34.450	0.720	0.351	1.670
thigh	15.412	0.403	0.171	0.212
leg	8.124	NA	0.330	0.199

Varying the release angle

The mean release angle reported by Brüggemann et al. (1994) was 8° below the horizontal. The number of dismounts analysed and the standard deviation for the release angle were four and 30° respectively. This meant that some of the dismounts had release angles above the horizontal. Mechanics suggest that this would result in the gymnast somersaulting back over the bar after release. Similarly releasing at an angle one standard deviation lower than the mean is likely to produce a poor dismount. Therefore, a release angle of half a standard deviation below the mean was chosen to represent the angle of release for the sensitivity analysis.

Varying the stiffness coefficients of the bar

The high bar is required to have certain elastic properties which are described by the Code of Points (FIG, 1979). The bar is required to produce a sag of 100 mm ± 10 mm when loaded at its centre with a weight of 2200 N. This would produce a range of stiffness coefficients of between 20000 N.m⁻¹ and 24444 N.m⁻¹. However, due to different manufacturers, different materials used in the construction and the tension in the supporting cables of the uprights it is possible for the high bar to have a greater range of

possible stiffness values. The high bar used in Chapter 5 was reported to have a stiffness of between 22000 N.m⁻¹ and 27500 N.m⁻¹ (Norm-testing, Continental, 1994). Since a gymnast may train on one high bar and compete on another, which may or may not be of equal stiffness, the effect of varying the stiffness of the bar was investigated.

Two optimisations were performed, one where the stiffness coefficients of the bar were increased by 5% and one where the stiffness of the bar was decreased by 5% (Table 8.10). All the parameters except for one (where the vertical stiffness of the bar was increased by 5%) lie within the norms set by both the Code of Points and the Norms-testing manual. In each optimisation the initial estimate of the parameters defining the joint angle time histories was taken from the solution of the original optimisation. As in the optimisation performed using the alternative inertia set the initial temperature and range of the upper and lower bounds were reduced so that a smaller number of simulations would be required to find a solution.

Table 8.10. Spring parameters used in the sensitivity analysis

	stiffness coefficient	
	hori. (N.m ⁻¹)	vert. (N.m ⁻¹)
original	22560.0	26297.0
5% increase	24816.0	28926.7
5% decrease	20304.0	23667.3

Varying the initial angular velocity

In a gymnastics routine on high bar the dismount will usually be performed after a number of circling skills. During the wind-up prior to the dismount the gymnast will be penalised for using too many giant circles to acquire the necessary rotation. Therefore an optimisation was performed where the initial angular velocity of each simulation was approximately 50% of that used in all previous simulations (approximately 1.10 rad.s⁻¹). This initial angular velocity is equivalent to that possessed by a gymnast on passing through the highest point of a regular giant circle performed during the data collection. The initial bar displacements and velocities corresponding to the new angular velocity were obtained from the video analysis of the regular giant circles and are presented in Table 8.11.

Table 8.11. Initial bar displacements and velocities obtained from the video analysis of the regular giant circles

direction	bar displacement [m]	bar velocity [m.s ⁻¹]
horizontal	0.0016	0.0287
vertical	-0.0126	0.0227

8.3.3 Results and Discussion

After performing 12000 simulations the optimum value for the angular momentum about the model's mass centre at release was 125.1 kg.m².s⁻¹. From the height and vertical velocity of the mass centre at release (Table 8.12) the time of flight for the dismount was calculated to be 1.1 s. With the body in a fully extended configuration with the arms by the side of the body the moment of inertia about the whole body mass centre was calculated to be 8.78 kg.m². The angular momentum at release was normalised into straight somersaults per unit flight time. If the model had let go of the bar at release it would have completed 2.5 straight somersaults during the flight time. If the angular momentum were normalised using just the moment of inertia of the gymnast in the layout position, a value of 14.2 rad.s⁻¹ would be obtained.

Table 8.12. Displacement and velocity of the mass centre at release

displacement		velocity	
hori. (m)	vert. (m)	hori. (m.s ⁻¹)	vert. (m.s ⁻¹)
1.03	-0.15	0.04	4.00

Yeadon et al. (1990) obtained a mean value of 1.53 (± 0.12) straight somersaults per unit flight time for four double layout somersault dismounts performed at the Seoul Olympics (1988). This value (1.53 units) is slightly less than the 1.75 somersaults (0.25 of a revolution is performed before the release) that would be expected for a successful completion of the double layout dismount. The gymnasts studied by Yeadon et al. (1990) were able to complete the double somersault dismounts because the straight body configuration was not maintained throughout the flight and the body must land short of vertical. The gymnasts released the bar in a dished shape, with flexion angles at the hips and shoulders. During the flight phase the gymnasts passed through the straight position into an arched shape, from which the gymnasts "piked down" at landing (Figure 8.18).

This meant that for the majority of the flight phase the gymnasts' moments of inertia about the lateral axis were less than if they had adopted a fully extended configuration. It may therefore be inferred from the optimum solution that gymnasts are more than capable of producing enough rotation at release to perform the double layout somersault dismount completely in the straight position.

The optimal solution for the backward giant circle is shown as a sequence of graphics which are spaced at intervals of 45° in Figure 8.19. The joint angle time histories of the hip and shoulder angles from the optimum solution are shown in Figures 8.20 and 8.21.

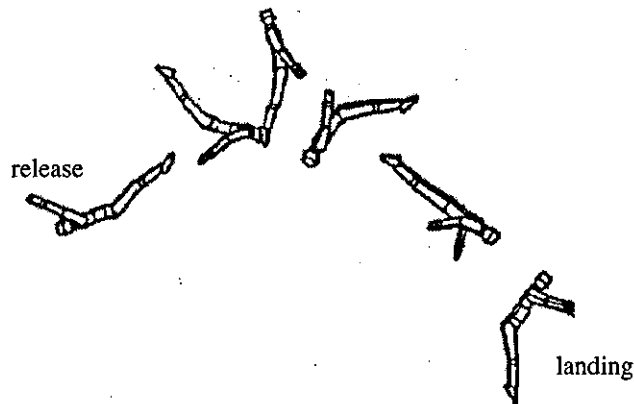


Figure 8.18. Simulation of an actual double layout somersault dismount performance from the Seoul Olympics (adapted from Yeadon et al., 1990).

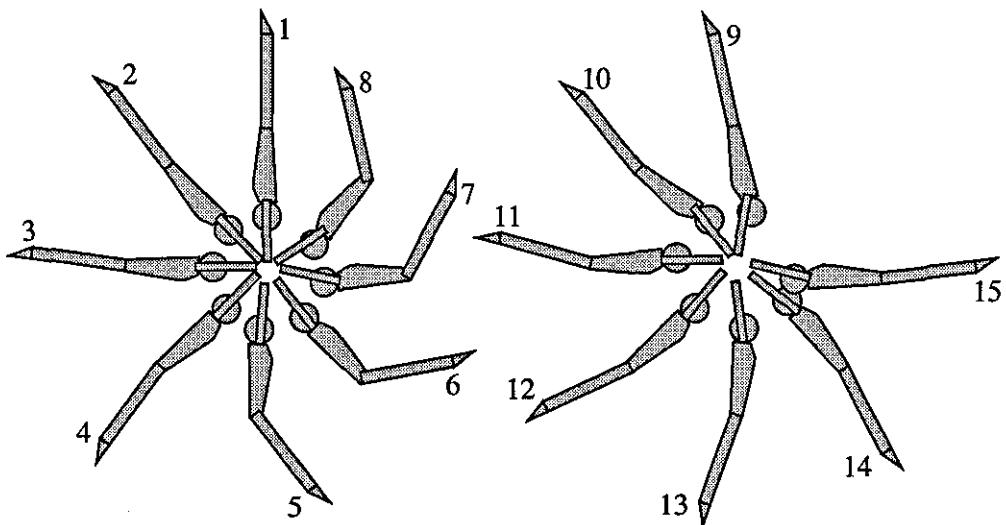


Figure 8.19. Sequence of figures representing the optimum technique.

In Figure 8.21 it can be seen that a small hyper-extension of the hips occurred during the first quadrant of the giant circle. The hyper-extension angle was smaller than that reported in Chapter 6. Once the model entered the second quadrant the hips began to flex. The majority of the hip flexion occurred throughout the second quadrant.

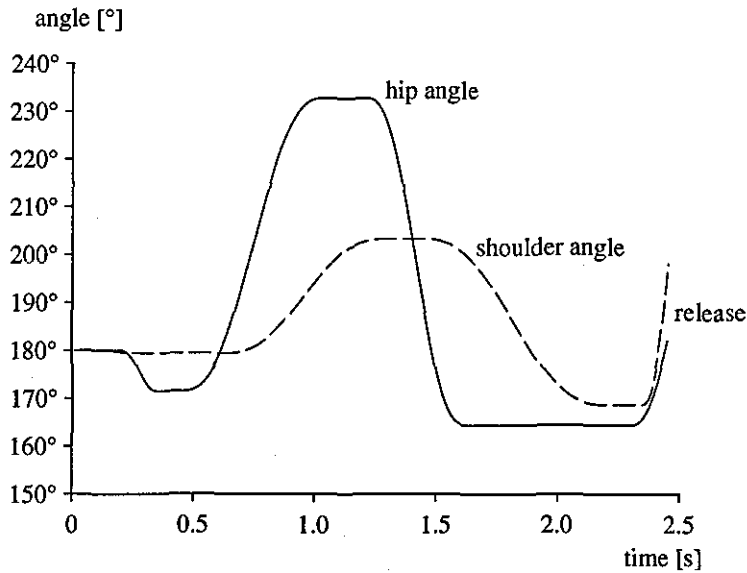


Figure 8.20. Joint angle time histories of the hip and shoulder joints from the optimal solution.

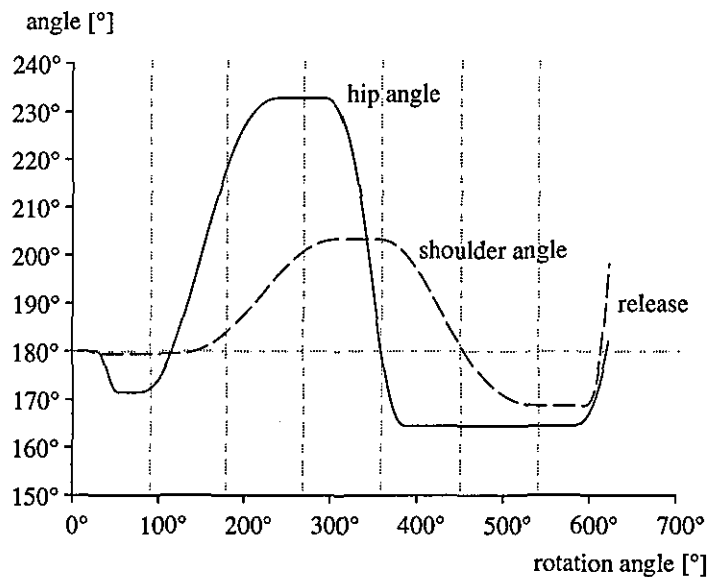


Figure 8.21. Histories of the hip and shoulder joints from the optimal solution plot against rotation angle.

In the video analysis the majority of the hip flexion occurred in the third quadrant. However, the flexion action performed in the present optimisation agrees with the results obtained from the three segment simulation model (section 8.2.3). It was shown with the three segment model that it is advantageous to perform the flexion before the lowest point of the giant circle. The introduction of a joint torque limit suggested that real gymnasts do not flex before the lowest point as they may not be strong enough to do so. It may be that the gymnast under investigation was strong enough to flex before the lowest point or it may be that the data collected for the muscle models over-estimated the gymnast's

strength.

The flexion of the hip angle continued into the third quadrant. The maximum hip flexion angle was maintained for a short period of time before the angle at the hip started to open in the fourth quadrant. The hips passed through full extension at a rotation angle of 360° . The hip angle continued to open until a hyper-extension angle of approximately 17° degrees was achieved. The hyper-extension angle was then maintained throughout the first and second quadrants of the second circle and into the third quadrant until the hips were flexed just prior to release. At release the flexion angle at the hips was only 3° beyond the fully extended position.

The history of the shoulder angle follows more closely that obtained from the video analysis of the accelerated backward giant circles in Chapter 6. During the downswing the angle at the shoulder was maintained close to full extension (180° in Figure 8.21). The closing of the shoulder angle occurred throughout the third and into the fourth quadrant of the first giant circle. Once the model had passed through the highest point of the circle the angle at the shoulders started to open. The shoulder angle passed through full extension at a rotation angle of 450° . The angle continued to open until just before the lowest point of the giant circle containing the release. This was found to be the case with the giant circles analysed in Chapter 6. Similar to the hip angle, the shoulder angle was closed prior to the release. At release a flexion angle of approximately 19° was achieved at the shoulder joint.

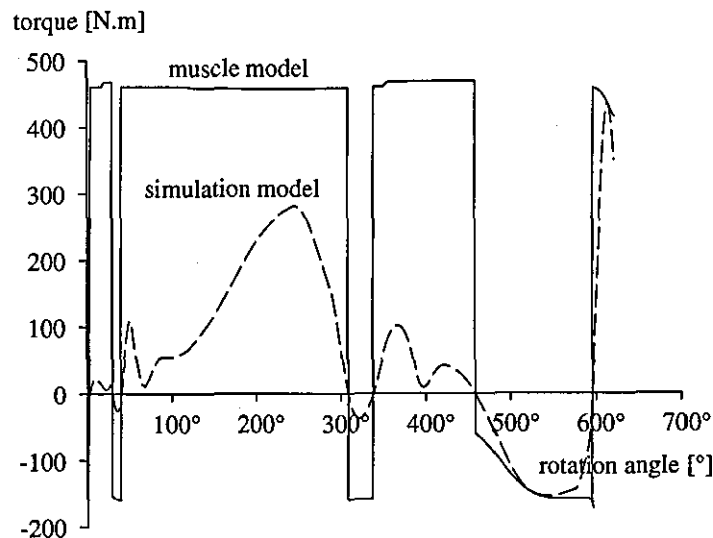


Figure 8.22. History of the maximum shoulder torques given by the muscle models and the torques produced by the simulation model.

The size of the maximum flexion angles at the hip and shoulder joint during the first accelerated giant circle were smaller than those obtained from Chapter 6 (see Figures 6.14 and 6.15). This might suggest that the flexion actions were restricted by the

joint torque limits imposed by the muscle models, counter to the idea suggested earlier that the muscle models may have over-estimated the muscle moments. The maximum joint torques given by the muscle models and those produced by the simulation model are shown in Figures 8.22 and 8.23 for the shoulders and hips respectively. Throughout the majority of the optimum simulation the joint torques produced by the simulation model were well within the torque limits set by the muscle models. This means that for the majority of the optimal technique the gymnast would not require maximum effort. The model was therefore strong enough to perform the majority of the first flexion action at the hips before the lowest point of the first giant circle. Since this would lead to an increase in the energy the optimisation confirms the results from section 8.2.3.

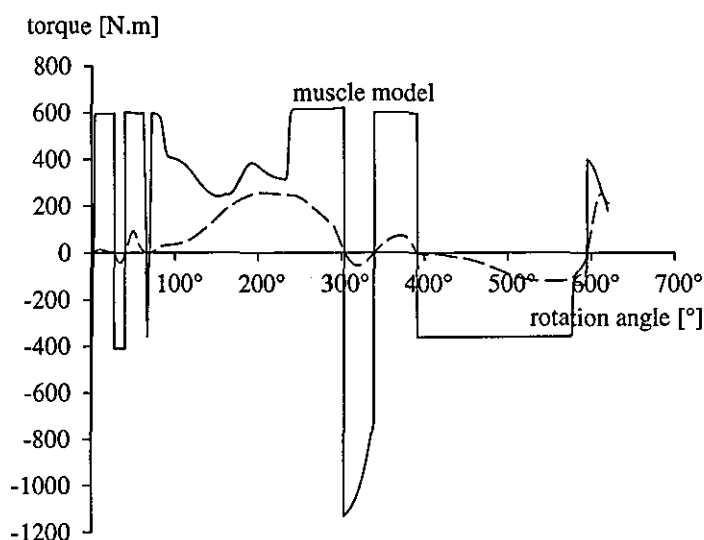


Figure 8.23. History of the maximum hip torques given by the muscle models and the torques produced by the simulation model.

Why then, does the optimum solution not require maximum effort for the majority of the simulation? Close to release the joint torques produced by the simulation model lie very close to the torque limits set by the muscle models. Therefore at release the gymnast requires maximum effort to perform the required actions. It is likely in the giant circles leading up to the release that the joint torque limits are not approached in order that the model is capable of producing the most effective joint actions at release. That is, if a more vigorous wind up had been performed prior to the release the model may not have been strong enough to close the hip and shoulder angles sufficiently to produce the maximum rotation. These ideas may be confirmed using the results of the sensitivity analyses.

The horizontal and vertical displacements of the bar for the optimum simulation are shown in Figure 8.24. The maximum displacement of the bar about its neutral resting

position was -0.12 m which occurred as the model passed through the lowest point of the giant circle containing the release. This value compares well with the peak vertical bar displacement obtained from the video analysis of the accelerated giant circles (mean of -0.12 m). However the double peak in vertical bar displacement seen in the trials of the accelerated giant circles was not present in the optimum solution. This is because of the timing of the extension performed in the first accelerated giant circle. In Chapter 6 the hip angle passed through full extension at a rotation angle of approximately 450° and reached maximum hyper-extension just after 500° . The shoulder angle followed a similar pattern of phasing. These actions lead to the initial peak in vertical force and bar displacement seen before the major peak which occurred as the gymnast passed through the lowest point. In the optimal technique the hip angle was opened much earlier (Figure 8.21) leading to a more gradual loading of the bar.

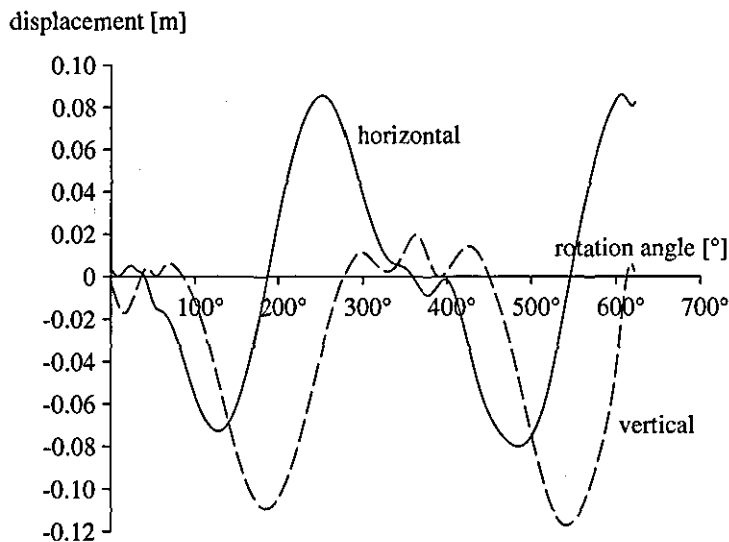


Figure 8.24. Histories of the horizontal and vertical bar displacements of the bar during the optimal solution.

An interesting feature of the bar displacements can be seen just prior to the release. As the gymnast approaches the point of release the bar is unloading (Figure 8.25 a), however, just before the model would have released the bar its velocity changes direction (Figure 8.25 b). At the point of release the bar was moving vertically downwards and horizontally to the right (i.e. in the direction of the dismount). The velocity and displacement of the bar are shown in Figure 8.25. The velocities of the bar would serve to further increase the rotation of the model about its mass centre. The loading of the bar produced by the joint angle time histories of the hips and shoulders may have served to produce this action of the bar at release to facilitate the subsequent rotation of the model. If this is true then it is likely that the change in velocity of the bar will also occur in the results of the sensitivity analyses.

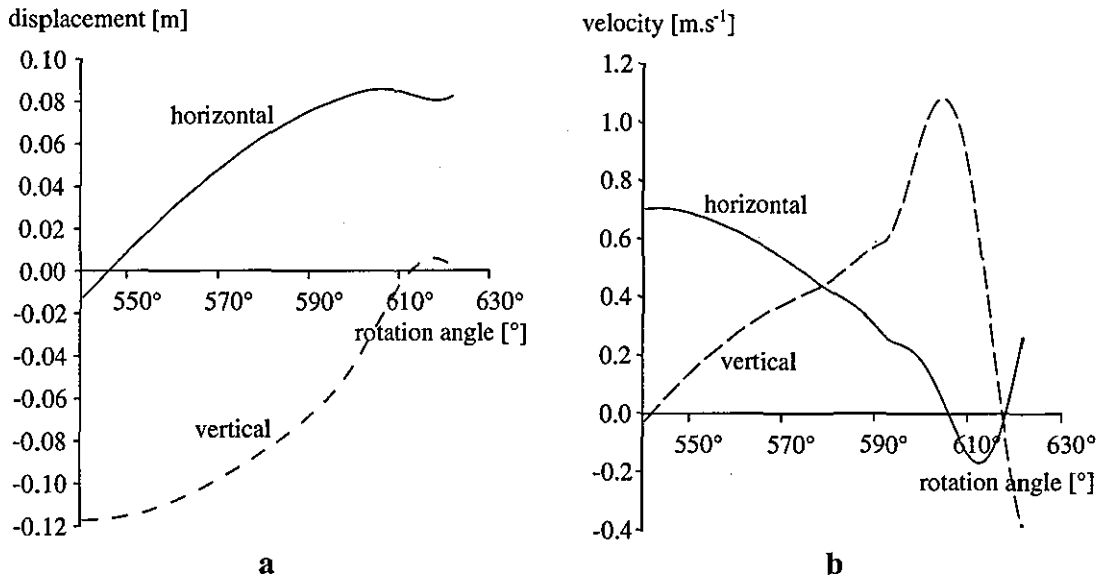


Figure 8.25. Displacements (a) and velocities (b) of the bar prior to release in the optimum solution.

The peak reaction forces that the gymnast would experience whilst performing the optimum technique are given in Table 8.13. The peak vertical reaction force occurred as the model passed through the lowest point on the giant circle containing the release. The peak vertical reaction force from the optimum simulation was approximately 11% greater than the peak reaction force recorded from trial 11 (Table 6.18). Although the peak vertical reaction force estimated by the optimal simulation is greater than those recorded during the force and video analysis of the accelerated giant circles it is still within the capabilities of the gymnast. Gervais (1993) recorded a similar reaction force during wind-up giant circles and Enchun (1989) reported reaction forces up to four bodyweights for single arm giant circles. Similarly gymnasts are able to hold onto the rings whilst experiencing reaction forces in the region of nine bodyweights (Brüggemann, 1987).

However, the peak horizontal reaction forces estimated by the optimum simulation were up to 19% less than those recorded in the force and video analysis. The decreased peak horizontal reaction forces are likely to be as a result of the different techniques adopted in the accelerated giant circles. The most notable difference between the horizontal reaction forces produced by the simulation model and those recorded in the force analysis of the accelerated giant circles occurs at release. For the optimum technique there is a large horizontal reaction force at release as opposed to a very small horizontal reaction force obtained from the video analysis (Figure 8.26). Again this is due to the different techniques used to load the bar.

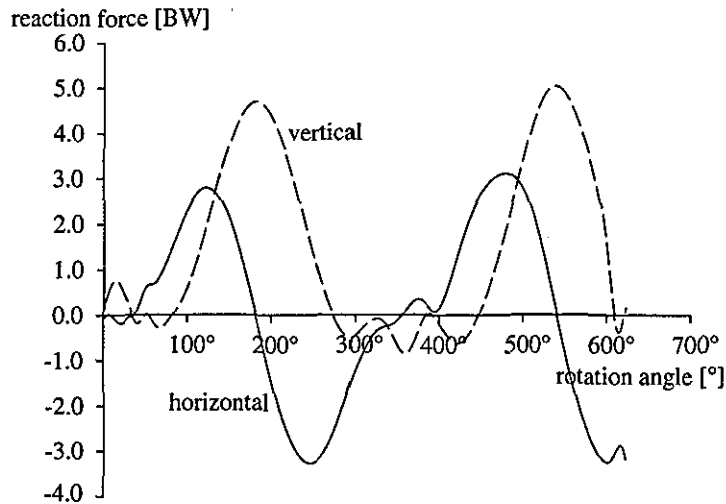


Figure 8.26. Histories of the horizontal and vertical reaction forces at the bar produced by the optimal solution.

Table 8.13. Maximum and minimum reaction forces during the optimum simulation

	reaction force			
	vertical (N, BW)		horizontal (N, BW)	
max	3106.0	5.03	1917.7	3.11
min	-529.8	-0.86	-2017.0	-3.27

Sensitivity analysis

Varying the strength of the muscle models

By increasing the strength of the gymnast one might expect an increase in performance given that the action prior to release requires maximum effort from the gymnast. After performing 7200 simulations the optimum value for the angular momentum about the model's mass centre at release was $127.4 \text{ kg}\cdot\text{m}^2\cdot\text{s}^{-1}$. Increasing the peak joint torques of the muscle models by 10% resulted in a 2% increase in angular momentum. When expressed in terms of straight somersaults this resulted in an increase in rotation of 0.04 revolutions in the given flight time.

Figure 8.27 shows the history of the hip and shoulder angles from the optimum solution where the strength of the muscle model was increased by 10%. The joint angle histories for the original optimisation are overlaid in dashed lines. The histories of both the hip and shoulder angles obtained from the two optimisations are similar in both the phasing and the size of the joint angle changes. As might have been expected the majority of the first hip flexion occurred before the lowest point of the giant circle (Figures 8.27).

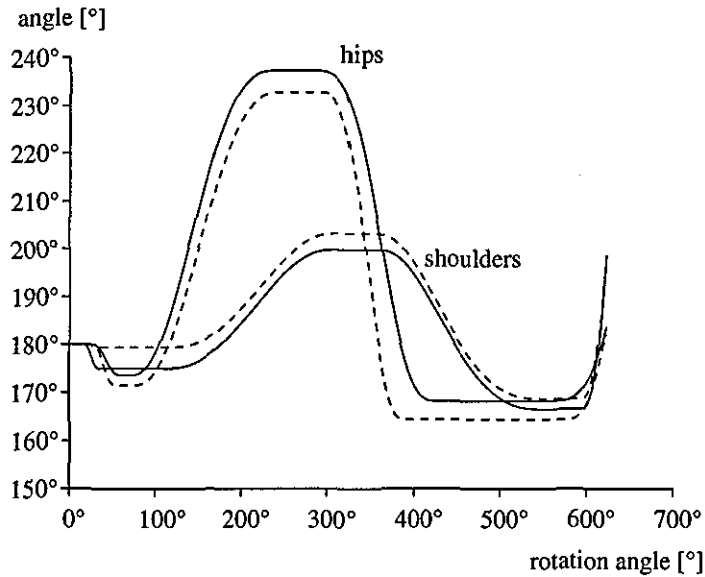


Figure 8.27. Histories of the hip and shoulder joint angles from the optimisation where the strength of the muscle models was increased by 10% (original optimisation overlaid in dashed lines).

Inspection of the joint torque histories also shows a similar story to the original optimisation (Figures 8.28 and 8.29). For the majority of the simulation the joint torques produced by the simulation model are well within the joint torque limits set by the muscle models. During the first flexion action the hip joint torque used by the simulation model approaches the torque limit set by the muscle model (Figure 8.29). In the flexion action just before the release the shoulder torque used by the simulation model approaches the shoulder joint torque limit (Figure 8.28). It appears that the hip flexion performed at release could have been performed more vigorously (i.e. there is room for the torque used by the simulation model to be greater without exceeding the torque limit). However, this would have an effect on the joint torque produced at the shoulder which may lead to the shoulder torque limit being exceeded.

Figure 8.30 shows the horizontal and vertical displacements of the bar for the optimisation where the torques given by the muscle models were increased by 10%. The trajectory of the bar is for all intents and purposes the same as in the original optimisation. Even the change in direction of the bar movement at release is reproduced in the second optimisation.

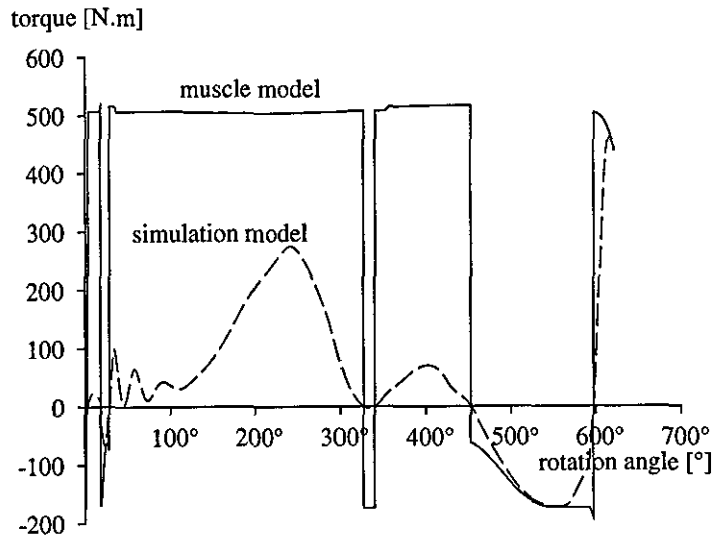


Figure 8.28. History of the maximum shoulder torques given by the muscle models and the torques produced by the simulation model where the strength of the muscle models was increased by 10%.

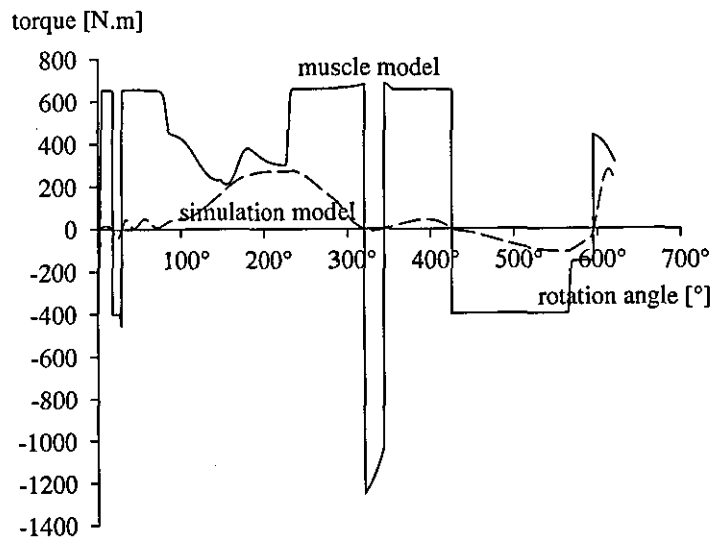


Figure 8.29. History of the maximum hip torques given by the muscle models and the torques produced by the simulation model where the strength of the muscle models was increased by 10%.

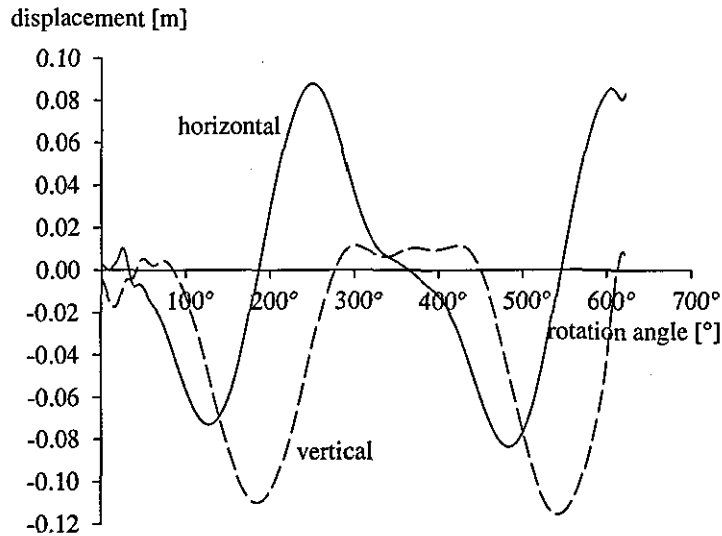


Figure 8.30. History of the horizontal and vertical displacements of the bar during the optimum simulation where the joint torque limits were increased.

The second optimisation used to test the sensitivity of the optimum solution reduced the peak joint torques given by the muscle models by 10%. After performing 7200 simulations the optimum value for the angular momentum about the model's mass centre at release was $120.9 \text{ kg.m}^2.\text{s}^{-1}$. Decreasing the peak joint torques of the muscle models by 10% resulted in a 3% decrease in angular momentum. When expressed in terms of straight somersaults per unit flight time this resulted in a decrease in rotation of 0.09 revolutions (still more than two thirds of a revolution more than required to perform a double layout dismount).

In section 8.2 introducing a joint torque affected the timing of the flexion action as the model passed through the lowest point. Instead of performing the action before the lowest point as in the unconstrained optimisation the majority of the flexion action was performed after the lowest point. Figure 8.31 shows the histories of the hip and shoulder angle from the optimum simulation where the strength of the muscle models used to limit the joint torques were reduced by 10%. It appears as though the first flexion action performed at the hips was still performed before the lowest point of the giant circle. A number of explanations are possible for this. In section 8.2 all angle changes were over a fixed range, that is, in every simulation the hip was flexed by an angle of 40° . In the present optimisation the size of the flexion could be varied from 0° to 240° (i.e. from 60° of hyper-extension through to 180° of flexion). Therefore, if the joint torques that the model is able to use were reduced, the options available are to (a) alter the timing of the flexion action (make the action longer and later), (b) reduce the size of the angle change (reduce the flexion angle) or (c) a combination of (a) and (b). From Figure 8.31 it appears as though the size of the flexion angle has been reduced (cf Figure 8.27).

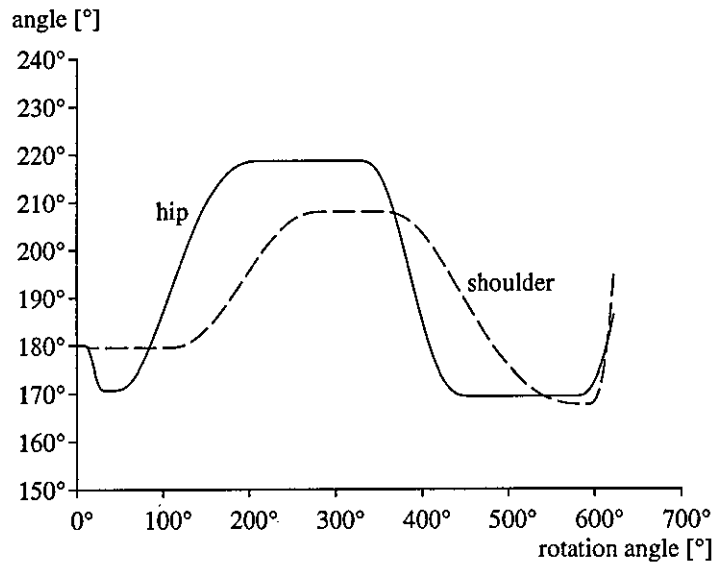


Figure 8.31. Histories of the hip and shoulder joint angles from the optimisation where the strength of the muscle models was decreased by 10%.

The timing of the actions at the hips and shoulders are similar to those from the original optimisation. Since the size of the hip flexion action in the first giant circle was reduced from approximately 53° to 39° , it might be expected that the joint torques produced by the simulation model would have approached those given by the muscle models. The histories of the hip and shoulder joint torques are shown in Figures 8.32 and 8.33.

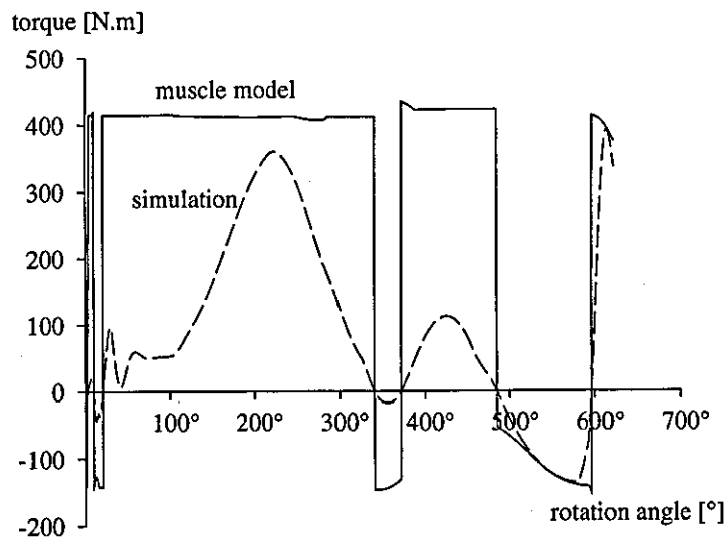


Figure 8.32. History of the maximum shoulder torques given by the muscle models and the torques produced by the simulation model when the strength of the muscle models was decreased by 10%.

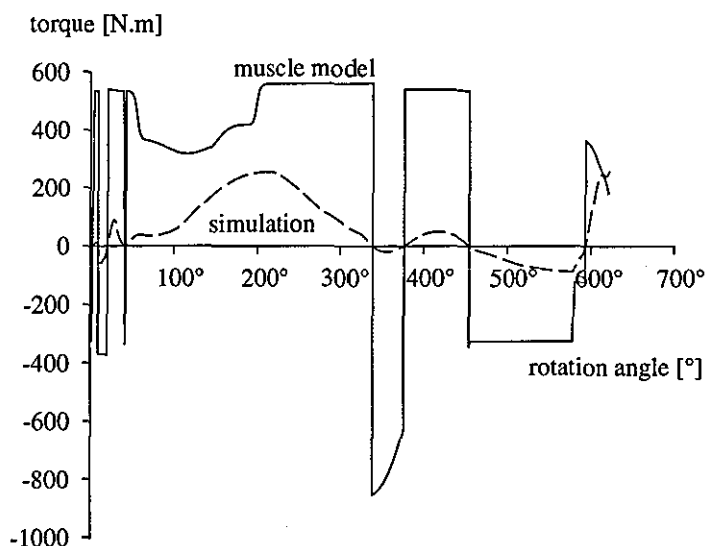


Figure 8.33. History of the maximum hip torques given by the muscle models and the torques produced by the simulation model when the strength of the muscle models was decreased by 10%.

As with the original optimisation the torques produced by the simulation model only approach the limits set by the muscle models in the action just before release. Again it appears as though the actions performed leading up to release have been limited to allow for the vigorous extension-flexion action at the shoulder joint just before release.

The bar displacements for the present optimisation are shown in Figure 8.34. When the histories of the bar displacements from the first three optimisations are overlaid it can be seen that the trajectory of the bar is almost identical in each case (Figure 8.35). In particular all three vertical traces show the change in velocity of the bar just before release. This negative vertical velocity of the bar would have facilitated the production of rotation about the model's mass centre at release.

In general the final values for the angular momentum about the model's mass centre at release were not greatly affected by the increase or decrease in peak joint torques given by the muscle models. In all cases the model had more than enough rotation to complete two and a half somersaults in the subsequent flight phase. In each case the techniques used at the hips and shoulders displayed similar patterns of timing, whether the torque limits were increased or decrease. However, the size of the joint actions were different, particularly when the joint torque limits were reduced. For the optimisations carried out so far the most important part of the technique appears to be the actions at the shoulder prior to release. The actions in the preceding giant circle do not appear to be as vigorous as might have been expected. In the video analysis of the accelerated giant circles the gymnast had a hip flexion angle of around 90° compared with 55° used in the original optimisation. The histories of the joint torque suggests that the model was capable of producing a more vigorous action at the hips yet the optimisation chose not to use this.

This may be explained in part by the actions occurring at release. When the shoulder angle is hyper-extended then flexed prior to release the shoulder joint torques produced by the model were at the joint torque limit. This meant that maximum effort was required to perform this action. It seems that the more vigorous this action the greater the increase in rotation at release. Therefore the actions performed in the wind up to the release are compromised to allow the model to perform as vigorous an action as possible. In addition the common timing of the actions used in the optimum simulations produce a change in vertical velocity of the bar just before release which facilitates the increase in rotation.

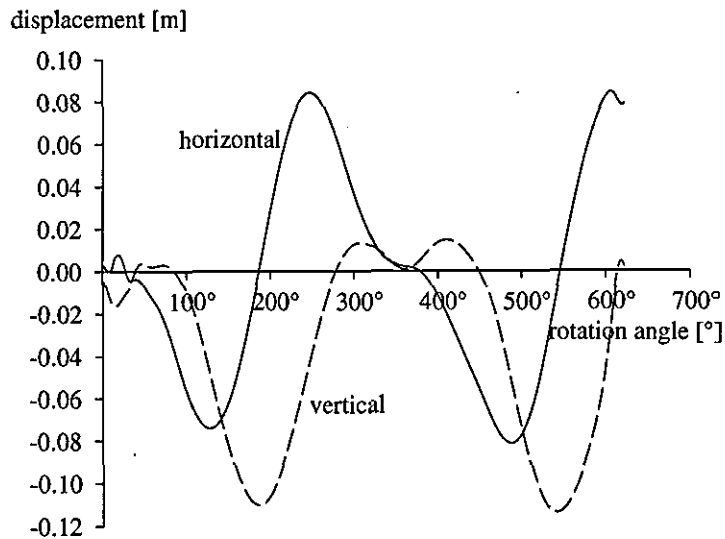


Figure 8.34. History of the horizontal and vertical displacements of the bar during the optimum simulation where the joint torque limits were decreased.

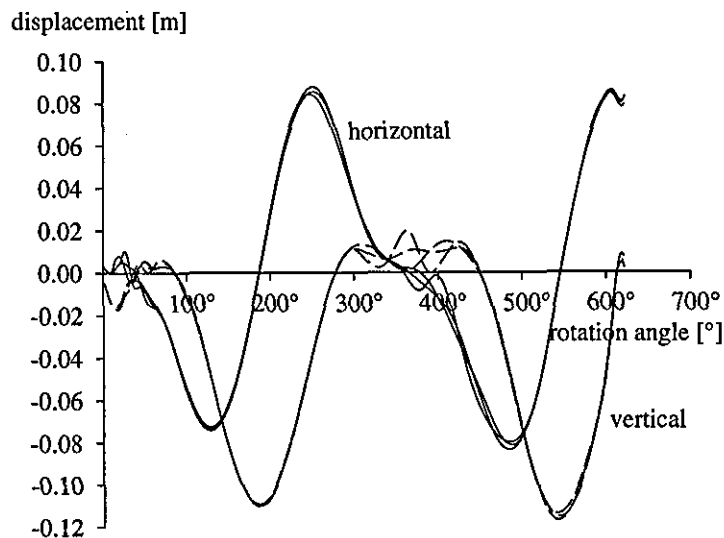


Figure 8.35. Histories from the first three optimisations of the horizontal and vertical bar displacements overlaid.

In an attempt to repeat the results obtained using the three segment model (section 8.2.3) a further optimisation was performed where the peak joint torques given by the muscle model were decreased by 25 percent. It was hoped that this reduction would be sufficient to cause the gymnast to flex at the hips after passing through the lowest point. Inspection of the joint torque time histories obtained from the evaluation of the four segment simulation model showed that for most of the simulation the joint torques produced by the simulation model were below 75 percent of the torques given by the muscle models.

After performing 7200 simulations the final value for the angular momentum about the model's mass centre at release was $110.9 \text{ kg.m}^2.\text{s}^{-1}$. The final value for the angular momentum was 11% less than for the original optimisation. Given that the optimum technique so far has relied on maximum effort at the end of the technique this drop in angular momentum would have been expected. When expressed as straight somersaults per unit flight time a value of 2.18 is obtained. Had the technique obtained from the present optimisation been used to perform a dismount the gymnast would have more than enough rotation to complete the double somersault.

The histories of the hip and shoulder angles from the optimisation where the strength of the muscle models were decreased by 25 percent are shown in Figure 8.36. As expected the timing of the flexion action has changed. With the reduction in the joint torque limits, over 70% of the flexion action at the hips was performed after the lowest point. Other changes to the history of the hip joint angle include the timing of the extension performed after the initial flexion action. In the previous optimisation the extension action was initiated before the highest point of the giant circle and was completed close to or just after the highest point. In the present optimisation the extension is not initiated until 20° past the highest point. The hips passed through full extension at a rotation angle of 442° and reached full hyper-extension at 480° . The hyper-extension was maintained until close to the end of the simulation where the hyper-extension angle was removed. The history of the shoulder angle follows a similar pattern to the optimisations already performed.

The joint torque at the shoulder joint, as in the previous optimisations, approached the joint torque limit only during the hyper-extension and flexion actions performed at the end of the simulation (Figure 8.37). The joint torque at the hips, however, approached the joint torque limit during the initial flexion action (Figure 8.38). This agrees with the findings from the three segment simulation model. By setting the joint torque limit low enough the model was forced to perform the flexion action later. In contrast, the joint torque limit, at the hips, was not approached during the extension performed at the hips between the rotation angles of 380° and 450° (Figure 8.38). This could point to a separate technique being used when compared with the original optimisation.

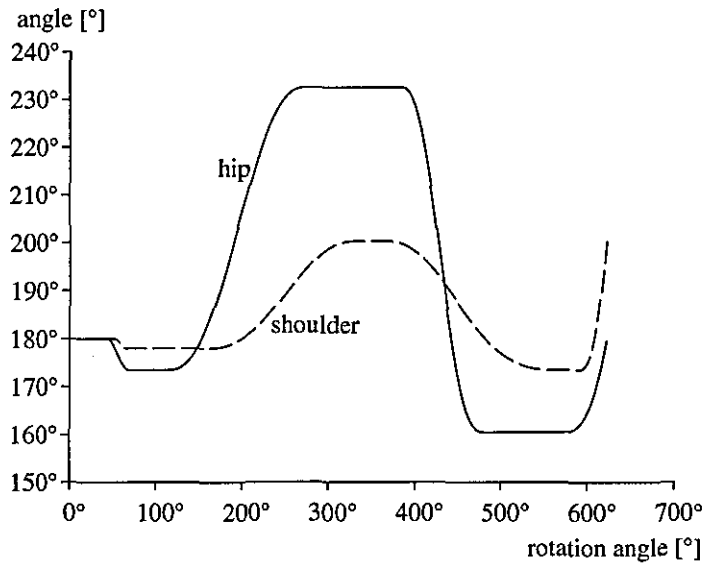


Figure 8.36. Histories of the hip and shoulder joint angles from the optimisation where the strength of the muscle models was decreased by 25%.

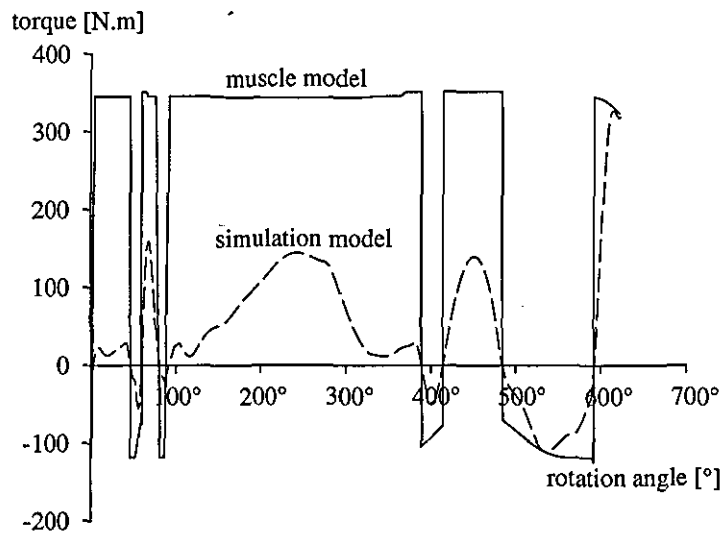


Figure 8.37. History of the maximum shoulder torques given by the muscle models and the torques produced by the simulation model when the strength of the muscle models was decreased by 25%.

When the present optimisation is shown as a set of graphic sequences it can be seen that the technique more closely represents the accelerated giant circles performed in the video analysis in Chapter 5/6. The model "scoops" over the top of the giant circle, passes through full extension close to the horizontal (450°), hyper-extends then flexes before release. The horizontal and vertical bar displacements for the present optimum simulation are shown in Figure 8.39. The vertical displacement of the bar is similar to those obtained from the previous optimisations, including the change in velocity of the bar just before the end of the simulation. One difference between the bar displacements of the

present optimisation and the previous optimisations is the small feature seen in the vertical trace as the bar is displaced vertically down for the second time. It appears as though the technique is starting to produce the double peak in vertical displacement seen in the video analysis of the accelerated giant circles. This is due to the later extension of the hip angle.

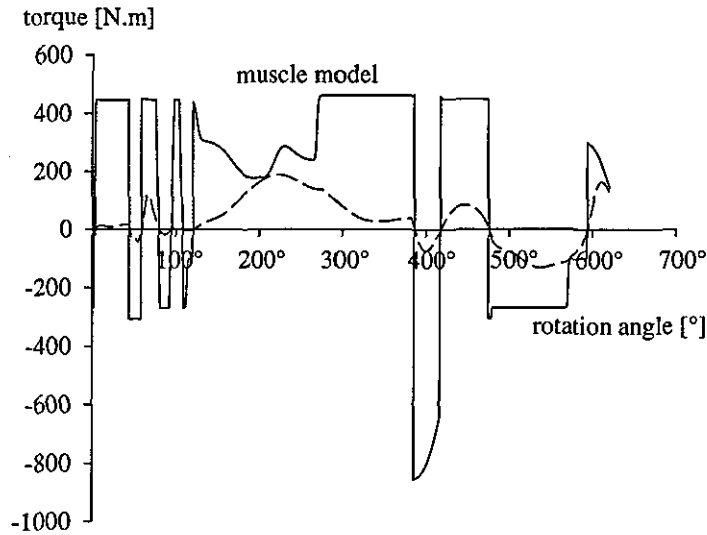


Figure 8.38. History of the maximum hip torques given by the muscle models and the torques produced by the simulation model when the strength of the muscle models was decreased by 25%.

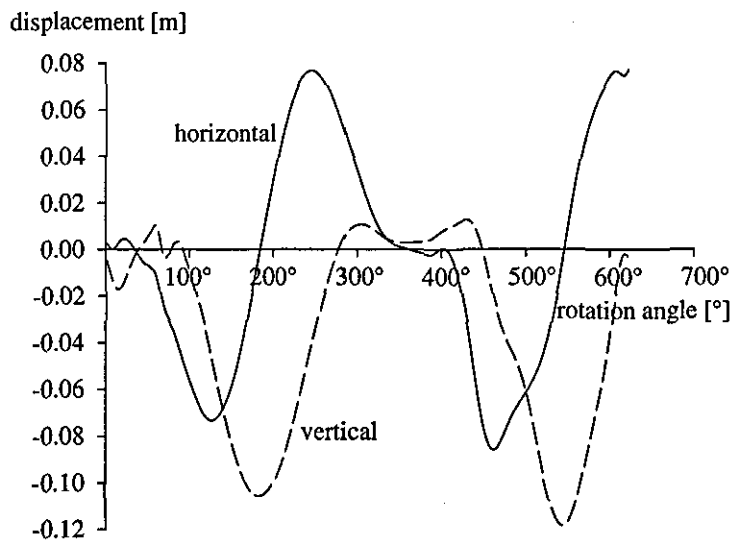


Figure 8.39. History of the horizontal and vertical displacements of the bar during the optimum simulation where the joint torque limits were decreased by 25%.

The technique found by optimising the accelerated giant circle with the strength of the muscle models decreased by 25% clearly bears closer resemblance to the technique used by the gymnast in the force and video analysis than the original optimisation does. Therefore, there may be two distinct techniques that may be used to perform the

accelerated giant circle. This could mean that the technique found by the optimisation with the 25% reduced muscle strength may be a local optimum with the original optimisation being the global solution. Since the final values for the angular momentum result in the gymnast having sufficient rotation to perform more than two straight somersaults the solution that required the least effort may be adopted by the gymnast. At the end of a gymnastic routine on the high bar the gymnast may not be capable of using maximum effort and would therefore choose a technique which did not rely on this for successful performance of the subsequent dismount.

To test whether the technique obtained from the reduced strength optimisation was a local optimum, another optimisation was performed. The optimisation was started from the solution obtained from the reduced strength optimisation but with the strength of the muscle models set to maximum. A lower initial temperature was set for the Simulated Annealing algorithm so that only simulations which are an improvement on the current optimum are accepted. In addition the rate at which the temperature dropped was increased so that a "quenching" effect would take place. If the starting point is a local optimum a solution close to this will be obtained. If not the optimisation should produce a technique similar to that obtained by the original optimisation.

After the "quenching" optimisation had been performed the optimum value for the angular momentum about the model's mass centre was $122.1 \text{ kg}\cdot\text{m}^2\cdot\text{s}^{-1}$. This represents a value that is less than 3% smaller than the global optimum. When expressed in terms of straight somersaults per unit flight time the present optimum produces 0.14 revolutions less than the original optimisation. Figure 8.40 shows the current optimum technique as a sequence of graphic figures. The technique obtained from the present optimisation has remained very similar to the technique obtained from the optimisation where the strength of the muscle models was reduced by 25% (Figures 8.36 and 8.41).

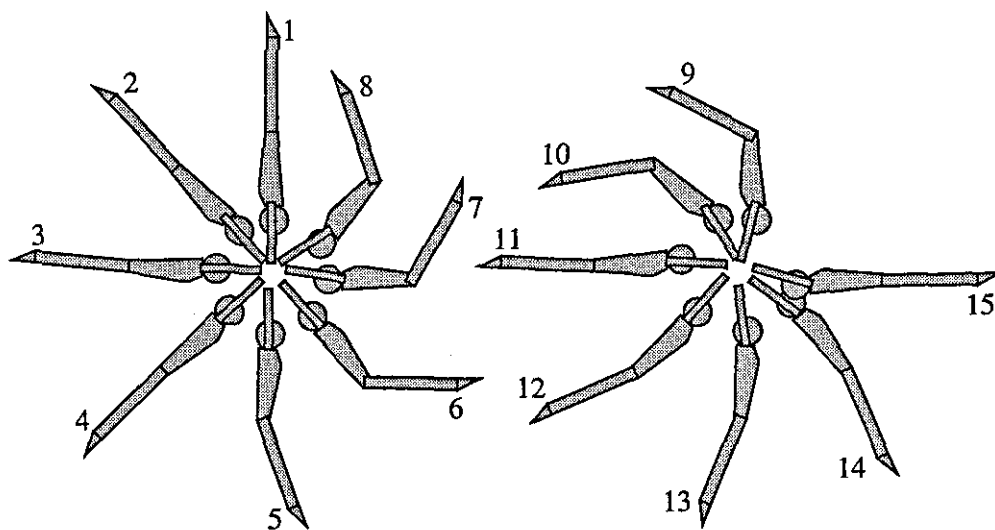


Figure 8.40. Sequence of figures representing the local optimum technique.

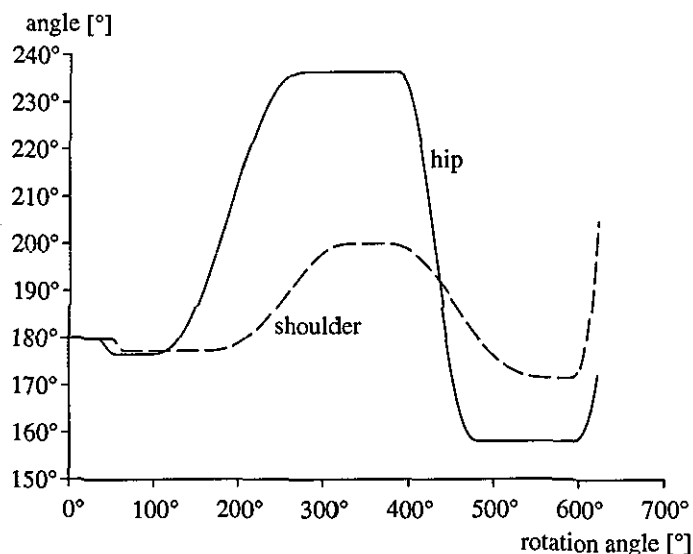


Figure 8.41. Histories of the hip and shoulder joint angles from the optimisation used to find the local optimum.

Small differences occurred between the local optimum and the optimum obtained from the optimisation where the strength of the muscle models were decreased. Both the initial hip flexion and second hip hyper-extension angles were slightly larger for the local optimum. This is to be expected since the local optimum used full strength muscle models to limit the joint torques at the hips and shoulders. Similarly in the local optimum the first hip flexion action was performed slightly earlier. Again this might be expected due to the higher joint torque limits.

The displacements of the bar during the local optimum are shown in Figure 8.42. As with the joint angle time histories, the displacements of the bar are very similar to those obtained from the optimisation where the strength of the muscle models was decreased by 25%.

It therefore appears as though there are two local optima on the solution surface which are very close to each other in terms of the final value of the cost function. In the first technique the gymnast extends shortly after passing through the highest point of the giant circle. This is a more "classic" style of backward giant circle. The second technique involves the gymnast "scooping" through the highest point and extending close to the horizontal. This is a modern technique which is now used by many elite gymnasts. The fact that both optima are so close in the angular momentum values they generate would explain why some gymnasts use the classic style of backward giant circle whilst others use the modern "scooping" technique. Since both techniques may be used to increase the gymnast's rotation by similar amounts it would seem that the choice of technique used lies with the gymnast's preference. However, under certain circumstances the "scooping" local optimum becomes the global optimum and the classical global

optimum becomes a local optimum. When the strength of the muscle models was decreased by 25% the "scooping" technique became the optimum technique. This presents a number of questions for the researcher and choices for the gymnast. A less well-conditioned gymnast may opt for the "scooping" technique since he can achieve more rotation given his state of physical preparation. Similarly a well-conditioned gymnast may choose the "scooping" technique because he feels that he can achieve similar amounts of rotation for slightly less effort than the classic technique. The gymnast is therefore using a technique where he knows he will not require maximal effort. This would be an obvious advantage since the gymnast is likely to be most fatigued at the end of his gymnastic routine which is when the dismount is performed.

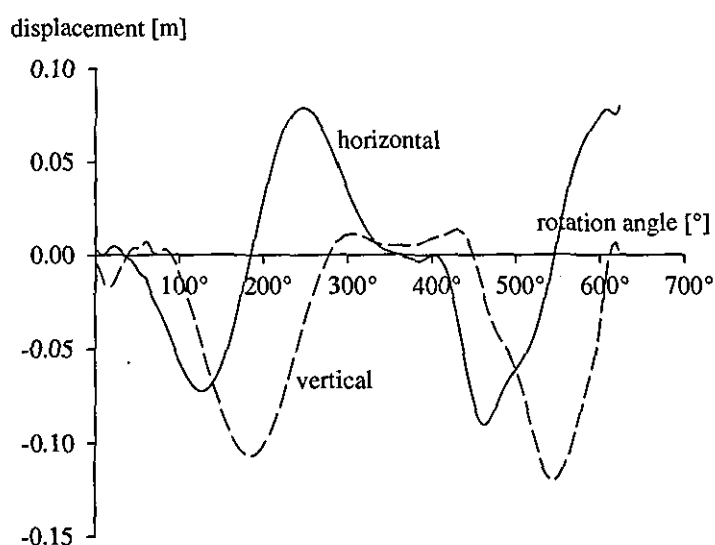


Figure 8.42. History of the horizontal and vertical displacements of the bar during the local optimum simulation.

Varying the inertia parameters

The optimum joint angle time histories obtained from the original optimisation were used to drive one simulation using the inertia data of subject tv01 (Table 8.9). It was found, using these joint angle time histories and the inertia data of subject tv01, that the joint torque limits at both the hip and shoulder joints were exceeded (Figures 8.43 and 8.44). In both cases the joint torque limits were exceeded at the points in the simulation where the joint torques produced when using inertia data jb01 approached the joint torque limits. Since the individual moments of inertia for subject tv01 were all slightly larger than those for subject jb01 (Tables 8.6 and 8.9) the fact that the joint torque limits were exceeded is not surprising.

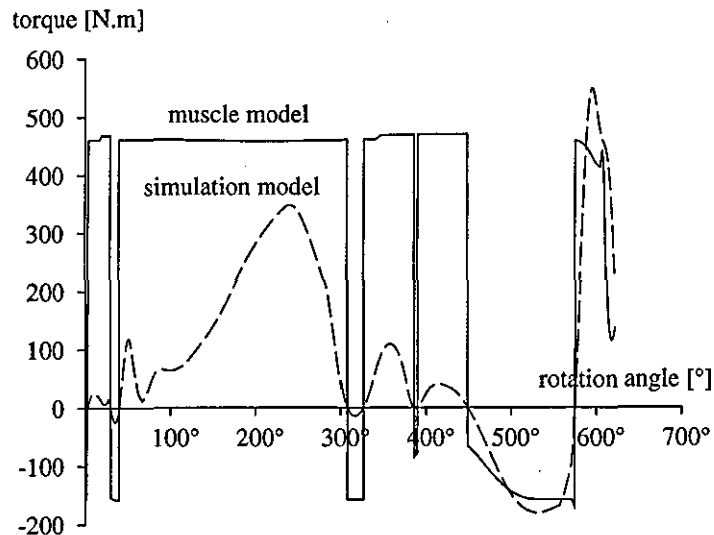


Figure 8.43. History of the shoulder joint torques and the maximum joint torques given by the muscle models when the optimum joint angle time histories were used with the inertia data of subject tv01.

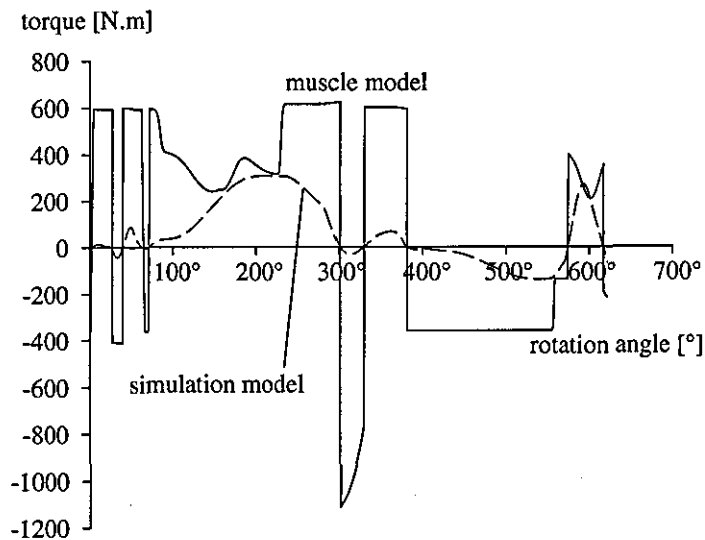


Figure 8.44. History of the hip joint torques and the maximum joint torques given by the muscle models when the optimum joint angle time histories were used with the inertia data of subject tv01.

An optimisation was then performed using the inertia data from subject tv01 with the joint torque limits of jb01. The optimum value for the angular momentum about the model's mass centre was $148.2 \text{ kg.m}^2.\text{s}^{-1}$. This is higher than the value reported for the original optimisation ($125.1 \text{ kg.m}^2.\text{s}^{-1}$). However, when normalised into rad.s^{-1} the percentage difference dropped to less than 3%. In the layout body shape subjects jb01 and tv01 had moments of inertia about their mass centre of 8.78 kg.m^2 and 10.11 kg.m^2 respectively.

The joint angle histories from the present optimisation are shown in Figure 8.45. As with the original optimisation the model passes through full extension at the hips shortly after passing through the highest point of the giant circle. It appears as though the optimum technique is again the "classic" backward giant circle technique. The initial flexion action at the hips was performed later in the present optimisation when compared with the original optimisation. However, from Figure 8.46 it can be seen that the joint torque at the hip approached the joint torque limit during this action, therefore the model was probably not strong enough to perform this action earlier. Again this would have most likely been as a result of the larger moments of inertia of subject tv01. Both the hip and shoulder joint torque limits were approached close to the end of the optimal simulation (Figure 8.46 and 8.47) which has been the case with each of the optimisations performed so far.

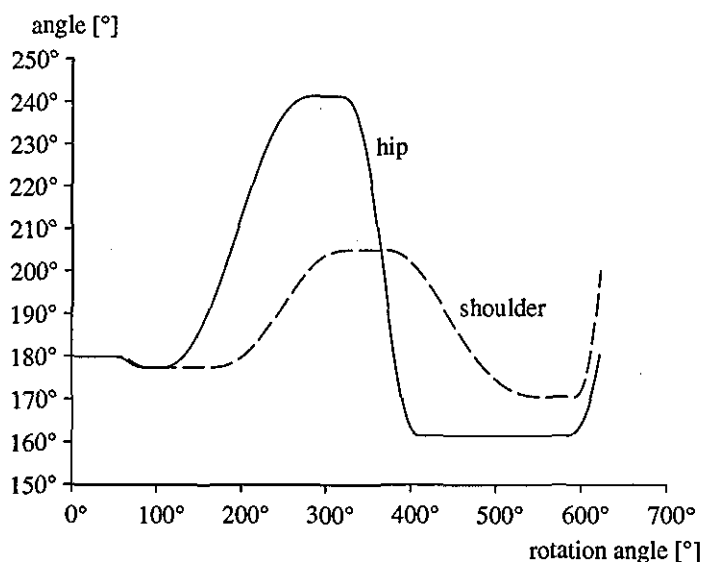


Figure 8.45. Histories of the hip and shoulder joint in the optimisation where the inertia data of subject tv01 was used.

Varying the release angle

When the original optimisation was performed each simulation ended at exactly the same rotation angle. There are cases where the gymnast may not always release at the desired angle due to the timing of the preceding actions or through spacial awareness. Therefore an optimisation was performed where the release angle was different to that used in the original optimisation. Each simulation performed in this sensitivity analysis ended after the model had passed through a rotation angle of 607° as opposed to 622°. After performing 7200 simulations the angular momentum about the model's mass centre at release was 129.6 kg.m².s⁻¹. This resulted in an increase of 4% in angular momentum at release and an increase in rotation of 0.07 revolutions in the subsequent flight phase.

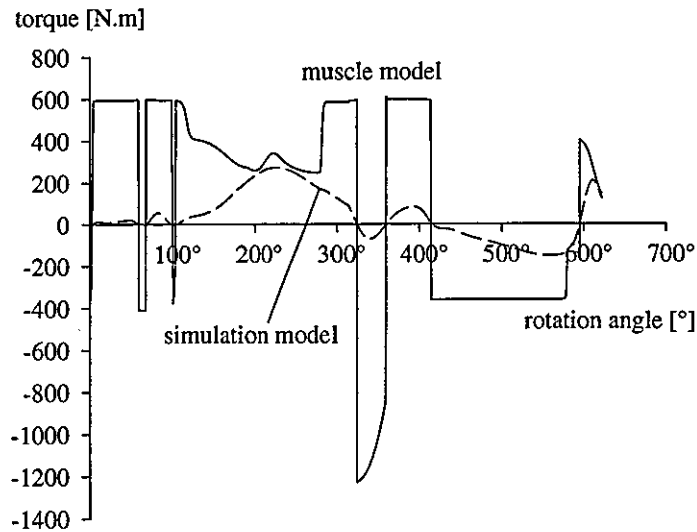


Figure 8.46. History of the hip joint torques and the maximum joint torques given by the muscle models during the optimum solution when the inertia data of subject tv01 was used with the torque limits of jb01.

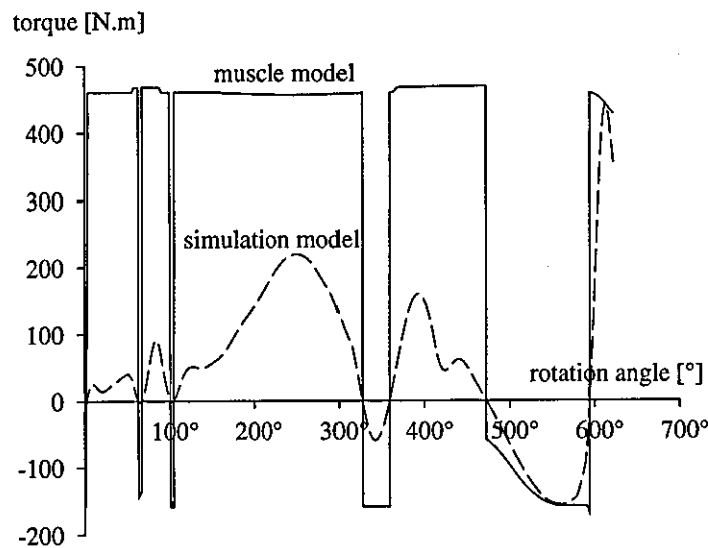


Figure 8.47. History of the shoulder joint torques and the maximum joint torques given by the muscle models during the optimum solution when the inertia data of subject tv01 was used with the torque limits of jb01.

The joint angle histories of the optimum simulation for the earlier release are shown in Figure 8.48. It can be seen that the model extends at the hips just after passing through the highest point of the giant circle. The timing of the first flexion action at the hips occurred later than in the original optimisation. This may have been as a result in the changing the angle at which each simulation finished.

The bar displacements from the current optimisation are shown in Figure 8.49. The characteristic change in direction of the vertical bar displacement appears just before the end of the simulation. This may explain why the joint angle time histories are slightly

different in the current optimisation. Slight alterations may have been required to produce the correct loading of the bar to produce this phenomenon.

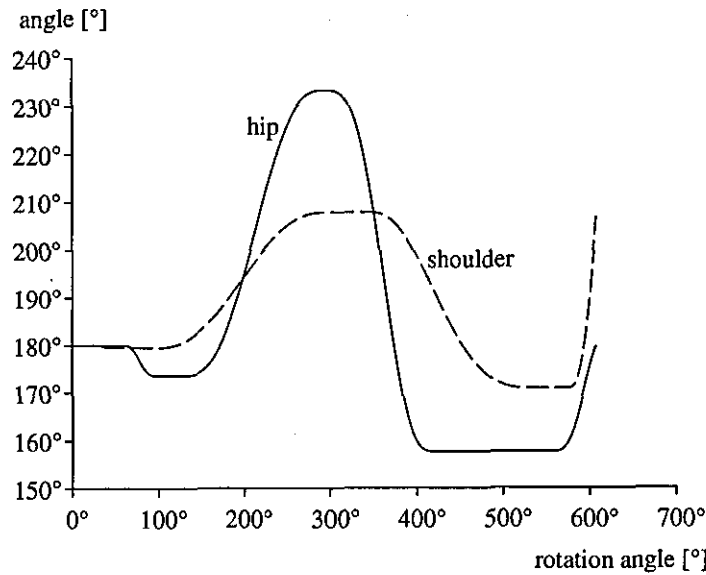


Figure 8.48. Histories of the hip and shoulder joint angles from the optimisation where each simulation finished at 607°.

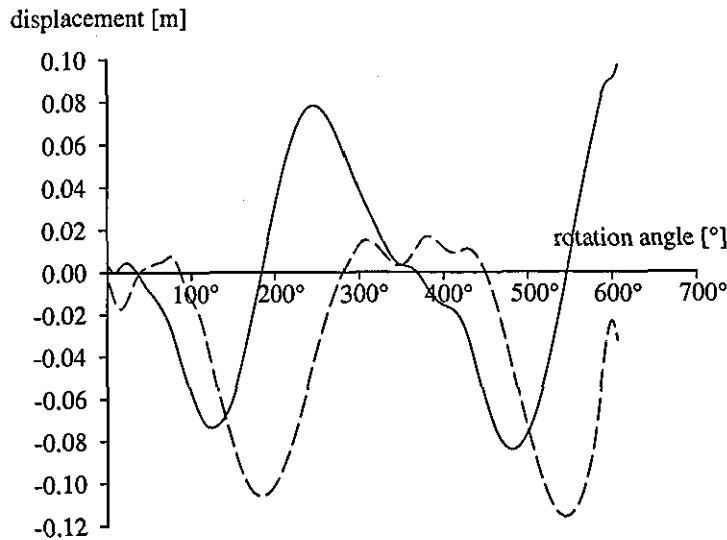


Figure 8.49. Histories of the horizontal and vertical bar displacements from the optimisation where each simulation finished at 607°.

Varying the stiffness coefficients of the bar

Initially two simulations were performed where the optimum joint angle time histories from the original optimisation were used with the increased and decreased bar stiffness coefficients. The final values for the angular momentum about the model's mass centre for the two simulations where the stiffness of the bar was increased and decreased

were $121.7 \text{ kg.m}^2.\text{s}^{-1}$ and $126.51 \text{ kg.m}^2.\text{s}^{-1}$, respectively. These two values are less than 3% different from the original optimum value. However, in both cases the shoulder joint torque limits were exceeded. These limits were exceeded within the last 20% of the simulation. In all the previous optimisations the joint torques produced by the simulation model have approached the joint torques given by the muscle models. Figures 8.50 and 8.51 show the joint torques produced by the simulation model expressed as a percentage of the peak joint torques given by the muscle models. For both simulations the joint torque limits are exceeded by less than 1.2%. Therefore performance at the optimum solution does not appear to be sensitive to the stiffness coefficients of the bar. The stiffness of the bar was increased and decreased to cover the range of stiffnesses that would be expected from the manufacture of the bar. This range was larger than the acceptable range quoted by the FIG.

To confirm the insensitivity of the optimum solution the backward giant circle was optimised using the increased and decreased high bar stiffness coefficients. After the optimisations were completed the values for the angular momentum about the model's mass centre were $125.1 \text{ kg.m}^2.\text{s}^{-1}$ and $124.6 \text{ kg.m}^2.\text{s}^{-1}$ respectively. Again, these values are very close to the original optimised values (<1/2% different).

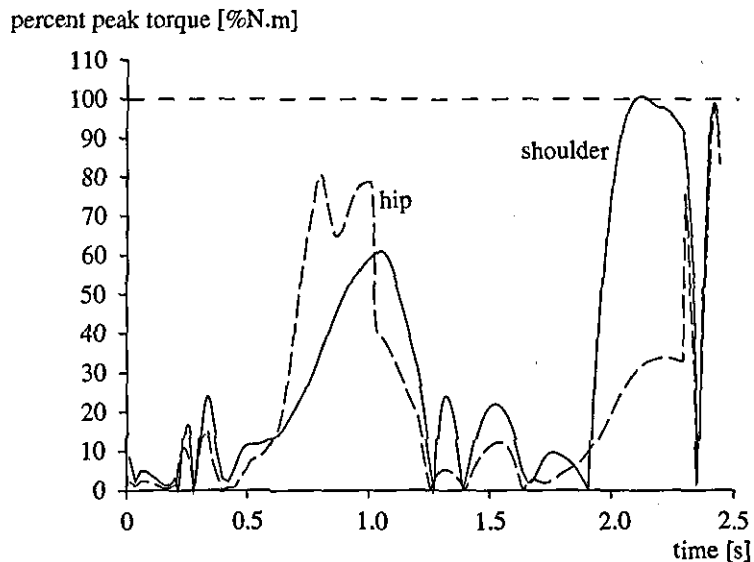


Figure 8.50. Time history of the hip and shoulder joint torques produced by the simulation model expressed as a percentage of the peak torques given by the muscle models when the stiffness of the bar was increased.

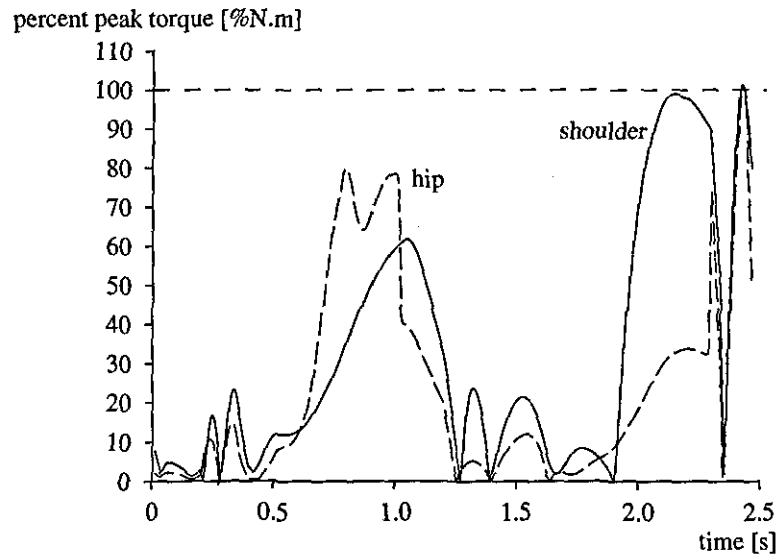


Figure 8.51. Time history of the hip and shoulder joint torques produced by the simulation model expressed as a percentage of the peak torques given by the muscle models when the stiffness of the bar was decreased.

Varying the initial angular velocity

The sensitivity analysis performed on the initial angular velocity of each simulation yielded a final value for the angular momentum about the model's mass centre of $120.8 \text{ kg}\cdot\text{m}^2\cdot\text{s}^{-1}$. This is a decrease of less than 5% when compared to the original optimisation. It therefore appears as though starting each simulation with an angular velocity of half that used in the original optimisation does not result in a large difference in final angular momentum.

The history of the hip and shoulder angles from the present optimum simulation are shown in Figure 8.52. The histories of the hip and shoulder angles are very similar to those obtained from the original optimisation. Obvious differences would be the timing of the action when compared in a temporal sense as opposed to the angular equivalent. The first flexion and extension actions at the hip joint are very similar in terms of where they occur in the giant circle. In the present optimisation the hip joint passes through full extension at a rotation angle of 345° .

It would be of interest to see what local optima lie around this solution. It may be that the "scooping" technique that was found close to the global optimum may have an equivalent close to the present solution. This would be a promising result since it would then appear as though both the global and "scooping" techniques could be used under numerous different conditions to produce equivalent amounts of rotation.

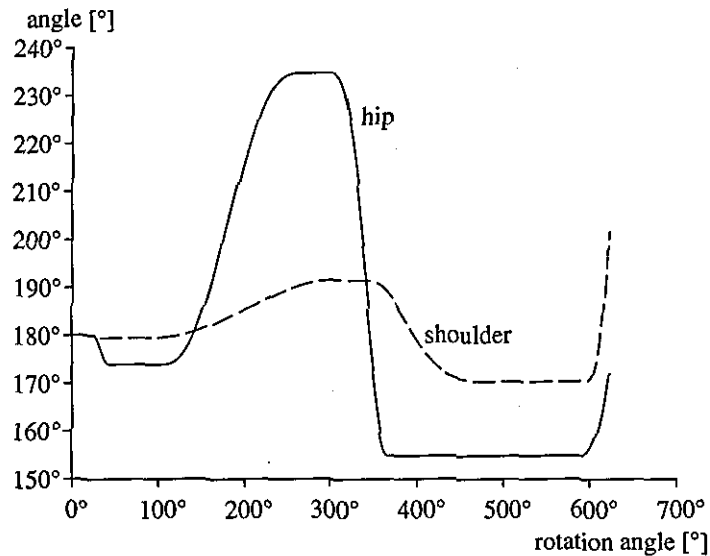


Figure 8.52. Time histories of the hip and shoulder joint angles from the optimisation where the initial angular velocity of the model was reduced by half.

8.3.4 Conclusions

The technique obtained from the global optimum produced more rotation than was required to perform a double layout backward somersault dismount from high bar. The technique followed the "classic" style of giant circle where the gymnast achieves full extension at the hips close to the highest point of the giant circle (360°). When the strength of the muscle models used to limit the simulation model were increased or decreased by 10% there appeared to be only small differences between the techniques obtained and the final value for the angular momentum about the model's mass centre. Most of the differences could be explained using the findings from section 8.2. However, when the strength of the muscle models was reduced by 25% a "scooping" optimum technique was obtained. That is, full extension at the hips was achieved closer to the horizontal (450°), than the vertical handstand (360°). When the strength of the muscle models was returned to 100% it was found that this technique was a local optimum whose final value for the angular momentum about the model's mass centre was only 3% less than the value obtained from the global optimum. Therefore, under certain circumstances the global and local optimum solutions can become interchanged.

The displacements of the bar all displayed similar trajectories close to the end of the optimum simulations. The vertical displacement of the bar changed from moving upward to moving downwards. When considering the angular momentum about the model's mass centre this phenomenon is of benefit to the gymnast. Even when the release angle of the model was changed the characteristic displacement of the bar was found by the optimisation procedure.

When the inertia data was changed from subject jb01 to subject tv01 a similar set of results were obtained. It was found that the optimum result was also not sensitive to changes in the stiffness of the high bar. Although, had the stiffness of the bar been increased or decreased by an unrealistic amount changes to the optimum technique would probably have been invoked.

The initial angular velocity of each simulation was halved in order to see its effect on optimum technique. It was found that reducing the initial angular velocity had only a small effect on the final angular momentum about the model's mass centre.

CHAPTER 9

SUMMARY AND DISCUSSION

9.1 Introduction

This section will outline the answers to the research questions posed in the first chapter and will refer to the relevant sections for further details and summaries. In addition a section on future research will pose questions relating to both the present work and work which may be carried out in the future.

9.2 Answers to the research questions

Question 1

How does the gymnast's technique differ between regular and accelerated giant circles?

As stated in Chapter 1 both the regular and accelerated giant circles use actions at the shoulders, hips and knees. This was shown to be the case in Chapter 6. In general the size of the flexion angles used in the accelerated giant circles were larger than those used in the regular giant circles. Other differences included the timing of the flexion at the hips and shoulders. The subject, used in the video analysis of the accelerated giant circles, used a "scooping" technique during his accelerated giant circles. This resulted in the flexion action at the hips being performed through a larger angle of rotation than a gymnast performing a more classical accelerated giant circle. Similarly the extension action during the "scooping" accelerated giant circle occurs later (after the gymnast has passed through the highest point) and is performed over a larger angle of rotation. In the regular giant circle the gymnast was fully extended as he passed through the highest point.

The displacements of the high bar were also larger for the accelerated giant circles. In the vertical direction the difference between the peak displacements was approximately 0.03 m. In the horizontal direction the difference in peak bar displacements was 0.04 m. An interesting feature of the accelerated giant circles was that the peak horizontal and vertical displacements of the bar were approximately equal. In the regular giant circles the horizontal displacement of the bar was consistently smaller than the peak vertical

displacements (approximately 20%). This indicates that the "scooping" technique adopted in the accelerated giant circles leads to a larger horizontal loading of the high bar.

Question 2

What are the reaction forces exerted by the bar on the gymnast as he performs both regular and accelerated giant circles ?

During the regular giant circles the peak reaction forces in the horizontal and vertical directions were 2.4 and 3.4 bodyweights, respectively. The peak resultant reaction force was also 3.4 bodyweights. This value compared well with the value of 3.6 bodyweights obtained by Kopp and Reid (1980). During the accelerated giant circles the peak reaction forces in the horizontal and vertical directions were 4.0 and 4.4 bodyweights, respectively. The peak resultant reaction force was 5.0 bodyweights. The 5.0 bodyweights equates to approximately 3092.2 N.

Question 3

Does the high bar behave like a damped linear spring ? If it does can the kinetic and kinematic analysis of regular and accelerated giant circles be used to obtain stiffness and damping coefficients for such a spring ?

The results from the regressions performed between the reaction forces at the bar and the linear velocities and displacements of the bar were presented in Chapter 6. Using just the linear regressions between the reaction forces and the bar displacements, standard errors for the regression line in the horizontal and vertical directions of 48.2 N and 60.1 N, respectively, were obtained. These values equate to less than 0.1 of a bodyweight. When the regression equation was used to estimate the reaction force for another regular giant circle (whose data had not been included in the regression analysis), based purely on the displacement of the bar during the trial, the rms difference between the recorded and the estimated reaction forces was 69.1 N (< 0.12 bodyweights). It therefore appeared as though the high bar behaved as a linear spring.

When the linear velocity of the bar was entered into the regressions the standard errors were reduced to 48.0 N and 48.5 N, respectively. The rms difference between the recorded and estimated reaction forces was 64.3 N (< 0.11 bodyweights). Although there did not appear to be a great difference between the two sets of regressions, the standard errors always improved with the introduction of bar velocity.

The coefficients from the linear regressions represent the stiffness and damping coefficients of the bar. These could be used to estimate the reaction forces at the bar or could be used as the stiffness and damping coefficients of a damped linear spring in a simulation model. In Chapter 7, section 7.2, the introduction of a damped linear spring to

a single segment simulation model was shown to improve the accuracy of the model (see section 7.2.3).

Question 4

Is there any evidence that the joints of the gymnast behave as elastic structures as he circles the high bar? If so which joints behave this way?

In Chapter 6 the video analysis program was used to output the segment lengths for each video field. Table 6.13 shows the mean length of each segment and its standard deviation. It was found that during the backward giant circles the gymnast increased in length as he circled the bar. As the gymnast passed through the lower part of the circle the increase in length was the greatest. By looking at the time histories of the length of each segment it was found that the majority of the increase in length occurred between the gymnast's wrists and hips. It is speculated that this could be attributed to shoulder extension and to extension between the vertebrae of the spine. During the giant circles analysed in this study the extension between the wrist and hips was between 0.10 and 0.14 m. This agreed with the findings of Suchilin (personal correspondence).

To see if this extension could be represented by a linear spring, the extension in the gymnast was regressed against the reaction force at the bar. When the regressions were performed on the data obtained from both regular and accelerated giant circle trials the stiffness coefficient ranged from 12816 to 16467 $\text{N}\cdot\text{m}^{-1}$. The standard error for the regression approached one bodyweight, with the correlation coefficient approaching 0.5. However, looking at the raw data there did appear to be a general trend that as the reaction force increased so did the extension in the gymnast. Had the internal joint forces been available a better correlation may have been obtained. This would be something to investigate in the future.

Question 5

What are the mechanics behind the flexion and extension actions performed by gymnasts during regular and accelerated giant circles?

Bauer (1983) represented the technique of swinging as a pendulum of varying length. In order to perform giant circles the pendulum maintained maximum length on the downswing, instantaneously shortened at the lowest point and then returned to maximum length instantaneously at the highest point. This is a simplistic approach since a gymnast is far more complex than a pendulum. The gymnast's segments have mass and moments of inertia which need to be considered.

In section 8.2 the three segment simulation model was used to optimise a backward giant circle. Initially there were no constraints placed on the size of the joint torques the

model could produce. The optimum solution had the model performing the flexion action at the hip and shoulder joint before the lowest point, a technique not used by gymnasts. By looking at the joint torques involved in performing an early flexion action it was shown that doing so lead to a greater increase in energy. A similar explanation was provided when it was found that the model extended before reaching the highest point.

The optimisation was repeated using a joint torque limit at the shoulders. The flexion action was then performed as the model passed through the lowest point. This was because the model was no longer strong enough to perform the action before the lowest point. Similarly the model performed the extension action as it passed through the highest point. This technique more closely represented the techniques used by gymnasts.

When using the four segment simulation model with the muscle models used to limit the joint torques at the hip and shoulder joints a similar result was obtained. The model performed the flexion action passing through the lowest point and the extension action passing through the highest point. Since the four segment model was used to optimise the angular momentum about the model's mass centre after performing $1\frac{3}{4}$ giant circles, had the more simple three segment model not been used to optimise the backward giant circle the underlying mechanics may have been missed.

Question 6

How does the strength of the gymnast effect optimum technique ?

In section 8.2 the introduction of a joint torque limit changed the optimum technique found by the three segment model from a theoretical solution to one which represented the techniques used by real gymnasts. When using the joint torque limit the model was not strong enough to perform the theoretical solution and adjusted the technique accordingly. Therefore it could be stated that gymnasts do not perform the flexion action before the lowest point either because they are not strong enough or because they choose to conserve energy. A third reason may be due to the skill performed after the giant circle. Flexing before the lowest point may produce an undesired loading of the bar. This is a question for further research.

In section 8.3 the strength of the muscle models was increased and decreased by 10% to see the effect this would have on the optimum solution. The change in rotation was found to be less than 3% when the strength of the muscle models was changed. The change in muscle strength caused small changes in the joint angle time histories which could be explained in terms of the results obtained in section 8.2.

When the strength of the muscle models was decreased by 25% the final angular momentum was reduced by 11%. Given that this still represented more rotation than is required to perform a double layout backward somersault dismount and that the gymnast is only $\frac{3}{4}$ as strong as he was, this is not a large drop in performance. However, when the

joint angle time histories were compared the model was performing a "scooping" technique through the upper part of the accelerated giant circle. This technique was found to be a local optimum when the strength of the muscle models was returned to 100% and the difference in angular momentum from the original optimisation was less than 3%.

For the majority of both the local and global optimum techniques the model used 30% of the maximum joint torques given by the muscle models. Only during the first flexion action and the last quadrant of the optimum simulations did the joint torques used by the simulation model approach the maximum values.

At the end of a gymnastic routine it may not be in the gymnast's interest to rely on a technique that will require maximum effort. Alternatively, since both techniques appear to produce similar amounts of rotation gymnasts are able to make a choice about which technique to use. As yet I have not found an intermediate technique which connects the two optima found so far. That is, the two techniques are distinct and separate. To perform a technique half way between these results in less angular momentum than either.

Question 7

Does optimum technique of the backward giant circle differ between gymnasts or is there a common technique that could be adopted by all gymnasts ?

In section 8.2 there was found to be only small differences between the joint angle time histories when the backward giant circle was optimised using the inertia data of jb01 and tv01. Even when the joint torque limit at the shoulder was introduced the two optimum giant circles were very similar (Figures 8.14 and 8.15). It may therefore be suggested that although small changes in the joint angle time histories will occur the underlying technique and mechanics will remain the same.

When the optimum joint angle time histories from the four segment model were used with the inertia data obtained from subject tv01 and the maximum torque data of subject jb01 it was found that the model was not strong enough to complete the $1\frac{3}{4}$ giant circles. However, after optimising the backward giant circle using the inertia set tv01 an optimum solution was obtained. Using the inertia set tv01 resulted in an increase in angular momentum about the model's mass centre of 28%. When this was normalised so that the two gymnasts could be compared the difference dropped to 3%. When the sets of joint angle time histories were compared they were very similar; again any small differences could be explained in terms of the results obtained from section 8.2.

Gymnasts are a select group of individuals whose inertia parameters differ from the general population. Given these characteristics and that the laws of mechanics apply to everyone it is likely that given a set of inertia data for a gymnast the optimum solution will lie close to the one found in the present study. Small differences in the joint angle time histories will occur due to the different strength characteristics; however, the general

technique can be explained by the mechanics highlighted in Chapter 8.

9.3 Future Directions

9.3.1 Introduction

The work carried out in this thesis has provided a platform from which to carry out further research. This section will highlight the limitations in the present research so as to offer avenues for future research.

9.3.2 Data collection

From the data collection it has been shown that the reaction force at the bar can be estimated from its horizontal and vertical displacements, as long as the stiffness of the bar is known. The use of a third camera trained on the centre of the bar may therefore lead to improved accuracy in the estimation of reaction forces. Should this be the case a protocol could be established for recording reaction forces at the bar without using strain gauge technology.

All the simulation models used in this thesis assumed zero friction between the bar and the model. In reality this is not the case (Hay, 1994; Kopp and Reid, 1980). Based on the evaluation of the simulation model this does not appear to have been a problem. Strain gauges can be arranged to measure the torque produced at the bar (Kopp and Reid, 1980). However, from personal experience it is a non-trivial task to apply known torques to the bar in order to calibrate the strain gauges.

9.3.3 Simulation

The bar

Arampatzis and Brüggemann (1995) modelled the high bar as a 12 segment structure. Compared with a damped linear spring this is very sophisticated. The damped linear spring performed well in terms of estimating bar displacements and reaction forces. However, the mass of the bar was represented as a point mass at the end of the model's proximal segment (the arm). It is likely that if the structure of the bar, in terms of mass distribution and moment of inertia, were to effect performance that these would have been incorporated into the spring coefficients during the optimisation of the spring coefficients.

A closer look at the structure of the bar may be necessary in the future so as to gain greater understanding of how its loading and unloading effect technique.

Knee flexion

In the literature the major contributions to technique were attributed to the hips and shoulders (Okamoto et al., 1987; Brüggemann et al., 1994). This was confirmed by the findings in Chapter 6. It was also found that the knees contributed to technique (Brüggemann et al., 1994; Chapter 6), with the knees flexing and extending through the lower part of the giant circle. These knee flexions were used in the evaluation of the simulation model but were left out of the optimisation. The knees were assumed to stay fully extended throughout the optimisation as this both represented good form and reduced the number of parameters to be optimised. The introduction of knee flexion and extension would have increased the number of parameters to be optimised from 24 to 36.

It would therefore be of interest to establish the contribution of knee flexion to either existing techniques or to the optimum technique. This could be achieved by removing the knee flexion and extensions from the simulations used to evaluate the simulation model. Alternatively knee flexion could be introduced into the optimum solution. Further, the knee flexion could be optimised by fixing the joint angle time histories of the hip and shoulder angles and varying the timing and size of knee flexion and extension each time the model passed through the lowest point.

For the introduction of the knee actions into the optimisation it may be necessary to collect more subject specific muscle data so that muscle models can be used to represent the maximum strength of the knee flexors and extensors.

Double layout backward somersault dismount

The optimisations performed in Chapter 8 have been geared to maximising the model's rotation. Normalised values for the angular momentum about the model's mass centre have so far exceeded those required to perform the double layout somersault dismount. It would therefore be of interest to optimise a set of accelerated giant circles to produce the best release conditions for the double layout somersault dismount. This would no longer be a case of maximising the angular momentum about the model's mass centre. A cost function could be developed to incorporate a score for producing the correct amount of rotation but also including bonus for time of flight.

Strength of the muscle models

In the optimised accelerated backward giant circles found in section 8.3 the model used 30% of the maximum peak joint torque throughout the majority of the simulation. How far could the strength of the muscle models be reduced with the model still able to perform a double layout somersault dismount? When the strength of the muscle models

was reduced in section 8.3 a local optimum was found which represented a distinctly different technique to the original optimum. Investigating further the strength of the muscle models may yet yield more interesting results.

Airborne skills

Simulation models have been used to investigate new skills and techniques which have not been tried by real gymnasts (Nissinen, Preiss and Brüggemann, 1985). The theoretical solutions obtained in this thesis could be used as a basis for finding out what would be possible in the subsequent release skill. By using the release conditions from the four segment simulation model as initial conditions for a simulation model of aerial movements (e.g. Yeadon, Atha and Hales, 1990) it would be possible to determine what dismount could be performed given the optimum amount of rotation.

Other skills

For some release skills maximising the rotation of the model during the wind-up giant circles is not appropriate. For instance, the Tkatchov has been shown to have rotation in flight in the opposite direction to the preceding backward giant circle (Brüggemann et al, 1994; Gervais and Tally, 1993). To optimise the backward giant circle prior to release may require the angular momentum about the model's mass centre to be minimised at the point of release. This could be incorporated into a cost function which included the release conditions which would allow the model to clear the bar in the subsequent release.

In short it would be possible to optimise the accelerated giant circles for most dismounts and release skills which are performed from either a backward or forward giant circle. Similarly it would also be interesting to investigate regrasping the bar after a release and regrasp skill. In the current Code of Points bonus is awarded for performing skills in succession. For example, it is not uncommon in elite competition to see three Tkatchovs (with varying technique) or two Kovacs to be performed in succession. When performing skills one after another the regrasp after the first skill is vital. Optimum regrasp conditions could be determined to allow for the subsequent release skill to be performed.

Asymmetric bars

The future directions outlined so far have all concerned the high bar. This thesis is entitled "The mechanics of swinging on the high bar". However, many of the ideas and techniques could be applied to swinging on the asymmetric bars. Obvious differences are the construction of the bar, inertia and strength characteristics of the female gymnast and the presence of a second bar which the gymnast must avoid during the downswing. The bar would require different spring coefficients and would therefore need to be calibrated

along the lines of the high bar. Due to the asymmetric bar's larger surface area frictional forces between the gymnast's hand and bar would also need to be quantified and taken into consideration.

The four segment simulation model assumed that the hand was an extension of the arm. The hand was forced, by this assumption, to slide around the bar. For the high bar this is a close representation of the bar - hand interface. However, the diameter of the asymmetric bar is larger than that of the high bar. This results in female gymnasts performing a distinct "wrist change" during the fourth quadrant of the giant circle. Although men also perform a wrist change it is not as large or as obvious as the one used by women. For this reason a hand segment may need to be incorporated into the simulation model. Even if the hand were not used the present simulation model could still be used to investigate the strategies used to avoid the lower bar.

The future directions outlined above show the power of an accurate simulation model to address unanswered research questions. The future directions have highlighted areas in which the simulation model could be improved and how the optimisation procedure could be adapted to answer different research questions. Through the findings of this study and further investigations it is hoped that the understanding of the whole area of swinging and swinging related skills will be increased.

REFERENCES

- Abdel-Aziz, Y.I., & Karara, H.M. (1971). Direct linear transformation from comparator coordinates into object space coordinates in close-range photogrammetry (ASP Symposium on Close-Range Photogrammetry). Falls Church, VA: American Society of Photogrammetry. pp. 1-18.
- Ackland, T.R., Henson, P.W. & Bailey, D.A. (1988). The uniform density assumption: Its effect upon the estimation of body segment inertia parameters. *International Journal of Sports Biomechanics*, 4, 146-155.
- Angulo, R.M. & Dapena, J. (1992). Comparison of film and video techniques for estimating three-dimensional coordinates within a large field. *International Journal of Sports Biomechanics*, 8, 145-151.
- Arampatzis, D. & Brüggemann, G.-P. (1995). Mathematical model of high bar gymnastics- Optimisation of the giant swing to release. In K. Hakkinen, K. Keskinen, P.V. Komi & A. Mero (Eds.), *Abstracts: XVth Congress of the International Society of Biomechanics* (pp. 62-63). University of Jyvaskyla.
- Barter, J.T. (1957). Estimation of the mass of body segments. WADC Technical Report 57-260. Wright-Patterson Air Force Base, Ohio.
- Baster Brooks, C. & Jacobs, A.M. (1975). The gamma mass scanning technique for inertial anthropometric measurement. *Medicine and Science in Sports*, 7 (4), 290-294.
- Bauer, W.L. (1981). Hip control mechanism of a gymnasts' giant swing maneuver. In A. Morecki, K. Fidelus, K. Kedzior, & A. Wit (Eds.), *Biomechanics VII* (pp. 548-551). University Park Press.
- Bauer, W.L. (1983). Swinging as a way of increasing the mechanical energy in gymnastic maneuvers. In H. Matsui & K. Kobayashi (Eds.), *Biomechanics VIII-B* (pp. 801-806). Human Kinetic. Champaign, IL.
- Bergemann, B.W. (1974). Three-dimensional cinematography : A flexible approach. *Research Quarterly*, 45 (3), 302-308.

- Boone, T. (1977). Understanding the mechanics of the over and reverse grip giant swings. *International Gymnast*, Feb, 58-59.
- Borms, J., Moers, R. and Hebbleinck, M. (1975). Biomechanical study of forward and backward swings. P. Komi (Ed.). *Vth International Congress of Biomechanics* (pp. 309-313). University of Jyvaskia.
- Brüggemann, G-P. (1987). Biomechanics in gymnastics. *Medicine and Sport Science*, **25**, 142-176.
- Brüggemann, G-P., Cheetham, P.J., Alp, Y. & Arampatzis, D. (1994). Approach to a biomechanical profile of dismounts and release-regrasp skills of the high bar. *Journal of Applied Biomechanics*, **10**, 291-312.
- Cappozzo, A., Leo, T. & Pedotti, A. (1975). A general computing method for the analysis of human locomotion. *Journal of Biomechanics*, **8**, 307-320.
- Challis, J.H. & Kerwin, D.G. (1988). An evaluation of splines in biomechanical data analysis. In G. de Groot, A.P. Hollander, P.A. Huijting and G.J. van Ingen Schenau (Eds.), *Biomechanics XI-B* (pp. 1057-1061). Free University Press. Amsterdam.
- Challis, J.H. (1995). A multiphase calibration procedure for the direct linear transformation. *Journal of Applied Biomechanics*, **11**, 351-358.
- Chalmers, G.F. (1992). Materials, construction, performance and characteristics. In A.L. Window (Ed.), *Strain Gauge Technology* (pp. 1-38). Elsevier Science. Essex.
- Chandler, R.F., Clauser, C.E., McConville, J.T., Reynolds, H.M. & Young, J.W. (1975). Investigations of inertial properties of the human body. AMRL Technical Report, 74-137. Dayton, OH: Wright-Patterson Air Force Base.
- Cheetham, P.J. (1984). Horizontal bar giant swing centre of gravity motion comparisons. In J. Terauds, K. Bartheis, R. Mann & J. Crakes (Eds.), *Proceedings: International Symposium of Biomechanics in Sports* (pp. 99-108). California, USA.
- Chow, J.W. (1994). The optimal camera setup for a technique of three-dimensional cinematography. *Journal of Human Movement Studies*, **26** (3), 131-152.

- Continental Sports. (1994). Norm-testing of functional properties of FIG equipment and FIG mats. Continental Sports Ltd. Huddersfield.
- Corana, A, Marchesi, M., Marini, C. & Ridella, S. (1987). Minimising Multimodal functions of continuous variables with the simulated annealing algorithm. *ACM Transactions on Mathematical Software*, **13** (3), pp. 262-280.
- Dainis, A. (1968). Analysis and synthesis of body movements utilising the simple n-link system. In R.C. Nelson and C.A. Morehouse (Eds.), *Biomechanics IV* (pp. 513-518). Macmillan. London.
- Dempster, W.T. (1955). Space requirement of the seated operator. WADC Technical Report, 55-158. Dayton, OH: Wright-Patterson Air Force Base.
- Duck, T.A. (1980). A mathematical model of a gymnast on the horizontal bar. *Doctoral dissertation*. Pennsylvania State University.
- Edman, K.A.P. (1988). Double-hyperbolic force-velocity relation in frog muscle fibres. *Journal of Physiology*, **404**, 301-321.
- Edman, K.A.P. (1993). Mechanism underlying double-hyperbolic force-velocity relation in vertebrate skeletal muscle. In H. Sugi & G.H. Pollack (Eds.), *Mechanism of Myofilament Sliding in Contraction* (pp. 667-678). Plenum Press. New York.
- Enchun, L. (1989). A study of the technique principals and characteristics of the one arm giant swing backward. *GRASP*, **7**, 94-96.
- Engin, A.E., Peindl, R.D., Berme, N. & Kaleps, I. (1984a). Kinematic and force data collection in biomechanics by means of sonic emitters-I: Kinetic data collection methodology. *Journal of Biomechanical Engineering*, **106**, 204-211.
- Engin, A.E., Peindl, R.D., Berme, N. & Kaleps, I. (1984b). Kinematic and force data collection in biomechanics by means of sonic emitters-II: Force data collection and application to the human shoulder complex. *Journal of Biomechanical Engineering*, **106**, 212-219.
- Engin, A.E. & Peindl, R.D. (1987). On the biomechanics of human shoulder complex-I. Kinematics for determination of the shoulder complex sinus. *Journal of Biomechanics*, **20** (2), 103-117.

- Forwood, M.R., Neal, R.J. & Wilson, B.D. (1985). Scaling segmental moments of inertia for individual subjects. *Journal of Biomechanics*, **18** (10), 755-761.
- Froese, E.A. & Houston, M.E. (1985). Torque-velocity characteristics and muscle fibre type in human vastus lateralis. *Journal of Applied Physiology*, **59**, 309-314.
- Fuglevand, A.J. (1987). Resultant muscle torque, angular velocity, and joint angle relationships and activation patterns in maximal knee extension. In B. Jonsson (Ed.), *Biomechanics X-A* (pp. 559-665). Champaign, IL: Human Kinetics
- Gajdos, A. & Gohler, J. (1988). Technicalities: The development of high bar gymnastics. *World Gymnastics*, **20**.
- Gatto, F. & Neal, R. (1992). A mathematical model of giant swings on the horizontal bar. *Abstracts: Mathematics and Computers in Sport* (pp. 94-100). Queensland.
- Gervais, P. (1993). Calculation of reaction forces at the hands on the horizontal bar from positional data. *Abstracts: XIVth Congress of the International Society of Biomechanics* (pp. 468-469). Paris.
- Gervais, P. & Tally, F. (1993). The beat swing and mechanical descriptors of three horizontal bar release-regrasp skills. *Journal of Applied Biomechanics*, **9**, 66-83.
- Greig, M.P. & Yeadon, M.R. (1994). Does approach velocity influence takeoff distance in high jumping. In *Proceedings of the Biomechanics Section of the British Association of Sports and Exercise Science*, **19**, 53-56. Glasgow: BASES.
- Goffe, W.L., Ferrier, G.D. & Rogers, J. (1994). Global optimisation of statistical functions with simulated annealing. *Journal of Econometrics*, **60**, pp. 65-99.
- Hanavan, E.P. (1964). A mathematical model of the human body. AMRL-TR-64-102, AD-603-463. Aerospace Medical Research Laboratories, Wright-Patterson Air Force Base, Ohio.
- Hatze, H. (1975). A new method for the simultaneous measurement of the moment of inertia, the damping coefficient and the location of the centre of mass of a body segment in situ. *European Journal of Applied Physiology*, **34**, 217-226.

- Hatze, H. (1981). A comprehensive model for human motion simulation and its applications to the takeoff phase of the long jump. *Journal of Sport Sciences*, **1**, 3-12.
- Hatze, H. (1980). A Mathematical model for the computation of parameter values of anthropomorphic segments. *Journal of Biomechanics*, **13**, 833-843.
- Hatze, H. (1988). High-precision three-dimensional photogrammetric calibration and object space reconstruction using a modified DLT-approach. *Journal of Biomechanics*, **21** (7), 533-538.
- Hay, J.G. (1994). *The biomechanics of sporting techniques*. Prentice-Hall. N.J.
- Hay, J.G., Putnam, C.A. & Wilson, B.D. (1979). Forces exerted during exercises on the uneven bars. *Medicine and Science in Sports*, **11** (2), 123-130.
- Herzog, W. (1988). The relation between the resultant moments at a joint and the moments measured by an isokinetic dynamometer. *Journal of Biomechanics*, **21** (1), 5-12.
- Hill, A.V. (1970). *First and last experiments in muscle mechanics*. University Press. Cambridge.
- Hinrichs, R.N. (1985). Regression equations to predict segmental moments of inertia from anthropometric measurements: An extension of the data of Chandler et al. (1975). *Journal of Biomechanics*, **18** (8), 621-624.
- Houston, M.E., Norman, R.W. & Froese, E.A. (1988). Mechanical measures during maximal exercise and their relation to fibre composition of the human vastus lateralis muscle. *European Journal of Applied Physiology*, **58**, 1-7.
- International Gymnastic Federation. (1979). *Measurements, Dimensions and Forms*. FIG. Switzerland.
- International Gymnastic Federation. (1993). *Code of Points for men's artistic gymnastics*. FIG. Switzerland.

- Ishii, K. & Komatsu, T. (1987). Changes of kinematic parameters and forces on the horizontal bar backward giant swing. In T.B. Hoshizaki, J.H. Salmela, & B. Petiot (Eds.), *Diagnostics, Treatment and Analysis of Gymnastic Talent* (pp. 107-117). Sports Psyche Editions. Montreal.
- Jarle, D., Morlon, B. & Canal, M. (1993). *Abstracts: IVth International Symposium on Computer Simulation in Biomechanics* (pp. 8-11). Paris.
- Jensen, R.K. (1976). Model for body segment parameters. In P.V. Komi (Ed.), *Biomechanics V-B* (pp. 380-386). University Park Press. Baltimore.
- Jensen, R.K. (1978). Estimation of the biomechanical properties of three body types using a photogrammetric method. *Journal of Biomechanics*, **11**, 349-358.
- Kerwin, D.G., Yeadon, M.R., & Lee, S. (1990). Body configuration in multiple high bar dismounts. *International Journal of Sports Biomechanics*, **6**, 149-159.
- Kerwin, D.G. & Challis, J.H. (1994). Comparative accuracy of cine and video digitisation. In L. Blankevoort & J. Kooloos (Eds.), *Abstracts (II): Second World Congress of Biomechanics* (pp. 362b). Stichting World Biomechanics. Nijmegen.
- Kerwin, D.G. (1995). Apex/Target high resolution video digitising system. In *Proceedings of the Biomechanics Section of the British Association of Sports and Exercise Science 20*, 1-4. Glasgow: BASES.
- Kennedy, P.W., Wright, D.L. & Smith, G.A. (1989). Comparison of film and video techniques for three-dimensional DLT repredictions. *International Journal of Sport Biomechanics*, **5**, 457-460.
- King, M.A., Yeadon, M.R. & Kerwin, D.G. (1996). Fitting torque data from an isokinetic dynamometer. In *Proceedings of the Biomechanics Section of the British Association of Sports and Exercise Science 21*, 45-48. Glasgow: BASES.
- King, M.A. (1998). Contribution to performance in dynamic jumps. *Unpublished Doctoral dissertation*. Loughborough University.
- Komor, A. & Ubukata, O. (1977). The dynamics of gymnast's movement on the high bar. *VIth International Congress of Biomechanics*. Copenhagen.

- Kornecki, A., Maronski, R., & Serain, R. (1987). A nonconventional method of identification of generalized forces in gymnastics. In G. de Groot, A.P. Hollander, P.A. Huijing and G.J. van Ingen Schenau (Eds.), *Biomechanics XI-B* (pp. 758-762). Free University Press. Amsterdam.
- Kopp, P.M. & Reid, J.G. (1980). A force torque analysis of giant swings on the horizontal bar. *Canadian Journal of Applied Sports Science*, **5**, 98-102.
- Kopp, P.M. & Reid, J.G. (1983). A force torque analysis of the kip on the horizontal bar. *Canadian Journal of Applied Sports Science*, **8**, 271-275.
- Lindsay, M.R. (1996). Three-dimensional reconstruction using the direct linear transformation. In *Proceedings of the Biomechanics Section of the British Association of Sports and Exercise Science* 21, 6-8. Glasgow: BASES.
- Loken, N.C., and Willoughby, R.J. (1959). Complete book of gymnastics. pp. 1-2/96. Prentice-Hall. N.J.
- Marshall, R.N., Mazur, S.M. & Taylor, N.A.S. (1990). Three-dimensional surfaces for human muscle kinetics. *European Journal of Applied Physiology*, **61**, 263-270.
- McLaughlin, T.M., Dillman, C.J. and Lardner, T.J. (1977). Biomechanical analysis with cubic spline functions. *Research Quarterly*, **48**, 569-582.
- McNitt-Gray, J.L., Yokoi, T. & Millward, C. (1993). Landing strategy adjustments made by female gymnasts in response to drop height and mat composition. *Journal of Applied Biomechanics*, **9**, 173-190.
- McNitt-Gray, J.L., Yokoi, T. & Millward, C. (1994). Landing strategies used by gymnasts on different surfaces. *Journal of Applied Biomechanics*, **10**, 237-252.
- Miller, N.R. & Nelson, R.C. (1973). Biomechanics of sport - A research approach. Philadelphia: Lea and Febiger.
- Miller, N.R., Shapiro, R. & McLaughlin, T.M. (1980). A technique for obtaining spacial kinematic parameters of segments of biomechanical systems from cinematographic data. *Journal of Biomechanics*, **13**, 535-547.
- Munrow, A.D. (1963). Pure and applied gymnastics. Edward Arnold. London.

- Morlock, M.M. & Yeadon, M.R. (1986). Regression equations for segmental inertia parameters. In Proceedings of the North American Congress on Biomechanics, pp. 231-232.
- Morlock, M.M. & Yeadon, M.R. (1988). A mechanical model of a gymnast at the high bar. In C.E. Cotton et al. (Eds.), *Proceedings: Canadian Society for Biomechanics* (pp. 176-177). Spodym. London, Ont.
- Neal, R.J., Kippers, V., Plooy, D. & Forwood, M.R. (1995). The influence of hand guards on forces and muscle activity during giant swings on the high bar. *Medicine and Science in Sports and Exercise*, **27**, 1550-1556.
- Nelder, J.A. & Mead, R. (1965). A simplex method for function minimisation. *Computer Journal*, **7**, pp. 308.
- Nigg, B.M. (1994). Inertial properties of the human or animal body. In B.M. Nigg & W. Herzog (Eds.), *Biomechanics of the Musculo-Skeletal System* (pp. 337-364). John Wiley & Sons. England.
- Nissinen, M.A. (1983). Kinematic and kinetic analysis of the giant swing on rings. In H. Matsui & K. Kobayashi (Eds.), *Biomechanics VIII-B* (pp. 781-786). Human Kinetics. Champaign, IL.
- Nissinen, M., Preiss, R., & Bruggemann, P. (1985). Simulation of human airborne movement on the high bar. In D.A. Winter, R.W. Norman, R.P. Wells, K.C. Hayes, & A.E. Patla (Eds.), *Biomechanics IX-B* (pp. 373-376). Human Kinetics. Champaign, IL.
- O'Connor, B.J., Yack, H.J. & White, S.C. (1995). Reducing errors in Kinetic calculations: Improved synchronisation of video and ground reaction force records. *Journal of Applied Biomechanics*, **11**, 216-223.
- Okamoto, A., Sakurai, S., Ikegami, Y. and Yabe, K. (1987). Mechanical work in the giant swing on the horizontal bar. In G. de Groot, A.P. Hollander, P.A. Huijting & G.J. van Ingen Schenan (Eds.), *Biomechanics XI-B* (pp. 758-762). Free University Press. Amsterdam.

- Peindl, R.D. & Engin, A.E. (1987). On the biomechanics of human shoulder complex-II. Passive resistive properties beyond the shoulder complex sinus. *Journal of Biomechanics*, **20** (2), 119-134.
- Perrine, J.J. & Edgerton, V.R. (1978). Muscle force-velocity and power-velocity relationships under isokinetic loading. *Medicine and Science in Sports and Exercise*, **10** (3), 159-166.
- Press, W.H., Flannery, B.P., Teukolsky, S.A. & Vetterling, W.T. (1988). *Numerical recipes: The art of scientific computing*. pp.274-326. Cambridge University Press: New York.
- Presidge, J. (1988). The history of British gymnastics. pp. 5-17. BAGA. Slough.
- Readhead, L. (1987). Men's gymnastics coaching manual. pp. 7/189. Springfield Books. Huddersfield.
- Reinsch, C.H. (1967). Smoothing by spline functions. *Numerische Mathematik*, **10**, 177-183.
- Reinsch, C.H. (1971). Smoothing by spline functions II. *Numerische Mathematik*, **16**, 451-454.
- Rusteberg, D., Figgen, M. & Nicol, K. (1993). Realtime simulation of two-dimensional gymnastics on the horizontal bar. *Abstracts: IVth International Symposium on Computer Simulation in Biomechanics* (pp. 12-15). Paris.
- Sale and Judd, (1974). Dynamometric instrumentation of the rings for analysis of gymnastic movements. *Medicine and Science in Sports*, **16** (3), 209-216.
- Sapega, A.A, Nicholas, J.A., Sokolow, D. & Saraniti, A. (1982). The nature of torque "overshoot" in Cybex isokinetic dynamometry. *Medicine and Science in Sports and Exercise*, **14** (5), 368-375.
- Scott, K. & Owens, A. (1992). Instrumentation. In A.L. Window (Ed.), *Strain Gauge Technology* (pp. 151-216). Elsevier Science. Essex
- Shapiro, R. (1978). Direct linear transformation method for three-dimensional cinematography. *Research Quarterly*, **49** (2), 197-205.

- Shapiro, R., Blow, C. & Rash, G. (1987). Video digitising analysis system. *International Journal of Sports Biomechanics*, **3**, 80-86.
- Smith, T. (1982). Gymnastics: A mechanical understanding. pp. 126-141. Holder and Stroughton. London.
- Stewart, G.W. (1973). Introduction to matrix computations. London: Academic Press.
- Tan, J., Kerwin, D.G. & Yeadon, M.R. (1995). Evaluation of the Apex video digitisation system. In *Proceedings of the Biomechanics Section of the British Association of Sports and Exercise Science* 20, 5-8. Glasgow: BASES.
- Thompson, C.W. (1989). Manual of structural kinesiology. Times Mirror/Mosby College Publishing. Boston.
- Thorstensson, A., Grimby, G. & Karlsson, J. (1976). Force-velocity relations and fibre composition in human knee extensor muscles. *Journal of Applied Physiology*, **40** (1), 12-16.
- Topping, J. (1962). Errors of observation and their treatment. Chapman and Hall.
- Van Gheluwe, B. (1978). Computerized three-dimensional cinematography for any arbitrary camera set up. In E. Asmussen & K. Jorgensen (Eds.), *Biomechanics VI-A* (pp. 343-448). Baltimore. University Park Press.
- Whitsett, C.E. (1963). Some dynamic response characteristics of weightless man. AMRL-TDR-63-18, AD-412-541. Aerospace Medical Research Laboratories, Wright-Patterson Air Force Base, Ohio.
- Wickiewicz, T.L., Roy, R.R., Powell, P.L., Perrine, J.J. & Edgerton, V.R. (1984). Muscle architecture and force-velocity relationships in humans. *Journal of Applied Physiology Respiration and Environmental Exercise Physiology*, **57**, 435-443.
- Winter, D.A. (1990). Biomechanics and motor control of human movement. John Wiley and Sons. New York.
- Winter, D.A., Sidwall, H.G. & Hobson, D.A. (1974). Measurement and reduction of noise in kinematics of locomotion. *Journal of Biomechanics*, **7**, 157-159.

- Winter, D.A., Wells, R.P. & Orr, G.W. (1981). Errors in the use of Isokinetic dynamometers. *European Journal of Applied Physiology*, **46**, 397-408.
- Witten, W.A., Brown, E.W., Witten, C.X. and Wells, R. (1996). Kinematic and kinetic analysis of the overgrip giant swing on the uneven parallel bars. *Journal of Applied Biomechanics*, **12**, 431-448.
- Wood, G.A. (1982). Data smoothing and differentiation procedures in biomechanics. *Exercise and Sports Science Reviews*, **10**, 308-362.
- Wood, G.A. & Jennings, L.S. (1979). On the use of spline functions for data smoothing. *Journal of Biomechanics*, **12**, 477-479.
- Wood, G.A. & Marshall, R.N. (1986). The accuracy of DLT extrapolation in three-dimensional film analysis. *Journal of Biomechanics*, **19** (9), 781-785.
- Wooten, K.S. (1934). *Gymnastics with and without apparatus*. pp. 55. Gale and Polden. Aldershot.
- Yeadon, M.R. & Challis, J.H., (1994). The future of performance related sports biomechanics research. *Journal of Sports Sciences*, **12**, 3-32.
- Yeadon, M.R., Lee, S., & Kerwin, D.G. (1990). Twisting techniques used in high bar dismounts. *International Journal of Sports Biomechanics*, **6**, 139-146.
- Yeadon, M.R. (1984). The mechanics of twisting somersaults. *Doctoral dissertation*. Loughborough University.
- Yeadon, M.R. (1989). A method for obtaining three-dimensional data on ski jumping using pan and tilt cameras. *International Journal of Sport Biomechanics*, **5**, 238-247.
- Yeadon, M.R. (1990a). The simulation of aerial movement-I. The determination of orientation angles from film data. *Journal of Biomechanics*, **23** (1), 59-66.
- Yeadon, M.R. (1990b). The simulation of aerial movement-II. A mathematical inertia model of the human body. *Journal of Biomechanics*, **23** (1), 67-74.

- Yeadon, M.R., Atha, J. & Hales, F.D. (1990). The simulation of aerial movement-IV. A computer simulation model. *Journal of Biomechanics*, **23** (1), 85-89.
- Yeadon, M.R. (1993a). The biomechanics of twisting somersaults Part II. Contact twist. *Journal of Sports Sciences*, **11**, 199-208.
- Yeadon, M.R. (1993b). The biomechanics of twisting somersaults Part IV. Partitioning performances using the tilt angle. *Journal of Sports Sciences*, **11**, 219-225.
- Yeadon, M.R. (1996). Three-dimensional reconstruction using the direct linear transformation. In *Proceedings of the Biomechanics Section of the British Association of Sports and Exercise Science* 21, 1-4. Glasgow: BASES.
- Yessis, M. (1972). Kinesiological research in the Soviet Union. *Journal of Health Physical Education and Recreation*, **43**, 93-95.
- Zatsiorsky, V. & Seluyanov, V. (1983). The mass and inertia characteristics of the main segments of the human body. In H. Matsui & K. Kobayashi (Eds.), *Biomechanics VIII-B* (pp. 1152-1159). Champaign, IL: Human Kinetics.
- Zatsiorsky, V. & Seluyanov, V. (1985). Estimation of the mass and inertia characteristics of the human body by means of the best predictive regression equations. In D.A. Winter, R.W. Norman, R.P. Wells, K.C. Hayes, & A.E. Patla (Eds.), *Biomechanics IX-B* (pp. 233-239). Champaign, IL. Human Kinetics.
- Zernicke, R.F., Caldwell, G. & Roberts, E.M. (1976). Fitting biomechanical data with cubic spline functions. *Research Quarterly*, **47**, 9-20.

APPENDIX 1

- Appendix 1a Listing of the Fortran 77 code from the single segment simulation model
- Appendix 1b Listing of the Fortran 77 code from the four segment simulation model (version used to optimise the backward giant circle)

c

c relating to the bar:

c xb - horizontal displacement of the bar

c xbd - horizontal velocity of the bar

c xbdd - horizontal acceleration of the bar

c zb - vertical displacement of the bar

c zbd - vertical velocity of the bar

c zbdd - vertical acceleration of the bar

c k - stiffness coefficient of the spring

c b - damping coefficient of the spring

c x - horizontal location of the segment mass centre

c xd - horizontal velocity of the segment mass centre

c xdd - horizontal acceleration of the segment mass centre

c z - vertical location of the segment mass centre

c zd - vertical velocity of the segment mass centre

c zdd - vertical acceleration of the segment mass centre

c rb - length of the spring

c ten - tension in the spring

c

cc

c

double precision

* xb, xbd, xbdd, zb, zbd, zbdd,

* k, b, x, xdd, z, zdd,

* xd, zd,

* rb, ten, vten, hten, rten

c

cc

c

c relating to the average acceleration loop

c terms ending with 0 are used in the calculation of new

c conditions at the start and end of the integration interval

c which are used for the average acceleration loop

c

cc

c

double precision

* xb0, zb0,

* phi0, phid0

c
cc

c
c relating to the calculation of energy
c pe - potential energy
c se - potential strain energy
c re - rotational kinetic energy
c ke - kinetic energy
c energy - total kinetic energy

c
cc

c
double precision
* pe, se,
* re, ke,
* energy

c
cc

c
c relating to the radial force

c
cc

c
double precision
* rf, r

c
cc

c
c relating to the output

c
cc

c
double precision
* phiw, phidw

c
cc

c
integer i, j

c


```

CALL PRTVEC(LB,N,'LOWER BOUND')
CALL PRTVEC(UB,N,'UPPER BOUND')
CALL PRTVEC(C,N,'C VECTOR')
WRITE(*,('," **** END OF DRIVER ROUTINE OUTPUT ****'
1    /," **** BEFORE CALL TO SA.      ****'))

CALL SA(N,X,MAX,RT,EPS,NS,NT,NEPS,MAXEVL,LB,UB,C,IPRINT,ISEED1,
1    ISEED2,T,VM,XOPT,FOPT,NACC,NFCNEV,NOBDS,IER,
2    FSTAR,XP,NACP)
c
WRITE(*,('," **** RESULTS AFTER SA **** "'))
CALL PRTVEC(XOPT,N,'SOLUTION')
CALL PRTVEC(VM,N,'FINAL STEP LENGTH')
WRITE(*,1001) FOPT, NFCNEV, NACC, NOBDS, T, IER
c
1000 FORMAT(/, 'SIMULATED ANNEALING EXAMPLE',/
1    /, 'NUMBER OF PARAMETERS: ',I3, ' MAXIMAZATION: ',L5,
2    /, 'INITIAL TEMP: ',G8.2, ' RT: ',G8.2, ' EPS: ',G8.2,
3    /, 'NS: ',I3, ' NT: ',I2, ' NEPS: ',I2,
4    /, 'MAXEVL: ',I10, ' IPRINT: ',I1, ' ISEED1: ',I4,
5    ' ISEED2: ',I4)
1001 FORMAT(/, 'OPTIMAL FUNCTION VALUE: ',G20.13
1    /, 'NUMBER OF FUNCTION EVALUATIONS: ',I10,
2    /, 'NUMBER OF ACCEPTED EVALUATIONS: ',I10,
3    /, 'NUMBER OF OUT OF BOUND EVALUATIONS: ',I10,
4    /, 'FINAL TEMP: ',G20.13, ' IER: ', I3)
c
STOP
END
c
c
cccccccccccccccccccccccccccccccccccccccccccccccccccccccccccccccc
c
subroutine FCN(N,V,amtmopt)
c
cccccccccccccccccccccccccccccccccccccccccccccccccccccccccccccccc
c
c subroutine FCN(N,V,amtmopt):-
c is a four segment two damped spring simulation model

```


* rxz(8),
 * tor1, tor2, tor3,
 * torq(3),tlt, shldtorq, hiptorq

c

c

cc

c

c relating to springs (disp/vel/acce/stif)

c

c ba - refers to the bar

c s - refers to the shoulders

c rba - resultant extension in the bar

c rs - resultant extension in the shoulders

c if preceded by z or x refers to vertical or

c horizontal displacement of the spring respectively

c if followed by d or dd refers to the linear velocity

c or acceleration of the spring respectively

c if preceded by k refers to the stiffness coefficient

c of the spring

c dmpb - damping coefficient of the bar

c dmpps - damping coefficient of the shoulders

c

cc

c

double precision

* xba, zba, xs, zs, rs,

* xbad, zbad, xsd, zsd,

* xbadd, zbadd, xsdd, zsdd,

* rba, ks, dmpps

c

c

cc

c

c relating to the mass centre locations of each segment

c and the linear velocities of that segment

c

c x - horizontal mass centre location of the segment

c z - vertical location of the segment mass centre

c if followed by a d refers to the velocity of the

angdata(7) = angdata(4) + abs(V(5))
 angdata(8) = angdata(7) + 0.025 + abs(V(6))

c

c

angdata(9) = angdata(6)
 angdata(10) = angdata(6) - abs(V(7))
 angdata(11) = angdata(8) + abs(V(8))
 angdata(12) = angdata(11) + 0.025 + abs(V(9))

c

c

angdata(13) = angdata(10)
 angdata(14) = angdata(13) + abs(V(10))
 angdata(15) = angdata(12) + abs(V(11))
 angdata(16) = angdata(15) + 0.025 + abs(V(12))

c

c

c Joint angle time history for the hips

c

angdata(17) = angd(2)
 angdata(18) = angd(2) - abs(V(13))
 angdata(19) = t + abs(V(14))
 angdata(20) = angdata(19) + 0.025 + abs(V(15))

c

angdata(21) = angdata(18)
 angdata(22) = angdata(18) + abs(V(16))
 angdata(23) = angdata(20) + abs(V(17))
 angdata(24) = angdata(23) + 0.025 + abs(V(18))

c

c

angdata(25) = angdata(22)
 angdata(26) = angdata(22) - abs(V(19))
 angdata(27) = angdata(24) + abs(V(20))
 angdata(28) = angdata(27) + 0.025 + abs(V(21))

c

c

angdata(29) = angdata(26)
 angdata(30) = angdata(26) + abs(V(22))
 angdata(31) = angdata(28) + abs(V(23))
 angdata(32) = angdata(31) + 0.025 + abs(V(24))


```
endif
c
if ((V(3)+V(6)+V(9)+V(12)).gt.(4.5)) then
    amtmopt = 0.0
    print*, 'time limit exceeded'
    goto 647
endif
c
c
if ((V(14)+V(17)+V(20)+V(23)).gt.(4.5)) then
    amtmopt = 0.0
    print*, 'time limit exceeded'
    goto 647
endif
c
if ((V(13)+V(16)+V(19)+V(22)).gt.(4.5)) then
    amtmopt = 0.0
    print*, 'time limit exceeded'
    goto 647
endif
c
c if statements limits the size of the shoulder
c hyperextension to 50 degrees
c
if (angdata(2).lt.(2.27)) then
    amtmopt = 0.0
    print*, 'shoulder hyperextension angle too large'
    goto 647
endif
c
if (angdata(10).lt.(2.27)) then
    amtmopt = 0.0
    print*, 'shoulder hyperextension angle 2 too large'
    goto 647
endif
c
c if statements limits the size of the shoulder
c flexion to 180 degrees
c
```

```
if (angdata(6).gt.(6.28)) then
    amtmopt = 0.0
    print*, 'shoulder flexion angle too large'
    goto 647
endif
c
c if statements limits the size of the hip hyperextension
c to 50 degrees
c
    if (angdata(18).lt.(2.27)) then
        amtmopt = 0.0
        print*, 'hip hyperextension angle too large'
        goto 647
    endif
c
    if (angdata(26).lt.(2.27)) then
        amtmopt = 0.0
        print*, 'hip hyperextension angle 2 too large'
        goto 647
    endif
c
c if statement limits the size of the hip flexion to
c 180 degrees
c
    if (angdata(22).gt.(6.28)) then
        amtmopt = 0.0
        print*, 'hip flexion angle too large'
        goto 647
    endif
c
endif
c
c
c cc(1) = angdata(1)
c cc(2) = angdata(2)
c cc(3) = angdata(3)
c cc(4) = angdata(4)
c
c if (t.gt.angdata(4)) then
```

```
cc(1) = angdata(5)
cc(2) = angdata(6)
cc(3) = angdata(7)
cc(4) = angdata(8)
endif
c
if (t.gt.angdata(8)) then
cc(1) = angdata(9)
cc(2) = angdata(10)
cc(3) = angdata(11)
cc(4) = angdata(12)
endif
c
if (t.gt.angdata(12)) then
cc(1) = angdata(13)
cc(2) = angdata(14)
cc(3) = angdata(15)
cc(4) = angdata(16)
endif
c
f = alp
call varang(f,cc,t)
alp = f
c
f = 0.0
call vdang(f,cc,t)
alpd = f
c
f = 0.0
call d2ang(f,cc,t)
alpdd = f
c
c
cc(1) = angdata(17)
cc(2) = angdata(18)
cc(3) = angdata(19)
cc(4) = angdata(20)
c
if (t.gt.angdata(20)) then
```

```
cc(1) = angdata(21)
cc(2) = angdata(22)
cc(3) = angdata(23)
cc(4) = angdata(24)
endif
c
if (t.gt.angdata(24)) then
cc(1) = angdata(25)
cc(2) = angdata(26)
cc(3) = angdata(27)
cc(4) = angdata(28)
endif
c
if (t.gt.angdata(28)) then
cc(1) = angdata(29)
cc(2) = angdata(30)
cc(3) = angdata(31)
cc(4) = angdata(32)
endif
c
f = bet
call varang(f,cc,t)
bet = f
c
f = 0.0
call vdang(f,cc,t)
betd = f
c
f = 0.0
call d2ang(f,cc,t)
betdd = f
c
cc(1) = angdata(33)
cc(2) = angdata(34)
cc(3) = angdata(35)
cc(4) = angdata(36)
f = tie
call varang(f,cc,t)
tie = f
```


c coefficients coefa(2,1-5)

c

$$\begin{aligned} \text{coefa}(2,1) &= \text{ma}*(-\text{a}*\sin(\text{phi})) + \text{mb}*(-\text{p}*\sin(\text{phi}) - \text{b}*\sin(\text{phi}2) \\ &*) + \text{mc}*(-\text{p}*\sin(\text{phi}) - \text{q}*\sin(\text{phi}2) - \text{c}*\sin(\text{phi}3)) + \\ &*\text{md}*(-\text{p}*\sin(\text{phi}) - \text{q}*\sin(\text{phi}2) - \text{r}*\sin(\text{phi}3) - \text{d}*\sin(\text{phi}4)) \end{aligned}$$

c

$$\begin{aligned} \text{coefa}(2,2) &= \text{mass} \\ \text{coefa}(2,3) &= 0.0 \\ \text{coefa}(2,4) &= \text{mass}2 \\ \text{coefa}(2,5) &= 0.0 \end{aligned}$$

c

c coefficients coefa(3,1-3)

c

$$\begin{aligned} \text{coefa}(3,1) &= \text{ma}*\text{xa}*(\text{a}*\cos(\text{phi})) - \text{ma}*\text{za}*(-\text{a}*\sin(\text{phi})) + \text{Ia} \\ &* + \text{mb}*\text{xb}*(\text{p}*\cos(\text{phi}) + \text{b}*\cos(\text{phi}2)) - \text{mb}*\text{zb}*(-\text{p}*\sin(\text{phi}) - \\ &*\text{b}*\sin(\text{phi}2)) + \text{Ib} + \text{mc}*\text{xc}*(\text{p}*\cos(\text{phi}) + \text{q}*\cos(\text{phi}2) + \\ &*\text{c}*\cos(\text{phi}3)) - \text{mc}*\text{zc}*(-\text{p}*\sin(\text{phi}) - \text{q}*\sin(\text{phi}2) - \\ &*\text{c}*\sin(\text{phi}3)) + \text{Ic} + \text{md}*\text{xd}*(\text{p}*\cos(\text{phi}) + \text{q}*\cos(\text{phi}2) + \\ &*\text{r}*\cos(\text{phi}3) + \text{d}*\cos(\text{phi}4)) - \text{md}*\text{zd}*(-\text{p}*\sin(\text{phi}) - \\ &*\text{q}*\sin(\text{phi}2) - \text{r}*\sin(\text{phi}3) - \text{d}*\sin(\text{phi}4)) + \text{Id} \end{aligned}$$

c

$$\begin{aligned} \text{coefa}(3,2) &= -\text{ma}*\text{za} - \text{mb}*\text{zb} - \text{mc}*\text{zc} - \text{md}*\text{zd} \\ \text{coefa}(3,3) &= \text{ma}*\text{xa} + \text{mb}*\text{xb} + \text{mc}*\text{xc} + \text{md}*\text{xd} \\ \text{coefa}(3,4) &= -\text{mb}*\text{zb} - \text{mc}*\text{zc} - \text{md}*\text{zd} \\ \text{coefa}(3,5) &= \text{mb}*\text{xb} + \text{mc}*\text{xc} + \text{md}*\text{xd} \end{aligned}$$

c

c coefficients coefa(4,1-5)

c

$$\begin{aligned} \text{coefa}(4,1) &= \text{ma}*\text{a}*\cos(\text{phi}) \\ \text{coefa}(4,2) &= 0.0 \\ \text{coefa}(4,3) &= \text{ma} \\ \text{coefa}(4,4) &= 0.0 \\ \text{coefa}(4,5) &= 0.0 \end{aligned}$$

c

c

c coefficients coefa(5,1-5)

c

$$\begin{aligned} \text{coefa}(5,1) &= -\text{ma}*\text{a}*\sin(\text{phi}) \\ \text{coefa}(5,2) &= \text{ma} \end{aligned}$$


```

subroutine newvals(newvs,solux,oldvs,step)
double precision newvs(10),solux(5),oldvs(10),step,phi,phid,
* phidd,xba,zba,xbad,zbad,xbadd,zbadd,xs,zs,xsd,zsd,xsdd,zsdd
c
  phidd = solux(1)
  xbadd = solux(2)
  zbadd = solux(3)
  xsdd = solux(4)
  zsdd = solux(5)
c

  phi = oldvs(1)
  phid = oldvs(2)
  xba = oldvs(3)
  xbad = oldvs(4)
  zba = oldvs(5)
  zbad = oldvs(6)
  xs = oldvs(7)
  xsd = oldvs(8)
  zs = oldvs(9)
  zsd = oldvs(10)
c
c   calculate new phi from angular acceleration
  phi = phi + phid*step + 0.5*phidd*step*step
  newvs(1) = phi
c
c   calculate new phid from angular acceleration
  phid = phid + phidd*step
  newvs(2) = phid
c
c   calculate new horizontal displacement of the bar
  xba = xba + xbad*step + 0.5*xbadd*step*step
  newvs(3) = xba
c
c   calculate new horizontal velocity of the bar
  xbad = xbad + xbadd*step
  newvs(4) = xbad
c
c   calculate new vertical displacement of the bar

```


$$lv(5) = phi3d$$

$$lv(6) = phi4d$$

c

c segment one - locations

$$xa = xba + a*\cos(phi)$$

$$za = zba + a*\sin(phi)$$

c

c segment one - velocities

$$xad = xbad - a*\sin(phi)*(phid)$$

$$zad = zbad + a*\cos(phi)*(phid)$$

c

c segment two - locations

$$xb = xba + xs + p*\cos(phi) + b*\cos(phi2)$$

$$zb = zba + zs + p*\sin(phi) + b*\sin(phi2)$$

c

c segment two - velocities

$$xbd = xbad - p*\sin(phi)*(phid) + xsd - b*\sin(phi2)*(phi2d)$$

$$zbd = zbad + p*\cos(phi)*(phid) + zsd + b*\cos(phi2)*(phi2d)$$

c

c segment three - locations

$$xc = xba + xs + p*\cos(phi) + q*\cos(phi2) + c*\cos(phi3)$$

$$zc = zba + zs + p*\sin(phi) + q*\sin(phi2) + c*\sin(phi3)$$

c

c segment three - veocities

$$xcd = xbad - p*\sin(phi)*(phid) + xsd - q*\sin(phi2)*(phi2d)$$

$$* - c*\sin(phi3)*(phi3d)$$

$$zcd = zbad + p*\cos(phi)*(phid) + zsd + q*\cos(phi2)*(phi2d)$$

$$* + c*\cos(phi3)*(phi3d)$$

c

c segment four - locations

$$xd = xba + xs + p*\cos(phi) + q*\cos(phi2) + r*\cos(phi3) +$$

$$* d*\cos(phi4)$$

$$zd = zba + zs + p*\sin(phi) + q*\sin(phi2) + r*\sin(phi3) +$$

$$* d*\sin(phi4)$$

c

c segment four - velocities

$$xdd = xbad - p*\sin(phi)*(phid) + xsd - q*\sin(phi2)*(phi2d)$$

$$* - r*\sin(phi3)*(phi3d) - d*\sin(phi4)*(phi4d)$$

$$zdd = zbad + p*\cos(phi)*(phid) + zsd + q*\cos(phi2)*(phi2d)$$

common/b2/Ia,Ib,Ic,Id

c

c

c angular momentum equals the sum of

c $m_i * [x_i * z_{di} - z_i * x_{di}] + I_i * \omega_i$

c where i is summed from 1 to 4

c

angmtm(1) = ma*(lv(7)*lv(10) - lv(8)*lv(9)) + Ia*phid

angmtm(2) = mb*(lv(11)*lv(14) - lv(12)*lv(13)) + Ib*lv(4)

angmtm(3) = mc*(lv(15)*lv(18) - lv(16)*lv(17)) + Ic*lv(5)

angmtm(4) = md*(lv(19)*lv(22) - lv(20)*lv(21)) + Id*lv(6)

c

angmtm(5) = angmtm(1) + angmtm(2) + angmtm(3) + angmtm(4)

c

c calculate the moment of inertia about the neutral bar

c

moi(1) = Ia + ma*(lv(7)**2 + lv(8)**2)

moi(2) = Ib + mb*(lv(11)**2 + lv(12)**2)

moi(3) = Ic + mc*(lv(15)**2 + lv(16)**2)

moi(4) = Id + md*(lv(19)**2 + lv(20)**2)

c

moi(5) = moi(1) + moi(2) + moi(3) + moi(4)

c

return

end

c

c

cc

c

c Subroutine cmangmtm:-

c Calculates the angular momentum of the model about the

c mass centre position

c

cc

c

subroutine cmangmtm(amcm,xloc,zloc,xlocd,zlocd,lv,phi,phid)

c

double precision amcm(5),xloc,zloc,xlocd,zlocd,lv(22),phi,

* phid,mk,Ik,ak,

APPENDIX 2

- Appendix 2a Written consent form signed by the subject
- Appendix 2b Mean and standard deviations of ADC counts recorded
 during calibration of the goniometer
- Appendix 2c Ranges of motion during trials on the isokinetic
 dynamometer
- Appendix 2d The eighteen parameters for each muscle model

Appendix 2b

Written consent form signed by the subject

PURPOSE

To obtain torque, angle and angular velocity data from a gymnast performing shoulder and hip flexions and extensions using an isokinetic dynamometer. In order to develop and evaluate a mathematical model of a gymnast swinging on the high bar.

PROCEDURES

An isokinetic dynamometer will be used to collect the torque, angle and angular velocity data. In addition a goniometer will be used to confirm/correct the angle data collected from the dynamometer. A number of trials will be requested for each joint action. These will include variations in the angular velocity of the joint action and a number of repeat measurements. Suitable breaks will be allowed between trials to minimise fatigue and boredom. A video camera will be used as a visual log of what occurred.

QUESTIONS

The researcher will be pleased to answer any questions which you may have at any time.

WITHDRAWAL

You are free to withdraw from the study at any time whatever reason without prejudice.

CONFIDENTIALITY

Your identity will remain confidential in any material resulting from this work.

I have read and understood the information on this form and agree to participate in this study. As far as I am aware I do not have any injury nor infirmity which would be affected by the procedures outlined.

Name..... Name.....

Signed.....(gymnast) Signed.....(parent)

In the presence of:

Name.....

Signed.....(coach) Date.....

Appendix 2b

Mean and standard deviations of ADC counts recorded during calibration of the goniometer

angle [°]	adc count (mean)	standard deviation
0.0	8598.4	30.00
22.5	7707.8	42.93
45.0	6909.0	45.23
67.5	6145.0	43.17
90.0	5402.1	42.08
112.5	4431.4	57.00
135.0	3522.1	61.45
180.0	2153.1	62.23
- 22.5	9549.3	36.73
- 45.0	10336.7	35.30
- 67.5	10990.5	35.01
- 90.0	11798.4	59.65
- 112.5	12666.0	59.31
- 135.0	13460.1	59.61
- 180.0	14973.2	56.57

Appendix 2c

Ranges of motion during trials on the isokinetic dynamometer

Shoulder extension			
angle	from (°)	to (°)	range (°)
crank	48.0	173.0	125.0
isokinetic crank			
minimum	71.4	116.1	44.7
average	62.5	132.6	70.1
maximum	49.9	154.2	104.3
isokinetic joint			
minimum	111.4	140.7	29.3
average	101.7	153.2	51.5
maximum	96.4	170.4	74.0

shoulder flexion			
angle	from (°)	to (°)	range (°)
crank	5.0	125.0	120.0
isokinetic crank			
minimum	24.8	89.8	65.8
average	12.2	114.1	101.9
maximum	5.3	125.9	120.6
isokinetic joint			
minimum	39.4	76.2	36.8
average	24.9	97.3	72.4
maximum	- 3.6	115.3	118.9

angle	hip extension		range (°)
	from (°)	to (°)	
crank	68.0	182.0	114.0
isokinetic crank			
minimum	95.5	169.0	73.5
average	77.2	175.9	98.7
maximum	68.1	182.3	114.2
isokinetic joint			
minimum	131.4	169.3	37.9
average	121.5	180.9	59.4
maximum	111.1	190.8	79.7

Appendix 2d

The eighteen parameters for each muscle model

parameter	hip extension	hip flexion	shoulder extension	shoulder flexion
x_1	- 152.56	- 178.04	- 43.48	- 156.38
x_2	340.93	271.08	100.13	332.45
x_3	565.73	210.16	141.76	119.02
x_4	- 4.88	6.84	- 186.91	155.42
x_5	10.60	- 9.76	686.88	443.72
x_6	27.39	5.18	- 16.68	872.72
x_7	0.28	0.08	2.37	- 0.57
x_8	- 1.27	- 0.11	- 8.23	5.96
x_9	1.51	0.04	10.61	2.20
x_{10}	0.01	0.04	0.03	1.01
x_{11}	- 0.03	- 0.06	- 0.04	- 1.12
x_{12}	0.03	0.03	0.03	0.31
x_{13}	- 74.68	167.04	- 221.07	424.04
x_{14}	559.91	- 136.54	388.99	- 808.51
x_{15}	- 834.81	39.23	540.81	392.70
x_{16}	- 0.04	- 3.24	1.04	0.25
x_{17}	- 2.69	6.61	- 3.04	0.23
x_{18}	8.89	- 1.00	2.79	0.10

APPENDIX 3

- Appendix 3a Anthropometric data taken from subjects jb01 and tv01
- Appendix 3b Written consent form signed by the subject
- Appendix 3c Three-dimensional locations of the 28 calibration markers
- Appendix 3d Calibration data obtained from the loading of the load cell
- Appendix 3e Average ADC counts for vertical loading
- Appendix 3f Average ADC counts for horizontal loading
- Appendix 3g Average ADC counts for vertical loading with two points
of support

Appendix 3a

Anthropometric measurements taken from subject jb01

ANTHROPOMETRIC MEASUREMENTS FOR SEGMENTAL INERTIA PARAMETERS

NAME AGE HEIGHT DATE
 MEASURER WEIGHT

All measurements in millimetres

TORSO

level	hip	umbilicus	ribcage	nipple	shoulder	neck	→ nose	ear	top	
length	0	182	230	390	485	569	0	119	149	259
perimeter	890	740	781	952		381		481	564	
width	298	276	265	300	280					
depth					196					

LEFT ARM

level	shoulder	midarm	elbow	forearm	wrist	→ thumb	knuckle	nails	
length	0		231	300	485	0	55	87	178
perimeter	362	291	256	270	171		252	218	112
width					57		101	82	48

RIGHT ARM

level	shoulder	midarm	elbow	forearm	wrist	→ thumb	knuckle	nails	
length	0		226	298	468	0	57	98	185
perimeter	372	290	264	260	169		250	197	113
width					58		101	80	47

LEFT LEG

level	hip	crotch	midthigh	knee	calf	ankle	→ heel	arch	ball	nails	
length	0	99		372	496	774	0	27	132	194	
perimeter		515	435	321	347	202		293	230	222	127
width									90	50	
depth								110			

RIGHT LEG

level	hip	crotch	midthigh	knee	calf	ankle	→ heel	arch	ball	nails	
length	0	101		375	498	778	0	27	130	195	
perimeter		527	445	326	347	202		291	229	219	124
width									85	49	
depth								111			

Appendix 3a

Anthropometric measurements taken from subject tv01

ANTHROPOMETRIC MEASUREMENTS FOR SEGMENTAL INERTIA PARAMETERS

NAME AGE HEIGHT DATE
 MEASURER WEIGHT

All measurements in millimetres

TORSO

level	hip	umbilicus	ribcage	nipple	shoulder	neck	→ nose	ear	top	
length	0	145	284	360	466	555	0	98	162	268
perimeter	870	744	760	980		402		495	584	
width	313	285	283	256	331					
depth					200					

LEFT ARM

level	shoulder	midarm	elbow	forearm	wrist	→ thumb	knuckle	nails	
length	0		250	314	509	0	55	92	180
perimeter	395	285	270	280	175		250	209	115
width					59		99	87	49

RIGHT ARM

level	shoulder	midarm	elbow	forearm	wrist	→ thumb	knuckle	nails	
length	0		258	323	520	0	53	92	180
perimeter	387	289	280	275	186		243	208	113
width					61		100	89	49

LEFT LEG

level	hip	crotch	midhigh	knee	calf	ankle	→ heel	arch	ball	nails	
length	0	65		395	540	795	0	28	140	202	
perimeter		537	476	329	350	203		310	240	239	147
width									100	65	
depth							119				

RIGHT LEG

level	hip	crotch	midhigh	knee	calf	ankle	→ heel	arch	ball	nails	
length	0	63		411	555	805	0	28	140	202	
perimeter		538	485	336	365	205		316	232	240	148
width									101	62	
depth							120				

Appendix 3b

Written consent form signed by the subject

PURPOSE

To obtain anthropometric and kinematic data of a gymnast during giant circles on high bar. In order to develop and evaluate a mathematical model of this activity.

PROCEDURES

Video cameras will be used to collect information during the performance of the giant circles on high bar, in addition forces and torques at the bar will be measured using strain gauges bonded to the high bar. A number of trials will be requested, with suitable breaks to minimise fatigue and boredom. Anthropometric data will be collected using tape measures and specialist anthropometers.

QUESTIONS

The researcher will be pleased to answer any questions which you may have at any time.

WITHDRAWAL

You are free to withdraw from the study at any time whatever reason without prejudice.

CONFIDENTIALITY

Your identity will remain confidential in any material resulting from this work.

I have read and understood the information on this form and agree to participate in this study. As far as I am aware I do not have any injury nor infirmity which would be affected by the procedures outlined.

Name..... Name.....

Signed.....(gymnast) Signed.....(parent)

In the presence of:

Name.....

Signed.....(coach) Date.....

Appendix 3c

Three-dimensional locations of the 28 calibration markers

Marker	Co-ordinate (m)		
	X	Y	Z
1	- 0.500	- 0.500	0.596
2	- 0.500	- 0.500	3.171
3	- 0.500	- 0.500	4.660
4	- 0.500	- 2.000	0.596
5	- 0.500	- 2.000	3.171
6	- 0.500	- 2.000	4.660
7	0.500	- 2.000	0.596
8	0.500	- 2.000	3.171
9	0.500	- 2.000	4.660
10	0.500	- 0.500	0.596
11	0.500	- 0.500	3.171
12	0.500	- 0.500	4.660
13	0.500	0.500	0.596
14	0.500	0.500	3.171
15	0.500	0.500	4.660
16	0.500	2.000	0.596
17	0.500	2.000	3.171
18	0.500	2.000	4.660
19	- 0.500	2.000	0.596
20	- 0.500	2.000	3.171
21	- 0.500	2.000	4.660
22	- 0.500	0.500	0.596
23	- 0.500	0.500	3.171
24	- 0.500	0.500	4.660
25	1.245	0.000	0.513
26	1.245	0.000	2.322
27	- 1.245	0.000	0.513
28	- 1.245	0.000	2.322

Appendix 3d

Calibration data obtained from the loading of the load cell

load [kN]	amplifier reading	micro-strain
0.0	- 500	0
0.5	- 486	14
1.0	- 475	25
1.5	-462	38
2.0	-450	50
2.5	- 437	63
3.0	- 426	74
3.5	- 415	85
4.0	- 403	97
4.5	- 392	108
5.0	- 380	120
5.5	-369	131
6.0	- 358	142
6.5	- 347	153
7.0	- 335	165
7.5	- 321	179
8.0	- 312	188

Appendix 3e

Average ADC counts for vertical loading

trial	load [kN]	amplifier reading	ADC counts		comments
			chan1	chan3	
calv00c	0.0	NA	28	18	no chains
calv01c	NA	- 500	- 164	- 176	loops and chains
calv05c	0.5	- 486	- 2648	- 2642	loading
calv10c	1.0	- 475	- 4670	- 4658	
calv15c	1.5	- 462	- 7188	- 7178	
calv20c	2.0	- 450	- 9254	- 9251	
calv25c	2.5	- 437	- 11397	-11386	
calv30c	3.0	- 426	- 13069	- 13049	
calv30cu	3.0	- 426	- 13415	- 13400	unloading
calv25cu	2.5	- 437	- 11859	-11850	
calv20cu	2.0	- 450	- 9771	- 9786	
calv15cu	1.5	- 462	- 7664	- 7669	
calv10cu	1.0	- 475	- 5185	- 5186	
calv05cu	0.5	- 486	- 3038	- 3037	
calv01cu	NA	- 500	- 211	- 209	loops and chains
calv00cu	0.0	NA	12	6	no chains
calv01d	NA	- 500	- 210	- 215	loops and chains
calv05d	0.5	- 486	- 2719	- 2698	loading
calv10d	1.0	- 475	- 4809	- 4787	
calv15d	1.5	- 462	- 7258	- 7205	
calv20d	2.0	- 450	- 9354	- 9295	
calv25d	2.5	- 437	- 11412	-11337	
calv30d	3.0	- 426	- 13015	- 12945	
calv25du	2.5	- 437	- 11765	-11686	
calv20du	2.0	- 450	- 9746	- 9686	
calv15du	1.5	- 462	- 7703	- 7657	
calv10du	1.0	- 475	- 5145	- 5125	
calv05du	0.5	- 486	- 2997	- 2984	
calv01du	NA	- 500	- 299	- 306	loops and chains
calv00du	0.0	NA	27	14	no chains

Appendix 3f

Average ADC counts for horizontal loading

trial	load [kN]	amplifier reading	ADC counts		comments
			chan1	chan3	
calh00c	0.0	NA	49	51	no chains
calh05c	0.5	- 486	- 2879	- 2934	loading
calh10c	1.0	- 475	- 5164	- 5152	
calh15c	1.5	- 462	- 7718	- 7766	
calh20c	2.0	- 450	- 9882	- 9863	
calh25c	2.5	- 437	- 12109	-12047	
calh20cu	2.0	- 450	- 10215	- 10168	unloading
calh15cu	1.5	- 462	- 8231	- 8218	
calh10cu	1.0	- 475	- 5444	- 5494	
calh05cu	0.5	- 486	- 3152	- 3165	
calh10d	1.0	- 475	- 5240	- 5225	loading
calh15d	1.5	- 462	- 7862	- 7830	
calh20d	2.0	- 450	- 9879	- 9800	
calh25d	2.5	- 437	- 12016	-11985	
calh20du	2.0	- 450	- 10380	- 10369	unloading
calh15du	1.5	- 462	- 8262	- 8281	
calh10du	1.0	- 475	- 5542	- 5573	
calh05du	0.5	- 486	- 3098	- 3115	
calh00du	0.0	NA	215	230	no chains

Appendix 3g

Average ADC counts for vertical loading with two points of support

trial	load [kN]	amplifier reading	ADC counts		comments
			chan1	chan3	
calv201	NA	- 500	- 387	- 431	loops and chains
calv205	0.5	- 486	- 2896	- 2914	loading
calv210	1.0	- 475	- 4918	- 4949	
calv215	1.5	- 462	- 7359	- 7415	
calv220	2.0	- 450	- 9508	- 9576	
calv225	2.5	- 437	- 11601	-11679	
calv220u	2.0	- 450	- 9847	- 9891	unloading
calv215u	1.5	- 462	- 7800	- 7855	
calv210u	1.0	- 475	- 5348	- 5390	
calv205u	0.5	- 486	- 3226	- 3260	
calv201u	NA	- 500	- 483	- 492	loops and chains
calvbaru		- 500	- 79	- 79	second bar only
calv200u	0.0	NA	13	17	no chains

APPENDIX 4

Appendix 4a Eleven segment inertia data for subject jb01

Appendix 4b Eleven segment inertia data for subject tv01

Appendix 4a

Eleven segment inertia data for subject jb01

SEGMENTAL INERTIA PARAMETER VALUES

UNITS: MASS IN KG

DISTANCE IN METRES

MOMENT OF INERTIA IN $\text{KG}\cdot\text{M}^2$

FORMAT AND SEQUENCE OF DATA PRESENTATION

SEGMENT NAME

MASS, DISTANCE OF MASS CENTRE FROM PROXIMAL JOINT,

SEGMENT LENGTH

PRINCIPAL MOMENTS OF INERTIA

SUBJECT: jb01

HEAD H

4.751 0.130 0.259

0.027 0.027 0.014

TRUNK PTC

28.815 0.277 0.569

0.856 0.903 0.256

UPPER ARM 1A

1.791 0.102 0.231

0.009 0.009 0.002

UPPER ARM 1B

1.801 0.099 0.226

0.009 0.009 0.002

FOREARM 2A

1.252 0.109 0.254

0.006 0.006 0.001

HAND 3A

0.448 0.071 0.178

0.001 0.001 0.000

FOREARM 2B

1.157 0.103 0.242

0.005 0.006 0.001

HAND 3B

0.419	0.072	0.185
0.001	0.001	0.000

THIGH 1J

6.880	0.150	0.372
0.084	0.084	0.021

THIGH 1K

7.194	0.152	0.375
0.089	0.089	0.023

CALF 2J

3.064	0.170	0.402
0.037	0.037	0.004

FOOT 3J

0.702	0.074	0.194
0.002	0.002	0.000

CALF 2K

3.085	0.170	0.403
0.038	0.038	0.004

FOOT 3K

0.692	0.074	0.195
0.002	0.002	0.000

WHOLE BODY

MASS = 62.05 DENSITY = 1.024

Appendix 4b

Eleven segment inertia data for subject tv01

SEGMENTAL INERTIA PARAMETER VALUES

UNITS: MASS IN KG

DISTANCE IN METRES

MOMENT OF INERTIA IN $\text{KG}\cdot\text{M}^2$

FORMAT AND SEQUENCE OF DATA PRESENTATION

SEGMENT NAME

MASS, DISTANCE OF MASS CENTRE FROM PROXIMAL JOINT,

SEGMENT LENGTH

PRINCIPAL MOMENTS OF INERTIA

SUBJECT: tv01

HEAD H

5.530 0.134 0.268

0.034 0.034 0.018

TRUNK PTC

28.920 0.286 0.555

0.829 0.877 0.277

UPPER ARM 1A

2.064 0.108 0.250

0.012 0.012 0.003

UPPER ARM 1B

2.156 0.114 0.258

0.014 0.014 0.003

FOREARM 2A

1.358 0.110 0.259

0.007 0.007 0.001

HAND 3A

0.420 0.069 0.180

0.001 0.001 0.000

FOREARM 2B

1.404 0.113 0.262

0.008 0.008 0.001

HAND 3B

0.394	0.066	0.180
0.001	0.001	0.000

THIGH 1J

7.488	0.167	0.395
0.099	0.099	0.023

THIGH 1K

7.924	0.175	0.411
0.113	0.113	0.025

CALF 2J

3.185	0.170	0.400
0.038	0.038	0.004

FOOT 3J

0.792	0.076	0.202
0.002	0.002	0.001

CALF 2K

3.347	0.167	0.394
0.038	0.038	0.005

FOOT 3K

0.800	0.076	0.202
0.002	0.002	0.001

WHOLE BODY

MASS = 65.78 DENSITY = 1.024

